Smart Power Conditioners for Electric Railway Power Grids

Luís André Magalhães de Barros

UMinho | 2023

Universidade do Minho
Escola de Engenharia

Luís André Magalhães de Barros

Smart Power Conditioners for Electric Railway Power Grids

July of 2023

Universidade do Minho
Escola de Engenharia

Luís André Magalhães de Barros

Smart Power Conditioners for Electric Railway Power Grids

Doctoral Thesis
Doctoral Program in Electronics and Computers Engineering
Power Electronics and Energy

Work carried out under the supervision of:
Professor Doctor José Gabriel Oliveira Pinto
(University of Minho)

And
Professor Doctor António José de Pina Martins
(University of Porto)

July of 2023

COPYRIGHTS AND TERMS OF USE OF WORK BY THIRD PARTIES

This is an academic work that can be used by third parties as long as the internationally accepted rules and good practices are respected, with regard to copyright and related rights.

Thus, this work can be used under the terms set out in the license below.

If the user needs permission to be able to make use of the work under conditions not provided for in the indicated license, he must contact the author, through the *RepositóriUM* of the University of Minho.

License granted to users of this work

Attribution-NonCommercial-NoDerivatives
CC BY-NC-ND

https://creativecommons.org/licenses/by-nc-nd/4.0/

Acknowledgment

During this Ph.D. work, I had the honor of the support, encouragement, and contribution of several people to whom I would like to thank, specially the following people:

To my supervisor Professor Doctor Gabriel Pinto for all the support and dedication provided since the beginning of this challenge. I also thank him for the critical spirit, demand, and rigor always showed, not forgetting his friendly words in the worst moments.

To my co-supervisor Professor Doctor António Pina Martins, for all the critical spirit, rigor, and questions left during the work that contributed to more critical analysis and a better perception of various concepts.

To all the laboratory colleagues who shared the same space over these last year, by the spirit of mutual help provided, and for the availability to discuss ideas, clarify doubts and solve problems.

Special thanks to my friends Brutus: Cabo, Prime, Pires, Rapha, Smile and Xeixas, for all the support and encouragement, always being there even when I wasn't there.

To my academic godfather Bruno Duarte, for all the help and friendship, shown throughout this long academic path.

Special thanks to my family for the support and the good times. Thanks to my parents for being one of the main pillars for the realization of this thesis, by the encouragement words, and emotional support. To my brother Davide for all the affection shown, as well as the mutual and contagious passion in the field of electronics, who always shared useful knowledge that contributed to a practical approach with greater confidence. To my nephew Renato for all the moments of joy provided.

This work has been supported by FCT – *Fundação para a Ciência e Tecnologia*, within the R&D Units Project Scope UIDB/00319/2020. Mr. Luis A. M. Barros is supported by the doctoral scholarship PD/BD/143006/2018, granted by the Portuguese FCT foundation.

STATEMENT OF INTEGRITY

I hereby declare having conducted this academic work with integrity. I confirm that I have not used plagiarism or any form of undue use of information or falsification of results along the process leading to its elaboration.

I further declare that I have fully acknowledged the Code of Ethical Conduct of the University of Minho.

Abstract

Railway transport presents itself as one of the greatest economic and social drivers of several nations in the world. Furthermore, it is considered the safest means of land transport, with the electric rail system being efficient and environmentally friendly. However, for the inclusion of more and larger electric locomotives, it is necessary to increase the capacity of the railway supply systems.

This doctoral thesis intends to contribute to the development of power electronics solutions capable of increasing the capacity of railway supply systems. As such, a power electronics converter connected in a neutral section located between two traction power substations (TPS) is proposed. The proposed algorithm makes it possible to dynamically balance the average active powers of the two substations, mitigating overload problems. In the event of deceleration or braking of a locomotive on one side, it is possible to use the energy from this regenerative braking to assist another locomotive on the other side of the neutral section. Moreover, the proposed solution still presents the interface with a photovoltaic solar system and an energy storage system. In this way, it is possible to minimize energy dependence on the power grid, as well as to include renewable energy sources. The storage system also makes it possible to store surplus production or energy from regenerative braking for later use.

The proposed solution is validated with the help of computer simulations considering a real implementation scale. The simulation model is based on cascaded multilevel modular converters, with each submodule also featuring solid-state transformers. Considering a reduced-scale prototype developed in the laboratory, computer simulations of the prototype are also presented and discussed.

The document also presents a chapter that portrays all the steps taken for the implementation of the reduced-scale sectioning post-Rail Power Conditioner (sp-RPC) laboratory prototype. Once its implementation was completed, its experimental validation was carried out, proving the correct functioning of the system based on the proposed algorithm.

Keywords: Cascade multilevel modular converters, photovoltaic solar system, energy storage system, railway system, regenerative braking.

Keywords: Cascade multilevel modular converters, photovoltaic solar system, energy storage system, railway system, regenerative braking.

Resumo

O transporte ferroviário apresenta-se como um dos maiores impulsionadores económicos e sociais de várias nações do mundo. Para além disso, é considerado como o meio de transporte terrestre mais seguro, sendo o sistema ferroviário elétrico eficiente e amigo do ambiente. Contudo, para a inclusão de mais e maiores locomotivas elétricas é necessário aumentar a capacidade dos sistemas de alimentação ferroviários.

Esta tese de doutoramento pretende contribuir com o desenvolvimento de soluções de eletrónica de potência capazes de aumentar a capacidade dos sistemas de alimentação ferroviários. Como tal, é proposto um conversor de eletrónica de potência conectado numa secção neutra que se encontra entre duas subestações de tração de energia. A algoritmia proposta permite equilibrar as potências ativas médias das duas subestações de forma dinâmica, mitigando os problemas de sobrecarga. Na ocorrência de uma desaceleração ou travagem de uma locomotiva num dos lados, é possível utilizar a energia proveniente desta travagem regenerativa para o auxílio de marcha de outra locomotiva existente no outro lado da secção neutra. Não obstante, a solução proposta apresenta ainda a interface com um sistema solar fotovoltaico e um sistema de armazenamento de energia. Desta forma, é possível minimizar a dependência energética da rede elétrica, bem como incluir fontes de energia renovável. O sistema de armazenamento permite ainda armazenar o excedente de produção ou a energia proveniente de uma travagem regenerativa para posterior utilização.

O conceito proposto é estudado com auxílio de simulações computacionais considerando uma escala de implementação real. O modelo de simulação é baseado em conversores modulares multinível em cascata, sendo que cada sub-módulo apresenta ainda transformadores de estado sólido. Considerando um protótipo de pequena escala desenvolvido em laboratório, simulações computacionais do protótipo são igualmente apresentadas e validadas.

O documento apresenta ainda um capítulo que retrata todos os passos realizados para a implementação do protótipo laboratorial do *sectioning post-Rail Power Conditioner* (sp-RPC) de pequena escala. Uma vez finalizada a sua implementação, procedeu-se à sua validação experimental, comprovando o correto funcionamento do sistema com base na algoritmia proposta.

Palavras-Chave: Conversores modulares multinível em cascata, sistema solar fotovoltaico, sistema de armazenamento de energia, sistema ferroviário, Travagem regenerativa.

Table of Contents

Acknowledgment iii

Abstract v

Resumo vi

Table of Contents vii

List of Figures x

List of Tables xxiii

Acronyms and Abbreviations xxvi

Nomenclature xxviii

Chapter 1 Introduction to the Electrified Railway System 1

1.1 Railway System Technological Development 1
1.1.1 Railway System Extension 2
1.1.2 Railway Transport Activity 4
1.1.3 Safety and Fatalities 5
1.1.4 Energy Demand 6
1.1.5 Environment 7
1.1.6 Population Growth and Economic Development 8
1.1.7 Railway System Evolution Perspectives 9
1.1.8 Discussion of Statistical Data Analysis 12
1.2 Railway in the World, Europe and Portugal 13
1.3 Railway Power System Technologies 17
1.3.1 Conventional Railway Power Systems 18
1.3.2 Railway Power Systems with Three-phase Power Transformers 18
1.3.2.1 V/V Three-phase Power Transformer 19
1.3.2.2 Scott Three-phase Power Transformer 19
1.3.3 The Future of Railway Power System 20
1.3.3.1 Cooperative Strategy 21
1.3.3.2 Energy Storage System 22
On-Board Energy Storage System 23
Off-Board Energy Storage System 24
1.3.3.3 Renewable Energies 25
1.3.3.4 Hybrid Power System 26
1.3.3.5 Wireless Power Transfer 27
1.3.3.6 Magnetic Levitation 27
1.3.3.7 Other Emerging Concepts 27
1.4 The Framework of the Doctoral Thesis 28
1.5 Motivation 30
1.6 Objectives 30
1.7 Thesis Organization and Structure 31
1.8 Publication of Scientific Papers 32
1.8.1 Papers in Journals 33
1.8.2 Book Chapters 33
1.8.3 Papers in Conferences 34
1.8.4 Review of Scientific Papers 35

Chapter 2 Railway Power System, Energy Storage Technologies and Renewable Energy Sources 36

2.1 Introduction 36
2.2 The History of the Electric Railway System 36
2.2.1 Electric Railway System in Direct Current 39
2.2.2 Electric Railway System in Alternating Current 40
2.2.3 Types of Existing Railway Power Systems 40
2.3 Energy Storage System 42
2.3.1 Flywheels Technology 43

2.3.2 Electric Double-Layer Capacitors (EDLC) Technology 45
2.3.3 Batteries Technology 46
2.3.3.1 Electrical Characteristics for a Battery 46
2.3.3.2 Battery Technology 48
Lead-Acid Battery Technology 48
Nickel Battery Technology 50
Lithium-ion (Li-Ion) Battery Technology 51
2.3.3.3 Electrical Equivalent Model of the Battery 52
2.3.4 Comparison Between Different ESS Technologies 53
2.4 Solar Photovoltaic Energy Source 54
2.4.1 Solar Photovoltaic Cells 55
2.4.2 Equivalent Electrical Model for a Solar Photovoltaic Cell 56
2.4.2.1 Influence of the Solar Radiation 58
2.4.2.2 Influence of the Temperature 58
2.4.2.3 Influence of the Shadow 59
2.4.3 Solar Photovoltaic Energy in Railway System 60
2.5 Conclusions 60

Chapter 3 Power Converters Topologies and Control Algorithms 62

3.1 Introduction 62
3.2 Multilevel Power Converter Concept 62
3.2.1 Analysis of Power Semiconductors in the Market 65
3.2.2 Multilevel Power Converter Topologies 67
3.2.2.1 Solid State Transformer 69
3.2.2.2 Full-Bridge Converter 72
3.2.2.3 Cascaded Full-Bridge Converter 73
3.2.2.4 Full-Bridge Converter with Cascaded Transformers 75
3.2.2.5 Dual-Active Bridge Converter 78
3.3 DC-dc Power Converter Topologies for the Solar PV System and BESS 80
3.3.1 Unidirectional dc-dc Boost Power Converter 80
3.3.2 Unidirectional Interleaved dc-dc Boost Power Converter 81
3.3.3 Bidirectional dc-dc Power Converter 82
Boost Operating Mode 83
Buck Operating Mode 84
3.3.4 Bidirectional Interleaved dc-dc Power Converter 84
3.4 Control Algorithms 85
3.4.1 Synchronization Technique with the Catenary Voltage 85
3.4.2 Current Control Techniques 86
3.4.2.1 Periodic Sampling 86
3.4.2.2 PI Current Control 87
3.4.2.3 Predictive Current Control 88
3.4.3 PWM Techniques for MLC 89
3.4.4 BESS Control Algorithms 90
3.4.5 MPPT Control Algorithms 91
3.4.5.1 Constant Voltage 91
3.4.5.2 Constant Current 92
3.4.5.3 Perturbation & Observation 92
3.4.5.4 Incremental Conductance 93
3.4.5.5 Hill Climbing 95
3.4.5.6 Fuzzy Logic Control 95
3.5 Conclusions 96

Chapter 4 Proposed System, Operation Principle and Simulation Results 99

4.1 Introduction 99
4.2 Proposed sp-RPC Topology based on SST 100
4.3 Control Algorithm Proposed for the sp-RPC based on SST 102
4.4 Simulation Results of the sp-RPC based on SST 110
4.4.1 Simulation Result of the sp-RPC based on SST with Dynamic Control 112
4.4.2 Simulation Result of the sp-RPC based on SST and Solar PV System with Dynamic Control 117
4.4.3 Simulation Result of the sp-RPC based on SST and BESS with Dynamic Control 120
4.4.4 Simulation Result of the sp-RPC based on SST with Solar PV System and BESS with Dynamic Control 122
4.4.5 Performance Analyses of the sp-RPC Based on Simulation Results 125
4.5 Control Algorithm and sp-RPC Reduced-Scale Prototype used for Simulation Validation 130
4.6 Reduced-Scale Prototype Simulations Results 133
4.6.1 Simulation Result of the Reduced-Scale Prototype sp-RPC with Dynamic Control 135

4.6.2 Simulation Result of the Reduced-Scale Prototype sp-RPC and Solar PV System with Dynamic Control 142
4.6.3 Simulation Result of the Reduced-Scale Prototype sp-RPC and BESS with Dynamic Control 146
4.6.4 Simulation Result of the Reduced-Scale Prototype sp-RPC with Solar PV System and BESS with Dynamic Control 150
4.6.5 Performance Analyses of the Reduced-Scale sp-RPC based on Simulation Results 153
4.7 Conclusions 158

Chapter 5 Development of a Reduced-Scale Laboratory Prototype of an sp-RPC 161

5.1 Introduction 161
5.2 Control System Hardware 164
5.2.1 Current Sensors 164
5.2.2 Voltage Sensors 165
5.2.3 External ADC 167
5.2.4 F28379D Control Card 174
5.2.5 External DAC 181
5.2.6 Command Board 181
5.2.7 Gate Driver Board 182
5.2.8 8 Relay PCB 184
5.2.9 User Interface PCB 185
5.3 Power System Hardware 186
5.3.1 Inductor for the dc-dc Power Converters 189
5.3.2 Inductor for the Connection with the Catenaries 192
5.3.3 Cascade Power Transformer 193
5.3.3.1 Theoretical Study of Transformers 193
5.3.3.2 Equivalent Transformer Model and Analysis Methodology 194
5.3.3.3 Implemented Transformers 196
5.3.3.4 Final Analysis and Comparison Between Transformers 205
5.3.4 IGBT Module and Assembly on the Heatsink 206
5.3.5 The Battery Used on the Prototype 208
5.3.6 Pre-Charge Resistor 209
5.3.7 Capacitor for dc-dc Power Converter 209
5.4 Conclusions 210

Chapter 6 Experimental Results 212

6.1 Introduction 212
6.2 BESS Experimental Validation 212
6.3 Solar PV System Experimental Validation 217
6.4 Cascaded Transformer Converter Experimental Validation 226
6.5 Experimental Validation of the sp-RPC 229
6.5.1 Experimental Validation of the *spRPCx* Standalone Operating Mode 231
6.5.2 Experimental Validation of the *spRPCy* Standalone Operating Mode 234
6.5.3 Experimental Validation of the v_{dc} Regulation 237
6.5.4 Experimental Validation of the sp-RPC with Dynamic Control 239
6.5.5 Experimental Validation of the sp-RPC and Solar PV System with Dynamic Control 251
6.5.6 Experimental Validation of the sp-RPC and BESS with Dynamic Control 259
6.5.7 Experimental Validation of the sp-RPC with Solar PV System and BESS with Dynamic Control 269
6.5.8 Performance Analyses of the sp-RPC Based on Experimental Results 276
6.6 Conclusions 281

Chapter 7 Conclusion 283

7.1 Conclusions 283
7.2 Learning Process 286
7.3 Main Scientific Contributions 287
7.4 Further Investigation 288

References 290

List of Figures

Figure 1.1 – Classification of various railway services and infrastructure. 2
Figure 1.2 – Extension evolution of the railway system from 2000 to 2018 (based on [2]). 2
Figure 1.3 – Evolution of the track length by region and railway type system from 1995 to 2016 (based on [1]). 3
Figure 1.4 – Evolution of the Portuguese railway system length, from 1968 to 2020, and evolution expectation for 2021 and 2022 (based on [4], [5]). 4
Figure 1.5 – Evolution of the passenger and freight rails activities by region, from 1995 to 2016 (based on [1]). 4
Figure 1.6 – Evolution of the passenger activity by rail type, from 1995 to 2016 (based on [1]). 5
Figure 1.7 – Fatality rates for different transport modes (average data from 2015 to 2019 based on [8]). 5
Figure 1.8 – Evolution of the final energy demand in railway transport by region and type, from 2000 to 2017 (based on [1]). 7
Figure 1.9 – Passenger and freight rail transport activity by fuel type (based on [1]). 7
Figure 1.10 – Share of CO_2 emissions from fuel combustion by sector in 2015 (based on [13]). 8
Figure 1.11 – World population by region projections to 2100 (based on [14]). 8
Figure 1.12 – World urban and rural population evolution and projection from 1800 to 2050 (based on [16]). 9
Figure 1.13 – Expectations for the evolution of global conventional passenger railway, freight railway activity and network capacity (based on [1]). 10
Figure 1.14 – Expectations for the evolution of global track-kilometers for metro and high-speed rail (based on [1]). 10
Figure 1.15 – Expectations for the evolution of the urban rail activity by region (based on [1]). 11
Figure 1.16 – Evolution expectation for global energy demand from transport (based on [1]). 11
Figure 1.17 – Expectations for the evolution of energy demand from the rail by region and type of technology (based on [1]). 12
Figure 1.18 – Traction power substations in Portugal [20]. 15
Figure 1.19 – Example of a neutral section in Portugal. 16
Figure 1.20 – Conventional topology using the phase shift method (based on [25]). 18
Figure 1.21 – Topology using three-phase balancing V/V and Scott transformers (based on [25]). 19
Figure 1.22 – Representation of future operating mode trend: cooperative strategy. 21
Figure 1.23 – Representation of future operating mode trend: regenerative braking energy stored in an on-board ESS; and regenerative braking energy stored in an off-board ESS. 22
Figure 1.24 - Representation of some future operating mode trends: catenary free zones. 24
Figure 1.25 – Representation of future operating mode trend: renewable energy interface. 25
Figure 1.26 – Representation of future operating mode trend: sp-RPC balancing active power in different TPS. 28
Figure 1.27 – Representative diagram of the twelve functionalities needed to realize the Shift2Rail paradigm (based on [55]). 29
Figure 2.1 – Topologies of the railway system in Europe (based on [20], [34]). 42
Figure 2.2 – Examples of energy storage technologies. 43
Figure 2.3 – Electric equivalent linear model for the battery. 53
Figure 2.4 – Examples of solar PV cell technologies. 55
Figure 2.5 – Projected solar PV cell efficiency from 2022 to 2025 (based on [85]). 55

Figure 2.6 – Equivalent electrical model of a crystalline-silicon-based solar PV cell. 56

Figure 2.7 – Typical waveforms of a solar PV module (i-V and P-V). 57

Figure 2.8 – Influence of solar radiation on the waveforms of a solar PV module: (a) I-V curves; (b) P-V curves. 58

Figure 2.9 – Influence of the temperature on the waveforms of a solar PV module: (a) I-V curves; (b) P-V curves. 59

Figure 2.10 – Influence of shadows on the waveforms from a solar PV module: (a) I-V curves; (b) P-V curves. 59

Figure 3.1 – Influence of the voltage levels that a power electronics converter can produce on the quality of the synthesized waveform (adapted from [95]). 64

Figure 3.2 – Evolution and the emergence of new MLC topologies. 67

Figure 3.3 – Different classifications of SST considering the power conversion stages: (a) single-stage (type A); (b) two-stage with low voltage dc-link (type B); (c) two-stage with high voltage dc-link (type C); (d) three-stage with high and low voltage dc-link (type D) (based on [179]). 70

Figure 3.4 – Three stage SST with high and low voltage dc-links. 71

Figure 3.5 – Full-bridge topology: (a) electrical schematic; (b) representation of the voltage in the dc-link, V_{DC_Link}, and the output voltage, v_{out}, of the converter. 72

Figure 3.6 – Electric schematic of the cascaded full-bridge power converter. 74

Figure 3.7 – Electrical schematic of the full-bridge with cascaded transformers power converter. 76

Figure 3.8 – Electrical schematic of the dual-active bridge power converter. 78

Figure 3.9 – Typical waveforms on the dual-active bridge with the single-phase shift technique: (a) PWM signals for the full-bridge connected to V_1; (b) PWM signals for the full-bridge connected to V_2; (c) voltage on the primary side of T_{trf1}; (d) voltage on the secondary side of T_{trf1}; (e) current on the primary side of T_{trf1}. 79

Figure 3.10 – Electrical schematic of the unidirectional dc-dc boost power converter. 80

Figure 3.11 – Operating principle and waveforms of the unidirectional dc-dc boost power converter: (a) IGBT S_1 turned-on; (b) IGBT S_1 turned-off; (c) driver signal for S_1; (d) voltage on the inductor L_1; (e) current on the inductor L_1; (f) load current I_2. 81

Figure 3.12 – Electrical schematic of the unidirectional interleaved dc-dc power converter. 82

Figure 3.13 – Electrical schematic of the bidirectional dc-dc power converter. 83

Figure 3.14 – Operating principle of the bidirectional dc-dc power converter during the boost operating mode: (a) IGBT S_2 turned-on; (b) IGBT S_2 turned-off. 83

Figure 3.15 – Operating principle of the bidirectional dc-dc power converter during the buck operating mode: (a) IGBT S_1 turned-on; (b) IGBT S_1 turned-off. 84

Figure 3.16 – Electrical schematic of the bidirectional interleaved dc-dc power converter. 85

Figure 3.17 – Block diagram of the PLL control algorithm (based on [237]). 86

Figure 3.18 – Block diagram of the periodic sampling current control. 87

Figure 3.19 – Block diagram of the PI current control with SPWM. 87

Figure 3.20 – Simplified diagram of the electrical system for the predictive control algorithm. 88

Figure 3.21 – Illustration of the carrier and modulation waveforms for the phase-shift carrier technique. 90

Figure 3.22 – Evolution of the voltage, V_{Bat}, and current, I_{Bat}, of the battery during a constant power, P_{Bat}, charging control algorithm. 91

Figure 3.23 – Flowchart of the P&O MPPT control algorithm. 93

Figure 3.24 – Flowchart of the incremental conductance MPPT algorithm. 94

Figure 3.25 – Flow diagram of the hill climbing MPPT algorithm. 95

Figure 3.26 – Block diagram of the fuzzy logic MPPT algorithm. 96

Figure 4.1 – Electrical schematic of the proposed topology for the sp-RPC with interface for the solar PV system and BESS. 101

Figure 4.2 – Simplified schematic of the proposed topology for the sp-RPC, highlighting the measurement points for the variables involved in the control algorithms. 103

Figure 4.3 – Block diagram of all the control algorithms implemented for the proposed sp-RPC. 104

Figure 4.4 – Flowchart of the control algorithm implemented on the BESS. 106

Figure 4.5 – Block diagram of the control algorithm responsible to regulate the voltage on the common dc-link. 107

Figure 4.6 – Block diagram of the control algorithm responsible to regulate the different dc-link voltages on the *spRPCx*. 107

Figure 4.7 – Block diagram of the control algorithm responsible to balance de power between the different submodules of the *spRPCx*. 108

Figure 4.8 – Simulation results of the power in each TPS, P_{PGx} and P_{PGy}, the voltages, v_{PGx}, v_{PGy}, v_{spRPCx} and v_{spRPCy}, and currents, i_{PGx} and i_{PGy}, for different load conditions: (a) P_{Loadx} = 0.998 MW and P_{Loady} = 6.12 MW; (b) P_{Loadx} = 0.998 MW and P_{Loady} = -3.88 MW; (c) P_{Loadx} = 0.998 MW and P_{Loady} = 4.12 MW; (d) P_{Loadx} = 2.99 MW and P_{Loady} = 0 MW; (e) P_{Loadx} = 2.99 MW and P_{Loady} = 0.99 MW; and (f) P_{Loadx} = 2.00 MW and P_{Loady} = 0.99 MW. 111

Figure 4.9 – Simulation results of the evolution of active powers and voltages over time, for the real scale sp-RPC during the case scenario A: (a) load active power, P_{Loadx} and P_{Loady}, and TPS active power, P_{PGx} and P_{PGy}; (b) sp-RPC active power, P_{spRPCx} and P_{spRPCy}, as well as the reference values, $P_{spRPCx*}$ and $P_{spRPCy*}$; (c) common dc-link voltage, v_{dc}, and dc-link voltages on each submodule, v_{dc_x1} to v_{dc_x6}, and v_{dc_y1} to v_{dc_y6}. 112

Figure 4.10 – Detailed simulation results, during the time interval from 0.3 s to 0.6 s, for the real scale sp-RPC during the case scenario A: (a) TPS voltages, v_{PGx} and v_{PGy}, the output voltages of the *spRPCx* and *spRPCy*, v_{spRPCx} and v_{spRPCy}, and voltages on the dc-link of each submodule, v_{dc_x1} to v_{dc_x6}, and v_{dc_y1} to v_{dc_y6}; (b) the multilevel voltage of the sp-RPC, v_{outx} and v_{outy}, and the voltage of the common dc-link voltage, v_{dc}; (c) TPS currents, i_{PGx} and i_{PGy}, and the output currents of the sp-RPC, i_{spRPCx} and i_{spRPCy}. 113

Figure 4.11 – Detailed simulation results, during the time interval from 0.95 s to 1.25 s, for the real scale sp-RPC during the case scenario A: (a) TPS voltages, v_{PGx} and v_{PGy}, the output voltages of the *spRPCx* and *spRPCy*, v_{spRPCx} and v_{spRPCy}, and voltages on the dc-link of each submodule, v_{dc_x1} to v_{dc_x6}, and v_{dc_y1} to v_{dc_y6}; (b) the multilevel voltage of the sp-RPC, v_{outx} and v_{outy}, and the voltage of the common dc-link voltage, v_{dc}; (c) TPS currents, i_{PGx} and i_{PGy}, and the output currents of the sp-RPC, i_{spRPCx} and i_{spRPCy}. 114

Figure 4.12 – Detailed simulation results, during the time interval from 1.95 s to 2.25 s, for the real scale sp-RPC during the case scenario A: (a) TPS voltages, v_{PGx} and v_{PGy}, the output voltages of the *spRPCx* and *spRPCy*, v_{spRPCx} and v_{spRPCy}, and voltages on the dc-link of each submodule, v_{dc_x1} to v_{dc_x6}, and v_{dc_y1} to v_{dc_y6}; (b) the multilevel voltage of the sp-RPC, v_{outx} and v_{outy}, and the voltage of the common dc-link voltage, v_{dc}; (c) TPS currents, i_{PGx} and i_{PGy}, and the output currents of the sp-RPC, i_{spRPCx} and i_{spRPCy}. 115

Figure 4.13 – Detailed simulation results, during the time interval from 2.9 s to 3 s, for the real scale sp-RPC during the case scenario A: (a) TPS voltages, v_{PGx} and v_{PGy}, the output voltages of the *spRPCx* and *spRPCy*, v_{spRPCx} and v_{spRPCy}, and voltages on the dc-link of each submodule, v_{dc_x1} to v_{dc_x6}, and v_{dc_y1} to v_{dc_y6}; (b) the multilevel voltage of the sp-RPC, v_{outx} and v_{outy}, and the voltage of the common dc-link voltage, v_{dc}; (c) TPS currents, i_{PGx} and i_{PGy}, and the output currents of the sp-RPC, i_{spRPCx} and i_{spRPCy}. 116

Figure 4.14 – Simulation results of the evolution of active powers and voltages over time, for the real scale sp-RPC during the case scenario B: (a) load active power, P_{Loadx} and P_{Loady}, and TPS active power, P_{PGx} and P_{PGy}; (b) sp-RPC active power, P_{spRPCx} and P_{spRPCy}, as well as the reference values, $P_{spRPCx}*$ and $P_{spRPCy}*$; (c) common dc-link voltage, v_{dc}, and dc-link voltages on each submodule, v_{dc_x1} to v_{dc_x6}, and v_{dc_y1} to v_{dc_y6}. 117

Figure 4.15 – Simulation results of the evolution of active powers and voltages over time, for the real scale sp-RPC with the solar PV system during the case scenario A: (a) load active power, P_{Loadx} and P_{Loady}, and TPS active power, P_{PGx} and P_{PGy}; (b) sp-RPC active powers, P_{spRPCx} and P_{spRPCy}, as well as the reference values, $P_{spRPCx}*$ and $P_{spRPCy}*$; (c) solar PV system active power and the maximum power value, P_{PV} and $P_{PV}*$; (d) variation of the common dc-link voltage, v_{dc}, variation of the voltage of the dc-link on each submodule, v_{dc_x1} to v_{dc_x6}, and v_{dc_y1} to v_{dc_y6}. 118

Figure 4.16 – Simulation results of the evolution of active powers and voltages over time, for the real scale sp-RPC with the solar PV system during the case scenario B: (a) load active power, P_{Loadx} and P_{Loady}, and TPS active power, P_{PGx} and P_{PGy}; (b) sp-RPC active powers, P_{spRPCx} and P_{spRPCy}, as well as the reference values, $P_{spRPCx}*$ and $P_{spRPCy}*$; (c) solar PV system active power and the maximum power value, P_{PV} and $P_{PV}*$; (d) variation of

the common dc-link voltage, v_{dc}, variation of the voltage of the dc-link on each submodule, v_{dc_x1} to v_{dc_x6}, and v_{dc_y1} to v_{dc_y6}. 119

Figure 4.17 – Simulation results of the evolution of active powers and voltages over time, for the real scale sp-RPC with the BESS during the case scenario A: (a) load active power, P_{Loadx} and P_{Loady}, and TPS active power, P_{PGx} and P_{PGy}; (b) sp-RPC active powers, P_{spRPCx} and P_{spRPCy}, as well as the reference values, P_{spRPCx}* and P_{spRPCy}*; (c) BESS active power and references value, P_{BESS} and P_{BESS}*; (d) variation of the common dc-link voltage, v_{dc}, variation of the voltage of the dc-link on each submodule, v_{dc_x1} to v_{dc_x6}, and v_{dc_y1} to v_{dc_y6}. 121

Figure 4.18 – Simulation results of the evolution of active powers and voltages over time, for the real scale sp-RPC with the BESS during the case scenario A: (a) load active power, P_{Loadx} and P_{Loady}, and TPS active power, P_{PGx} and P_{PGy}; (b) sp-RPC active powers, P_{spRPCx} and P_{spRPCy}, as well as the reference values, P_{spRPCx}* and P_{spRPCy}*; (c) BESS active power and references value, P_{BESS} and P_{BESS}*; (d) variation of the common dc-link voltage, v_{dc}, variation of the voltage of the dc-link on each submodule, v_{dc_x1} to v_{dc_x6}, and v_{dc_y1} to v_{dc_y6}. 122

Figure 4.19 – Simulation results of the evolution of active powers and voltages over time, for the real scale sp-RPC with the solar PV system and BESS during the case scenario A: (a) load active power, P_{Loadx} and P_{Loady}, and TPS active power, P_{PGx} and P_{PGy}; (b) sp-RPC active powers, P_{spRPCx} and P_{spRPCy}, as well as the reference values, P_{spRPCx}* and P_{spRPCy}*; (c) solar PV system, the BESS active powers and references value for the BESS, P_{PV}, P_{BESS} and P_{BESS}*; (d) variation of the common dc-link voltage, v_{dc}, variation of the voltage of the dc-link on each submodule, v_{dc_x1} to v_{dc_x6}, and v_{dc_y1} to v_{dc_y6}. 123

Figure 4.20 – Simulation results of the evolution of active powers and voltages over time, for the real scale sp-RPC with the solar PV system and BESS during the case scenario B: (a) load active power, P_{Loadx} and P_{Loady}, and TPS active power, P_{PGx} and P_{PGy}; (b) sp-RPC active powers, P_{spRPCx} and P_{spRPCy}, as well as the reference values, P_{spRPCx}* and P_{spRPCy}*; (c) solar PV system, the BESS active powers and references value for the BESS, P_{PV}, P_{BESS} and P_{BESS}*; (d) variation of the common dc-link voltage, v_{dc}, variation of the voltage of the dc-link on each submodule, v_{dc_x1} to v_{dc_x6}, and v_{dc_y1} to v_{dc_y6}. 125

Figure 4.21 – Electrical schematic of the reduced-scale sp-RPC implemented in simulation based on the laboratory prototype. 131

Figure 4.22 – Simulation results of the power in each TPS, P_{PGx} and P_{PGy}, the voltages, v_{PGx}, v_{PGy}, v_{spRPCx} and v_{spRPCy}, and currents, i_{PGx} and i_{PGy}, for different load conditions: (a) P_{Loadx} = 1033.9 W and P_{Loady} = 0 W; (b) P_{Loadx} = 1033.9 W and P_{Loady} = 1995.7 W; (c) P_{Loadx} = 1033.9 W and P_{Loady} = 1519.1 W; (d) P_{Loadx} = 0 W and P_{Loady} = 1519.1 W; (e) P_{Loadx} = 0 W and R_{Loady} = 1995.7 W; and (f) P_{Loadx} = 1033.9 W and P_{Loady} = -2881.5 W. 135

Figure 4.23 – Simulation results of the evolution of active powers and voltages over time, for the reduced-scale sp-RPC during the case scenario A: (a) load active power, P_{Loadx} and P_{Loady}, and TPS active power, P_{PGx} and P_{PGy}; (b) sp-RPC active power, P_{spRPCx} and P_{spRPCy}, and the reference values, P_{spRPCx}* and P_{spRPCy}*; (c) variation of the dc-link voltage, v_{dc}. 136

Figure 4.24 – Detailed simulation results, during the time interval from 0.46 s to 0.56 s, for the reduced-scale sp-RPC during the case scenario A: (a) TPS voltages, v_{PGx} and v_{PGy}, the output voltages of the *spRPCx* and *spRPCy*, v_{spRPCx} and v_{spRPCy}, and dc-link voltage, v_{dc}; (b) the output voltages of the cascaded transformers, v_{trfx} and v_{trfy}; (c) TPS currents, i_{PGx} and i_{PGy}, and the sp-RPC output currents, i_{spRPCx} and i_{spRPCy}. 137

Figure 4.25 – Detailed simulation results, during the time interval from 1.35 s to 1.65 s, for the reduced-scale sp-RPC during the case scenario A: (a) TPS voltages, v_{PGx} and v_{PGy}, the output voltages of the *spRPCx* and *spRPCy*, v_{spRPCx} and v_{spRPCy}, and dc-link voltage, v_{dc}; (b) the output voltages of the cascaded transformers, v_{trfx} and v_{trfy}; (c) TPS currents, i_{PGx} and i_{PGy}, and the sp-RPC output currents, i_{spRPCx} and i_{spRPCy}. 138

Figure 4.26 – Detailed simulation results, during the time interval from 2.4 s to 2.7 s, for the reduced-scale sp-RPC during the case scenario A: (a) TPS voltages, v_{PGx} and v_{PGy}, the output voltages of the *spRPCx* and *spRPCy*, v_{spRPCx} and v_{spRPCy}, and dc-link voltage, v_{dc}; (b) the output voltages of the cascaded transformers, v_{trfx} and v_{trfy}; (c) TPS currents, i_{PGx} and i_{PGy}, and the sp-RPC output currents, i_{spRPCx} and i_{spRPCy}. 138

Figure 4.27 – Detailed simulation results, during the time interval from 3.1 s to 3.4 s, for the reduced-scale sp-RPC during the case scenario A: (a) TPS voltages, v_{PGx} and v_{PGy}, the output voltages of the *spRPCx* and *spRPCy*, v_{spRPCx} and v_{spRPCy}, and dc-link voltage, v_{dc}; (b) the output voltages of the cascaded transformers, v_{trfx} and v_{trfy}; (c) TPS currents, i_{PGx} and i_{PGy}, and the sp-RPC output currents, i_{spRPCx} and i_{spRPCy}. 139

Figure 4.28 – Detailed simulation results, during the time interval from 3.9 s to 4 s, for the reduced-scale sp-RPC during the case scenario A: (a) TPS voltages, v_{PGx} and v_{PGy}, the output voltages of the *spRPCx* and *spRPCy*,

v_{spRPCx} and v_{spRPCy}, and dc-link voltage, v_{dc}; (b) the output voltages of the cascaded transformers, v_{trfx} and v_{trfy}; (c) TPS currents, i_{PGx} and i_{PGy}, and the sp-RPC output currents, i_{spRPCx} and i_{spRPCy}. 140

Figure 4.29 – Simulation results of the evolution of active powers and voltages over time, for the reduced-scale sp-RPC during the case scenario B: (a) load active power, P_{Loadx} and P_{Loady}, and TPS active power, P_{PGx} and P_{PGy}; (b) sp-RPC active power, P_{spRPCx} and P_{spRPCy}, and the reference values, P_{spRPCx}* and P_{spRPCy}*; (c) variation of the dc-link voltage, v_{dc}. 141

Figure 4.30 – Simulation results of the evolution of active powers and voltages over time, for the reduced-scale sp-RPC during the case scenario C: (a) load active power, P_{Loadx} and P_{Loady}, and TPS active power, P_{PGx} and P_{PGy}; (b) sp-RPC active power, P_{spRPCx} and P_{spRPCy}, and the reference values, P_{spRPCx}* and P_{spRPCy}*; (c) variation of the dc-link voltage, v_{dc}. 142

Figure 4.31 – Simulation results of the evolution of active powers and voltages over time, for the reduced-scale sp-RPC with solar PV system during the case scenario A: (a) load active power, P_{Loadx} and P_{Loady}, and TPS active power, P_{PGx} and P_{PGy}; (b) sp-RPC active power, P_{spRPCx} and P_{spRPCy}, and the reference values, P_{spRPCx}* and P_{spRPCy}*; (c) solar PV system active power, P_{PV}; (d) variation of the dc-link voltage, v_{dc}. 143

Figure 4.32 – Simulation results of the evolution of active powers and voltages over time, for the reduced-scale sp-RPC with solar PV system during the case scenario B: (a) load active power, P_{Loadx} and P_{Loady}, and TPS active power, P_{PGx} and P_{PGy}; (b) sp-RPC active power, P_{spRPCx} and P_{spRPCy}, and the reference values, P_{spRPCx}* and P_{spRPCy}*; (c) solar PV system active power, P_{PV}; (d) variation of the dc-link voltage, v_{dc}. 144

Figure 4.33 – Simulation results of the evolution of active powers and voltages over time, for the reduced-scale sp-RPC with solar PV system during the case scenario C: (a) load active power, P_{Loadx} and P_{Loady}, and TPS active power, P_{PGx} and P_{PGy}; (b) sp-RPC active power, P_{spRPCx} and P_{spRPCy}, and the reference values, P_{spRPCx}* and P_{spRPCy}*; (c) solar PV system active power, P_{PV}; (d) variation of the dc-link voltage, v_{dc}. 145

Figure 4.34 – Simulation results of the evolution of active powers and voltages over time, for the reduced-scale sp-RPC with BESS during the case scenario A: (a) load active power, P_{Loadx} and P_{Loady}, and TPS active power, P_{PGx} and P_{PGy}; (b) sp-RPC active power, P_{spRPCx} and P_{spRPCy}, and the reference values, P_{spRPCx}* and P_{spRPCy}*; (c) BESS active power and references value, P_{BESS} and P_{BESS}*; (d) variation of the dc-link voltage, v_{dc}. 147

Figure 4.35 – Simulation results of the evolution of active powers and voltages over time, for the reduced-scale sp-RPC with during the case scenario B: (a) load active power, P_{Loadx} and P_{Loady}, and TPS active power, P_{PGx} and P_{PGy}; (b) sp-RPC active power, P_{spRPCx} and P_{spRPCy}, and reference values, P_{spRPCx}* and P_{spRPCy}*; (c) BESS active power and references value, P_{BESS} and P_{BESS}*; (d) variation of the dc-link voltage, v_{dc}. 148

Figure 4.36 – Simulation results of the evolution of active powers and voltages over time, for the reduced-scale sp-RPC with BESS during the case scenario C: (a) load active power, P_{Loadx} and P_{Loady}, and TPS active power, P_{PGx} and P_{PGy}; (b) sp-RPC active power, P_{spRPCx} and P_{spRPCy}, and the reference values, P_{spRPCx}* and P_{spRPCy}*; (c) BESS active power and references value, P_{BESS} and P_{BESS}*; (d) variation of the dc-link voltage, v_{dc}. 149

Figure 4.37 – Simulation results of the evolution of active powers and voltages over time, for the reduced-scale sp-RPC with solar PV system and BESS during the case scenario A: (a) load active power, P_{Loadx} and P_{Loady}, and TPS active power, P_{PGx} and P_{PGy}; (b) sp-RPC active power, P_{spRPCx} and P_{spRPCy}, and the reference values, P_{spRPCx}* and P_{spRPCy}*; (c) solar PV system and BESS active powers and references value, P_{PV}, P_{BESS} and P_{BESS}*; (d) variation of the dc-link voltage, v_{dc}. 150

Figure 4.38 – Simulation results of the evolution of active powers and voltages over time, for the reduced-scale sp-RPC with solar PV system and BESS during the case scenario B: (a) load active power, P_{Loadx} and P_{Loady}, and TPS active power, P_{PGx} and P_{PGy}; (b) sp-RPC active power, P_{spRPCx} and P_{spRPCy}, and the reference values, P_{spRPCx}* and P_{spRPCy}*; (c) solar PV system and BESS active powers and references value, P_{PV}, P_{BESS} and P_{BESS}*; (d) variation of the dc-link voltage, v_{dc}. 152

Figure 4.39 – Simulation results of the evolution of active powers and voltages over time, for the reduced-scale sp-RPC with solar PV system and BESS during the case scenario C: (a) load active power, P_{Loadx} and P_{Loady}, and TPS active power, P_{PGx} and P_{PGy}; (b) sp-RPC active power, P_{spRPCx} and P_{spRPCy}, and the reference values, P_{spRPCx}* and P_{spRPCy}*; (c) solar PV system and BESS active powers and references value, P_{PV}, P_{BESS} and P_{BESS}*; (d) variation of the dc-link voltage, v_{dc}. 153

Figure 5.1 – Final laboratory prototype of the sp-RPC. 162

Figure 5.2 – Metallic rack of the control system. 163

Figure 5.3 – Additional structure for the BESS, power transformers and inductors used to emulate the line impedance. 163

Figure 5.4 – Block diagram representing the interaction of the different systems that compose the sp-RPC prototype. 164

Figure 5.5 – Current sensor CYHCS-B6-100A: (a) Adaptation PCB; (b) Electric schematic recommended for the sensor. 165

Figure 5.6 – Voltage sensor CYHVS5-25A: (a) Adaptation PCB; (b) Electric schematic recommended for the sensor. 166

Figure 5.7 – PCB developed for the signal conditioning and external ADC: (a) PCB layout; (b) three-dimensional image of the PCB developed in Altium; (c) final PCB developed with all the components soldered. 168

Figure 5.8 – Signal conditioning circuit with MFB second-order filter. 169

Figure 5.9 – Bode and phase diagram of the MFB circuit for different cut-off frequencies. 170

Figure 5.10 – Detail of the phase delay caused by the MFB for different cut-off frequencies. 170

Figure 5.11 – Electric schematic of the hardware error detection circuit implemented on the signal conditioning PCB. 171

Figure 5.12 – Logic circuits implemented on the external ADC PCB: (a) Logic circuit to convert the V_{Error} signal (can vary between +15 V and -15 V) to a logic signal of 5 V; (b) Error memory circuit with NE555; (c) Enable logic circuit. 173

Figure 5.13 – PCB of the F28379D control card used in this work. 174

Figure 5.14 – Adaptation PCB for the *F28379D controlCARD*: (a) PCB layout; (b) 3D view of the PCB developed on Altium; (c) Final PCB assembled with the *F28379D controlCARD* connected; (d) detailed final PCB assembled (Developed by author). 176

Figure 5.15 – Simplified electrical schematic of the system with the main control algorithms. 177

Figure 5.16 – Flow diagram of the code implemented in the DSC: (a) Code flow on the CPU1; (b) Code flow on the CPU2. 178

Figure 5.17 – Block diagram of the state machine implemented on CPU2 of the DSC F28379D. 179

Figure 5.18 – DSC processing times for the CPU1 and CPU2, during the: (a) *State 1*; (b) *State 2*;(c) *State 4*. 180

Figure 5.19 – PCB of the external DAC. 181

Figure 5.20 – Command board PCB: (a) with 6 PWM signal output configuration; (b) with 4 PWM signal output configuration. 182

Figure 5.21 – PCB of the gate driver used on the dc-ac power converters. 183

Figure 5.22 – Driver PCB used on the dc-dc power converters. 183

Figure 5.23 – Detail of the connection for the driver PCB: (a) top view; (b) side view. 184

Figure 5.24 – 8 channel relay PCB. 184

Figure 5.25 – Electric schematic of the relay circuit. 185

Figure 5.26 – Interface user PCB: (a) Top view; (b) Bottom view. 185

Figure 5.27 – Detailed view of the first two platforms of the prototype where the power converters was assembled. 186

Figure 5.28 – Detailed view of the lower platform of the prototype where the electrical connections were assembled. 187

Figure 5.29 – Electrical diagram of the main electrical connections on the laboratory sp-RPC prototype. 188

Figure 5.30 – Electric schematic of the contactor command circuit. 189

Figure 5.31 – Developed inductor for the dc-dc power converters: (a) L_A inductor used on the solar PV system; (b) L_B inductor used on BESS. 191

Figure 5.32 – Saturation current test graph: (a) of the inductor L_A; (b) of the inductor L_B. 192

Figure 5.33 – Inductor used for the line impedance and for coupling the dc-ac power converter. 192

Figure 5.34 – Electric schematic of the equivalent model of a transformer. 194

Figure 5.35 – Developed transformers: (a) Handmade ferrite transformer (T_{trf_f}); (b) Primarsec ferrite transformer (T_{trf_fp}); (c) Handmade amorphous alloy transformer (T_{trf_a}); (d) Primarsec amorphous alloy transformer (T_{trf1}). 197

Figure 5.36 – Analysis of flux density variation for different numbers of ferrite cores that compose the transformer with ferrite cores: (a) beginning of operation at 90°; (b) beginning of operation at 0°. 199

Figure 5.37 – Analysis of flux density variation performed in Ansys Maxwell software tool for the ferrite transformer: (a) Beginning of operation at 90°; (b) Beginning of operation at 0°. 199

Figure 5.38 – First ferrite transformer developed: (a) Ferrite cores used; (b) During the transformer T_{trf_f} assembly process. 200

Figure 5.39 – Results of the ferrite transformer prototype T_{trf_f}: (a) Simulation results considering the real measured values; (b) Detailed simulation; (c) Experimental test; (d) Detailed experimental test. 201

Figure 5.40 – Results of the handmade ferrite transformer T_{trf_fp}: (a) Simulation results considering the real measured values; (b) Detailed simulation; (c) Experimental test; (d) Detailed experimental test. 202

Figure 5.41 – Analysis of flux density variation for different numbers of amorphous alloy cores that compose the transformer with amorphous alloy cores: (a) beginning of operation at 90°; (b) beginning of operation at 0°. 203

Figure 5.42 – Analysis of flux density variation performed in Ansys Maxwell software tool for the amorphous alloy core transformer: (a) Beginning of operation at 90°; (b) beginning of operation at 0°. 203

Figure 5.43 – Amorphous alloy used for the amorphous cascade transformers. 204

Figure 5.44 – Results of the handmade ferrite transformer T_{trf_a}: (a) Simulation results considering the real measured values; (b) Detailed simulation; (c) Experimental test; (d) Detailed experimental test. 204

Figure 5.45 – Experimental result of transformer T_{trf1} developed on Primarsec. 205

Figure 5.46 – IGBT module SKM100GB125DN from *Semikron*. 206

Figure 5.47 – Gate protection PCB for the Semikron IGBT module. 207

Figure 5.48 – EPCOS capacitor used on the dc-link. 208

Figure 5.49 – Battery with the reference IFP 36230218-100Ah used for the BESS. 208

Figure 5.50 – Pre-charge resistor box developed. 209

Figure 5.51 – Developed box with the capacitors used on the dc-dc power converters. 209

Figure 6.1 – Electrical schematic of the bidirectional dc-dc power converter implemented to validate the BESS charging operating mode. 213

Figure 6.2 – Power and current waveforms during the BESS charging operating mode: (a) P_{BESS}* = -700 W; (b) P_{BESS}* = -1000 W (CH1: 500 W/div; CH2: 500 W/div; CH3: 5 A/div; CH4: 5 A/div). 213

Figure 6.3 – Waveforms of power, current and voltages during the charging process of the BESS: (a) varying P_{BESS}* (CH1: 500 W/div; CH2: 500 W/div; CH3: 5 A/div; CH4: 5 A/div); (b) with P_{BESS}* constant during 400 seconds (CH1: 50 V/div; CH2: 25 V/div; CH3: 5 A/div; CH4: 5 A/div). 214

Figure 6.4 – Thermal image of the inductor developed, L_B, for the BESS interface bidirectional dc-dc power converter at the end of the charging experimental tests (Note: this image was taken on 21/02/2022, winter in Portugal). 215

Figure 6.5 – Electrical schematic of the dc-dc power converter implemented to validate the BESS discharging operating mode. 215

Figure 6.6 – Power and current waveforms during the BESS discharging operating mode: (a) P_{BESS}* = 700 W; (b) P_{BESS}* = 1000 W (CH1: 50 W/div; CH2: 50 W/div; CH3: 5 A/div; CH4: 5 A/div). 216

Figure 6.7 – Waveforms of power, current and voltages during the discharging process: (a) varying P_{BESS}* (CH1: 500 W/div; CH2: 500 W/div; CH3: 5 A/div; CH4: 5 A/div); (b) with P_{BESS}* constant during 400 seconds (CH1: 50 V/div; CH2: 25 V/div; CH3: 5 A/div; CH4: 5 A/div). 216

Figure 6.8 – Waveforms of current and voltages during the discharging process: with P_{BESS}* constant during 400 seconds (CH2: 25 V/div; CH3: 5 A/div; CH4: 5 A/div). 217

Figure 6.9 – Thermal image of the inductor developed, L_B, for the BESS interface DC-DC power converter at the end of the discharging experimental tests (Note: this image was taken on 21/02/2022, winter in Portugal). 217

Figure 6.10 – Electrical scheme of the system implemented to emulate the solar PV panel. 218

Figure 6.11 – Comparative study of the MPPT P&O algorithm for different increment values of the reference and different execution frequency values: (a) Response of the MPPT P&O algorithm for a frequency of 500 Hz;

(b) Detail of the response of the MPPT P&O algorithm for a frequency of 500 Hz; (c) Response of the MPPT P&O algorithm for a frequency of 250 Hz; (d) Detail of the response of the MPPT P&O algorithm for a frequency of 250 Hz; (e) Response of the MPPT P&O algorithm for a frequency of 100 Hz; (f) Detail of the response of the MPPT P&O algorithm for a frequency of 100 Hz. 219

Figure 6.12 – Comparative study of the MPPT IC algorithm for different increment values of the reference and different execution frequency values: (a) Response of the MPPT CI algorithm for a frequency of 500 Hz; (b) Detail of the response of the MPPT CI algorithm for a frequency of 500 Hz; (c) Response of the MPPT CI algorithm for a frequency of 250 Hz; (d) Detail of the response of the MPPT CI algorithm for a frequency of 250 Hz; (e) Response of the MPPT CI algorithm for a frequency of 100 Hz; (f) Detail of the response of the MPPT CI algorithm for a frequency of 100 Hz. 220

Figure 6.13 – Comparative study of the MPPT HC algorithm for different increment values of the reference and different execution frequency values: (a) Response of the MPPT HC algorithm for a frequency of 500 Hz; (b) Detail of the response of the MPPT HC algorithm for a frequency of 500 Hz; (c) Response of the MPPT HC algorithm for a frequency of 250 Hz; (d) Detail of the response of the MPPT HC algorithm for a frequency of 250 Hz; (e) Response of the MPPT HC algorithm for a frequency of 100 Hz; (f) Detail of the response of the MPPT HC algorithm for a frequency of 100 Hz. 221

Figure 6.14 – Comparative study of the MPPT FLC algorithm for different increment values of the reference and different execution frequency values: (a) Response of the MPPT FLC algorithm for a frequency of 500 Hz; (b) Detail of the response of the MPPT FLC algorithm for a frequency of 500 Hz; (c) Response of the MPPT FLC algorithm for a frequency of 250 Hz; (d) Detail of the response of the MPPT FLC algorithm for a frequency of 250 Hz; (e) Response of the MPPT FLC algorithm for a frequency of 100 Hz; (f) Detail of the response of the MPPT FLC algorithm for a frequency of 100 Hz. 222

Figure 6.15 – Validation of the MPPT control algorithm with t_i R_{Rh} = 6.55 Ω, t_{ii} R_{Rh} = 4.33 Ω, t_{iii} R_{Rh} = 6.5 Ω: (a) voltages, v_{PV} and v_{Rh}, and power, P_{PV} and P_{Rh}, on power converter and rheostat (CH1: 25 V/div; CH2: 200 W/div; CH3: 25 V/div; CH4: 200 W/div); (b) voltages, v_{PV} and v_{Rh}, on power converter and rheostat, and current and reference current of the power converter, i_{PV} and i_{PV}* (CH1: 25 V/div; CH2: 5 A/div; CH3: 25 V/div; CH4: 5 A/div). 224

Figure 6.16 – Validation of the MPPT control algorithm, considering the voltages v_{PV} and v_{Rh}, on power converter and rheostat, and current and reference current of the power converter, i_{PV} and i_{PV*} , for: (a) R_{Rh} = 6.5 Ω; (b) R_{Rh} = 4.3 Ω. 224

Figure 6.17 – Validation of the voltages and currents in the dc-dc boost power converter during the CI MPPT control algorithm performance: (a) with R_{Rh} = 6.5 Ω; (b) with R_{Rh} = 4.33 Ω. 225

Figure 6.18 – Waveforms of power, P_{PV} and P_{Rh}, and voltages, v_{PV} and v_{Rh}, during the CI MPPT (CH1: 25 V/div; CH2: 200 W/div; CH3: 25 V/div; CH4: 200 W/div). 225

Figure 6.19 – Thermal image of the inductor developed, L_B, for the dc-dc boost power converter at the end of the CI MPPT experimental tests (Note: this image was taken in 04/03/2022, winter in Portugal). 226

Figure 6.20 – Electrical schematic implemented to validate the dc-ac power converter with cascaded transformers. 227

Figure 6.21 – Preliminary tests of the dc-ac multilevel power converter with cascaded transformers open-loop control and without coupling inductor: (a) beginning of the operation on the *x*-side; (b) steady-state operation on the *x*-side; (c) detailed view on steady-state operation on *x*-side; (d) beginning of the operation on the *y*-side; (e) steady-state operation on the *y*-side; (f) detailed view on steady-state operation on *y*-side. 228

Figure 6.22 – Preliminary tests of the dc-ac multilevel power converter with cascaded transformers with open-loop control and using the coupling inductors, L_{PGx} and L_{PGy}: (a) beginning of the operation on the *x*-side; (b) steady-state operation on the *x*-side; (d) beginning of the operation on the *y*-side; (d) steady-state operation on the *y*-side. 229

Figure 6.23 – Electrical schematic of the implemented reduced-scale sp-RPC laboratory prototype. 230

Figure 6.24 – Experimental result of voltages, v_{spRPCx} and v_{trfx}, and currents, i_{spRPCx} and i_{spRPCx}*, of the *spRPCx* starting its operation at 90°. 231

Figure 6.25 – Experimental results obtained with the *spRPCx* in steady-state operation with different reference powers: (a) P_{spRPCx}* = 500 W; (b) P_{spRPCx}* = 750 W; (c) P_{spRPCx}* = 1000 W; and (d) P_{spRPCx}* = 1500 W. 232

Figure 6.26 – Experimental result concerning the analyses of the system response when the reference power is updated: (a) P_{spRPCx}* = 700 W; (b) P_{spRPCx}* = 1400 W; (c) P_{spRPCx}* = 900 W. 233

Figure 6.27 – Experimental result concerning the analyses of the system in steady-state operation for different power references: (a) P_{spRPCx}* = 700 W; (b) P_{spRPCx}* = 1400 W; (c) P_{spRPCx}* = 900 W. 234

Figure 6.28 – Experimental result of voltages, v_{spRPCy} and v_{trfy}, and currents, i_{spRPCy} and i_{spRPCy}*, of the *spRPCy* starting its operation at 90°. 234

Figure 6.29 – Experimental results obtained with the *spRPCy* in steady-state operation with different reference powers: (a) P_{spRPCy}* = 500 W; (b) P_{spRPCy}* = 750 W; (c) P_{spRPCy}* = 1000 W; and (d) P_{spRPCy}* = 1500 W. 235

Figure 6.30 – Experimental result concerning the analyses of the system response when the reference power is updated: (a) P_{spRPCy}* = 700 W; (b) P_{spRPCy}* = 1400 W; (c) P_{spRPCy}* = 900 W. 236

Figure 6.31 – Experimental result concerning the analyses of the system in steady-state operation for different power references: (a) P_{spRPCy}* = 700 W; (b) P_{spRPCy}* = 1400 W; (c) P_{spRPCy}* = 900 W. 236

Figure 6.32 – Experimental results concerning the beginning of operation of the system with the v_{dc} regulation (all the regulation steps). 237

Figure 6.33 – Experimental results concerning the beginning of the operation of the system characterized by the connection of contactor K_1 (first step of the v_{dc} regulation, the pre-charge of the dc-link capacitors). 237

Figure 6.34 – Experimental results concerning the beginning of the operation of the system characterized by activation of the dc-link regulation control algorithm activation (last step of the v_{dc} regulation, with the control algorithm enabled). 238

Figure 6.35 – Experimental results concerning the regulation on the dc-link voltage in steady state. 238

Figure 6.36 – Experimental results concerning the detail of the ripple on the v_{dc} in steady-state (CH5 in ac coupling). 239

Figure 6.37 – Waveforms of active powers, voltages and currents for different load configurations: (a) R_{Loadx} = 12.6 Ω and R_{Loady} = ∞ Ω; (b) R_{Loadx} = ∞ Ω and R_{Loady} = 8.5 Ω; (c) R_{Loadx} = 0 W and R_{Loady} = 6.4 Ω; (d) R_{Loadx} = 12.6 Ω and R_{Loady} = 8.5 Ω; (e) R_{Loadx} = 12.5 Ω and R_{Loady} = 6.4 Ω. 240

Figure 6.38 – Experimental results of the transient response of the sp-RPC (start of operation, R_{Loadx} = 12.6 Ω and R_{Loady} = ∞ Ω): (a) TPS active power, P_{PGx} and P_{PGy}, and sp-RPC active power, P_{spRPCx} and P_{spRPCy}; (b) TPS voltage, v_{PGx} and v_{PGy}, sp-RPC output voltage, v_{spRPCx} and v_{spRPCy}, and dc-link voltage, v_{dc}; (c) TPS currents, i_{PGx} and i_{PGy}, and sp-RPC output currents, i_{spRPCx} and i_{spRPCy}. 241

Figure 6.39 – Experimental results of the detailed steady-state operation of the sp-RPC (start of operation, R_{Loadx} = 12.6 Ω and R_{Loady} = ∞ Ω): (a) TPS active power, P_{PGx} and P_{PGy}, and sp-RPC active power, P_{spRPCx} and P_{spRPCy}; (b) TPS voltage, v_{PGx} and v_{PGy}, sp-RPC output voltage, v_{spRPCx} and v_{spRPCy}, and dc-link voltage, v_{dc}; (c) TPS currents, i_{PGx} and i_{PGy}, and sp-RPC output currents, i_{spRPCx} and i_{spRPCy}. 242

Figure 6.40 – Experimental results of the transient response of the sp-RPC (load changed from R_{Loadx} = 12.6 Ω and R_{Loady} = ∞ Ω to R_{Loadx} = 12.6 Ω and R_{Loady} = 8.5 Ω): (a) TPS active power, P_{PGx} and P_{PGy}, and sp-RPC active power, P_{spRPCx} and P_{spRPCy}; (b) TPS voltage, v_{PGx} and v_{PGy}, sp-RPC output voltage, v_{spRPCx} and v_{spRPCy}, and dc-link voltage, v_{dc}; (c) TPS currents, i_{PGx} and i_{PGy}, and sp-RPC output currents, i_{spRPCx} and i_{spRPCy}. 243

Figure 6.41 – Experimental results of the detailed steady-state operation of the sp-RPC (R_{Loadx} = 12.6 Ω and R_{Loady} = 8.5 Ω): (a) TPS active power, P_{PGx} and P_{PGy}, and sp-RPC active power, P_{spRPCx} and P_{spRPCy}; (b) TPS voltage, v_{PGx} and v_{PGy}, sp-RPC output voltage, v_{spRPCx} and v_{spRPCy}, and dc-link voltage, v_{dc}; (c) TPS currents, i_{PGx} and i_{PGy}, and sp-RPC output currents, i_{spRPCx} and i_{spRPCy}. 244

Figure 6.42 – Experimental results of the transient response of the sp-RPC (load changed from R_{Loadx} = 12.6 Ω and R_{Loady} = 8.5 Ω to R_{Loadx} = 12.6 Ω and R_{Loady} = 6.4 Ω): (a) TPS active power, P_{PGx} and P_{PGy}, and sp-RPC active power, P_{spRPCx} and P_{spRPCy}; (b) TPS voltage, v_{PGx} and v_{PGy}, sp-RPC output voltage, v_{spRPCx} and v_{spRPCy}, and dc-link voltage, v_{dc}; (c) TPS currents, i_{PGx} and i_{PGy}, and sp-RPC output currents, i_{spRPCx} and i_{spRPCy}. 245

Figure 6.43 – Experimental results of the detailed steady-state operation of the sp-RPC (R_{Loadx} = 12.6 Ω and R_{Loady} = 6.4 Ω): (a) TPS active power, P_{PGx} and P_{PGy}, and sp-RPC active power, P_{spRPCx} and P_{spRPCy}; (b) TPS voltage, v_{PGx} and v_{PGy}, sp-RPC output voltage, v_{spRPCx} and v_{spRPCy}, and dc-link voltage, v_{dc}; (c) TPS currents, i_{PGx} and i_{PGy}, and sp-RPC output currents, i_{spRPCx} and i_{spRPCy}. 245

Figure 6.44 – Experimental results of the transient response of the sp-RPC (start of operation, R_{Loadx} = ∞ Ω and R_{Loady} = 6.4 Ω): (a) TPS active power, P_{PGx} and P_{PGy}, and sp-RPC active power, P_{spRPCx} and P_{spRPCy}; (b) TPS voltage, v_{PGx} and v_{PGy}, sp-RPC output voltage, v_{spRPCx} and v_{spRPCy}, and dc-link voltage, v_{dc}; (c) TPS currents, i_{PGx} and i_{PGy}, and sp-RPC output currents, i_{spRPCx} and i_{spRPCy}. 246

Figure 6.45 – Experimental results of the detailed steady-state operation of the sp-RPC (R_{Loadx} = ∞ Ω and R_{Loady} = 6.4 Ω): (a) TPS active power, P_{PGx} and P_{PGy}, and sp-RPC active power, P_{spRPCx} and P_{spRPCy}; (b) TPS voltage, v_{PGx} and v_{PGy}, sp-RPC output voltage, v_{spRPCx} and v_{spRPCy}, and dc-link voltage, v_{dc}; (c) TPS currents, i_{PGx} and i_{PGy}, and sp-RPC output currents, i_{spRPCx} and i_{spRPCy}. 247

Figure 6.46 – Experimental results of the transient response of the sp-RPC (load changed from R_{Loadx} = ∞ Ω and R_{Loady} = 6.4 Ω to R_{Loadx} = 12.6 Ω and R_{Loady} = 6.4 Ω): (a) TPS active power, P_{PGx} and P_{PGy}, and sp-RPC active power, P_{spRPCx} and P_{spRPCy}; (b) TPS voltage, v_{PGx} and v_{PGy}, sp-RPC output voltage, v_{spRPCx} and v_{spRPCy}, and dc-link voltage, v_{dc}; (c) TPS currents in the, i_{PGx} and i_{PGy}, and sp-RPC output currents, i_{spRPCx} and i_{spRPCy}. 248

Figure 6.47 – Experimental results of the detailed steady-state operation of the sp-RPC (R_{Loadx} = 12.6 Ω and R_{Loady} = 6.4 Ω): (a) TPS active power, P_{PGx} and P_{PGy}, and sp-RPC active power, P_{spRPCx} and P_{spRPCy}; (b) TPS voltage, v_{PGx} and v_{PGy}, sp-RPC output voltage, v_{spRPCx} and v_{spRPCy}, and dc-link voltage, v_{dc}; (c) TPS currents, i_{PGx} and i_{PGy}, and sp-RPC output currents, i_{spRPCx} and i_{spRPCy}. 248

Figure 6.48 – Experimental results of the transient response of the sp-RPC (load changed from R_{Loadx} = 12.6 Ω and R_{Loady} = 6.4 Ω to R_{Loadx} = 12.6 Ω and R_{Loady} = ∞ Ω): (a) TPS active power, P_{PGx} and P_{PGy}, and sp-RPC active power, P_{spRPCx} and P_{spRPCy}; (b) TPS voltage, v_{PGx} and v_{PGy}, sp-RPC output voltage, v_{spRPCx} and v_{spRPCy}, and dc-link voltage, v_{dc}; (c) TPS currents, i_{PGx} and i_{PGy}, and sp-RPC output currents, i_{spRPCx} and i_{spRPCy}....249

Figure 6.49 – Experimental results of the detailed steady-state operation of the sp-RPC (R_{Loadx} = 12.6 Ω and R_{Loady} = ∞ Ω): (a) TPS active power, P_{PGx} and P_{PGy}, and sp-RPC active power, P_{spRPCx} and P_{spRPCy}; (b) TPS voltage, v_{PGx} and v_{PGy}, sp-RPC output voltage, v_{spRPCx} and v_{spRPCy}, and dc-link voltage, v_{dc}; (c) TPS currents, i_{PGx} and i_{PGy}, and sp-RPC output currents, i_{spRPCx} and i_{spRPCy}. 250

Figure 6.50 – Thermal image of the sp-RPC laboratory prototype at the end of the balance experimental tests (Note: this image was taken in 26/04/2022, spring in Portugal) 250

Figure 6.51 – Experimental results of the transient response of the sp-RPC with the initialization of the solar PV system (P_{PV}* = 500 W; R_{Loadx} = 12.6 Ω and R_{Loady} = ∞ Ω): (a) TPS active power, P_{PGx} and P_{PGy}, and sp-RPC active power, P_{spRPCx} and P_{spRPCy}; (b) solar PV system active power, P_{PV}; (c) TPS voltage, v_{PGx} and v_{PGy}, sp-RPC output voltage, v_{spRPCx} and v_{spRPCy}, and dc-link voltage, v_{dc}; (d) TPS currents, i_{PGx} and i_{PGy}, sp-RPC output currents, i_{spRPCx} and i_{spRPCy}, and solar PV system input current, i_{PV}. 252

Figure 6.52 – Experimental results of the detailed steady-state operation of the sp-RPC with the solar PV system (P_{PV}* = 500 W; R_{Loadx} = 12.6 Ω and R_{Loady} = ∞ Ω): (a) TPS active power, P_{PGx} and P_{PGy}, and sp-RPC active power, P_{spRPCx} and P_{spRPCy}; (b) solar PV system active power, P_{PV}; (c) TPS voltage, v_{PGx} and v_{PGy}, sp-RPC output voltage, v_{spRPCx} and v_{spRPCy}, and dc-link voltage, v_{dc}; (d) TPS currents, i_{PGx} and i_{PGy}, sp-RPC output currents, i_{spRPCx} and i_{spRPCy}, and solar PV system input current, i_{PV}. 252

Figure 6.53 – Experimental results of the transient response of the sp-RPC with the initialization of the solar PV system (P_{PV}* = 500 W; R_{Loadx} = ∞ Ω and R_{Loady} = 6.4 Ω): (a) TPS active power, P_{PGx} and P_{PGy}, and sp-RPC active power, P_{spRPCx} and P_{spRPCy}; (b) solar PV system active power, P_{PV}; (c) TPS voltage, v_{PGx} and v_{PGy}, sp-RPC output voltage, v_{spRPCx} and v_{spRPCy}, and dc-link voltage, v_{dc}; (d) TPS currents, i_{PGx} and i_{PGy}, sp-RPC output currents, i_{spRPCx} and i_{spRPCy}, and solar PV system current, i_{PV}. 253

Figure 6.54 – Experimental results of the detailed steady-state operation of the sp-RPC with the solar PV system (P_{PV}* = 500 W; R_{Loadx} = ∞ Ω and R_{Loady} = 6.4 Ω): (a) TPS active power, P_{PGx} and P_{PGy}, and sp-RPC active power, P_{spRPCx} and P_{spRPCy}; (b) solar PV system active power, P_{PV}; (c) voltage in the TPS, v_{PGx} and v_{PGy}, sp-RPC output voltage, v_{spRPCx} and v_{spRPCy}, and dc-link voltage, v_{dc}; (d) TPS currents, i_{PGx} and i_{PGy}, sp-RPC output currents, i_{spRPCx} and i_{spRPCy}, and solar PV system input current, i_{PV}. 254

Figure 6.55 – Experimental results of the transient response of the sp-RPC with the initialization of the solar PV system (P_{PV}* = 500 W; R_{Loadx} = 12.6 Ω and R_{Loady} = 8.5 Ω): (a) TPS active power, P_{PGx} and P_{PGy}, and sp-RPC active power, P_{spRPCx} and P_{spRPCy}; (b) solar PV system active power, P_{PV}; (c) TPS voltage, v_{PGx} and v_{PGy}, sp-RPC output voltage, v_{spRPCx} and v_{spRPCy}, and dc-link voltage, v_{dc}; (d) TPS currents, i_{PGx} and i_{PGy}, sp-RPC output currents, i_{spRPCx} and i_{spRPCy}, and solar PV system current, i_{PV}. 255

Figure 6.56 – Experimental results of the detailed steady-state operation of the sp-RPC with the solar PV system (P_{PV}* = 500 W; R_{Loadx} = 12.6 Ω and R_{Loady} = 8.5 Ω): (a) TPS active power, P_{PGx} and P_{PGy}, and sp-RPC active power, P_{spRPCx} and P_{spRPCy}; (b) solar PV system active power, P_{PV}; (c) voltage in the TPS, v_{PGx} and v_{PGy}, sp-RPC output voltage, v_{spRPCx} and v_{spRPCy}, and dc-link voltage, v_{dc}; (d) TPS currents, i_{PGx} and i_{PGy}, sp-RPC output currents, i_{spRPCx} and i_{spRPCy}, and solar PV system current, i_{PV}. 256

Figure 6.57 – Experimental results of the transient response of the sp-RPC with the initialization of the solar PV system (P_{PV}* = 900 W; R_{Loadx} = 12.6 Ω and R_{Loady} = 6.4 Ω): (a) TPS active power, P_{PGx} and P_{PGy}, and sp-RPC active power, P_{spRPCx} and P_{spRPCy}; (b) solar PV system active power, P_{PV}; (c) TPS voltage, v_{PGx} and v_{PGy}, sp-RPC output voltage, v_{spRPCx} and v_{spRPCy}, and dc-link voltage, v_{dc}; (d) TPS currents, i_{PGx} and i_{PGy}, sp-RPC output currents, i_{spRPCx} and i_{spRPCy}, and solar PV system current, i_{PV}. 257

Figure 6.58 – Experimental results of the detailed steady-state operation of the sp-RPC with the solar PV system (P_{PV}* = 900 W; R_{Loadx} = 12.6 Ω and R_{Loady} = 6.4 Ω): (a) TPS active power, P_{PGx} and P_{PGy}, and sp-RPC active power, P_{spRPCx} and P_{spRPCy}; (b) solar PV system active power, P_{PV}; (c) voltage in the TPS, v_{PGx} and v_{PGy}, sp-RPC output voltage, v_{spRPCx} and v_{spRPCy}, and dc-link voltage, v_{dc}; (d) TPS currents, i_{PGx} and i_{PGy}, sp-RPC output currents, i_{spRPCx} and i_{spRPCy}, and solar PV system current, i_{PV}. 258

Figure 6.59 – Experimental results of the transient response of the sp-RPC with the solar PV system being turned off (P_{PV}* = 900 W; R_{Loadx} = 12.6 Ω and R_{Loady} = 6.4 Ω): (a) TPS active power, P_{PGx} and P_{PGy}, and sp-RPC active power, P_{spRPCx} and P_{spRPCy}; (b) solar PV system active power, P_{PV}; (c) TPS voltage, v_{PGx} and v_{PGy}, sp-RPC output voltage, v_{spRPCx} and v_{spRPCy}, and dc-link voltage, v_{dc}; (d) TPS currents, i_{PGx} and i_{PGy}, sp-RPC output currents, i_{spRPCx} and i_{spRPCy}, and solar PV system current, i_{PV}. 258

Figure 6.60 – Experimental results of the transient response of the sp-RPC with the initialization of the BESS (P_{PV}* = 0 W; P_{BESS_Max}* = 500 W; R_{Loadx} = 12.6 Ω and R_{Loady} = ∞ Ω): (a) TPS active power, P_{PGx} and P_{PGy}, and sp-RPC active power, P_{spRPCx} and P_{spRPCy}; (b) solar PV system, P_{PV}, and BESS active power, P_{BESS}; (c) TPS voltage, v_{PGx} and v_{PGy}, sp-RPC output voltage, v_{spRPCx} and v_{spRPCy}, and dc-link voltage, v_{dc}; (d) TPS currents, i_{PGx} and i_{PGy}, sp-RPC output currents, i_{spRPCx} and i_{spRPCy}, and the BESS current, i_{BESS}. 259

Figure 6.61 – Experimental results of the detailed steady-state operation of the sp-RPC with the BESS (P_{PV}* = 0 W; P_{BESS_Max}* = 500 W; R_{Loadx} = 12.6 Ω and R_{Loady} = ∞ Ω): (a) TPS active power, P_{PGx} and P_{PGy}, and sp-RPC active power, P_{spRPCx} and P_{spRPCy}; (b) solar PV system, P_{PV}, and BESS active power, P_{BESS}; (c) TPS voltage, v_{PGx} and v_{PGy}, sp-RPC output voltage, v_{spRPCx} and v_{spRPCy}, and dc-link voltage, v_{dc}; (d) TPS currents, i_{PGx} and i_{PGy}, sp-RPC output currents, i_{spRPCx} and i_{spRPCy}, and BESS current, i_{BESS}. 260

Figure 6.62 – Experimental results of the transient response of the sp-RPC with P_{BESS}* change (P_{PV}* = 0 W, R_{Loadx} = 12.6 Ω and R_{Loady} = ∞ Ω, with changing from P_{BESS}* = 500 W to P_{BESS}* = -500 W;): (a) TPS active power, P_{PGx} and P_{PGy}, and sp-RPC active power, P_{spRPCx} and P_{spRPCy}; (b) solar PV system, P_{PV}, and BESS active power, P_{BESS}; (c) TPS voltage, v_{PGx} and v_{PGy}, sp-RPC output voltage, v_{spRPCx} and v_{spRPCy}, and dc-link voltage, v_{dc}; (d) TPS currents, i_{PGx} and i_{PGy}, sp-RPC output currents, i_{spRPCx} and i_{spRPCy}, and BESS current, i_{BESS}. 261

Figure 6.63 – Experimental results of the detailed steady-state operation of the sp-RPC with the BESS (P_{PV}* = 0 W; P_{BESS}* = -500 W; R_{Loadx} = 12.6 Ω and R_{Loady} = ∞ Ω): (a) TPS active power, P_{PGx} and P_{PGy}, and sp-RPC active power, P_{spRPCx} and P_{spRPCy}; (b) solar PV system, P_{PV}, and BESS active power, P_{BESS}; (c) TPS voltage, v_{PGx} and v_{PGy}, sp-RPC output voltage, v_{spRPCx} and v_{spRPCy}, and dc-link voltage, v_{dc}; (d) TPS currents, i_{PGx} and i_{PGy}, sp-RPC output currents, i_{spRPCx} and i_{spRPCy}, and BESS current, i_{BESS}. 262

Figure 6.64 – Experimental results of the transient response of the sp-RPC with P_{BESS}* change (P_{PV}* = 0 W, R_{Loadx} = 12.6 Ω and R_{Loady} = ∞ Ω, with changing from P_{BESS} = -500 W to P_{BESS} = 500 W;): (a) TPS active power, P_{PGx} and P_{PGy}, and sp-RPC active power, P_{spRPCx} and P_{spRPCy}; (b) solar PV system, P_{PV}, and BESS active power, P_{BESS}; (c) TPS voltage, v_{PGx} and v_{PGy}, sp-RPC output voltage, v_{spRPCx} and v_{spRPCy}, and dc-link voltage, v_{dc}; (d) TPS currents, i_{PGx} and i_{PGy}, sp-RPC output currents, i_{spRPCx} and i_{spRPCy}, and BESS current, i_{BESS}. 263

Figure 6.65 – Experimental results of the transient response of the sp-RPC with the initialization of the BESS (P_{PV}* = 0 W; P_{BESS}* 500 W; R_{Loadx} = ∞ Ω and R_{Loady} = 6.4 Ω): (a) TPS active power, P_{PGx} and P_{PGy}, and sp-RPC active power, P_{spRPCx} and P_{spRPCy}; (b) solar PV system, P_{PV}, and BESS active power, P_{BESS}; (c) TPS voltage, v_{PGx} and v_{PGy}, sp-RPC output voltage, v_{spRPCx} and v_{spRPCy}, and dc-link voltage, v_{dc}; (d) TPS currents, i_{PGx} and i_{PGy}, sp-RPC output currents, i_{spRPCx} and i_{spRPCy}, and BESS current, i_{BESS}. 264

Figure 6.66 – Experimental results of the detailed steady-state operation of the sp-RPC with the BESS (P_{PV}* = 0 W; P_{BESS}* = 500 W; R_{Loadx} = ∞ Ω and R_{Loady} = 6.4 Ω): (a) TPS active power, P_{PGx} and P_{PGy}, and sp-RPC active power, P_{spRPCx} and P_{spRPCy}; (b) solar PV system, P_{PV}, and BESS active power, P_{BESS}; (c) TPS voltage, v_{PGx} and v_{PGy}, sp-RPC output voltage, v_{spRPCx} and v_{spRPCy}, and dc-link voltage, v_{dc}; (d) TPS currents, i_{PGx} and i_{PGy}, sp-RPC output currents, i_{spRPCx} and i_{spRPCy}, and BESS current, i_{BESS}. 264

Figure 6.67 – Experimental results of the transient response of the sp-RPC with P_{BESS}* change (P_{PV}* = 0 W, R_{Loadx} = ∞ Ω and R_{Loady} = 6.4 Ω, with changing from P_{BESS}* = 500 W to P_{BESS}* = -500 W;): (a) TPS active power, P_{PGx} and P_{PGy}, and sp-RPC active power, P_{spRPCx} and P_{spRPCy}; (b) solar PV system, P_{PV}, and BESS active

power, P_{BESS}; (c) TPS voltage, v_{PGx} and v_{PGy}, sp-RPC output voltage, v_{spRPCx} and v_{spRPCy}, and dc-link voltage, v_{dc}; (d) TPS currents, i_{PGx} and i_{PGy}, sp-RPC currents, i_{spRPCx} and i_{spRPCy}, and BESS current, i_{BESS}.....265

Figure 6.68 – Experimental results of the detailed steady-state operation of the sp-RPC with the BESS (P_{PV}* = 0 W; P_{BESS}* = -500 W; R_{Loadx} = ∞ Ω and R_{Loady} = 6.4 Ω): (a) TPS active power, P_{PGx} and P_{PGy}, and sp-RPC active power, P_{spRPCx} and P_{spRPCy}; (b) solar PV system, P_{PV}, and BESS active power, P_{BESS}; (c) TPS voltage, v_{PGx} and v_{PGy}, sp-RPC output voltage, v_{spRPCx} and v_{spRPCy}, and dc-link voltage, v_{dc}; (d) TPS currents, i_{PGx} and i_{PGy}, sp-RPC output currents, i_{spRPCx} and i_{spRPCy}, and BESS current, i_{BESS}.....266

Figure 6.69 – Experimental results of the transient response of the sp-RPC with P_{BESS*} change (P_{PV}* = 0 W, R_{Loadx} = ∞ Ω and R_{Loady} = 6.4 Ω, with changing from P_{BESS}* = -500 W to P_{BESS}* = 500 W;): (a) TPS active power, P_{PGx} and P_{PGy}, and sp-RPC active power, P_{spRPCx} and P_{spRPCy}; (b) solar PV system, P_{PV}, and BESS active power, P_{BESS}; (c) TPS voltage, v_{PGx} and v_{PGy}, sp-RPC output voltage, v_{spRPCx} and v_{spRPCy}, and dc-link voltage, v_{dc}; (d) TPS currents, i_{PGx} and i_{PGy}, sp-RPC output currents, i_{spRPCx} and i_{spRPCy}, and BESS current, i_{BESS}.....267

Figure 6.70 – Experimental results of the transient response of the sp-RPC with the initialization of the BESS (P_{PV}* = 0 W; P_{BESS_Max}* = 500 W; R_{Loadx} = 12.6 Ω and R_{Loady} = 6.4 Ω): (a) TPS active power, P_{PGx} and P_{PGy}, and sp-RPC active power, P_{spRPCx} and P_{spRPCy}; (b) solar PV system, P_{PV}, and BESS active power, P_{BESS}; (c) TPS voltage, v_{PGx} and v_{PGy}, sp-RPC output voltage, v_{spRPCx} and v_{spRPCy}, and dc-link voltage, v_{dc}; (d) TPS currents, i_{PGx} and i_{PGy}, sp-RPC output currents, i_{spRPCx} and i_{spRPCy}, and BESS current, i_{BESS}. 268

Figure 6.71 – Experimental results of the detailed steady-state operation of the sp-RPC with the BESS (P_{PV}* = 0 W; P_{BESS_Max}* = 500 W; R_{Loadx} = 12.6 Ω and R_{Loady} = 6.4 Ω): (a) TPS active power, P_{PGx} and P_{PGy}, and sp-RPC active power, P_{spRPCx} and P_{spRPCy}; (b) solar PV system, P_{PV}, and BESS active power, P_{BESS}; (c) TPS voltage, v_{PGx} and v_{PGy}, sp-RPC output voltage, v_{spRPCx} and v_{spRPCy}, and dc-link voltage, v_{dc}; (d) TPS currents, i_{PGx} and i_{PGy}, sp-RPC output currents, i_{spRPCx} and i_{spRPCy}, and BESS current, i_{BESS}.....268

Figure 6.72 – Experimental results of the transient response of the sp-RPC with the initialization of the solar PV system (P_{PV}* = 500 W; P_{BESS}* = 0 W; R_{Loadx} = 12.6 Ω and R_{Loady} = 8.5 Ω): (a) TPS active power, P_{PGx} and P_{PGy} and sp-RPC active power, P_{spRPCx} and P_{spRPCy}; (b) solar PV system, P_{PV} and BESS active power, P_{BESS}; (c) TPS voltage, v_{PGx} and v_{PGy}, sp-RPC output voltage, v_{spRPCx} and v_{spRPCy} and dc-link voltage, v_{dc}; (d) TPS currents, i_{PGx} and i_{PGy}, sp-RPC output currents, i_{spRPCx} and i_{spRPCy}, and BESS current, i_{BESS}. 269

Figure 6.73 – Experimental results of the transient response of the sp-RPC and solar PV system with the initialization of the BESS (P_{PV}* = 500 W; P_{BESS_Max}* = 900 W; R_{Loadx} = 12.6 Ω and R_{Loady} = 8.5 Ω): (a) TPS active power, P_{PGx} and P_{PGy}, and sp-RPC active power, P_{spRPCx} and P_{spRPCy}; (b) solar PV system, P_{PV}, and BESS active power, P_{BESS}; (c) TPS voltage, v_{PGx} and v_{PGy}, sp-RPC output voltage, v_{spRPCx} and v_{spRPCy}, and dc-link voltage, v_{dc}; (d) TPS currents, i_{PGx} and i_{PGy}, sp-RPC output currents, i_{spRPCx} and i_{spRPCy}, and BESS current, i_{BESS}. 270

Figure 6.74 – Experimental results of the transient response of the sp-RPC with solar PV system and BESS with the load variation (P_{PV}* = 500 W; P_{BESS_Max}* = 900 W; load changed from R_{Loadx} = ∞ Ω and R_{Loady} = 6.4 Ω to R_{Loadx} = 12.6 Ω and R_{Loady} = 6.4 Ω): (a) TPS active power, P_{PGx} and P_{PGy}, and sp-RPC active power, P_{spRPCx} and P_{spRPCy}; (b) solar PV system, P_{PV}, and BESS active power, P_{BESS}; (c) TPS voltage, v_{PGx} and v_{PGy}, sp-RPC output voltage, v_{spRPCx} and v_{spRPCy}, and dc-link voltage, v_{dc}; (d) TPS currents, i_{PGx} and i_{PGy}, sp-RPC output currents, i_{spRPCx} and i_{spRPCy}, and BESS current, i_{BESS}. 271

Figure 6.75 – Experimental results of the detailed steady-state operation of the sp-RPC with the solar PV system and BESS (P_{PV}* = 500 W; P_{BESS}* = 900 W; R_{Loadx} = 12.6 Ω and R_{Loady} = 6.4 Ω): (a) TPS active power, P_{PGx} and P_{PGy}, and sp-RPC active power, P_{spRPCx} and P_{spRPCy}; (b) solar PV system, P_{PV}, and BESS active power, P_{BESS}; (c) TPS voltage, v_{PGx} and v_{PGy}, sp-RPC output voltage, v_{spRPCx} and v_{spRPCy}, and dc-link voltage, v_{dc}; (d) TPS currents, i_{PGx} and i_{PGy}, sp-RPC output currents, i_{spRPCx} and i_{spRPCy}, and BESS current, i_{BESS}. 272

Figure 6.76 – Experimental results of the detailed steady-state operation of the sp-RPC with the solar PV system and BESS (P_{PV}* = 800 W; P_{BESS_Max}* = 900 W; R_{Loadx} = 12.6 Ω and R_{Loady} = ∞ Ω): (a) TPS active power, P_{PGx} and P_{PGy}, and sp-RPC active power, P_{spRPCx} and P_{spRPCy}; (b) solar PV system, P_{PV}, and BESS active power, P_{BESS}; (c) TPS voltage, v_{PGx} and v_{PGy}, sp-RPC output voltage, v_{spRPCx} and v_{spRPCy}, and dc-link voltage, v_{dc}; (d) TPS currents, i_{PGx} and i_{PGy}, sp-RPC output currents, i_{spRPCx} and i_{spRPCy}, and BESS current, i_{BESS}. 273

Figure 6.77 – Experimental results of the transient response of the sp-RPC with solar PV system and BESS with the load variation (P_{PV}* = 800 W; P_{BESS_Max} = 900 W; load changed from R_{Loadx} = 12.6 Ω and R_{Loady} = ∞ Ω to R_{Loadx} = 12.6 Ω and R_{Loady} = 6.4 Ω): (a) TPS active power, P_{PGx} and P_{PGy}, and sp-RPC active power, P_{spRPCx} and P_{spRPCy}; (b) solar PV system, P_{PV}, and BESS active power, P_{BESS}; (c) TPS voltage, v_{PGx} and v_{PGy}, sp-RPC

output voltage, v_{spRPCx} and v_{spRPCy}, and dc-link voltage, v_{dc}; (d) TPS currents, i_{PGx} and i_{PGy}, and sp-RPC output currents, i_{spRPCx} and i_{spRPCy}, and BESS current, i_{BESS}. 274

Figure 6.78 – Experimental results of the transient response of the sp-RPC with solar PV system and BESS with the load variation (P_{PV}* = 500 W; P_{BESS}* = 900 W; load changed from R_{Loadx} = ∞ Ω and R_{Loady} = 6.4 Ω to R_{Loadx} = 12.6 Ω and R_{Loady} = 6.4 Ω): (a) TPS active power, P_{PGx} and P_{PGy}, and sp-RPC active power, P_{spRPCx} and P_{spRPCy}; (b) solar PV system, P_{PV}, and BESS active power, P_{BESS}; (c) TPS voltage, v_{PGx} and v_{PGy}, sp-RPC output voltage, v_{spRPCx} and v_{spRPCy}, and dc-link voltage, v_{dc}; (d) TPS currents, i_{PGx} and i_{PGy}, sp-RPC output currents, i_{spRPCx} and i_{spRPCy}, and BESS current, i_{BESS}. 275

Figure 6.79 – Experimental results of the detailed steady-state operation of the sp-RPC with the solar PV system and BESS (P_{PV}* = 800 W; P_{BESS}* = 900 W; R_{Loadx} = 12.6 Ω and R_{Loady} = 6.4 Ω): (a) TPS active power, P_{PGx} and P_{PGy}, and sp-RPC active power, P_{spRPCx} and P_{spRPCy}; (b) solar PV system, P_{PV}, and BESS active power, P_{BESS}; (c) TPS voltage, v_{PGx} and v_{PGy}; (d) TPS currents, i_{PGx} and i_{PGy}, and sp-RPC output currents, i_{spRPCx} and i_{spRPCy}; (e) solar PV system, v_{PV}, and BESS input voltages, v_{BESS}; (f) solar PV system, i_{PV}, and BESS input current, i_{BESS}. 276

List of Tables

Table 1.1 – Recent and future trends on high-speed electric locomotives. 13

Table 1.2 – Examples of electric locomotives in circulations in Portugal (based on [22]). 16

Table 1.3 – ESS Technologies (based on [35], [39], [42]). 23

Table 2.1 – Electrical characteristics of the catenary of the railway systems and of the different types of locomotives (based on [34]). 41

Table 2.2 – Extension of the electric railway system in the world (based on [30]). 41

Table 2.3 – Future trends on high-speed electric locomotives [based on [68]]. 53

Table 3.1 – Comparative table of power semiconductor modules used in electrified railway systems. 66

Table 3.2 – Permitted operating states for the full-bridge topology. 73

Table 3.3 – Summary of the power behavior with the incremental conductance MPPT control algorithm. 93

Table 3.4 – Rules for the FLC MPPT control algorithm. 96

Table 4.1 – Main parameters of the topology. 101

Table 4.2 – Main parameters of the electric components used on the sp-RPC topology based on SST. 102

Table 4.3 – Average values of the operating powers and unbalanced values for different load conditions when the sp-RPC is disabled. 126

Table 4.4 – Currents and voltages rms values for different load conditions when the sp-RPC is disabled. 126

Table 4.5 – Average values of the operating powers and unbalanced values for different load conditions when the sp-RPC is enabled (solar PV system and BESS are disabled). 127

Table 4.6 – Currents and voltages rms values for different load conditions when the sp-RPC is enabled (solar PV system and BESS are disabled). 127

Table 4.7 – Average values of the operating powers and unbalanced values for different load conditions when the sp-RPC and the solar PV system are enabled (BESS is disabled). 128

Table 4.8 – Currents and voltages rms values for different load conditions when the sp-RPC and the solar PV system are enabled (BESS is disabled). 128

Table 4.9 – Average values of the operating powers and unbalanced values for different load conditions when the sp-RPC and the BESS are enabled (solar PV system is disabled). 129

Table 4.10 – Currents and voltages rms values for different load conditions when the sp-RPC and the BESS are enabled (solar PV system is disabled). 129

Table 4.11 – Average values of the operating powers and unbalanced values for different load conditions when the sp-RPC, the solar PV system and the BESS are enabled. 130

Table 4.12 – Currents and voltages rms values for different load conditions when the sp-RPC, the solar PV system and the BESS are enabled. 130

Table 4.13 – Main parameters considered for the reduced-scale sp-RPC simulation model. 131

Table 4.14 – Main parameters of the electric components used on the sp-RPC reduced-scale simulation model system. 132

Table 4.15 – Average values of the operating powers and unbalanced values for different load conditions when the sp-RPC is disabled. 154

Table 4.16 – Currents and voltages rms values for different load conditions when the sp-RPC is disabled. 154

Table 4.17 – Average values of the operating powers and unbalanced values for different load conditions when the sp-RPC is enabled (solar PV system and BESS are disabled). 155

Table 4.18 – Currents and voltages rms values for different load conditions when the sp-RPC is enabled (solar PV system and BESS are disabled). 155

Table 4.19 – Average values of the operating powers and unbalanced values for different load conditions when the sp-RPC and the solar PV system are enabled (BESS is disabled). 156

Table 4.20 – Currents and voltages rms values for different load conditions when the sp-RPC and the solar PV system are enabled (BESS is disabled). 156

Table 4.21 – Average values of the operating powers and unbalanced values for different load conditions when the sp-RPC and the BESS are enabled (solar PV system is disabled). 157

Table 4.22 – Currents and voltages rms values for different load conditions when the sp-RPC and the BESS are enabled (solar PV system is disabled). 157

Table 4.23 – Average values of the operating powers and unbalanced values for different load conditions when the sp-RPC, the solar PV system and the BESS are enabled. 158

Table 4.24 – Currents and voltages rms values for different load conditions when the sp-RPC, the solar PV system and the BESS are enabled. 158

Table 5.1 – Electrical specifications of the prototype operating conditions. 164

Table 5.2 – Configuration values and resistors used on the voltage sensors. 167

Table 5.3 – Components and configuration values for the voltages measurement on the external ADC. 172

Table 5.4 – Components and configuration values for differnts currents measurement on the external ADC. 173

Table 5.5 – Main parameters of the developed inductors. 190

Table 5.6 – Main operation parameters for the cascaded transformers. 194

Table 5.7 – Main properties of the ferromagnetic materials used for the cascaded transformers. 196

Table 5.8 – Main technical parameters considered for the implementation of different transformers. 198

Table 5.9 – Parameters of different transformers for the initial analyses. 205

Table 5.10 – Parameters of the amorphous transformers used in the final prototype. 206

Table 5.11 – Operating parameters of the SKM100GB125DN *Semikron* IGBT module at 85°C. 207

Table 6.1 – Values used in the FLC MPPT control algorithm. 222

Table 6.2 – Comparative analysis (average power and stability performance) of different MPPT algorithms for different values of execution frequency and increment value. 223

Table 6.3 – Main parameters of the electric components used on the system prototype. 231

Table 6.4 – Values of the resistive loads used and respective theoretical value of active power consumed in 115 V ac system. 239

Table 6.5 – Average values of the operating powers and unbalanced values for different load conditions when the sp-RPC is disabled. 277

Table 6.6 – Currents and voltages rms values for different load conditions when the sp-RPC is disabled. 277

Table 6.7 – Average values of the operating powers and unbalanced values for different load conditions when the sp-RPC is enabled (solar PV system and BESS are disabled). 278

Table 6.8 – Currents and voltages rms values for different load conditions when the sp-RPC is enabled (solar PV system and BESS are disabled). 278

Table 6.9 – Average values of the operating powers and unbalanced values for different load conditions when the sp-RPC and the solar PV system are enabled (BESS is disabled). 279

Table 6.10 – Currents and voltages rms values for different load conditions when the sp-RPC and the solar PV system are enabled (BESS is disabled). 279

Table 6.11 – Average values of the operating powers and unbalanced values for different load conditions when the sp-RPC and the BESS are enabled (solar PV system is disabled). 280

Table 6.12 – Currents and voltages rms values for different load conditions when the sp-RPC and the BESS are enabled (solar PV system is disabled). 280

Table 6.13 – Average values of the operating powers and unbalanced values for different load conditions when the sp-RPC, the solar PV system and the BESS are enabled. 281

Table 6.14 – Currents and voltages rms values for different load conditions when the sp-RPC, the solar PV system and the BESS are enabled....281

Acronyms and Abbreviations

Acronyms/Abbreviations	Meaning
ac	alternate current (AC at the start of the sentence)
ADC	analog to digital converter
AWG	american wire gauge
BESS	battery energy storage system
°C (unit)	degree Celsius
CLA	control law accelerators
CMOS	complementary metal-oxide-semiconductor
CPU	central processing unit
DAB	dual active bridge
DAC	digital to analog converter
dc	direct current (DC at the start of the sentence)
DSC	digital signal controller
EDLC	electric double-layer capacitor
ESS	energy storage system
FLC	fuzzy logic control
FPGA	field programmable gate array
HVDC	high-voltage direct current
IC	integrated circuit
IGBT	isolated gate bipolar transistor
IGCT	insulated gate collector transistor
LED	light-emitting diode
MFB	multiple feedback
MLC	multilevel converter

MLT	mean length turn [cm]
MOSFET	metal-oxide-semiconductor field-effect transistor
MPL	magnetic path length [cm]
MPP	maximum power point
MPPT	maximum power point tracker
MMC	modular multilevel converter
MMCC	modular multilevel cascaded converter
NS	neutral section
PCB	printed circuit board
PI	proportional integral
PLA	polylactic acid
PLL	phase-locked loop
PSIM	Power Simulation (software)
PV	photovoltaic
PWM	pulse width modulation
SMD	surface mount technology
sPWM	sinusoidal pulse width modulation
SiC	silicon carbide
SST	solid state transformer
STATCOM	static synchronous compensator
STC	standard test conditions
rms	root mean square
RPC	rail power conditioner
sp-RPC	sectioning post – rail power conditioner
THD	total harmonic distortion
TPS	traction power substation
VSI	voltage source inverter

Nomenclature

Symbol	Meaning	Units
i_{BESS}	Instantaneous current on the BESS	A
i_{BESS*}	Instantaneous reference current on the BESS	A
i_{Loadx}	Instantaneous current on the load connected on the *x*-side	A
i_{Loady}	Instantaneous current on the load connected on the *y*-side	A
i_{PGx}	Instantaneous current of the railway power grid (traction power substation) on the *x*-side	A
i_{PGy}	Instantaneous current of the railway power grid (traction power substation) on the *y*-side	A
i_{spRPCx}	Instantaneous current of the *spRPCx* (*x*-side of the sp-RPC)	A
i_{spRPCy}	Instantaneous current of the *spRPCy* (*y*-side of the sp-RPC)	A
i_{PV}	Instantaneous current on the solar PV system	*A*
i_{PV*}	Instantaneous reference current on the solar PV system	*A*
P_{BESS}	Active power on the BESS	W
P_{BESS*}	Active power reference on the BESS	W
P_{PGx}	Active power of the power grid (traction power substation) on the *x*-side	W
P_{PGy}	Active power of the power grid (traction power substation) on the *y*-side	W
P_{PV}	Average active power on the solar PV system	W
P_{spRPCx}	Active power of the *spRPCx* (*x*-side of the sp-RPC)	W
P_{spRPCy}	Active power of the *spRPCy* (*y*-side of the sp-RPC)	W
$P_{spRPCx}*$	Active reference power of the *spRPCx* (*x*-side of the sp-RPC)	W
$P_{spRPCy}*$	Active reference power of the *spRPCy* (*y*-side of the sp-RPC)	W
v_{PGx}	Instantaneous voltage of the railway power grid (traction power substation) on the *x*-side	V
v_{PGy}	Instantaneous voltage of the railway power grid (traction power substation) on the *y*-side	V
v_{spRPCx}	Instantaneous voltage of the *spRPCx* (*x*-side of the sp-RPC)	V
v_{spRPCy}	Instantaneous voltage of the *spRPCy* (*y*-side of the sp-RPC)	V
v_{PV}	Instantaneous voltage on the solar PV system	V
v_{Rh}	Instantaneous voltage on the rheostat	V

v_{BESS}	Instantaneous voltage on the BESS	V
v_{dc}	Instantaneous voltage on the dc-link	V
V_{dc}	Average voltage on the dc-link	V

Chapter 1

Introduction to the Electrified Railway System

1.1 Railway System Technological Development

Since the beginning, human beings have always had the curiosity to move around and discover the world. With this desire, ingenuity, and cunning, the human being went from walking and riding to driving and traveling. This provided a greater diversity of possibilities for employment, study, travel, and interact with people from different cultures. Considering all modes of transport, this Ph.D. thesis document will focus on the railway system.

The railway system has maintained its long-standing position as one of the main pillars for passenger and freight transport. This leads to the fact that the railway system can add a distinct footprint for the economy of each country, which has encouraged investment in the railway sector. The railway system, when compared to other ways to travel, already accounts for almost one-sixth of the long-distance journeys between cities [1]. Nowadays, the high-speed railway system is increasingly attracting interest as a safe, economical, and environmentally-friendly substitute for short-haul intracontinental flights. However, to reduce congestion, pollution, and travel time in metropolitan areas, the metro is a more interesting service for this requirement. On the other hand, regarding freight transport, railway solutions are equipped to transport large quantities of goods. Overall, the electric railway systems are the most efficient and the lowest emitters of carbon dioxide (CO_2) compared to other transportation modes [1].

In the following topics, the different adjectives that characterize the railway system are analyzed. In order to understand the potential and growth of the railway system, three railway infrastructures are considered: conventional; high-speed; and urban (composed of metro train and light railway systems). These infrastructures are illustrated in Figure 1.1. The conventional railway system covers the entire medium and long-distance railway transport system, passenger and freight, whose maximum speed is less than 250 km/h [1]. In turn, the high-speed railway system is considered to be all long-distance infrastructure whose maximum speed exceeds 250 km/h. The metro railway system refers to railway transport systems with high capacity (number of people) and high frequency of use (several stops along the route), having an underground or superficial transport line. The metro railway system is also characterized by being

completely independent of the rest of the railway lines. Finally, the light railway refers to tram and other urban transport systems, with a higher frequency of use at street level, offering less capacity and speed compared to the metro railway system [1].

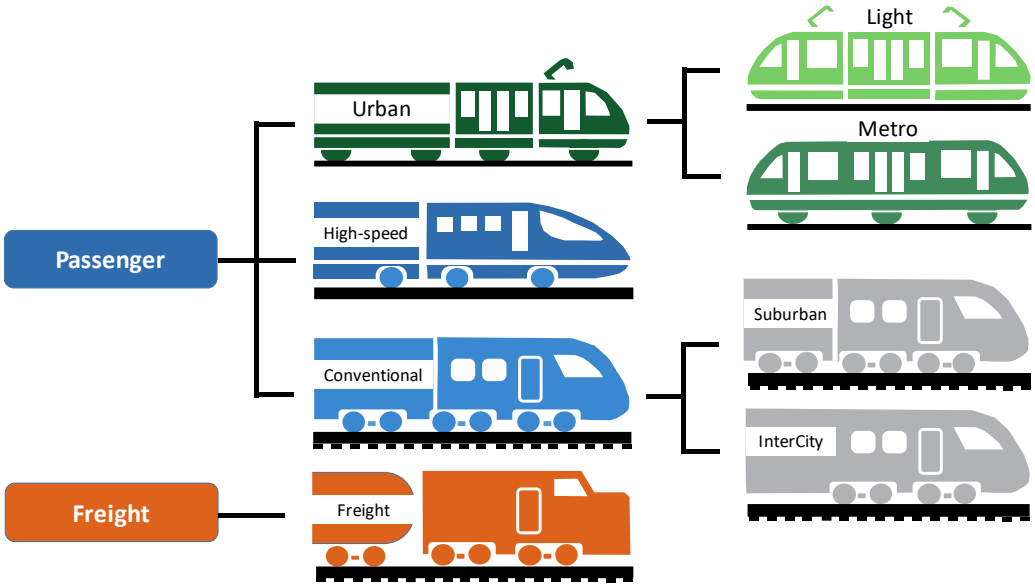

Figure 1.1 – Classification of various railway services and infrastructure.

1.1.1 Railway System Extension

The potential of the railway system to meet the forthcoming mobility demand of the future is enormous. This fact is reflected in the strong investment in railway infrastructure, showing a growth of almost three times between 2005 and 2015 [1]. Analyzing Figure 1.2, representing the evolution of line-km of different types of railway systems, it is possible to see this strong growth essentially in high-speed railway systems, with China being the main driver for this growth. Nevertheless, it is important to note that the rest of the railway systems, on average, have been maintaining a constant extension over the years.

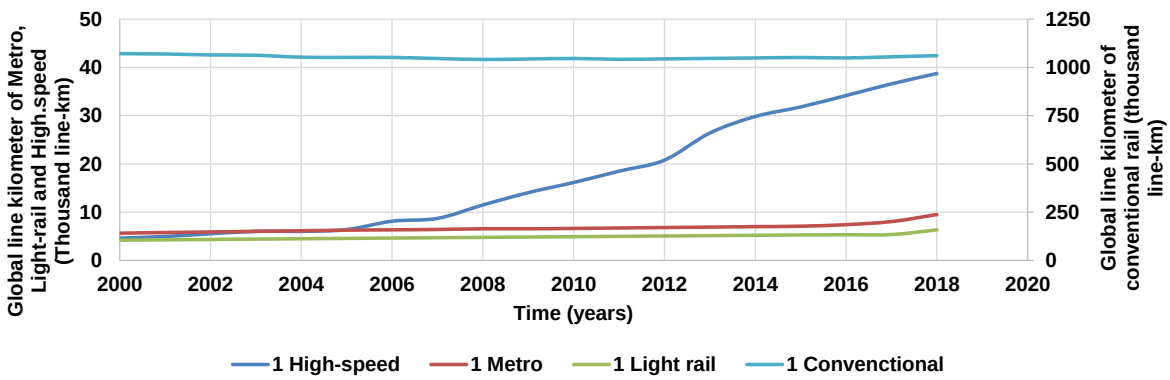

Figure 1.2 – Extension evolution of the railway system from 2000 to 2018 (based on [2]).

Worldwide speaking, the combined length of the metro railway (32 000 km) with the light railway (21 000 km), results in a total track length of 53 000 km for the urban railway lines. Regarding the

high-speed railway line, it has a total length of 68 000 km, representing an annual growth of 11 % per year, from 2000 to 2016 [1].

Despite the conventional railway system representing 94 % of the entire line-kilometer railway structure, it has grown slowly over the last few years, as can be seen in Figure 1.3. On the other hand, the investment in urban systems and high-speed rail systems is noticeable, where their extension has doubled or tripled in several countries in recent years [1]. This fact is reflected in China's strong investment in high-speed railway systems, moving from a nonexistent infrastructure in 2008 to one with a total length of 41 000 km within 10 years. Nowadays, the total extension of the Chinese high-speed railway system represents 2/3 of the world's extension. Additionally, the metro rail network of China becomes the largest in the world, in just one decade, overtaking in 2015 the European Union (EU) metro railway network [1].

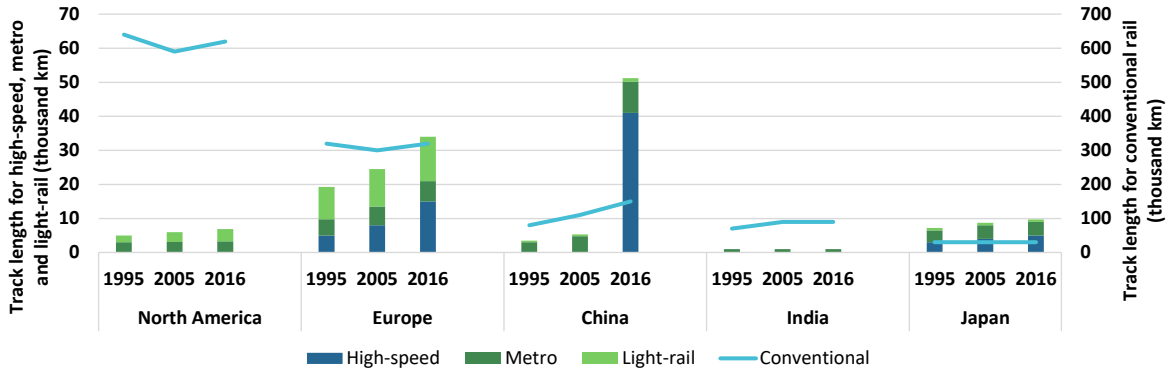

Figure 1.3 – Evolution of the track length by region and railway type system from 1995 to 2016 (based on [1]).

Analyzing the railway extension of different EU-28 countries, it can be seen that these have been, to a certain extent, constant over time. In 2018, the total length of the railway line in the EU-28 was 216 480 km compared to the 227 329 km presented in 1995. Over these 24 years, it is possible to see slight fluctuations in the total length caused by the migration to an electrified railway system. The different incentives of the European Union provided a constant growth of the electrified railway system in the European region, presenting a total extension of 119 925 km in 2018 [3].

Portugal is an evident case of this migration to an electrified railway system. Over the past few decades, it has been renouncing the conventional diesel system and investing in electrification. Nowadays, in 2021, 1791 km of a total of 2527 km are electrified, as can be seen in Figure 1.4 [4], [5].

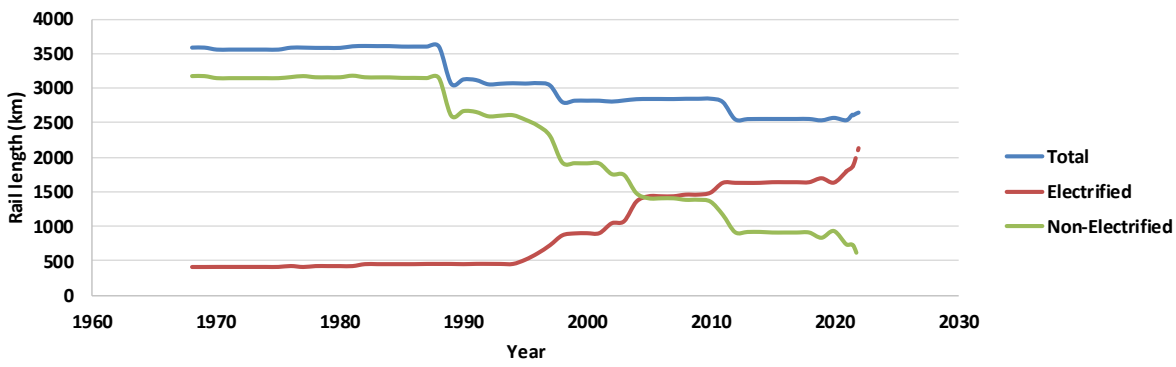

Figure 1.4 – Evolution of the Portuguese railway system length, from 1968 to 2020, and evolution expectation for 2021 and 2022 (based on [4], [5]).

1.1.2 Railway Transport Activity

The continuous commitment to the railway system has become a system of choice both in the transport of passengers and in the transport of goods by different world nations. As far as passenger transport is concerned, it can be seen from Figure 1.5 (a) that there has been a continuous increase over the last few years in the number of passenger-kilometers per year. In the past two decades, railway passenger activity has risen by 91 %, reaching in 2016 the value of 4.1 trillion passenger-kilometer. In turn, freight transport showed rapid growth at the beginning of the 21st century, stagnating its growth after 2010, as can be seen in Figure 1.5 (b). Freight transport activity is measured in tonne-kilometers [1].

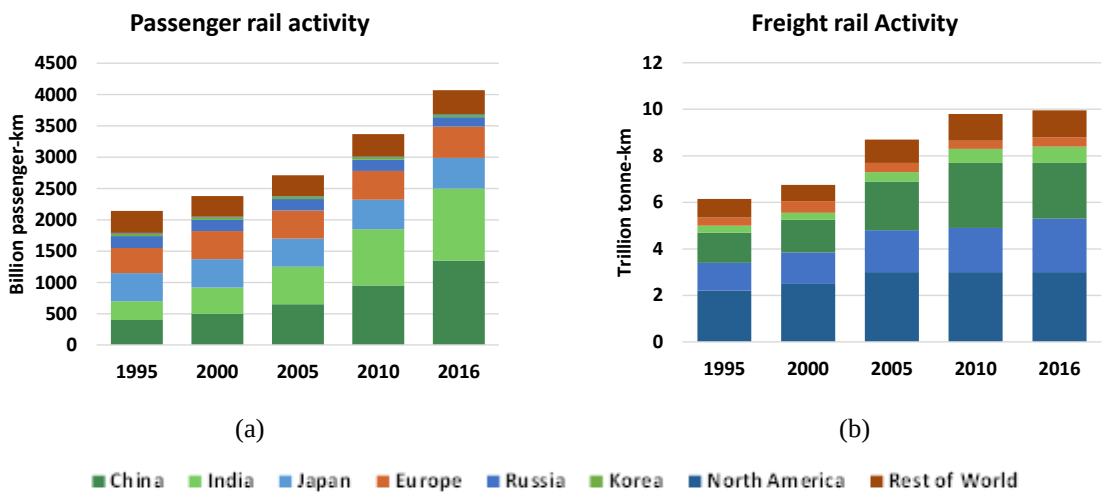

Figure 1.5 – Evolution of the passenger and freight rails activities by region, from 1995 to 2016 (based on [1]).

It can be concluded that the railway passenger system is a growing bet in countries with high population densities, in order to respond to the passenger mobility demand. In turn, freight transport is more frequent in more extensive countries, such as the United States of America, Russia, China and India [1].

In Figure 1.6, it is possible to see, in greater detail, the evolution of passenger transport over the past few years in the nations with the greatest contribution. The largest activity comes from conventional railway transport, despite the constant growth of high-speed and metropolitan transport. Although a greater predominance of the conventional system in China, it is possible to verify that the high-speed system has shown exponential growth [1]. Additionally, in 2015, the metro railway system in China became the largest in the world, surpassing the European metro system in just a decade [1].

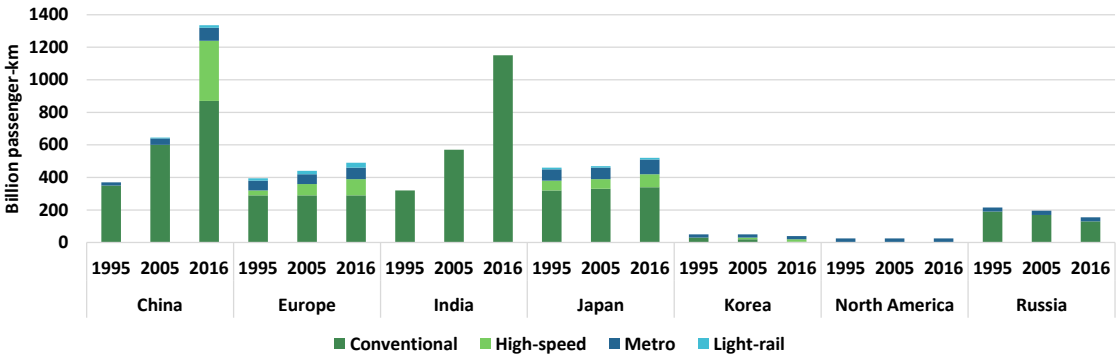

Figure 1.6 – Evolution of the passenger activity by rail type, from 1995 to 2016 (based on [1]).

1.1.3 Safety and Fatalities

Railway transport has had an average annual passenger value of 26.9 billion (26 900 000 000). Being that 8.9 billion passengers use conventional railway transport, 9.5 billion use the metro and 8.5 billion use the light rail [6]. Despite this total number of passengers every year, not forgetting the freight transport, the railway system presents itself as the safest overland transport. Analyzing the data presented in Figure 1.7, it is possible to conclude that the railway system is 27 times safer than the car and 2.3 times safer than the bus/coach [7], [8].

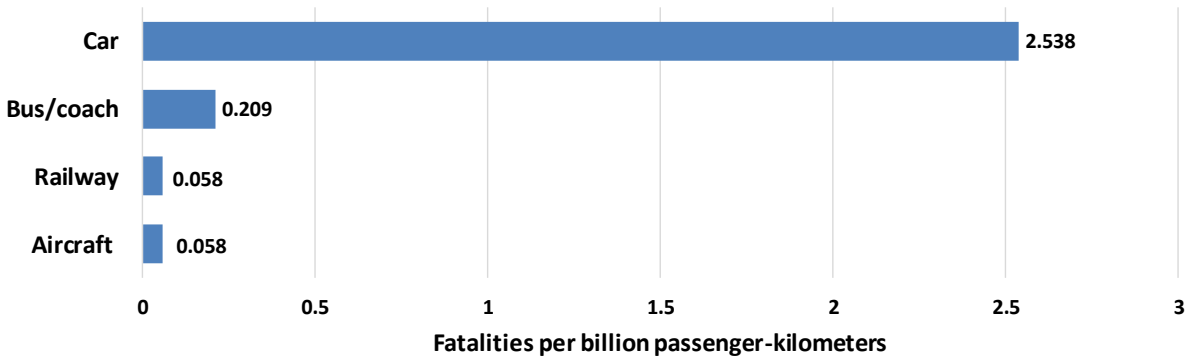

Figure 1.7 – Fatality rates for different transport modes (average data from 2015 to 2019 based on [8]).

Even so, it is important to say that in 2019, in the space of the European Union (27 countries), 802 deaths occurred. However, 520 deaths occurred due to accidents with people using rolling stock in

motion, 265 deaths occurred in accidents at level crossings, including pedestrians, and only 16 occurred due to collisions. There is only one event caused by another reason and there is no representative data on derailments [9].

In the Portuguese scenario, two recent accidents that caused fatal victims can be mentioned. The first case occurred on July 31, 2020, when an Alpha Pendular train collided with a catenary repair machine in *Soure*, district of *Viseu*. This collision resulted in two fatalities, the two workers who were maintaining the catenary line [10]. The next day, another accident with one deadly victim occurred. This time in *Leiria*, the result of a train colliding with a goods vehicle that was passing through a level crossing. The victim was the driver of the goods vehicle [11]. On September 14, 2021, a 16 years-old teenager died when was run over by a train. The reason for the event was that the teenager was crossing the railway line at the stop of *Coimbrões, Gaia* [12].

1.1.4 Energy Demand

Although transport contributes 29 % of the final energy consumption globally, the railway system is only responsible for 2 % of that consumption. It can be said that it is a modest participation, taking into account the railway activity of passengers and freights. Taking into account the evolution of the activity of the railway system, both at the level of passengers and freights, a continuous and strong increase in the energy consumed for locomotion would be expected. However, and analyzing Figure 1.8 (a), the same is not true, concluding that the migration to the electrical system provided greater energy efficiency in the railway sector [1]. It can be seen that energy demand has remained constant, with a slight increase in energy demand in some periods.

The main reason for the modest share of energy lies in the high efficiency of railway systems compared to road and air systems. The frictional losses of the rail system can be between 85 % and 95 % lower than the frictional losses of the tire's road. The railway systems have a high load capacity and do not suffer from transport congestion, such as road traffic congestion. In addition, and based on Figure 1.8 (b), it is possible to verify a constant migration to electrified railway transport systems. The electric motors that equip the locomotives are characterized by high efficiency [1]. In this way, it is possible to maintain an intense railway activity with relatively low energy demand.

In 2017, electricity was responsible for 47 % of the energy used in the railway system, totaling 25 million tonnes of oil equivalent (Mtoe), which translates to 290 terawatt-hours (TWh). In turn, the diesel railway system is responsible for the consumption of 53 % of energy, equivalent to 29 Mtoe. It should be noted

that 55 % of the electrical energy used is for the transport of passengers and, in turn, 85 % of the energy in the diesel railway system is for the transport of goods [1].

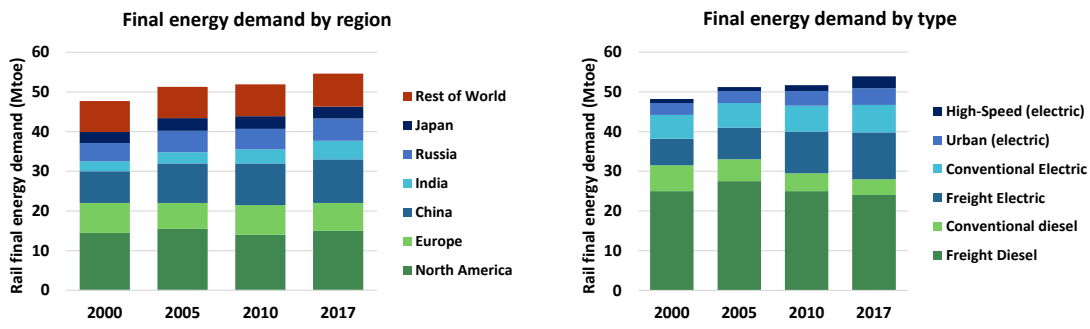

(a) (b)

Figure 1.8 – Evolution of the final energy demand in railway transport by region and type, from 2000 to 2017 (based on [1]).

The railway system makes an important contribution to energy reduction with the demand for mobility. That is, if all railway activity, passengers and freights, migrated to another transportation alternative, the global energy demand for oil for transportation would be 16 % higher than the current one [1].

In Figure 1.9, it can be seen that in 2016, three-quarters of the passenger railway activity uses the electrical system, representing an increase of 60 % compared to 2000. In turn, 48 % of the total tonne-kilometers of freight transport was based on the electrical system. However, it should be noted that only one-third of the railway system was electrified [1]

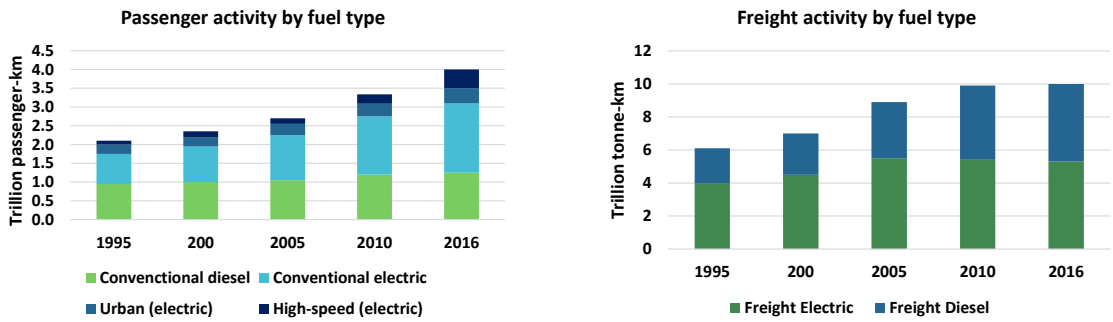

(a) (b)

Figure 1.9 – Passenger and freight rail transport activity by fuel type (based on [1]).

1.1.5 Environment

Concerning environmental pollution, transport is one of the major contributors to the emission of CO_2 into the atmosphere with a 24.7 % share. Only the service related to industrial manufacturing and construction manages to exceed this value with 36.9 % of the share. However, even with the transport activity presented, it should be noted that the railway system is the mean of transport (of the most traditional)

with a smaller ecological footprint, contributing only 1.04 % of total emissions. In turn, the road system contributes 17.9 %, the air system 2.7 % and the sea system 2.5 % of the total CO_2 emissions.

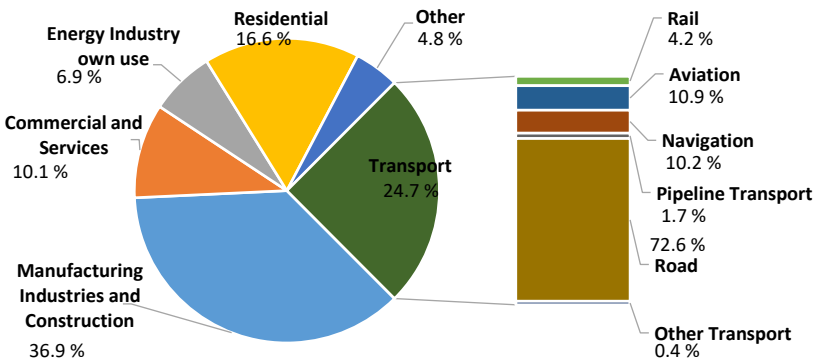

Figure 1.10 – Share of CO_2 emissions from fuel combustion by sector in 2015 (based on [13]).

1.1.6 Population Growth and Economic Development

Taking into account the evolution of the railway system in recent years and its impact, it remains to be analyzed the prospects. With this, it will be possible to identify the needs and the points to be improved to respond to future needs. One of the most evident points is the population increase and migration.

It is expected that the world population will reach in 2100 the value of 10.88 billion people, which represents a growth of more than 38 % compared to the current population of 7.84 billion in 2021, as is presented in Figure 1.11 [14]. The focus of this population growth will be on the Asian and African continents. For European Union countries, a slight decrease is expected.

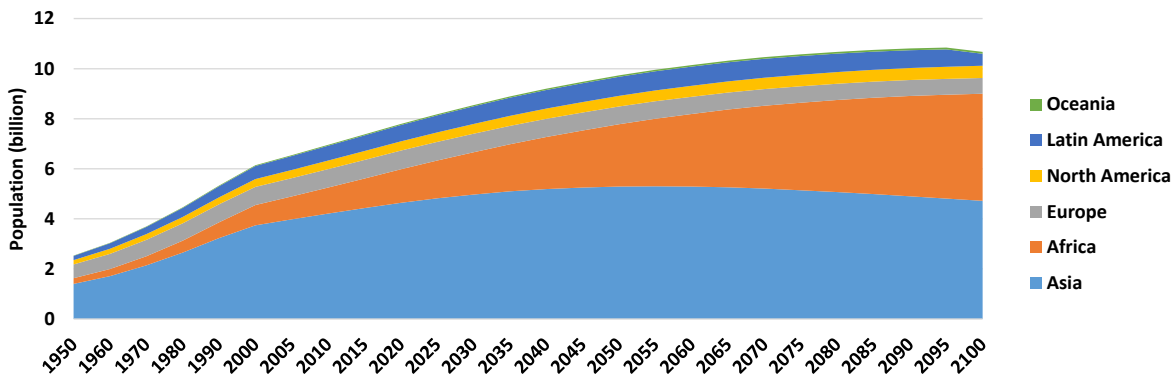

Figure 1.11 – World population by region projections to 2100 (based on [14]).

Despite population growth, even with population stagnation in Europe, one of the factors of greatest concerns is population migration to urban areas. In the graph of Figure 1.12 this migration is noticeable, being expected in 2050 several inhabitants in urban areas very close to the world population today. Knowing that 5 out of 10 people live in urban areas today, in 2050 the ratio will be 7 out of 10 people [15].

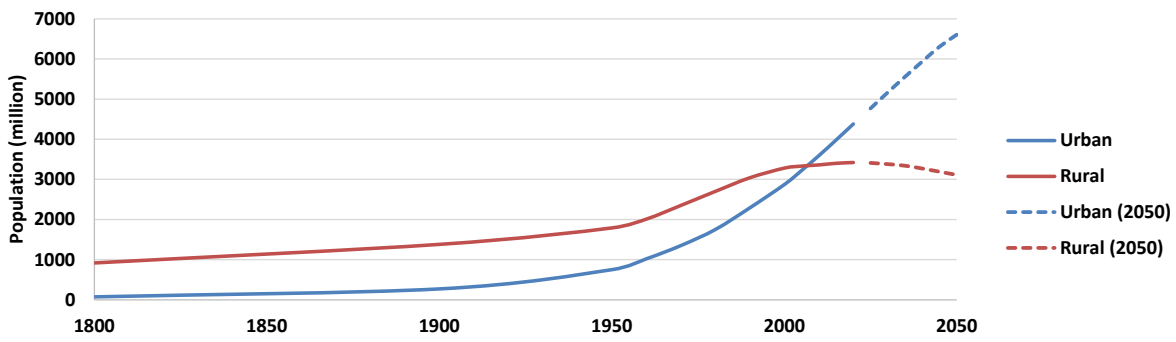

Figure 1.12 – World urban and rural population evolution and projection from 1800 to 2050 (based on [16]).

With population growth and migration to urban areas, road congestion and the space used by road vehicles will be very obvious problem. It is, therefore, necessary to develop the railway system to prevent such problems and provide efficient solutions to the demand for mobility that is expected. However, the European railway system employs more than one million workers, allowing indirect employment for 1.3 million people. This translates into an annual gross value added (GVA) of EUR 165 billion, of which EUR 75 billion (46 %) are produced directly [7].

1.1.7 Railway System Evolution Perspectives

It is expected quite ambitious challenges for the railway system to maintain its competitiveness with the other means of transport as well as to meet the demand for mobility that lies ahead. One of the predictions lies in the expansion of the world railway line (conventional, urban and high-speed) to values of 2.1 million track-km in 2050. This represents an increase of 26 % in 34 years, compared to the value of 2016 (1.6 million track-km). In 2050 the railway system will be completely dominated by the conventional system, totaling 92 % of the total track-km extension. To this end, by 2050, more than 430 thousand track-km for this system will be built, which represents an increase of over 25 % [1]. However, due to the high activity of passengers and freight, the value of passengers-km and tonne-km more than double in 2050, as is represented in Figure 1.13. On the other hand, the construction of new railways will grow at a slower pace than the growth of railway activity. In other words, the high capacity utilization, both for passengers and freight, means that the activity grows at a faster rate than the railway line construction.

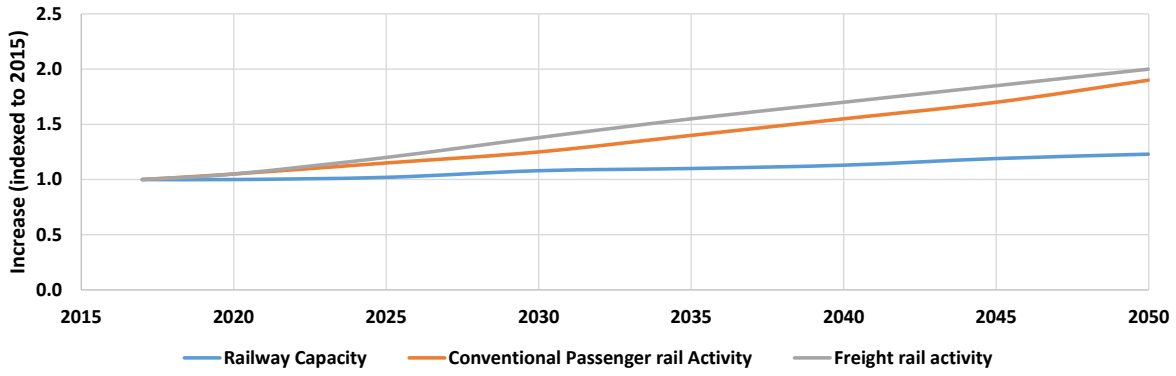

Figure 1.13 – Expectations for the evolution of global conventional passenger railway, freight railway activity and network capacity (based on [1]).

Regarding the metro and the high-speed railway system, despite little extension compared to the conventional system, continuous investment in this railway sector is expected. It is projected that by 2050 it will be possible to reach a total length of 76 000 track-km for the metro and 163 000 track-km for the high-speed rail system, as shown in Figure 1.14. China will be a major driver of these two rail systems, followed by Europe [1].

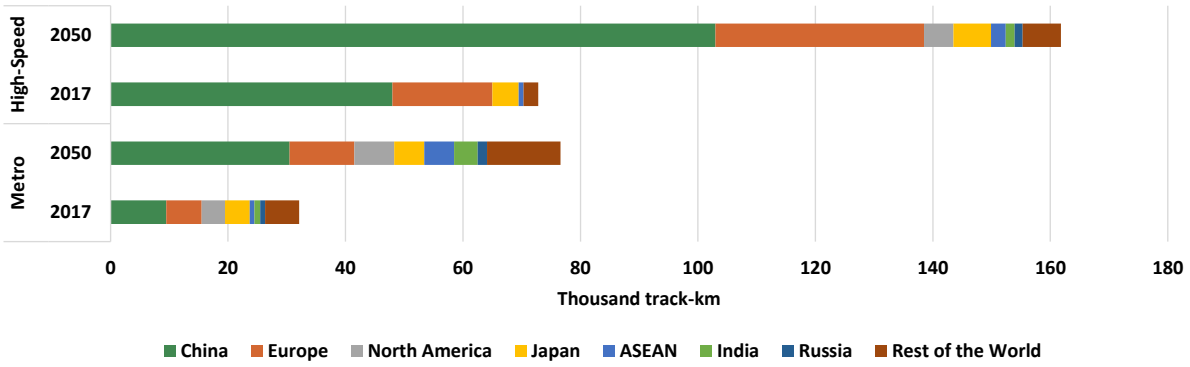

Figure 1.14 – Expectations for the evolution of global track-kilometers for metro and high-speed rail (based on [1]).

With population growth coupled with population migration to urban centers, the continued demand for mobility is expected, reflected in greater rail activity. Analyzing Figure 1.15, it is possible to conclude in a short time, China will more than double its railway activity in urban rail activity. Substantial growth will happen in the next years until 2030. Subsequently, growth will be more moderate until 2050. The same will happen in other countries.

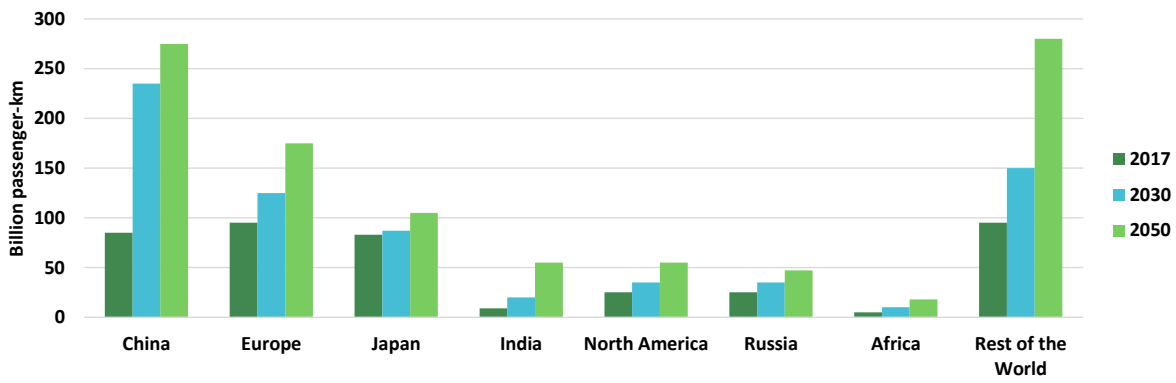

Figure 1.15 – Expectations for the evolution of the urban rail activity by region (based on [1]).

The demand for mobility will inevitably increase energy consumption, increasing by 43 % as shown in Figure 1.16. It can be identified that the biggest consumers of energy in terms of transport will continue to be the road and maritime systems. In turn, despite the 72 % increase in energy consumption, the rail system continues to maintain a total share of 2 % in energy consumption in transport [1].

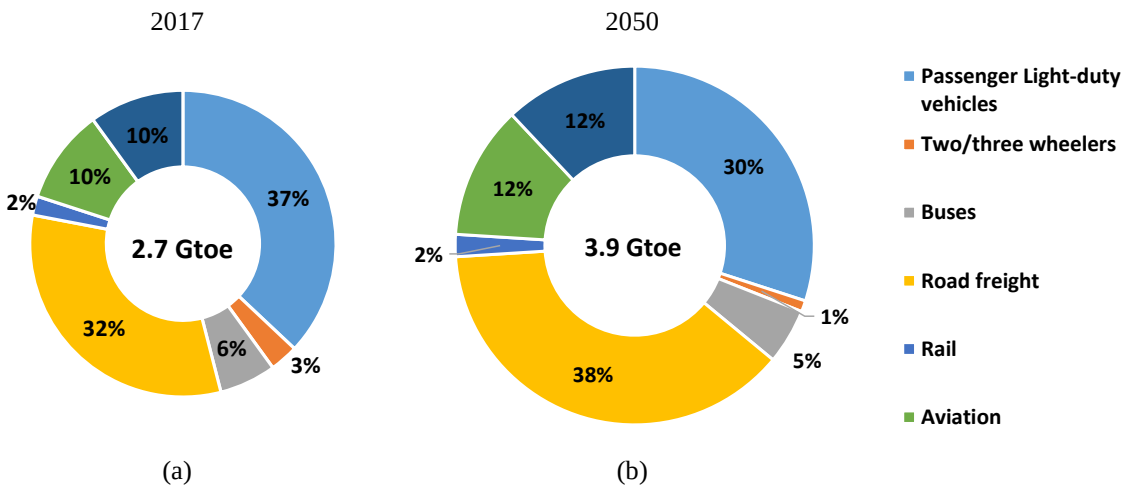

Figure 1.16 – Evolution expectation for global energy demand from transport (based on [1]).

One of the great challenges is to respond to the demand for electricity that lies ahead, which will grow from 300 TWh (2017) to an annual value of 700 TWh in 2050. It is perceived based on Figure 1.17 that in 2050 most rail systems will be electrified. However, it should be noted that, for the European case, the conventional system will be in continuous evolution, being the main consumer of energy.

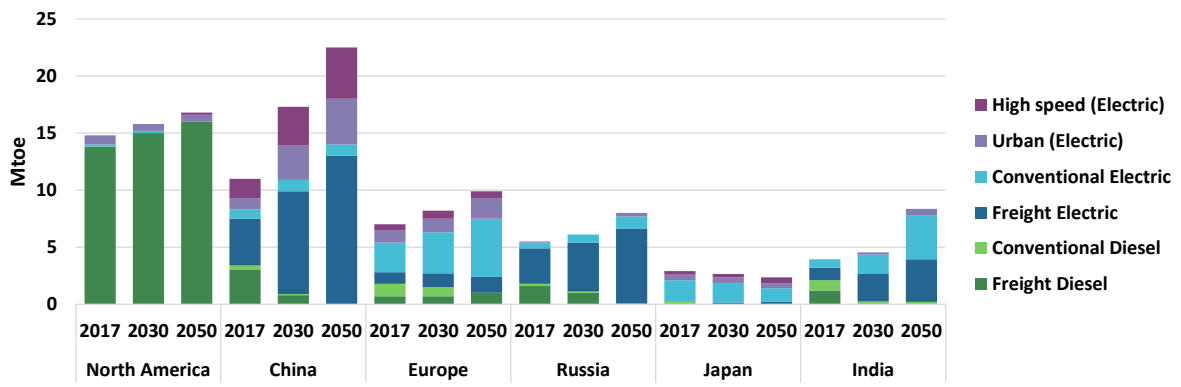

Figure 1.17 – Expectations for the evolution of energy demand from the rail by region and type of technology (based on [1]).

1.1.8 Discussion of Statistical Data Analysis

Analyzing the data presented, the rail system's predominant role is expected to respond to the demand for mobility in the coming years. With population migration to urban centers and population growth, the rail system presents itself as a potential solution to minimize urban traffic congestion.

Regarding technologies, it can be concluded that the electrified rail system is the most energy-efficient solution. Despite the continuous increase in railway length, with the migration to the Electric System, it was possible to minimize energy dependence.

The railway potential, mainly the electrified one, to respond to the upcoming requirements is high, requiring constant investment in its development. One of the main boosters of the railway system in the 21st century is the financial initiatives of several world nations. For instance, Shift2Rail presents itself as a European organization committed to contributing to technological development in this area, as well as reducing rail life cycle cost by up to 50 %, doubling rail capacity, and increasing reliability by up to 50 % [17]. To accomplish this objective, it is necessary to develop innovative solutions for railway systems, where power electronics play an important role. To study the opportunities and challenges of power electronics in railway systems, special importance was given to the new concepts of emerging locomotives.

Analyzing the rail system across different regions of the world, it was possible to identify different implementation approaches. The independence in railway development originated by different countries has led to the adoption of varying track gauges (i.e. the spacing between rails), power systems (using direct current (dc) or alternating current (ac), and different voltage values), and signaling. These choices led to greater isolation of countries with neighboring nations, making integration and interoperability of the rail system more difficult.

In order to respond to these requirements in the short term, the best solution is to improve the efficiency of the electrified railway system, incorporating intelligent power electronics converters that allow for better energy management as well as enabling the integration of nearby renewable energy sources on the places with the highest energy consumption.

1.2 Railway in the World, Europe and Portugal

In order to provide a constant and rapid expansion of the electric railway system, it is necessary to develop innovative solutions, where power electronics play an important role. To study the opportunities and challenges of power electronics in railway systems, special importance was given to the new concepts of emerging locomotives. Table 1.1 shows the 11 fastest locomotives recently in service and are to be commercialized shortly [18].

Table 1.1 – Recent and future trends on high-speed electric locomotives.

	Locomotive	Start Service	Maximum Speed (km/h)	Power (MW)
11	CRH3X	2020	350	2 (per traction unit)
10	Oaris	2015	350	5.28 – 10.56
9	Avelia Liberty	2021	350	n.a.
8	Avelia horizon	2023	350	8
7	Velaro novo	2023	360	8
6	Talgo Avril	2020	365	8.8 – 10
5	Alfa-x e956 Shinkansen	2030	400	n.a.
4	Hemu – 430x	2015 (ktx-III version)	430	8.2
3	CRRC Maglev	2021	600	24
2	L0 series Maglev	2027	603	n.a.
1	Hyperloop	2030	1200	21

n.a. not available

As can be seen, there is a tendency to increase the speed of the locomotives and, consequently, their power. There is also an interest in increasing the number of wagons in the locomotives as well as increasing the number of electric locomotives in the railway system.

In the Portuguese scenario, the company that manages the Portuguese railway system, *Infraestruturas de Portugal*, aims to achieve different goals on the different Portuguese railway lines by 2020. In the northern international line, it intends to promote railway interoperability with the Spanish and European networks, eliminating speed restrictions, as well as increasing the daily capacity of 14 compositions from 500 m to 20 locomotives of 750 m, representing an increase of the daily capacity of more than double. More specifically, in the *Beira-Baixa* line, they want their total electrification [19]. In turn, the international south line intends to reduce the route between *Sines* and *Elvas/Caia* by 1:30 h (approximately 200 km) with the use of electric traction throughout the route. This intervention will allow for a daily increase from 36 locomotives with 400 m to 51 locomotives with 750 m, corresponding to an increase in a daily capacity greater than two and a half times. More specifically to the east line, between *Elvas* and the border with Spain, they intend to modernize and electrify the line, to promote interoperability with the Spanish and with other European countries [19]. Regarding the north-south corridor, it also predicts the modernization of the line, reduction of travel times as well as the increase in capacity, especially for the *Minho* line, where they aim to increase the daily capacity of 15 locomotives from 300 m to 20 locomotives of 750 meters, representing an increase of more than 3 times the current capacity. Regarding the complementary lines, it is possible to verify the intention of migrating the 1500 V dc system currently in use on the *Cascais* line to ac system of 25 kV – 50 Hz, as well as the installation of a Global System for Mobile Communications – Railway (GSM-R) systems. More specifically on the *Algarve* line, they want the electrification between *Faro* and *Vila Real de Santo António*, as well as between *Tunes* and *Lagos*. Consequently, it is necessary to expand the electrical traction power substation (TPS) in *Tunes* as well as the construction of a new TPS in *Olhão* [19].

In general, there are more than 1 000 km of railways lines in intervention in Portugal, with an investment of more than EUR 2 billion (2 000 000 000 €). These incentives are intended to increase the competitiveness of the railway system, reducing travel times, reducing transportation costs (€/km/carriage), and increasing the capacity (number and length of locomotives). Additionally, it is intended to improve the conditions for railway interoperability, with the electrification of more than 480 km, increase the length of the locomotives to 750 m, as well as the installation of multi-purpose crosstie that allows the change of the track gauge in the international corridors [19].

Analyzing Figure 1.18, is possible to conclude that in Portugal exist 43 neutral sections for 22 TPS powered by 25 kV – 50 Hz. Regarding the dc system, all 6 TPS 1500 V dc are located in *Cascais-Lisbon*.

Figure 1.19 represents an aerial photograph of a railway section with a neutral section. This neutral section is located in the north of Portugal, in *Arcozelo*, *Porto* (41°03'21.5"N 8°39'11.6"W). Analyzing

Figure 1.19, it is possible to identify different signals that indicate to the locomotive driver that he is approaching the neutral section, needing to lower the pantograph, and then raise it again. This neutral section also has a transformer station that allows the electrical connection of the two sections, bypassing the neutral section, in case of need.

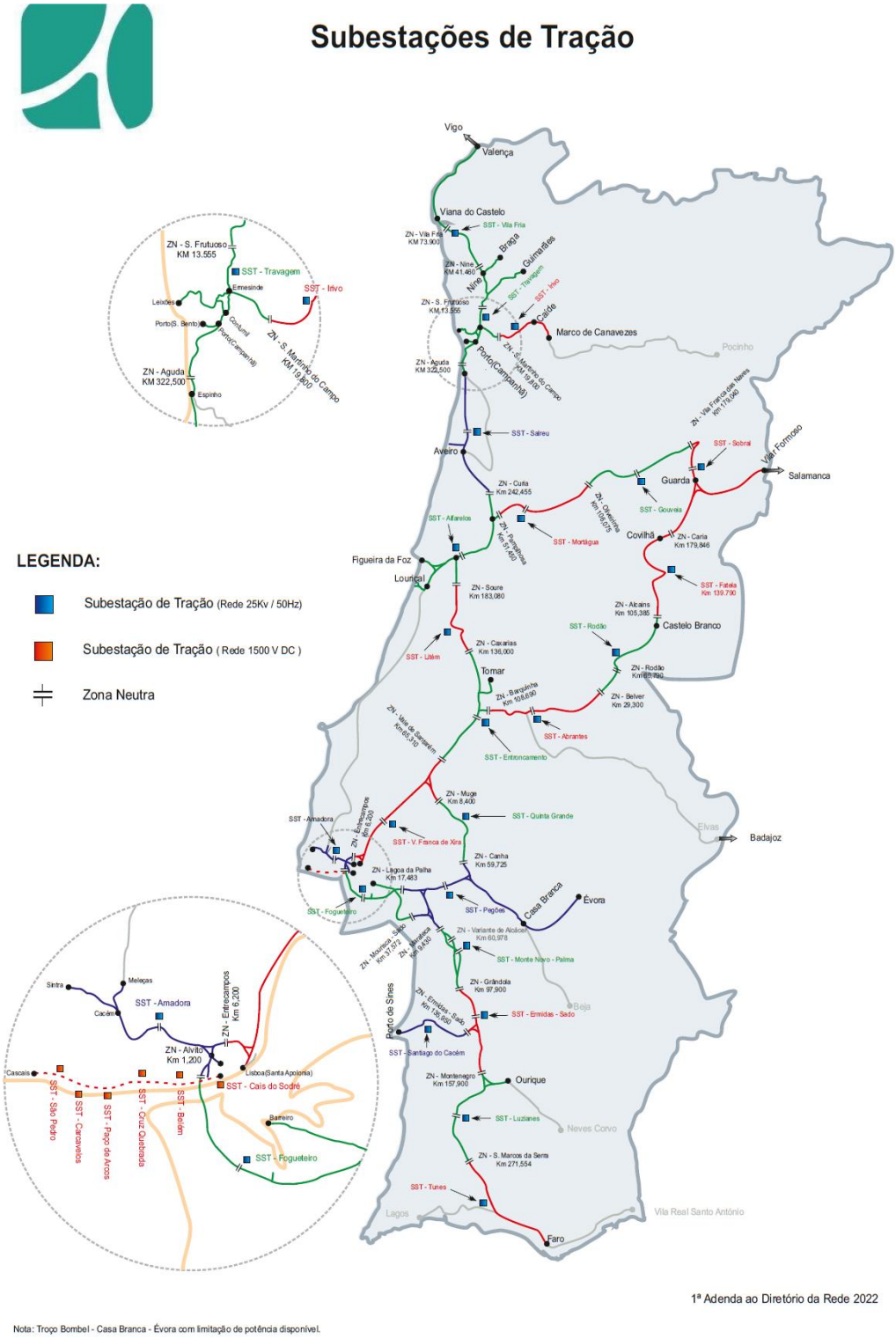

Figure 1.18 – Traction power substations in Portugal [20].

Analyzing Figure 1.19, it is possible to identify a signaling sequence when the locomotive runs from left to right (signals i) to iii)). In this case, the driver of the locomotive is initially faced with signaling i) which indicates the approach to an area where the electrical system must be turned off or the pantograph lowered. This signaling must be placed at a distance of 100 to 150 meters from the referred location. Subsequently, signage ii) appears, indicating to the driver that he must disconnect the main circuit breaker connected to the pantograph. Once passed through the restricted area, signage iii) appears, indicating to the driver that he can restore the electrical connection to the pantograph [21]. The same sequence of events arises when the locomotive runs from right to left.

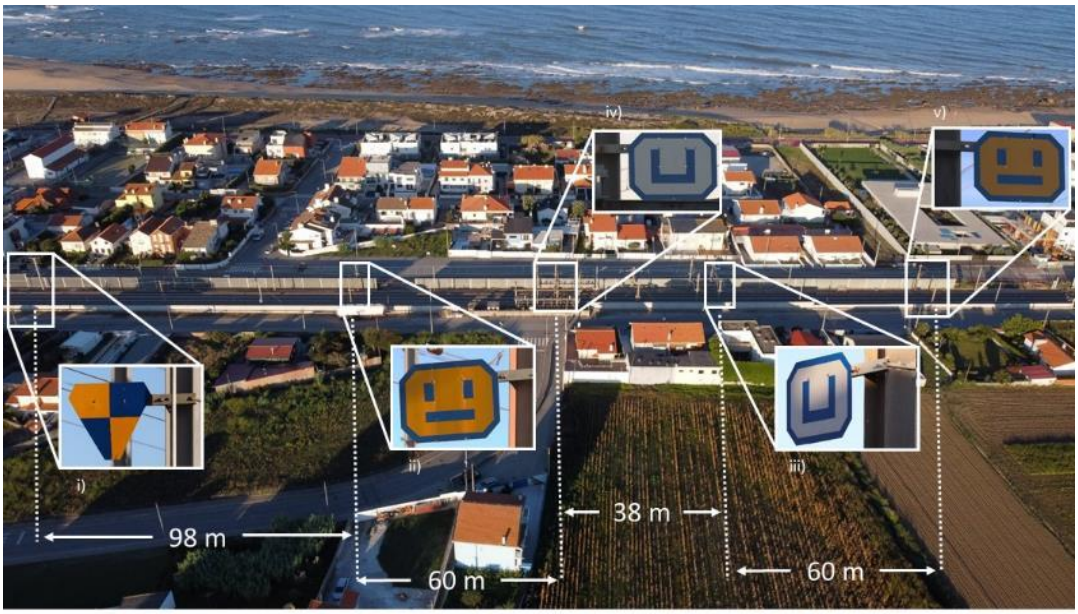

Figure 1.19 – Example of a neutral section in Portugal.

In order to understand the existing railway fleet as well as analyze the operating powers of existing locomotives in circulation, Table 1.2 shows the electric railway locomotives in circulation in Portugal. Locomotives powered by dc and ac systems can be identified, with the majority focusing on ac systems, with operating powers greater than 1 MW.

Table 1.2 – Examples of electric locomotives in circulations in Portugal (based on [22]).

• Series: 2241-2297; • Operational units: 55; • First-year on service: 2003 (after updates); • Maximum speed (km/h): 120; • Type of connection: Electric, 25 kV, 50 Hz, three-phase asynchronous motors; • Power: 1 281 kW.	• Series: 2301-2342 and 2351-2392; • Operational units: 42; • First-year on service: 1992; • Maximum speed (km/h): 120; • Type of connection: Electric, 25 kV, 50 Hz, three-phase asynchronous motors; • Power: 3 100 kW.

 • Series: 2401-2414 and 2451-2664; • Operational units: 14; • First-year on service: 1997; • Maximum speed (km/h): 120; • Type of connection: Electric, 25 kV, 50 Hz, three-phase asynchronous motors; • Power: 3 100 kW.	 • Series: 3401-3434 and 3451-3484; • Operational units: 34; • First-year on service: 2002; • Maximum speed (km/h): 140; • Type of connection: Electric, 25 kV, 50 Hz, three-phase asynchronous motors; • Power: 1 700 kW.
 • Series: 3519-3530 and 3569-3580; • Operational units: 12; • First-year on service: 1999; • Maximum speed (km/h): 140; • Type of connection: Electric, 25 kV, 50 Hz, three-phase asynchronous motors; • Power: 3 475 kW.	 • Series: 4001-4010 and 4051-4060; • Operational units: 10; • First-year on service: 1999; • Maximum speed (km/h): 220; • Type of connection: Electric, 25 kV, 50 Hz, three-phase asynchronous motors; • Power: 4 000 kW.
 • Series: 3151-3163, 3251-3271 3255 and 3261-3263; • Operational units: 31; • First-year on service: 1998 (after updates); • Maximum speed (km/h): 90; • Type of connection: Electric, 1 500 V dc, dc motors; • Power: 960 kW	 • Series: 5601-5630; • Operational units: 24; • First-year on service: 1993; • Maximum speed (km/h): 220; • Type of connection: Electric, 25 kV, 50 Hz, three-phase asynchronous motors; • Power: 5 600 – 7 560 kW.

1.3 Railway Power System Technologies

Taking into account the ambitions and needs of the railway system, it is necessary to carry out a state-of-the-art study of technological trends that will make it possible to respond to all the requirements of the railway system. In this way, some of the emerging concepts for the railway system are presented below, from systems that are easy to adapt to the current railway system to the most revolutionary systems that need their railway structure. Some emerging concepts that result from the combination of different concepts are also highlighted.

1.3.1 Conventional Railway Power Systems

Given the predominance of the 220 kV three-phase distribution system and the single-phase 25 kV, 50 Hz ac railway power system, it is necessary some kind of process to adapt the voltage levels of the TPS, from the power system to the railway system. The following study focuses on the available ac railway supply system. The most basic, inexpensive, and older method is to alternate the phase connection of the TPS power transformer with the power grid, as exemplified in Figure 1.20, which is commonly referred to in the literature as the phase-shift method. This method minimizes the system unbalance and, consequently, the negative sequence components [23]. For better performance, two power transformers, in different phases, are usually installed in a given substation, with connections in the adjacent substations being alternated. Indeed, installing a single power transformer in a substation would intensify the system unbalance locally [24].

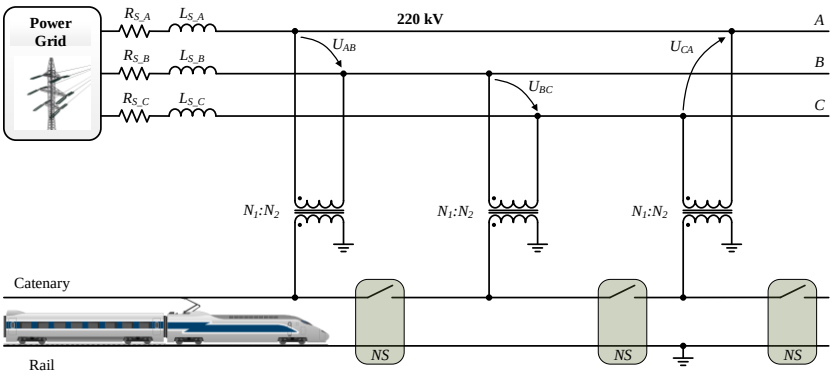

Figure 1.20 – Conventional topology using the phase shift method (based on [25]).

Given that the catenary can be powered by power grids with different voltage amplitudes and phases, a neutral section (NS) needs to be created. The neutral sections are designed for safety reasons in order to avoid short-circuits between phases of the supply system and can have several tens to hundreds of meters [24], [26], [27]. This requirement impedes the flow of energy from the adjacent substations, as well as causes intermittent operation when passing through the neutral section, resulting in phenomena of power quality problems [25], [26].

Despite being a minimalist solution, it is highly robust due to the long life of the power transformers. However, the major disadvantage lies in the unbalance of the currents in the three-phase power grid, since this topology is strongly dependent on the balance of the remaining loads connected to the catenary.

1.3.2 Railway Power Systems with Three-phase Power Transformers

Considering the rapid expansion of the railway system and, consequently, the introduction of more electric locomotives, it is necessary to implement solutions capable of meeting the new requirements. Thus, new

configurations using three-phase power transformers begin to emerge, enumerating the V/V, Scott, Le Blanc, Impedance Matching and Woodbridge power transformers [28]. Considering the greater predominance of V/V and Scott power transformers, the study only focused on these solutions. An example of the integration of these two solutions in the railway system is presented in Figure 1.21.

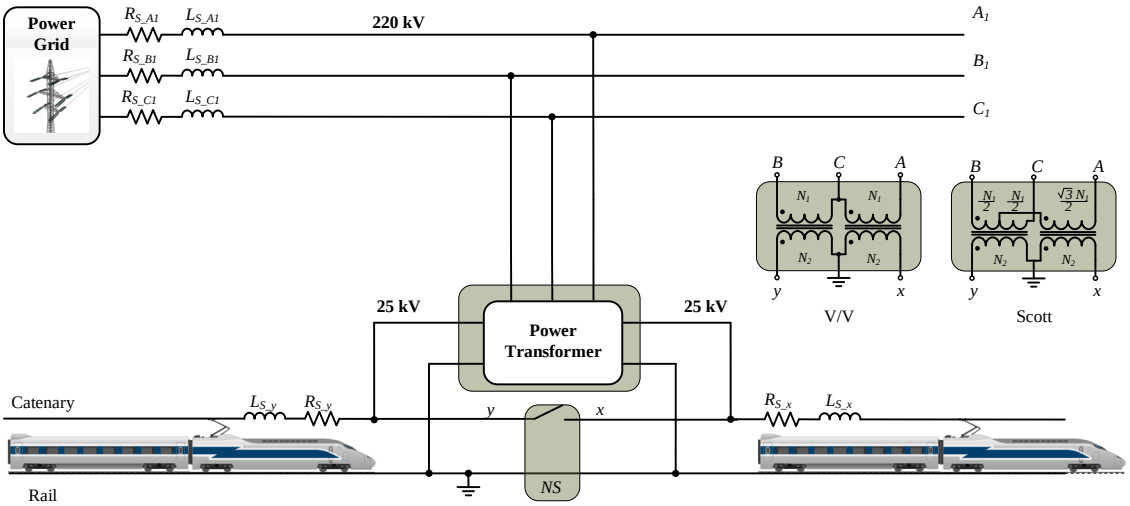

Figure 1.21 – Topology using three-phase balancing V/V and Scott transformers (based on [25]).

1.3.2.1 V/V Three-phase Power Transformer

The simplicity of construction of the V/V power transformer, basically two single-phase two-winding transformers, makes this technology one of the most widely used in railway applications to mitigate some of the power quality problems. The transformation ratio is given by N_1:N_2, exemplified in Figure 1.21, where N_1 is the value of the voltage between phases of the power grid, i.e. 220 kV, and N_2 takes the value of the existing voltage in the catenary, being 25 kV [28], [29]. These power transformers are dimensioned to provide all the power that the railway electric system needs over a given catenary. Given the power of a locomotive, each V/V power transformer can be expected to have considerable weight and volume. Typically, these power transformers have a nominal power between 40 MVA and 60 MVA [23], [30]. An analysis of this system using computer simulations was carried out and the final results and conclusions were presented by Barros et al. in [31].

1.3.2.2 Scott Three-phase Power Transformer

The Scott power transformer presents itself as one of the improved power supply solutions for railway systems. Its versatility in balancing the operating conditions on the power grid side contrasts with the complexity at the construction level. This solution still uses two power transformers, one with two windings and one with three windings, two windings on the primary side and one on the secondary side. In the power transformer with three windings, the midpoint of the two primary side windings is connected in series with the adjacent transformer primary winding as shown in Figure 1.21.

Similarly, to the V/V power transformer, computational simulations were used to study the operation principle of the Scott power transformer with more detail, being presented by Barros et al. in [31].

With the configuration of these power transformers, some of the power quality problems are eliminated by the magnetic field created by the power transformers [31]. However, dynamic compensation of these power quality problems is required, being interesting to integrate Active Power Conditioners to dynamically compensate these problems. From this perspective, Active Power Conditioners in conjunction with three-phase transformers present an interesting solution to mitigate these power quality problems.

1.3.3 The Future of Railway Power System

The development of electronics has enabled the introduction of new systems in everyday life. One of the revolutions of the last years is the real-time monitoring of the systems, and the railway system was not an exception. With sensing it is possible to determine and control the geographical location of each locomotive as well as to predict the energy consumption to create a more efficient feeding system. The European Rail Traffic Management System (ERTMS) has become a widely used solution, becoming world dominant in sensing and controlling the railway system. The ERTMS was a project executed by the European Railway Agency (ERA). This system enables the prediction and adaptability of the system to increase catenary capacity by 40%, reduce power grid dependency by 15%, reduce carbon emissions, and increase safety, among other characteristics [1].

One of the most important topics in power electronics research is the development of solutions that allow the interfacing with alternative propulsion technologies, such as fuel cells or hybrid systems, essentially for non-electrified sections, to reduce the cost associated with installing and expanding the electrical supply system [17], [32]–[34]. They also discuss the installation of an Energy Storage System (ESS), both internal and external to the locomotive, for a better distribution of energy according to their needs, thereby enabling the recovery of energy from regenerative braking [34]–[37]. However, the integration of renewable energy sources and concepts such as smart grids would not only enable local energy generation more efficiently but also increase the flexibility in the supply and exchange of electricity. Additionally, with the integration of local energy sources, it would be possible to increase energy efficiency as well as to reduce the overload on the power grid and thus enabling the integration of more or larger electric locomotives in the same railway system [35]. Some of the future railway trends are described in the following topics.

1.3.3.1 Cooperative Strategy

As the mobility demand increases at a faster pace than technological developments and consequent market integration, rail sensing helps to manage locomotive distance and travel time, providing a more efficient railway system and improving the experience of the passenger. This offers the possibility to develop cooperative strategies easily integrated.

One of the most commonly used cooperative strategies is to combine the time between the arrival of one train and the start of another. This makes the possibility to directly take advantage of regenerative braking energy to assist the running of another train, as represented in Figure 1.22. Nevertheless, and with the sensing of the entire railway, it would be possible to implement control algorithms capable of detecting the best moments of acceleration and deceleration of the locomotives to optimize the energy consumed. In [36] two different driving strategies for the same trip are presented, showing different consumption and regenerative braking curves.

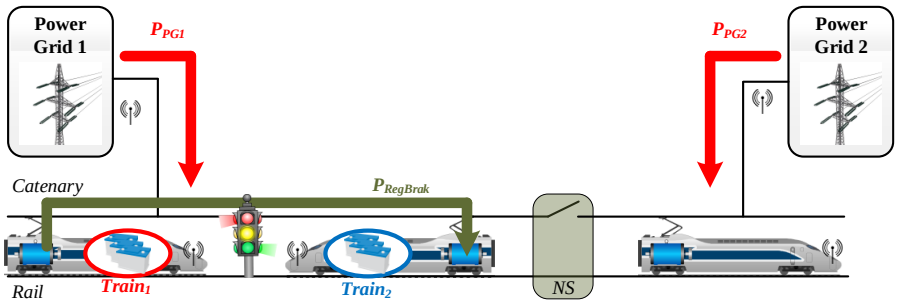

Figure 1.22 – Representation of future operating mode trend: cooperative strategy.

In [18], [36] two different driving strategies are presented that allow synchronizing the acceleration of a locomotive with the deceleration of another. Consequently, part of the energy coming from regenerative braking is directly used to aid the movement of another locomotive, thus minimizing energy consumption from the TPS.

Another very interesting short-term cooperative strategy is the bidirectional energy flow between adjacent TPS, being necessary to include an additional power converter to control the flux of energy between the TPS. Moreover, this type of solution would increase energy efficiency as well as reduce the local power consumption from the TPS. In other words, this solution enables higher power capacity as well as the insertion of more locomotives in the overhead catenary line. In some cases, this enables a decrease in the sizing of certain elements such as transformers, converters and transmission lines [36]. Hitachi has been exploring this concept and the initial results have exceeded the expectations. In [38] a system called sectioning post - Railway Power Conditioner (sp-RPC) was installed in a Neutral Section (NS) located between two TPS that allowed the direct use of energy from regenerative braking. The major challenges

of this strategy lie essentially in the sensing and consequent management of the generated data. Sensing is a key step for developing an autonomous system that can predict and detect faults. However, big data generation needs to be managed and transmitted over long distances

1.3.3.2 Energy Storage System

One of the strong research trends is the inclusion of an ESS close to local consumption, making the railway system more independent from the power grid. In some cases, the ESS can be directly included inside the locomotive, as can be seen in Figure 1.23. Therefore, a feasibility study of different energy storage technologies (presented in Table I) is required. Depending on the design requirements, there are technologies more recommended for mobile and others for stationary applications. In [35], [39] is presented with more detail a comparison of different ESS. In [40] an experimental test is presented of the installation of an off-board inertia flywheel in a TPS in Madrid, Spain, stating that the combination of different ESS technologies could provide a more efficient and reliable system. With the advancement of technology, it was possible to create solutions based on very compact and desirable implemented on-board flywheels, as used in Rotterdam [41]. In charging systems for such applications using electrochemical batteries, there is a strong concern in the development of power electronics to enable rapid charging. To do this, many systems use an intermediate stage consisting of supercapacitors that provide a better power response, and batteries are responsible for storing the largest amount of energy [34]. In this context, it is possible to manage the charging method imposed on the batteries, allowing them to preserve their lifetime. Regarding the fuel cells, different results on hydrogen consumption, efficiency and battery charging state intervals are shown in [17] in locomotives with different rail uses. The introduction of ESS in the railway system makes it possible to improve service availability even in the event of a power failure by providing both on-board and off-board power to the locomotive. The on-board and off-board configurations are presented in more detail in the following items *On-Board Energy Storage System* and *Off-Board Energy Storage System*.

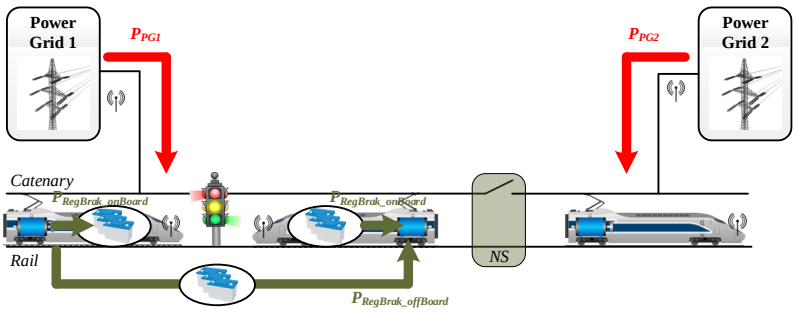

Figure 1.23 – Representation of future operating mode trend: regenerative braking energy stored in an on-board ESS; and regenerative braking energy stored in an off-board ESS.

Table 1.3 – ESS Technologies (based on [35], [39], [42]).

	Fuel Cell (Hydrogen)	**Batteries**	**Flywheel**	**Supercapacitor**
Energy Density	Very High	High	Low	Medium
Power	Medium	Low	High	High
Fast Charging	Yes	No	Yes	Yes
Lifetime	Medium	Low	High	High
Cost	High	Medium	High	Medium

On-Board Energy Storage System

By integrating an ESS on-board the locomotive, it is possible to create a more independent means of transport than the conventional stationary feeding system, which allows the creation of catenary-free zones in some locations, as presented in the labels (i), (ii) and (iii) in Figure 1.24. This fact is especially favored in historical areas as well as in areas with greater difficulty of construction as bridges and tunnels [34], [39], [43]. The essence of this feature is the fact that the locomotive has an internal power source allowing uninterrupted service in the event of power failure or when the locomotive is immobilized in an NS supply zone. In addition, taking into account the cost of implementing the power system and its extension along the railway, the most commonly used lines have priority in rail electrification. As a consequence, there are several non-electrified railway sections where on-board ESS can be a very viable solution [44]. Additionally, this configuration allows for greater efficiency in the event of regenerative braking, as there are no energy losses along the power transmission lines [34]. Experimental results of the integration of an ESS in Seville metro, Spain, are presented in [45], showing an overall efficiency of 84.4 %. Nevertheless, with on-board ESS, each locomotive within a railway line can be considered as a microgrid, generating and consuming energy. The surplus energy can be transmitted to the catenary, to directly aid another locomotive, can be injected into the power grid, or can be directly stored in an on-board ESS. From a technical point of view, on-board ESS facilitates the implementation of control algorithms with virtually instant access to the variables to be controlled. In contrast, one of the major disadvantages of this configuration is its difficult adaptability to the existing conventional systems.

For the power supply of on-board systems, there are different solutions: [35] and [43] presented some examples of a fast loading incorporated in the ground and placed in the middle of the railway track, where the ESS is charging continuously along the rail section. In [34] is presented another type of this system, where the feed cage is made laterally on the third rail (as represented in Figure 1.24 (i)). A cheaper and more adaptable solution is presented in [14], incorporating small catenaries only in the railway stations, being the stored energy used for the locomotion of the locomotive until the next station, as represented in Figure 1.24 (ii), initiating a new ESS charging process. A more innovative solution is presented in [43] where a wireless power transfer system is used to charge the ESS, identifying the different existing projects as well as the biggest advantages and disadvantages of each solution. Finally, the inductive system,

presented in Figure 1.24 (iii), appears as another solution under investigation that allows the elimination of catenaries. This system is analyzed in a topic below *1.3.3.5 Wireless Power Transfer*.

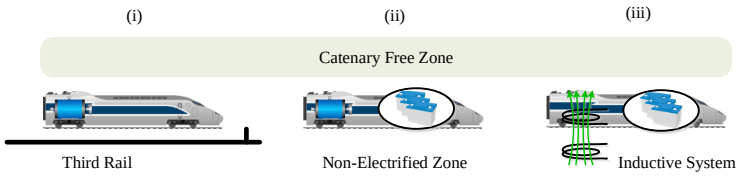

Figure 1.24 - Representation of some future operating mode trends: catenary free zones.

The biggest challenges regarding the implementation of such technology lie in creating an ESS with a high specific energy density: a high amount of stored energy with lightweight. Another challenge lies in adapting existing locomotives and vehicles to such an ESS. An example of an adaptation of a locomotive with the creation of a lower contact for power supply is presented in [46]. However, projects to adapt an on-board ESS are normally rare due to the costs and the inherent difficulty to adapt the existing structure.

The *Siemens cityjet eco* project consisted of the adaptation of a conventional locomotive, developing a functional prototype with a 500 kWh battery ESS that provides a range of 80 km and achieves a maximum power of 1.3 MW and a top speed of 140 km/h. The main objective is to obtain knowledge for the serial production of on-board battery locomotives. Another project is the *Bombardier talent 3*, completed in 2020, composed of six locomotives with on-board batteries that allow them to reach speeds of 160 km/h and autonomies up to 100 km in catenary-free zones.

Off-Board Energy Storage System

The off-board ESS can be used in conjunction with renewable energy sources to store energy at peak production times. Additionally, it can also be used to store energy from regenerative braking, as presented in Figure 1.23. However, all stored energy can be used not only to help the locomotive movement, as represented in Figure 1.23, but can also be used to feed the inherent railway system, such as passenger railway stations and car parks [47]. With the inclusion of ESS in strategically chosen locations along the railway it would be possible to impose a more efficient and independent railway system with energy sources closer to the consumption places.

As it is a fixed solution, specific energy density is not a priority, thus having a smaller initial investment [30]. Additionally, this solution is easily adaptable to conventional feeding systems and is very attractive for nowadays applications as well as in the near future, considering the sufficient fleet of locomotives without the possibility of internally including an ESS. An example of this adaptability is presented in [48], where *Hitachi* Branch, East Japan Railway Company, has been implementing ESS between TPS to take advantage of regenerative braking. One of the conclusions obtained was that in metropolitan stations,

where the flow of locomotives is less than 5 minutes, the energy from regenerative braking is directly used by adjacent locomotives at start-up. The opposite scenario is in stations outside the metropolitan area, where trains flow is over 10 minutes, the total energy from regenerative braking does not justify the investment of an ESS. In order to take advantage of ESS, the correct location of installation is required, and a station where the flow of locomotives is on average 7 minutes is recommended. An example is the *Ushiku* station where it is estimated (based on the first 8 months of operation) savings of 2500 MWh/year [48].

The biggest challenge of this system lies in implementing control algorithms that can detect regenerative braking from a specific locomotive hundreds of meters or tens of kilometers away. The control system should orientate the energy resulting from the regenerative braking to flow near the ESS. An example of this concern is the migration of the Global System for Mobile Communications – Railway (GSM-R) system to the Long-Term Evolution – Railway (LTE-R), enabling communication up to 12 km, at 50 Mbps of downlink and 10 Mbps of uplink data rate, with a success rate of over 99.9% for speeds up to 500 km/h [49].

1.3.3.3 Renewable Energies

Electric energy, as represented in Figure 1.25, is indispensable for the electrification of the railway system. The inclusion of energy sources, namely renewable, near the places of consumption has been arousing a special interest in the scientific community. Initially, the major focus of integrating renewable energy sources was to feed the railway stations rather than the catenary. Thus, all renewable energy production would be for direct consumption, with the surplus stored in the ESS for later usage [50]. In [47] is presented a study based on computational simulations of the conjugation of various renewable energy sources with regenerative braking to charge the electric vehicles that are parked in the substation neighborhoods. This conjugation of different energy sources looks very interesting considering the varied energy production of the solar photovoltaic (PV) installation throughout the day as well as throughout the year.

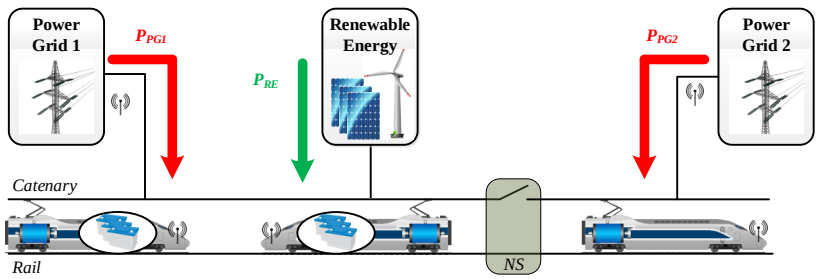

Figure 1.25 – Representation of future operating mode trend: renewable energy interface.

Although these concepts are quite commonplace today in lower power applications, renewable energy sources have not triggered a major investment focus for rail power. Considering the length of the railway lines, and the vast majority in constant sun exposure, at first glance it would be very attractive to install solar PV panels along de tracks. However, the inherent logistical problems in such fragile installations can be questioned. There are already studies for the integration of this type of installation in Hyperloop, where they intend to analyze the best configuration of solar PV modules for better solar exposure. The results of these studies are presented in [51], whether the priority is to maximize energy production or to minimize the costs.

The biggest challenge for the integration between renewable energy sources and the railway power system is the implementation of power electronics solutions. Power electronics converters have to be able to draw the maximum power over time from intermittent sources. Nevertheless, and taking into consideration an example of a typical value of 200 W_p solar PV module with an area of 1.5 m^2, it would take 50 000 PV modules and an area of at least 75 000 m^2 to generate equivalent power of 10 MW_p solar PV installation, raising some logistical questions regarding the large area of the installation. In addition, this area assumes that all photovoltaic solar modules are close together, with no space between them; however, it should be noted that usually, they need some inclination to maximize sun exposure, giving shade to the solar PV modules behind. Thus, it is likely that integrating solar photovoltaic installations will be more suited to lower the energy demand in smaller railway systems or in railway stations to feed lower power loads.

1.3.3.4 Hybrid Power System

Despite the progresses in railway electrification, there are still several non-electrified extension zones due to the types of locomotives and the impossibility of extending the power line. In this context, an on-board hybrid system presents itself as one of the most viable solutions. This system can combine the autonomy of a diesel engine with the efficiency, higher starting torque and the silence of electric motors. Low noise is one of the requirements in certain areas and/or periods of the day. As a consequence of this junction, the diesel engine can be smaller, reducing CO_2 emissions [34]. In addition, the electrical system will cover the torque gaps of the diesel engine, the diesel engine responsible for providing average power, and the electrical system responsible for providing power variations. This way, it is possible not only to improve efficiency but also to make travel more comfortable for passengers [34].

1.3.3.5 Wireless Power Transfer

Despite being a concept characterized by low energy efficiency, inductive wireless power transfer solutions, with efficiencies of more than 80 % and 1 MW of power already exist [52]. Additionally, the low efficiency of wireless energy transfer is identified by the imperfect alignment of the inductive winding present in the power source with the winding present in the load. However, in a railway system, this problem can be minimized to only one axle, since the locomotive maintains a fixed alignment both in height and width with the railway lines, varying only its longitudinal position.

From a more technical point of view, it is possible to identify resonant LC converters that combine inductors (L) and capacitors (C). These converters are characterized by their high volume and weight. In addition, this system is sensitive to the presence of any nearby metallic body, such as locomotives and wagons. Therefore, a careful design is necessary. Ferromagnetic cores can be placed to concentrate the generated magnetic fields. However, this solution will inflate the final cost.

1.3.3.6 Magnetic Levitation

Another innovative concept is electromagnetic levitation, using permanent magnets to levitate and propel the train wagons. Since there is no need for rail wheels, this solution has lower friction which enables higher speeds and lower maintenance [53]. In this concept, it is possible to highlight two main projects that use Magnetic Levitation: *Hyperloop* and *Maglev*. In [53], a detailed description of these two technologies is presented.

Magnetic levitation technology has been struggling to enter the market decades ago. One of the main factors for this system is the long-term contracts for the exploration, manufacture, and maintenance of traditional locomotives and railways. At this point, it is possible to identify another factor with the interoperability of the service. These innovative, high-speed systems can only be effective when completely independent of slower and conventional systems. In addition, rail transport with totally different speeds at the same rail line raises safety concerns [54].

1.3.3.7 Other Emerging Concepts

One of the major concerns in railway systems lies in the constant power unbalance in adjacent overhead lines. In order to allow a greater flow of locomotives, it is necessary to increase the capacity of overhead contact lines without overloading them. Thus, one of the trends lies in the implementation of solutions capable of balancing the power in the overhead contact lines to allow the integration of more and larger locomotives in the railway system and/or to reduce the oversizing of the power transformers and cable

section. With this concept, as is represented in Figure 1.26, it would be possible to make the railway system more efficient and less expensive [36].

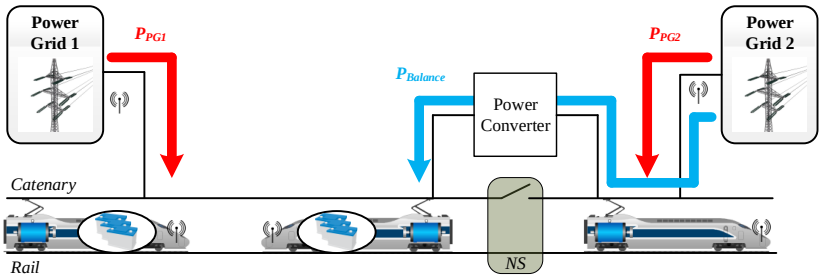

Figure 1.26 – Representation of future operating mode trend: sp-RPC balancing active power in different TPS.

1.4 The Framework of the Doctoral Thesis

The European Union is aiming the development of a single European railway area, called the Single European Railway Area (SERA) [55]. To achieve this goal, several European funds and incentives have emerged to promote technological development in railway systems, with the integration of new materials and subsystems that allow for increased functionality.

Following on to make the railway system more efficient, safer, and more environmentally friendly, comes the *Fundação para a Ciência e Tecnologia* (FCT) iRail – Innovation in Railway Systems and Technologies doctoral program, in which the doctoral thesis of the author fits in. Nevertheless, this doctoral program is aligned with the objectives of the European Shift2Rail organization, which aims to contribute to: reduce the life cycle cost of rail transport by up to 50 %; double railway capacity; and increase reliability by up to 50 % [55], [56]. As it turns out, Shift2Rail is committed to making the railway system more efficient, safer and greener, with a view to "*providing, through rail research and innovation, the capabilities needed to achieve a more sustainable, cost-effective mode of transport, high performance, time-oriented, digital and competitive for Europe*" [55]. In order to realize this vision, it is necessary to implement new solutions in the railway system, allowing the sector to produce higher-value products and services. To this end, was created twelve capabilities, shown in Figure 1.27, representative of the Shift2Rail paradigm.

Within these twelve added features, highlight the 5th, regarding energy optimization. In this topic, it advocates the use of alternative propulsion means, such as fuel cells or hybrid systems, essentially for non-electrified sections, to reduce the cost associated with installing and expanding the electric railway system. It is also argued for the installation of ESS, both internal and external to the locomotive, for a better distribution of energy according to their needs and thereby enabling the recovery of energy from regenerative braking. However, the integration of renewable energy sources and concepts such as smart grids would not only enable local energy generation more efficiently but also more flexibility in the supply

and exchange of energy. Additionally, with the integration of local energy sources, it would be possible to increase energy efficiency as well as reduce the overload on the power grid. Thus, allowing the integration of more or larger electric locomotives into the same railway system.

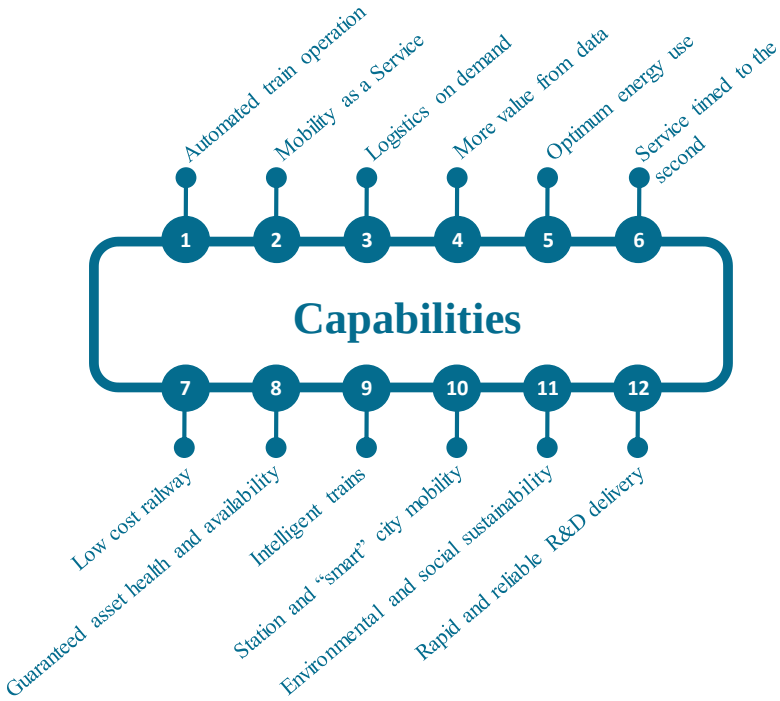

Figure 1.27 – Representative diagram of the twelve functionalities needed to realize the Shift2Rail paradigm (based on [55]).

By realizing the features identified in Figure 1.27, the European Union anticipates the following economic benefits [55]:

- Indirect aid for industrial product research and development industries exploiting the H2020 innovations, worth up to EUR 9 billion in the period 2017 – 2023;
- Creation of up to 140 thousand new jobs in the period from 2015 to 2030;
- Creation of and additional European Union Gross Domestic Product (GDP) of EUR 49 billion over the period 2015 – 2030, which will be distributed to most member states;
- Additional exports of EUR 20 billion over the period 2015 – 2030, thanks to the worldwide commercialization of new railway technologies developed over the H2020;
- Product lifecycle savings of around EUR 1 billion over the first 10 years and, with continued implementation, achieve EUR 150 million per year;

In the Portuguese case, an investment of over EUR 5 billion is foreseen, of which EUR 2 800 million will be directed to the railway structures [57].

1.5 Motivation

Being a field of research that is still recent, this area of development is very fertile for technological contribution and for boosting the author's name. Most of the technological contributions in this area are still in the prototyping phase, and there are no solutions on the market for this type of dynamic compensation for power quality problems applied to rail systems. Additionally, taking into account the operating voltages and powers, the analyzed power electronics concepts (topologies and control algorithms) present some versatility, being able to be adapted and used in other applications.

In general, it is intended to contribute to improving the energy efficiency of railway systems, introducing new concepts and new features, such as the possibility of renewable energy interfaces, which are of personal interest to the author and who already has experience both in research or in the development of new topologies. Additionally, it aims to introduce added features into the system such as dynamic control and how to control the flow of energy during regenerative braking.

From a more specific perspective, the ambition is to develop modular multilevel converters, which is an emerging concept applicable in the most diverse applications of power electronics with high voltage levels. With this, the author will be able to develop skills that can be applied not only in rail systems but also in wind systems or the context of Smart Grids.

The multidisciplinary nature of the work developed in the Group of Power Electronics and Energy (GEPE), should be highlighted. As such, it will enable the author to develop skills in terms of simulation tools, hardware development, and printed circuit board (PCB) design, among others. In addition to the development of critical analysis, all this knowledge will provide the author with better skills for a professional world in the field of research and development of power electronics.

1.6 Objectives

This doctoral work will contribute to the Shift2Rail objectives, namely in terms of the development and modernization of the TPS. The smart power conditioner studied and developed in this project intends to:

- minimize unbalances between TPS;
- improve the efficiency of the rail system, integrating energy sources closer to the places of consumption;
- provide dynamic control in terms of balancing the operating active powers of different TPS, mitigating problems arising from algorithms based on hourly forecasts;

- take advantage of regenerative braking, introducing the functionality of local energy storage to soften the accentuated consumption when starting another locomotive;
- introduce micro grid concepts with the possibility of integrating renewable energy sources;
- increase the energy capacity of the railway system, allowing the integration of more and larger locomotives;
- contribute to the development of computational models of an sp-RPC with dynamic control and interface with a solar photovoltaic system and with BESS;
- from a practical point of view, contribute to the analysis and development of modular and multilevel converters;
- publication of scientific articles in journals and international conferences of the work carried out, being submitted to the evaluation of the scientific community, specialized in the research area, allowing to spread the ideas proposed in this doctoral thesis.

1.7 Thesis Organization and Structure

This doctoral thesis document is divided into 7 chapters, describing all the analysis steps and decisions taken to achieve the proposed objectives. A more detailed description of each chapter contents is presented below.

In Chapter 1 there is a summary description of the importance of the railway system, with a special focus on the electrified system, highlighting future trends. The analysis allowed identify a scientific problem that this doctoral thesis intends to contribute to solving.

In Chapter 2, a brief introduction is made to the history and evolution of the railway electrical system, analyzing some types of electrification, with a special focus on the 25 kV - 50 Hz, ac electrical system. The chapter proceeds with a description of energy storage systems, identifying the different technologies that allow incorporation into rail systems. Regarding electrochemical battery technologies, it was necessary to study the equivalent model. Knowledge of the equivalent electrical model is an essential practice for a correct prediction of the behavior of the implemented system, emulating the battery charge and discharge processes. The chapter ends with the study of the solar photovoltaic concept, analyzing the equivalent model of a solar photovoltaic cell, the related concepts, and the influence of external climatic factors.

Chapter 3 focuses on a more technical analysis of power converter topologies and control algorithms. The chapter starts with an analysis of different topologies of power electronics converters that allow the interface with different energy systems: the ac catenary, the solar photovoltaic and the battery energy storage. The study continues with the analysis of control techniques with a view to the concept of modular and multilevel converters. The chapter ends with the presentation of different necessary control algorithms, from current control algorithms, maximum energy extraction algorithms from the solar photovoltaic system and battery charging algorithms.

In chapter 4, the sp-RPC for the real scale of the railway system is introduced, presenting all the necessary control algorithms. The proposed algorithm for the sp-RPC is analyzed using computational simulations, and results are presented for different operating modes (with and without the solar PV and battery energy storage interfaces enabled). A quantitative analysis of the sp-RPC performance is presented at the end of the study. The chapter presents the second part of simulations, and this part is related to the simulation results of the proposed system at a reduced-scale. Thus, the results of the simulation model based on the developed reduced-scale experimental prototype are presented and analyzed. The chapter ends with a quantitative analysis and discussion of the results obtained.

Chapter 5 describes all the hardware developed and used for the reduced-scale laboratory prototype of the sp-RPC. Throughout the description, all procedures performed for dimensioning some components and circuits are presented.

In Chapter 6 all the experimental results obtained from laboratory tests carried out on the sp-RPC prototype are presented. The validation went through different processes, starting with hardware validation with open-loop control, and proceeding with the closed-loop of each sp-RPC subsystem. The final validation of the sp-RPC is presented at the end, with quantitative data being presented.

Finally, chapter 7 presents the final conclusions obtained with the development of this doctoral work. Due to the complexity, difficulties and restrictions, some suggestions for improvement for possible future works are also presented.

1.8 Publication of Scientific Papers

This item presents publications related to the work carried out in this thesis, namely publications in international journals, publications in book chapters and publications in international conferences.

1.8.1 Papers in Journals

9 J.P.D. Miranda, **L.A.M. Barros**, J.G. Pinto, "**A Review on Power Electronic Converters for Modular BMS with Active Balancing**", *Energies* 2023, 16, 3255. https://doi.org/10.3390/en16073255

8 **L. A. M. Barros**, A.P. Martins, J.G. Pinto, "**Balancing the Active Power of a Railway Traction Power Substation with an sp-RPC**", *Energies* 2023, vol. 16, 3074. https://doi.org/10.3390/en16073074

7 S. Coelho, V. Monteiro, T. J. C. Sousa, **L. A. M. Barros**, D. Pedrosa, C. Couto, and J. L. Afonso, "**A Unified Power Converter for Solar PV and Energy Storage in dc Microgrids**", *Batteries*, vol. 8, no. 10, p. 143, 2022, doi: 10.3390/batteries8100143

6 **L. A. M. Barros**, A. P. Martins, and J. G. Pinto, "**A Comprehensive Review on Modular Multilevel Converters, Submodule Topologies, and Modulation Techniques**", *Energies*, vol. 15, no. 3, p. 1078, 2022, doi: 10.3390/en15031078.

5 C. F. Oliveira, **L. A. M. Barros**, J. L. Afonso, J. G. Pinto, B. Exposto, and V. Monteiro, "**A Novel Single-Phase Shunt Active Power Filter Based on a Current-Source Converter with Reduced Dc-Link**", *EAI Endorsed Transactions on Energy Web*, 2021

4 M. Tanta, J. Cunha, **L. A. M. Barros**, V. Monteiro, J. G. Pinto, A. P. Martins, and J. L Afonso, "**Experimental Validation of a Reduced-Scale Rail Power Conditioner Based on Modular Multilevel Converter for AC Railway Power Grids**", *Energies*, vol. 14, no. 2, p. 484, 2021, doi: 10.3390/en14020484

3 **L. A. M. Barros**, M. Tanta, T. J. C. Sousa, J. L. Afonso, and J. G. Pinto, "**New Multifunctional Isolated Microinverter with Integrated Energy Storage System for PV Applications**", *Energies*, vol. 13, p.4016, 2020, doi: 10.3390/en13154016

2 J. G. Pinto, V. Monteiro, B. Exposto, **L. A. M. Barros**, T. J. C. Sousa, L. F. C. Monteiro, and J. L. Afonso. "**Power electronics converters for an electric vehicle fast charging station with energy storage system and renewable energy sources**". *EAI Endorsed Transactions on Energy Web*, p. 119, 2020, doi:10.4108/eai.13-7-2018.161749

1 J. G. Pinto, R. Macedo, V. Monteiro, **L. A. M. Barros**, T. J. C. Sousa, and J. L. Afonso, "**Single-Phase Shunt Active Power Filter Based on a 5-Level Converter Topology**". *Energies*, vol. 11, p. 119, 2018, doi: 10.3390/en11041019

1.8.2 Book Chapters

4 D.F.S.Fernandes, R.F.O.Costa, **L.A.M. Barros**, D.Pedrosa, J.L. Afonso and J.G. Pinto, "**A Comprehensive Comparison of Voltage and Current Control Techniques for Three-Phase VSI Converters**", In: Afonso, J.L., Monteiro, V., Pinto, J.G. (eds) *Sustainable Energy for Smart Cities. SESC 2021*. Lecture Notes of the Institute for Computer Sciences, Social Informatics and Telecommunications Engineering, vol 425. Springer, Cham., ISBN: 978-3-030-97026-0, doi: 10.1007/978-3-030-97027-7_2

3 **L. A. M. Barros**, M. Tanta, A. P. Martins, J. L. Afonso, and J. G. Pinto, "**STATCOM Evaluation in Electrified Railway Using V/V and Scott Power Transformers**", In: Afonso J., Monteiro V., Pinto J. (eds) *Sustainable Energy for Smart Cities. SESC 2019*. Lecture Notes of the Institute for Computer Sciences, Social Informatics and Telecommunications Engineering, vol 315. Springer, Cham. , ISBN: 978-3-030-45693-1, doi:10.1007/978-3-030-45694-8_2

2 C. F. Oliveira, **L. A. M. Barros**, J. L. Afonso, J. G. Pinto, B. Exposto, and V. Monteiro, "**A Novel Single-Phase Shunt Active Power Filter Based on a Current-Source Converter with Reduced Dc-Link**", In: Afonso J., Monteiro V., Pinto J. (eds) *Sustainable Energy for Smart Cities. SESC 2019*. Lecture Notes of the Institute for Computer Sciences, Social Informatics and Telecommunications Engineering, vol 315. Springer, ISBN: 978-3-030-45693-1, doi: 10.1007/978-3-030-45694-8_21

1 J. G. Pinto, V. Monteiro, B. Exposto, **L. A. M. Barros**, T. J. C. Sousa, L. F. C. Monteiro, and J. L. Afonso, "**Power Electronics Converters for an Electric Vehicle Fast Charging Station with Storage Capability**", In: Afonso J., Monteiro V., Pinto J. (eds) *Green Energy and Networking. GreeNets 2018*. Lecture Notes of the Institute for Computer Sciences, Social Informatics and Telecommunications Engineering, vol 269. Springer, Cham., ISBN: 978-3-030-12949-1, doi:10.1007/978-3-030-12950-7_10

1.8.3 Papers in Conferences

11 J. P. D. Miranda, D. M. N. Rodrigues, **L. A. M. Barros**, and J. G. Pinto, "**DC-DC Power Converter for High-Power Solar Photovoltaic System**", *EAI SESC 2022 - 4th EAI International Conference on Sustainable Energy for Smart Cities*; 2022

10 J. Rego, F. L. Pereira, **L. A. M. Barros**, A. P. Martins, and J. G. Pinto, "**Development of a Modular Multilevel Cascade Converter Based on Full-Bridge Submodules with a Common DC Bus**", In: Afonso, J.L., Monteiro, V., Pinto, J.G. (eds) *Sustainable Energy for Smart Cities. SESC 2021*. Lecture Notes of the Institute for Computer Sciences, Social Informatics and Telecommunications Engineering, vol 425. Springer, Cham., doi:10.1007/978-3-030-97027-7_3

9 D. F. S. Fernandes, R. F. O. Costa, **L.A.M. Barros**, D.Pedrosa, J.L. Afonso, and J.G. Pinto, "**A Comprehensive Comparison of Voltage and Current Control Techniques for Three-Phase VSI Converters**", In: Afonso, J.L., Monteiro, V., Pinto, J.G. (eds) *Sustainable Energy for Smart Cities. SESC 2021*. Lecture Notes of the Institute for Computer Sciences, Social Informatics and Telecommunications Engineering, vol 425. Springer, Cham., doi:10.1007/978-3-030-97027-7_2

8 **L.A.M. Barros**, M.Tanta, A.P. Martins, J.L. Afonso, and J.G. Pinto, "**Opportunities and Challenges of Power Electronics Systems in Future Railway Electrification**", *CPE-POWERENG - 2020 IEEE 14th International Conference on Compatibility, Power Electronics and Power Engineering*, Setubal, Portugal, July 2020, vol. 1, pp 530-537, doi: 10.1109/CPE-POWERENG48600.2020.9161695

7 M. Tanta, **L. A. M. Barros**, J. G. Pinto, A. P. Martins, and J. L. Afonso, "**Modular Multilevel Converter in Electrified Railway Systems: Applications of Rail Static Frequency Converters and Rail Power Conditioners**", *International Young Engineers Forum (YEF-ECE)*, Costa da Caparica, Portugal, 2020, pp. 55-60, doi: 10.1109/YEF-ECE49388.2020.9171814.

6 **L. A. M. Barros**, J. L. Afonso, P. Ferreira, M. Araújo, J. G. Pinto, "**Study on the technological and economic viability of introducing energy storage systems with solar photovoltaic panels**", In *4th International Conference on Energy and Environment - ICEE: bringing together Engineering and Economics*, 2019

5 **L.A.M.Barros**, M.Tanta, A.P.Martins, J.L.Afonso and J.G.Pinto, "**STATCOM Evaluation in Electrified Railway Using V/V and Scott Power Transformers**", *SESC* 2019 - EAI International Conference on Sustainable Energy for Smart Cities, 2019

4 J.L.Torre, **L.A.M. Barros**, J.L.Afonso and J.G. Pinto, "**Development of a Proposed Single-Phase Series Active Power Filter without External Power Sources**", *2019 International Conference on Smart Energy Systems and Technologies (SEST)*, Porto, Portugal, 2019, pp. 1-6, doi: 10.1109/SEST.2019.8849010.

3 R. Duarte, L. Moreira, **L. A. M. Barros**, V. Monteiro, J. L. Afonso, and J. G. Pinto "**Power Converters for a Small Islanded Microgrid Based on a Micro Wind Turbine and an Battery Energy Storage System**", *ECOS 31st International Conference on Efficiency, Cost, Optimization, Simulation and Environmental Impact of Energy Systems*, pp.1-12, Guimarães, Portugal, 2018. ISBN: 978-972-99596-4-6

2 J. G. Pinto, M. Tanta, V. Monteiro, **L. A. M. Barros**, and J. L. Afonso "**Active Power Conditioner Based on a Voltage Source Converter for Harmonics and Negative Sequence Components Compensation in Electrified Railway Systems**", In the 7th Transport Research Arena (TRA 2018), 16-19 April 2018, p.p 1-10,Vienna, Austria, DOI: 10.5281/zenodo.1491309

1 **L. A. M. Barros**, V. Monteiro, B. Exposto, A. A. Nogueiras Meléndez, J. L. Afonso, and J. G. Pinto, "**New multifunctional push-pull converter operating with MPPT and integrated energy storage system for PV micro-inverter applications**", *IECON 2017 - 43rd Annual Conference of the IEEE Industrial Electronics Society*, Beijing, 2017, pp. 7807-7812, doi: 10.1109/IECON.2017.8217368.

1.8.4 Review of Scientific Papers

The author contributed to the review of scientific documents, accounting for 11 papers submitted to international conferences and 4 papers submitted to journals. The author also participated in the organization of the Sustainable Energy for Smart Cities - SESC conference from 2019 to 2022, exercising the role of publicity chair between the years 2019 to 2021, and the role of publications chair in 2022.

Chapter 2

Railway Power System, Energy Storage Technologies and Renewable Energy Sources

2.1 Introduction

With constant population growth and migration to large urban centers, the weakness of existing means of transport has been demonstrated. The electric railway system is a safe, environmentally friendly and energy-efficient solution. However, it follows a centralized paradigm, which is one of its weaknesses. In order to increase the capacity of the existing TPS to integrate more and larger locomotives, the replacement of these systems is necessary for greater operating powers. It becomes evident the need to develop new solutions that allow a simple and fast integration in the railway systems, to mitigate the existing problems and satisfy future needs while keeping investments and operation costs low.

In this chapter, three systems are analyzed: i) a railway system; ii) renewable energy; iii) and energy storage system. The first stage focuses essentially on the analysis of the existing railway electrical systems, as well as their historical evolution. The analysis proceeds with the study of different technologies for energy storage with possible applications in electric railway systems. This study aims to identify the best solution for its integration with a smart power conditioner, to control the stored surplus energy, either it being from renewable energy sources or regenerative braking. The stored energy can be used later to minimize the consumption of energy from the catenaries. The same study also presents electrical models of systems that were important in the development of computer simulations. Finally, to contribute to the integration of renewable energy sources in the railway system, a study on solar PV energy is presented. The objective is to study the operation principle of the solar PV cell, the equivalent electrical model and climatic influences.

2.2 The History of the Electric Railway System

Railway transport is the safest and most economical inland transport, recognized as one of the main catalysts for the economic growth of any country [1], [6]. In Europe, more than 26.9 billion trips were

made in 2012 by railways. They employ more than 2.3 million people, resulting in a gross amount of EUR 143 billion, which is more than air and sea transport combined [6]. Despite its strong impact on the industrial revolution in the early eighteenth century, the electrification of the railway system did not happen until almost seventy years later.

The first electric locomotive only appeared at the Berlin industrial exhibition in 1879 in Germany. Werner von Siemens exhibited a 2.2 kW dc electric locomotive, powered by a 150 V system [30], [44]. This small electric locomotive was capable of pulling three small wagons, each with six seats, and reaching a speed of 13 km/h [30], [44]. It should be noted that in four months, it was able to carry over 86 000 passengers over 300 meters of the circular runway [44]. The locomotive engine weighed two tons, with a power ratio of 1 100 kg/kW. Nowadays, the locomotive's engines have a ratio of 14 kg/kW [58]. Two years later, in 1881, Siemens & Halske created the first streetcar, with a power of 7.5 kW and running a 2.5 km line near Berlin (Germany) [30].

The success of this system was so big that it was rapidly expanded to other cities, such as Vienna (Austria) and Frankfurt (Germany), and countries, such as Switzerland, France, as well as the United States of America (USA). In the USA, van Depoele built an electric streetcar network in 1886 [30]. Its major innovation was the power supply system. In which a power cable was used on a metal contact slid affixed to a wooden grip. Frank J. Sprague improved van Depoele's invention in the following year, by using a pulley for contact with the feed system. By this time, the power system was between 500 V – 600 V, with this configuration prevailing over five decades [30]. The first steps were taken to electrify the railway system.

By the year 1890, the electric railway expansion had reached 20 more American cities and was spreading all over the world. It should be noted, that by this time, there were concerns about the heavy smoke of traditional locomotives, mainly due to the invisibility that caused accidents [30]. This problem was more evident in congested areas, tunnels, and suburban areas. In this line of reasoning, the electric railway began to be introduced into the urban areas of London and Liverpool (United Kingdom) and, five years later, in 1895, into the suburban Baltimore area (USA) over 5 km [30]. In the latter case, and due to the high currents involved in the feed system, the above feed system was replaced by a transversal steel wire, which resulted in the "third side rail". Notably, the Baltimore locomotives were 90 tons and 1 060 kW for a 675 V rail electric system. By the end of the century, more than 20 000 km of railways were electrified [30].

Further on, during the 20th century, with the expansion of the railway system, highlighting the creation of tunnel segments (in mountains, metropolitan areas, etc.), the introduction of electrified railway systems

became a priority. This paradigm change, the electrification, made it possible to mitigate the problems in the conventional system, not only economically, due to the cost associated with coal, but also health, due to smoke inhalation, mainly in tunnels [30]. By this time, there were two solutions for the traction system of electric locomotives: dc motor and ac motor. The dc solutions were the first to be adopted, not showing any major difficulties in their practical implementation. On the other hand, ac solutions fed with the power grid frequency presented problems with the commutator switch. Hence, the railway system had to be powered at lower frequencies, 25 Hz in the United States and 15 Hz in Germany, representing 1/3 of the power grid frequency (at the time, the frequency was 45 Hz) [30]. Such configuration was intended to minimize the interference of the energy consumed by the locomotives in the power grid distribution system [58]. However, it required the installation of several generations and distribution systems, which contributes to the inflation of the final cost. Despite this disadvantage, the 3 – 4 kV ac system had as the greatest advantage the easy interruption in case of need [30]. The complexity and hence the cost to interrupt a dc is much higher compared to an ac system. In addition, and considering the same power level, the ac value in the railway system was much lower, which enables the installation of smaller cross-section wire, thereby reducing costs [30].

In railway systems that use frequencies lower than the frequency of the power grid, the reactance and resistance of the transmission line will also be lower, approaching that of the dc system [30]. This ensures a smaller voltage drop on the transmission line. However, since the frequency of the railway system is different from the frequency of the power grid, it is necessary to install dedicated power systems exclusively to interface with the railway system. Initially, still with little development in the area of power electronics, which would provide static solutions, the solution adopted was the rotating electric machines [30].

After the second world war, which ended in 1945, and with the advancement of power electronics, enabled the adaptation of the voltage level on-board the electric locomotive. Thus, the traction system became independent of the type of power system, which enabled the creation of a single-phase distribution system in 50 Hz ac in Europe and 60 Hz ac in the USA [30]. More specifically in France, the railway power grid in the war former occupancy zones has been upgraded to 25 kV [59].

At present, the single-phase ac power supply system with the power grid frequency is considered to be the most efficient and versatile for both regional and suburban transport. It should be noted that, considering the existing power in the railway system, the power grid voltage level has to be high, for the absorbed current level to be within the tolerable values during regenerative braking. Otherwise, cables with larger sections would be needed and would create problems between the pantograph and the

overhead contact line, which would prevent speeds exceeding 250 km/h [30]. In turn, dc rail electrical systems continue to be present mainly in urban areas, notably electric road locomotives and subways, with 750 – 1 500 V power supply systems [30].

In the next topics, a more detailed analysis of each type of electrification in the railway system is presented, highlighting its limitations and applicability.

2.2.1 Electric Railway System in Direct Current

The dc power system was the major driver of the railway system electrification. The evolution of power electronics has allowed the railway system voltage to gradually increase, currently operating at 750 V, 1 500 V and 3 000 V. The dc railway system is often found in tunnels, where diesel locomotives cause several problems [30].

In 1890, the major European capitals, Paris, Berlin and London, adopted the 1 500 V dc system for the urban railway system. In turn, to allow for a greater flow of electric locomotives, Italy has adopted a 3 000 V system. This voltage was considered the most efficient for systems that had electrical machines as power supply. However, required more complex and expensive boot systems to start the operation. It would be necessary to connect two engines in a series and at least four engines in starting conditions [30]. These requirements were subsequently neglected with the development of power electronics equipment capable of adjusting the operating voltages of motors, independently from the voltages in the power grid [30]. This 3 000 V system has also been implemented in Belgium, Spain, Russia and Poland [2][4].

In general, the major disadvantages of the dc railway system are the difficulty of creating a mechanism capable of interrupting the flow of a high direct current. Thus, several studies have been developed to implement a thyristor interrupt mechanism at the ac-dc connection point [44]. On the other hand, in the United Kingdom, the maximum current a locomotive can receive is 6 800 A for a 750 V system. These power stations require constant monitoring and, in many cases, only one locomotive is allowed in a given section. Note that the distance between two power substations on 750 V systems is 2.5 km, increasing to 25 km for 3 000 V railway systems [44].

2.2.2 Electric Railway System in Alternating Current

Considering the associated powers, a system with a high voltage level and, therefore, a low current level would naturally be valued in its implementation, not only for technical but also for economic reasons [30], [44].

In the German case, a 15 kV railway system was used and the voltage was reduced using a power transformer installed on-board the electric locomotive. As highlighted in item *2.2 The History of the Electric Railway* System, the major disadvantage of this system was the motor commutator switching, which is why a frequency lower than that of the power grid frequency was adopted. Additionally, ac induces parasitic currents, particularly in non-laminated ferromagnetic cores, which results in system overheating and consequently a decrease in efficiency [44]. As a result, systems with 1/3 of the power grid frequency were used. Hence, considering the frequency of 50 Hz and 60 Hz on the power grid, railway systems with 16 and ⅔ Hz and with 20 Hz were created, respectively. Several European countries such as Switzerland, Austria, Sweden and Norway have adopted the 16 and ⅔ Hz system [30].

2.2.3 Types of Existing Railway Power Systems

The adopted topologies for the railway electric power supply are strongly related to its applicability. As previously mentioned, the dc system is more prevalent in metropolitan applications, with the ac system being more geared to long-distance and high-speed railway electrification. Table 2.1 presents some electrical characteristics of the different railway systems. Analyzing the presented data, it can be concluded that the light and metro railway systems make better use of the dc power systems, because of the urban environment. On the other hand, for long-distance trips as well as high-speed, ac railway systems are more predominant.

Table 2.1 – Electrical characteristics of the catenary of the railway systems and of the different types of locomotives (based on [34]).

		LIGHT	METRO	CONVENTIONAL
CATENARY	dc	600 V 750 V 900 V	750 V 1500 V	750 V 1500 V 3000 V
	ac	-	-	15 kV (16 Hz and ⅔) 25 kV (50 Hz)
VEHICLE	Motors Power	75 kW – 150 kW	150 kW – 250 kW	200 kW – 600 kW
	Power Converters Power	150 kW – 300 kW	350 kW –1 MW	200 kW – 1.4 MW
	Maximum Speed	50 – 70 km/h	80 km/h	120 – 350 km/h
	Number of wagons	3 – 6	4 – 8	3 – 12
	Weigh per wagon	7 tons	40 tons	13 tons

The railway power supply has evolved over the years and is intrinsically influenced by economic, political and health issues [34]. Generically, it is possible to verify that dc systems are often found in metropolitan areas, and ac systems in interregional and high-speed areas. In Table 2.2 it is possible to see the extension of the electric railway system worldwide. It can be concluded that the ac systems have an extension comparable to that of the dc systems, having a slight advantage of 4 % in terms of the installed railway extension.

Table 2.2 – Extension of the electric railway system in the world (based on [30]).

DC SYSTEM		
< 1 kV	7 650 km	96 980 (47.3 %)
1 – 2 kV	20 440 km	
>2 kV	68 890 km	
SINGLE PHASE AC SYSTEM		
15 kV; 16 ⅔ Hz	32 940 km	105 050 km (51.2 %)
25 kV; 50/60 Hz	72 110 km	
Other systems	3 000 km	3 000 km (1.5 %)

Similarly, and based on Figure 2.1, is possible to verify the presence and consequent distribution of the different topologies for the railway feeding system. According to Figure 2.1, it can be seen that the ac railway system with a frequency of 16 and ⅔ Hz is found mainly in central and northern Europe, in countries such as Germany, Switzerland, Austria, Norway and Sweden. The 25 kV system at 50 Hz is the most predominant, being present in 14 countries. The dc system is mainly located in Italy, the Netherlands, Poland and Ukraine.

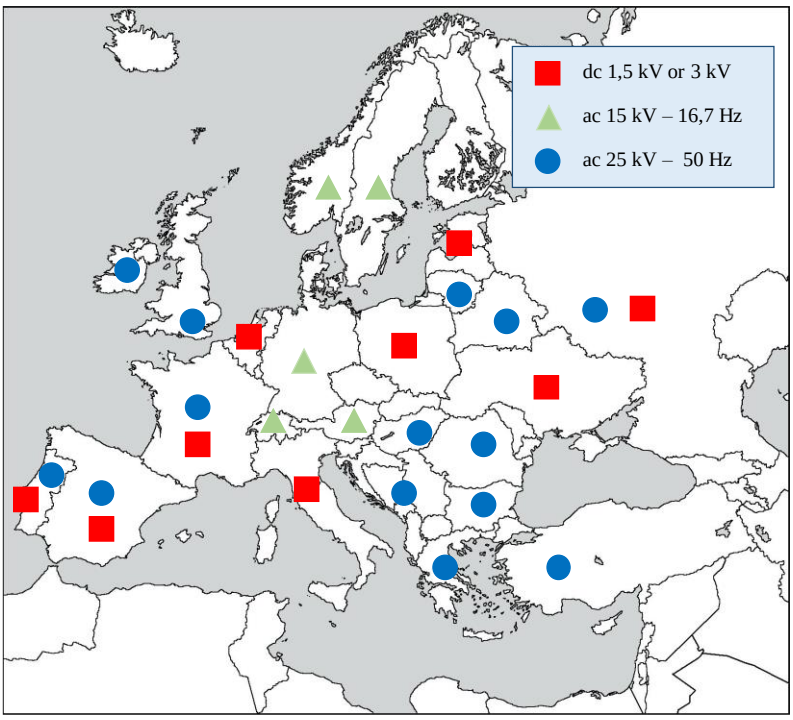

Figure 2.1 – Topologies of the railway system in Europe (based on [20], [34]).

Many of the countries shown in Figure 2.1 have technology development incentive programs for the electric railway system. These programs emerge as drivers to meet the mass travel needs of both people and goods in an environmentally and energy-efficient manner. Programs such as AVE (Spanish high speed), FRECC (Frecciarosa Trains), ICE (Intercity Express) and TGV (Train à Grande Vitesse) have allowed the rail sector to grow by 17 % from 2001 to 2013 [6]. However, the proliferation of electric locomotives has been causing problems with electric power quality in the power grid, namely in the overload of TPS.

2.3 Energy Storage System

Energy storage systems are solutions that allow the storage of energy from a conversion process. For the Railway Electric System, the origin of the energy is electrical and can be stored in different forms, being later converted to send back to the Electric System. Energy can be stored in thermal, mechanical, chemical, electrochemical, or electrical forms. Different technologies for energy storage systems are represented in Figure 2.2.

In the current paradigm of energy production and distribution, there are large remote energy production centers, with a unidirectional distribution line. However, unpredictable events lead to consumption peaks, requiring an oversized production system that leads to lower energy efficiency. The use of ESS allows the TPS to supply constant power, with the ESS being responsible for supplying power variations [60]. From the point of view of the electric railway system, these variations can be identified as the instants of acceleration or deceleration, when entering the regenerative braking mode of an electric locomotive.

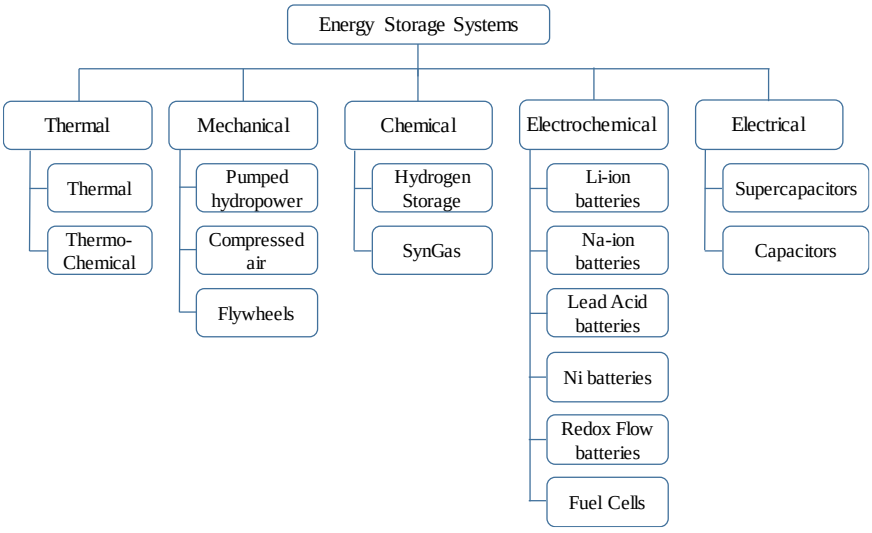

Figure 2.2 – Examples of energy storage technologies.

In order to mitigate these consumption variations and increase the efficiency of the railway system, whilst taking advantage of the energy from regenerative braking, different ESS technologies that can be implemented in railway electrical systems are analyzed.

2.3.1 Flywheels Technology

Flywheels are mechanical devices that allow for energy storage. They possess four key constituents: i) the rotor; ii) the electrical machine; iii) the power electronics converter to interface; iv) and auxiliary components such as bearings, cooling system and vacuum pumps [61], [62]. Flywheels thus enable the conversion of electrical energy into kinetic energy by storing the mechanical energy in the high-speed rotor. Since the rotor is connected to the electrical machine employing mechanical bearings, kinetic energy can be converted into electrical energy when needed [62]. This technology is gaining interest for integration of an ESS, in applications such as telecommunications, electric mobility, marine, aeronautics, and interfacing with renewable energy sources [63].

From analyzing their constitution and technical issues, it is possible to conclude some advantages and characteristics when using flywheels as ESS: i) high power density; ii) fast transition between charging and discharging operating modes; iii) high efficiency; iv) low maintenance costs; v) high life cycle; vi) high lifetime; vii) wide temperature ranges for operation; viii) clean and ix) environmentally friendly operation [63]. Flywheel ESS (FESS) with 300 kW and 1 MW have been installed in metropolitan dc railway systems in the United Kingdom and the USA, respectively [64]. In [65] they demonstrate that a flywheel can transition between generator to motor operating mode in 5 ms. A FESS can have an efficiency in the range of 90 – 95 %, however, it requires additional systems, such as cooling and vacuum pumps, which

decreases the overall efficiency of the FESS [61], [63]. With proper maintenance, a FESS can allow up to 100 000 operating cycles, with a lifetime of 20 years [61].

Some fewer positive aspects of this technology can be highlighted, namely: i) the need for periodic maintenance; ii) the need for auxiliary systems (cooling and vacuum pumps); iii) high initial investment; iv) low energy density; v) considerable self-discharge in non-utility. Due to the existence of mechanical bearings, periodic lubrication and maintenance of the system are required [62]. In large-scale, high-power applications, the energy losses due to bearing friction are considerable. In a flywheel of 200 tons, the energy losses due to friction can reach 200 kW, which decreases the system efficiency to 78 % after 5 hours of operation. If the flywheel operates for 24 hours, the efficiency can drop to 45 % [63].

Regarding technical issues, this type of technology requires the rotor to be installed in a vacuum (or low pressure using helium gas) chamber to decrease friction and, consequently, mechanical losses [62], [63]. Nevertheless, the amount of kinetic energy stored is proportional to the mass of the flywheel and the square of the angular velocity [62], [63]. As such, one way to determine the state-of-charge (SoC) of the system is by monitoring the angular velocity [61], [63]. A flywheel-based ESS can have low angular velocity values (down to 5 000 rpm), as it can reach high angular velocity values (100 000 rpm) [61]. Consequently, it is evident the need for metal alloys or other materials that have greater strength.

Considering practical applications, some studies have shown that the inclusion of a FESS allowed an efficiency increase of 21.6 % and 22.6 % for a single train and multiple trains, respectively, in a light railway dc system [64].

One of the first applications of flywheels in railway systems appeared in 1988 in Japan. The system had a maximum power of 2 MW and rated energy of 25 kWh, contributing to energy savings of 12 % until 2010 [62], [64], [66]. On the dc metro lines in the United Kingdom and in the United States of America, two flywheels with 300 kW and 1 MW were included. These systems allow transitioning from the generator to engine operating mode in 5 ms, and present low maintenance. Another example of an application exists in South Korea, with a monthly savings of 24 000 $ with a reduction in peak power consumption of 36.7 % [64]. In the city of Los Angeles, United States of America, there is another similar system, with 2 MW of rated power and 8.33 kWh of rated energy. Each charging/discharging process took an average of 15 seconds, with 1.25 min being required to carry out the complete charging/discharging process. Over 20 years, the FESS allowed daily energy savings of between 10 % to 18 % [64].

As far as new developments are concerned, it can be highlighted the study and development of superconducting or magnetic bearings to reduce mechanical friction [62], [63]. As far as magnetic

bearings are concerned, if a passive solution through magnets is adopted, their design is quite complex (due to Earnshaw's theorem) and expensive [62]. On the other hand, if an active solution is adopted, despite having greater control, an excitation current is required, which will decrease efficiency [62]. Another field of research lies in the integration of lightweight high-strength metallic material or carbon fiber-reinforced composites. The integration of these types of materials will increase the rotation speed and decrease the weight, which will consequently increase the energy density of flywheels [63].

In conclusion, flywheels are a very robust and efficient system for short-term energy storage applications. In applications where energy is intermittent, such as interfacing with renewable energy sources or regenerative braking and acceleration of a locomotive, flywheels present themselves as a good solution.

2.3.2 Electric Double-Layer Capacitors (EDLC) Technology

Electric double-layer capacitors (EDLC), better known as super-capacitors, have a different structure from conventional capacitors. Their operating principle is based on the Helmholtz double-layer principle [61]. As energy is stored directly as an electric field, and no chemical reaction takes place, supercapacitors have interesting characteristics for different applications [67]. Besides being used in electric road mobility, supercapacitors serve also electric railway applications, like assisting acceleration, climbing, and regenerative braking [64]. They are also used in spacecraft, electromagnetic launches, and on ships with high-power radars [68]. However, supercapacitors are normally used in hybrid energy systems, for example alongside lithium batteries. Thus, reconciling a solution that has a high specific power with a solution that has a high specific energy. Airbus uses supercapacitors in the emergency doors of the A380 model [63].

Since supercapacitors have a low internal resistance, they allow operation with high currents, with a wide range of temperatures and weather conditions (hot, cold, humid) [68]. Considering that it has no chemical process for energy storage along with low internal resistance, this ESS has high efficiency [67], [69]. Supercapacitors also have high life cycles, reaching 1 million cycles, all the materials are environmentally friendly and have low heating levels [61]. Compared to batteries, supercapacitors can have a specific power 10 to 100 times higher [68].

There is, however, an inherent high-cost associated with supercapacitors, which can reach 10 000 $/kWh, and they also have low energy density [61]. On the other hand, it has a high self-discharge rate, which can range from 10 % to 40 % of the stored energy in just one day [67]. Finally, it should be mentioned that the typical nominal voltages are low, ranging from 2 V to 3 V.

Regarding issues related to technical use, during the charging and discharging process, the supercapacitor voltage varies linearly. As such, it is simpler to determine the state of charge of the supercapacitor [63]. In [70] presents different electric equivalent models for the supercapacitor analyses.

Between *Agano* station and *Shomaru*, Japan, there is a 2.5 % gradient over 7 km rail path, with an ESS based on supercapacitors installed. The ESS consisted of 70 cells, capable to store 7.7 kWh during the charging process and 5.9 kWh during the discharging process. It is estimated that 77 % of the energy from regenerative braking has been successfully reused [66]. A more powerful system was installed in 2002 near the Ventas station in Madrid, Spain [62]. The supercapacitor-based ESS had a maximum power of 1 MW and an energy capacity of 2.3 kWh. This system made it possible to reduce energy consumption by 30 %, resulting in annual savings of 320 MWh. Another similar result was obtained by a system developed by Bombardier Transportation and installed in a prototype in 2003, allowing an energy reduction of 30 % [64].

2.3.3 Batteries Technology

Batteries are one of the most used ESS in recent years, storing electrical energy in chemical form. When an external circuit is added, chemical reactions occur internally, originating a flow of electrons and, consequently, of electric current. This process is reversible, requiring an external voltage source to be applied to the battery terminals.

This topic portrays the main concepts that allow characterizing the batteries, and the electrical models as well as a comparative analysis between the different battery technologies that allow integration in the railway electrical system.

2.3.3.1 Electrical Characteristics for a Battery

Batteries vary in terms of technology, causing them to have different weights, volumes and electrical characteristics. As such, the main concepts used for the characterization of batteries are [71]:

- Capacity (Ah): represents the electrical charge that the battery can supply. This is defined by the current that the battery can supply in a given period, usually in hours;
- C-Rate (C): establishes the relationship between battery capacity and current. For example, if a 100 Ah battery has a C-rate of 1 C for discharge, this means that the battery can supply 100 A for 1 hour. Some batteries have C values greater than 1, which would be completely discharged

in less than 1 h. Battery manufacturers present these values in the datasheet and introduce different values for charge and discharge, requiring consultation;

- Energy density (Wh/l): defines the relationship between the maximum amount of stored energy and the volume of the battery (in liters);
- Power density (W/l): defines the relationship between nominal power and battery volume (in liters);
- Fluctuation: consists of the final charging process used in some battery technologies. This process is normally used in lead-acid batteries, applying a state of charge close to full-charge, preventing it from remaining long periods of time in a partial state of charge;
- Life cycles: Represents the number of charges and discharge cycles that a battery can perform, under specific electrical and environmental conditions, without the battery reaching the minimum charge value;
- Lifetime: represents the number of charge-discharge cycles that the battery can carry out;
- Memory effect: consists of reducing battery capacity. This effect is identified in some battery technologies, usually related to short charge and discharge cycles;
- Specific energy (Wh/kg): Defines the relationship between the maximum amount of stored energy and the weight of the battery (in kg);
- State of charge (SoC): defines the energy capacity available in a battery at a given moment, expressed as a percentage of the nominal capacity;
- State of Health (SoH): Defines the relationship between the current average capacity of the battery and the initial capacity with zero cycles. Determining this parameter makes it possible to check the degradation of the battery and identify the ideal period for its replacement;
- Specific power (W/kg): defines the relationship between nominal power and battery weight (in kg);
- Sulfation: consists of a chemical phenomenon that occurs in the plates of lead-acid batteries. When this phenomenon occurs, there is a formation and deposition of lead sulfate crystals, decreasing the conductivity of the battery. This phenomenon is caused by the battery remaining discharged for long periods of time, or by having it subjected to severe and repetitive discharge processes;
- Open circuit voltage (V_{oc}): represents the value of the voltage at the battery terminals, for a given temperature and state of charge, when there is no current flowing through the terminals;

- Cut-off voltage: represents the minimum recommended operating voltage, up to which the manufacturer guarantees that the battery can be discharged without being damaged. Once this value is reached, the discharge must be deactivated.

2.3.3.2 Battery Technology

Throughout this topic, different battery technologies are presented and analyzed. The analysis carried out presents a similar structure for each one, initially identifying the technology, some characteristics and generic applications. The analysis proceeds with the identification of the advantages and disadvantages of the technology under study, also presenting some technical considerations and precautions to be taken in the integration of the power electronics system. Finally, some examples of integration in rail systems are presented.

Lead-Acid Battery Technology

Lead-acid batteries are the oldest battery technology, initially created by the French physicist Gaston Planté in 1859. Due to their maturity, reliability, and low cost, they are the preferred solution for different applications, such as vehicles, forklifts, telecommunications systems, interfaces with renewables, and uninterruptible power supply systems (UPS) [62], [69], [72]. Within the group of lead-acid batteries, the following can be listed: i) the traditional ones, technically known as flooded lead acid (VLA); and ii) those with regulated valves (VRLA). VLA lead-acid batteries require periodic maintenance and water replacement, having a larger volume. The VRLA is maintenance-free and has a valve that allows oxygen to be replenished to generate water during the chemical process that is generated during loading [72]. VRLA can be classified into two types, considering their composition: i) absorbed glass material (AGM); ii) and gelled electrolyte (GEL). AGM batteries use glass fiber to seal and reduce evaporation. GEL batteries use silica gel to increase the battery's operating temperature [73].

Analyzing the constitution of lead-acid batteries, it is possible to enumerate some advantages, namely: i) high voltage per cell (compared to nickel battery); ii) relatively good efficiencies (70 % to 90 %); iii) low cost; iv) fast discharge response; v) reduced daily self-discharge rate [62], [68], [72], [73]. Typically, each lead-acid battery cell has a nominal voltage of 2.15 V and a charging current rating of 0.25 C to 4 C [68]. Lead-acid battery constituents, namely lead and sulfuric acid, are abundant and easy to produce, allowing a reduced cost when compared to other battery technologies [72]. The self-discharge rate of this type of battery can reach a value of 0.1 %, being more suited to energy storage for long periods of time [74].

In turn, less positive aspects of this technology can be highlighted, namely: i) sensitivity to temperature; ii) sensitivity to discharge rates; iii) sensitivity to the number of discharge cycles; iv) sensitivity to long

periods of high capacity charging; v) non-linearity in the output power; vi) reduced lifetime; vii) low specific energy; viii) high toxicity impact; ix) necessary maintenance (VLA type batteries) [60], [62].

Low ambient temperatures decrease battery capacity [60]. On the other hand, the higher the temperature, the greater the mobility of electrons, accelerating chemical reactions and, consequently, causing corrosion on the plates, and reducing their useful life. Nevertheless, the mobility of electrons will increase the self-discharge rate, as well as the sulfation phenomenon [74]. This phenomenon will be accelerated in partially charged batteries. During the battery over-discharge process, lead sulfate crystals form at voltages below 1.75 V [69]. If the battery remains discharged for long periods of time, the lead crystals gather and crystallize. At this stage the process is irreversible, thus reducing the useful life of the batteries. Additionally, as the electrical conductivity of lead sulfate crystals is lower, the battery's internal resistance increases [69]. If the battery is discharged at a high rate, large amounts of hydrogen will be generated, decreasing efficiency and increasing the risk of explosion [73].

Since lead is a predominant chemical element in the battery and due to its density, lead-acid batteries have a low specific energy value [69]. Despite being a preponderant factor in electric mobility applications with on-board systems, in stationary off-board ESS, this characteristic does not have significant importance when lead-acid batteries are chosen. Despite high toxicity, 97 % of lead in batteries can be recycled [68].

Concerning technical issues, it essentially falls back on the issue of temperature. Unlike solar PV modules whose characteristics are presented at 25°C in STC, the nominal temperature of the batteries is not standardized, it is specified by the respective manufacturer. If lead-acid batteries are installed in cold geographical areas, it is recommended to install temperature control systems, which inflate the cost of implementation. According to some authors, the capacity decreases by 1 % for each 1 °C reduction in the temperature of the batteries [75]. An example of this phenomenon is the difficulty of car starter batteries to ignite on colder days. It is recommended to oversize the battery bank by 30 % if they operate at an average temperature below 15 °C or above 35 °C [75]. It should be mentioned that lead-acid batteries charge and discharge at negative temperatures down to -20 °C, better than other battery technologies. However, the charging process must be carried out at a rate of 0.3 C [68].

During the lead-acid battery charging process, it is recommended to implement a charge rate between 0.25 C and 4 C [68]. In case of overload, exceeding the cell value of 2.39 V, the electrode loses water, requiring water replacement and maintenance [68].

New studies have also shown that the insertion of carbon in small concentrations (0.15 % to 0.25 %) mitigates the sulfation phenomenon, and prolong the lifetime of lead-acid batteries [68].

Nickel Battery Technology

Nickel Cadmium (NiCd) was the most used battery technology, between 1970 and 1990, and showed high development maturity. NiCd batteries were used in power tools, portable devices, emergency signal lamps, UPS and generator starters [69]. However, due to the toxicity in Cadmium, there were investigations into the development of a better solution. That led to the Nickel-Metal Hydride (NiMH) batteries [62]. NiMH batteries were the batteries of choice for portable devices over the two decades after 1990 [60], [69].

NiCd batteries have a higher energy density and a longer lifetime compared to acid batteries [69]. Due to the low internal resistance, NiCd batteries can withstand high charge and discharge rates [62]. Furthermore, NiCd batteries perform well for temperatures down to -40°C [61]. NiMH batteries, on the other hand, have high power density, robustness and safety, and longer lifespan even for partial state-of-charge use [64]. Additionally, the operating temperature limits for NiMH batteries are between 50°C and -10°C [61].

NiCd batteries, in general, have a high cost of implementation, and had a memory effect, making it necessary to carry out several cycles of total discharge to be able to fully charge them again [64], [74]. The NiCd batteries have the following disadvantages when compared with NiMH batteries: short lifetime, more susceptibility to the memory effect, Cadmium toxicity that requires a more complex recycling process, and lower energy density [62], [64], [69]. Conversely, NiMH batteries had a high self-discharge rate, however, this problem could be mitigated by introducing other materials in the batteries [64], [69].

Although NiMH batteries are considered maintenance-free, releasing water during the chemical process that occurs when they are overcharged, additional care must be taken. If a high load process is applied, the chemical reaction will release large amounts of hydrogen, leading to cell rupture [69]. If the battery is over-discharged, it can lose capacity. Due to the reduced nominal voltage, approximately 1.2 V, it is necessary to add several cells in series to reach the desired voltage values [61]. However, considering different internal characteristics and different high discharge rates, it originates a battery pack with highly unbalanced voltages, thus requiring a BMS, which increases the implementation cost [62].

An example of a NiMH-based ESS can be found at *Swimo LRV*, Japan. The system installed in 2007 allowed an increase in system efficiency by 6 %. Another example can be found in the city of New York,

United States of America, where the system allowed storing 71.4 % of the energy coming from regenerative braking [64].

Lithium-ion (Li-Ion) Battery Technology

The first battery cells using lithium-ion were developed by Sony Corporation and appeared on the market in 1991 [60], [72]. Since then, this technology has shown greater assiduity in the market in different applications, as well as awakening interest in the scientific community for the improvement of this technology [62]. Lithium-ion batteries are classified according to their composition: lithium cobalt oxide, lithium manganese oxide, lithium iron phosphate, and lithium nickel manganese [68]. Phosphate ion batteries are considered the most economical, and provide the highest power density and highest discharge current capacity [62]. As such, they are widely used in electric vehicles, presenting a very assiduous future due to their capacity for fast charging [64], [69].

Li-ion batteries feature high energy density (up to 8 times that of VLA lead-acid batteries), low self-discharge rate (less than 8 % per month), long life-cycle, lightweight, high charge and discharge capacity with fast response time, and high efficiency[62]. It should also be mentioned that they have a higher cell voltage, higher energy density, greater charging efficiency and a longer life cycle when compared to lead-acid and nickel batteries [64], [72]. Moreover, this type of battery does not require maintenance [69]. These characteristics make it the solution of choice for portable electronic devices. It is also the subject of constant study and is used in the development of new solutions. Consequently, over the last few years, the cost has been decreasing and the energy density has increased.

Despite the attractive features for different applications, it needs careful use to preserve them [61]. Among the main disadvantages during discharge: i) over-discharge sensitivity, ii) operating temperatures above 45 °C; iii) aging [68], [74]. On the other hand, while charging: i) sensitivity to high temperatures, overcharging, ii) accumulation of internal pressure, which can increase in volume and risk of explosion [68]. These facts appear as the biggest obstacle to the inclusion of large energy storage sites, despite being quite attractive in other aspects. Lithium scarcity, acquisition cost, and environmental issues associated with its extraction or recycling are other disadvantages of lithium-ion batteries [62], [69], [72].

Lithium iron phosphate batteries are characterized by having a smooth and level voltage curve during the charging and discharging processes, which allows for more constant output power control. However, while the remaining lithium batteries have a nominal output voltage of 3.6 V to 3.7 V, iron phosphate batteries only have a nominal value of 3.2 V [62]. Due to the different characteristics between batteries in the same set, there can be unbalanced in the charging and discharging process. Therefore, it is

recommended to use a battery management system to monitor operating voltages and currents, as well as operating temperatures [69].

One technology under development is the lithium polymer battery. It features a higher operating tolerance for temperatures up to 80 °C, less flammable and a longer lifetime for variable operating conditions. Furthermore, they are easily moldable, and the shape of the battery can be customized depending on the application, mainly in mobile phones and laptops. They also have lower conductivity as well as lower power density. From an application point of view, lithium-ion batteries present interesting characteristics for high-power and short-duration applications. An example of this is that there are more than 300 MW of projects worldwide [68].

Near the substation of Myodani, Japan, there is a 2.9 % gradient over 4 km. In this installation, an ESS based on lithium batteries was included in 2007, which contributed to an annual reduction of energy consumed by 310 MWh [66]. Another system was installed in 2013 at Haijama station, in Japan. The ESS based on lithium batteries was dimensioned with the following characteristics: 76.12 kWh, 1650 V and 1200 A. This system allowed an annual saving of 400 MWh [64].

2.3.3.3 Electrical Equivalent Model of the Battery

For the analysis of the charge and discharge of the energy storage system, different electrical models were studied. To emulate the behavior of a battery, the electrical model combines the use of active elements, such as voltage and current sources, with passive elements, such as resistors and capacitors.

Different electrical models are presented in the literature and vary in their complexity and the necessary precision in the obtained simulation results [72]. Among the electric equivalent models that were found: i) ideal, with only one source; ii) linear, with series source and resistance; iii) Thevenin equivalent, with a voltage source, a capacitor, a series resistance and a resistor in parallel with the capacitor [72]. The first listed models present limitations in terms of analysis of SoC variation and responses to transients. The Thevenin model already allows for a more accurate replication of the battery output voltage variation. However, the series resistance value and the constant dc voltage source remain constant, regardless of the SoC. An adaptation of the Thevenin model which uses a combination of resistors and diodes to obtain different responses during the charging and discharging process is presented in [76]. A more complex model that uses dependent voltage and current sources is presented in [77], [78], and is divided into two circuits. The first circuit is responsible for emulating the battery capacity variation during the charging and discharging process, the self-discharge phenomenon as well as the state of charge. Whereas, the second circuit allows modeling the battery response to transients and the internal resistance of the

battery. The dependent voltage source used allows relating the battery voltage to the SoC. In [72], it is possible to verify proposed electrical models for different battery technologies.

Considering the analysis carried out, the electrical model shown in Figure 2.3 was chosen. It presents a simple and representative implementation of the charge and discharge instants.

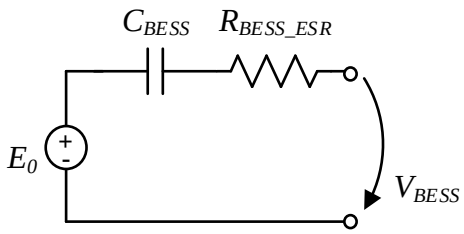

Figure 2.3 – Electric equivalent linear model for the battery.

This model uses a dc voltage supply. E_0, an internal resistance in series, R_{BESS_ESR}, and a capacitor in series, C_{BESS}. While the source represents the minimum voltage of the battery, the resistance represents its internal resistance of the battery and, consequently, the losses. The capacitor allows the simulation of the state of charge and discharge of the battery.

2.3.4 Comparison Between Different ESS Technologies

Table 2.3 shows a summary of some technical characteristics of the different ESS technologies under analysis. The flywheel-based ESS features high efficiency and a long lifetime. On the other hand, it has a slow response, with high investment, and the existing solutions are limited to a maximum power of 0.25 MW. The EDLC has the same limitations, as existing solutions only have a maximum power of 0.3 MW. However, presenting a faster response. On the other hand, batteries present market solutions for operating powers that can exceed 1 MW. Within this type of ESS, highlight the lithium technology, which features fast response, high efficiency and long life. Despite a high initial investment, the ESS based on lithium batteries has interesting long-term characteristics.

Table 2.3 – Future trends on high-speed electric locomotives [based on [68]].

	Flywheels	EDLC	Lead Acid	NiCd	NiMH	li-ion
Power range (MW)	0.01 - 0.25	0.01-0.3	<20	<40	<0.03	0.05-100
Energy rating (kWh)	25 – 5k	0.001-5	18k-100k	6.75k	0.01-500	250-25k
Discharge time	sec – 15min	ms - min	sec-5h	1-8h	h	min-h
Response time	sec	ms	ms	ms	ms	ms
Efficiency (%)	90-95	85-95	70-90	75	70-80	85-95

Lifetime (years)	15-20	25-30	5-15	10-20	5-10	20-25
Lifetime (cycles)	20k-100k	100k-500k	500-2k	800-2.5k	800-3k	1k-10k
Daily self-discharge (%)	1.3-100	10-40	0.1-0.4	0.2-0.3	0.4-1.2	0.15-0.3
Power Cost ($/kW)	100-300	100-300	175-600	500-1500	120% of NiCd	1200-4000
Energy Cost ($/kWh)	1000-5000	300-2000	150-400	600-2400	120% of NiCd	400-2500

2.4 Solar Photovoltaic Energy Source

The sun is a clean and infinite source of energy, releasing enormous amounts of energy into space in the form of radiation. According to [79], [80], the sun continuously radiates a power of 3845 x 10^{23} W in all directions. Considering the distance of planet Earth from the sun, only 1367 W/m^2 is incident under the atmosphere, and only 61 % of this value (835 W/m^2) is incident under the earth's surface. However, due to indirect radiation, it is possible to obtain an additional portion, totaling 1000 W/m^2 [79], [81]. This value is used as a standard test condition, STC, value in tests carried out on solar PV modules in the laboratory. Due to the energetic potential of solar energy, several engineers and scientists have been exploring new solutions. Among them, solar PV cell allows the conversion of solar energy into electrical energy.

Although the PV effect was discovered in 1839, only in 1883 the first solar PV cell was developed with 30 cm^2 and an efficiency of 1 %. In 1954 the Bell laboratory managed to develop a cell with 2 cm^2 and an efficiency that surpassed 6 % [79]. Over the years, new solutions and materials have been studied and presented as a market product. Nowadays, one of the most efficient solar PV modules, in the residential applications market, is the Sunpower Maxeon 6, reaching an efficiency of 22.8 % [82]. Furthermore, the manufacturer still offers a 40-year warranty and presents a degradation of only 0.25 % in terms of efficiency per year. Compared to the other modules that deliver a value of 0.75 % per year, this means that at the end of 25 years, the Maxeon 6 PV module offers 94 % efficiency compared to the initial year, while the conventional ones give a value of 83 %. Due to competition in the market as well as investment in new technologies, solar PV modules with higher efficiencies and longer lifetimes are expected to emerge.

2.4.1 Solar Photovoltaic Cells

Three different groups of solar PV cells reflect different technologies and years of research: crystalline cells, those with thin film; and the called third generation cells [80]. These groups and their variants are represented in Figure 2.4. They have different costs, efficiencies and durability. By studying these properties, it is possible to then determine the best solution for the lifetime of the system. In order to maximize solar radiation and increase the energy extracted, some technologies can be integrated with solar concentrators.

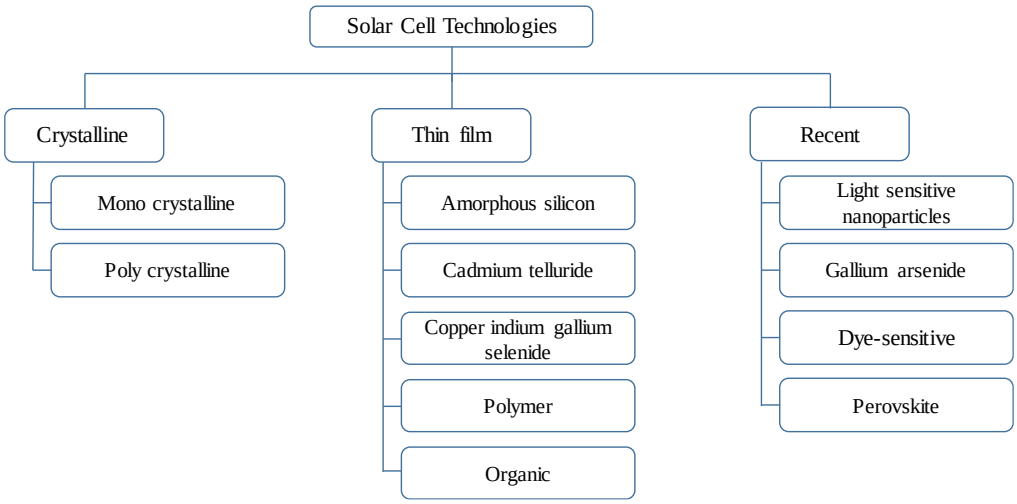

Figure 2.4 – Examples of solar PV cell technologies.

The studies presented in [80] show a record achieved of 46.1 % with a four-junction cell in combination with a solar concentrator. However, most of the values obtained were in a fully controlled laboratory environment. In [83] is presented the efficiency data obtained for different solar PV cell technologies, including market solutions, as well as different environments and experimental test conditions.

Different manufacturing processes followed in developing solar PV cells are analyzed in [84]. Considering the existing solutions on the market, it can be seen that they undergo an antireflection coating and textured process, to minimize radiation losses by reflection and increase light trapping. The evolution of the efficiency of solutions on the market is illustrated in Figure 2.5, as well as the projection of efficiency in the following years, considering the first half (H1) and the second half (H2) of each year.

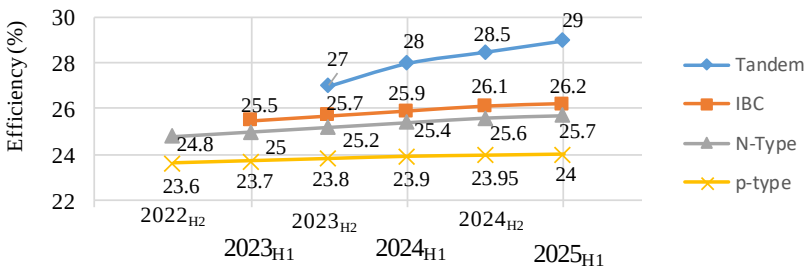

Figure 2.5 – Projected solar PV cell efficiency from 2022 to 2025 (based on [85]).

Due to the low efficiency of the system, a careful study is necessary, to better understand the principle of operation of a solar PV cell, its practical limitations and solutions on how to always maximize the extraction of energy from a solar PV module.

2.4.2 Equivalent Electrical Model for a Solar Photovoltaic Cell

This topic details the equivalent electrical model of a solar PV cell, and the main concepts inherent to the solar PV system.

Crystalline-silicon-based solar PV cells behave like a current source. As such, they are normally analyzed based on the electrical model shown in Figure 2.6 [86]. It is possible to identify a current source, I_{ph}, in parallel with a diode, D, as well as a combination of resistors R_s and R_{sh}. R_s has a low value and is influenced by the bulk resistance values of the semiconductor materials that compose the solar PV cell, by the metallic contacts, and by the existing electrical connections. Conversely, R_{sh} has a high value and is influenced mostly by non-ideal p-n junctions and by impurities close to the junctions. Thus, it can be neglected in the electrical model and the calculations [86].

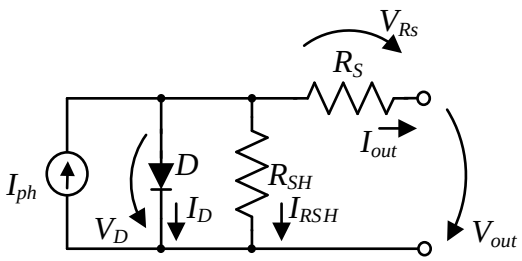

Figure 2.6 – Equivalent electrical model of a crystalline-silicon-based solar PV cell.

In the literature, several works present the modeling and parameterization of the solar PV cell. I_0 represents the maximum saturation current of the diode, η the ideality factor of the diode, and V_{th} the thermal voltage. The characteristic equation of the output current of the solar PV cell is presented in equation (2.1). For high R_{sh} values, the last portion of the equation will present a residual value, which can be negligible. This concludes the mode of operation as a current source of a solar PV cell [81]

$$I_{out} = I_{ph} - I_0\left(e^{\frac{V_D}{\eta\, V_{th}}} - 1\right) - \frac{V_{out} + V_{R_S}}{R_{SH}} \tag{2.1}$$

Ideally, the solar PV module should always work at its rated power. However, the output power is influenced by external factors, such as solar radiation, operating temperature, and incident shadows. These factors cause variations in generated currents and/or voltages, which consequently will affect the total generated power. As such, for a given instant there will be an ideal combination between current

and voltage, to extract the maximum power provided by the solar PV module. The solar PV modules possess some of the following characteristics:

- Maximum power point (P_{MPP}): Maximum power point (MPP) value that the solar PV module can supply. This value results from the product between the nominal voltage value and the nominal current value, at the point of maximum power;
- Nominal voltage (V_{MPP}): Value of the nominal voltage provided by the solar PV module at the point of maximum power under reference conditions;
- Nominal current (I_{MPP}): Value of the nominal current provided by the solar PV module at the MPP under reference conditions;
- Open circuit voltage (V_{OC}): Value of the maximum voltage at the solar PV module terminals when they are in an open circuit. In practice, this case represents when a load of infinite resistance is connected to the module terminals and the current flowing through the load is zero;
- Short-circuit current (I_{SC}): Value of the maximum current flowing through the solar PV module when its terminals are short-circuited. In this case, the load voltage is zero, which represents a load resistance equal to zero.

Figure 2.7 depicts a typical waveform from a solar PV module, and marks the I_{MPP} and V_{MPP}, as well as the maximum power delivered by the solar PV module is obtained, P_{MPP}. The maximum current corresponds to the short-circuit current, obtaining zero power at this point. Analogously, the maximum voltage is obtained in an open circuit, also obtaining zero power [81].

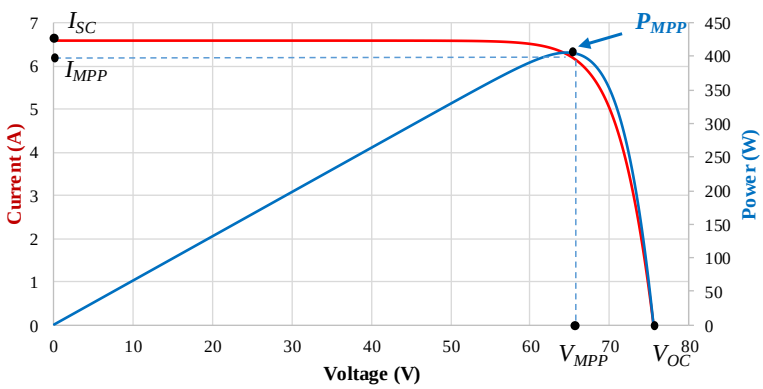

Figure 2.7 – Typical waveforms of a solar PV module (i-V and P-V).

However, depending on the operating conditions, the voltage, and current characteristic curves will vary, resulting in a different curve. These external influences on the solar PV module curves are presented in the following topics.

2.4.2.1 Influence of the Solar Radiation

The incident solar radiation on the solar PV module depends on several factors: its geographical location, the number of hours of sunlight exposure, the angle at which the module is in relation to the sun's rays, and the incident shadows. The influence of solar radiation on the power produced by the solar PV module is exemplified in Figure 2.8. The current generated by the solar PV module is directly related to the incident solar radiation, and the lower the radiation value, the lower the current value, as can be seen in Figure 2.8 (a). Consequently, the lower the current generated, the lower the power available from the solar PV module, as illustrated in Figure 2.8 (b).

These results were obtained in PSIM, considering the 400 W Maxeon 3 solar PV module model [87]. The solar PV module was maintained at a constant temperature of 25 °C, with the incident radiation value varying.

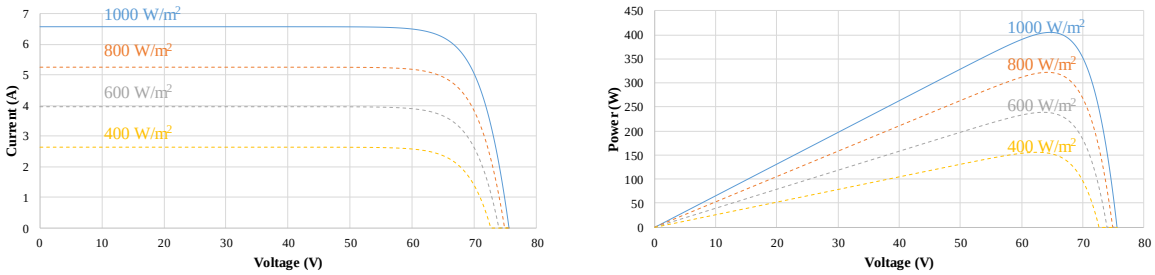

(a) (b)

Figure 2.8 – Influence of solar radiation on the waveforms of a solar PV module: (a) I-V curves; (b) P-V curves.

2.4.2.2 Influence of the Temperature

Dually, the temperature variation in the solar PV cells will cause more significant variations in the open circuit voltage. More specifically, the increase in temperature causes a drop in the V_{oc} open circuit voltage, as illustrated by Figure 2.9 [39], [40]. The decrease in V_{oc} causes a drop in the V_{MPP} voltage, as depicted by Figure 2.9 (a), which, consequently, causes a decrease in the maximum power of the panel, as illustrated in Figure 2.9 (b). It should be noted that the increase in temperature in the cells may not be directly related to the ambient temperature, but due to the thermal characteristics of the surrounding material. These results were obtained in PSIM, considering the 400 W Maxeon 3 solar PV module model [87]. The solar PV module was maintained at a constant incident radiation of 1000 W/m², with the operation temperature value varying.

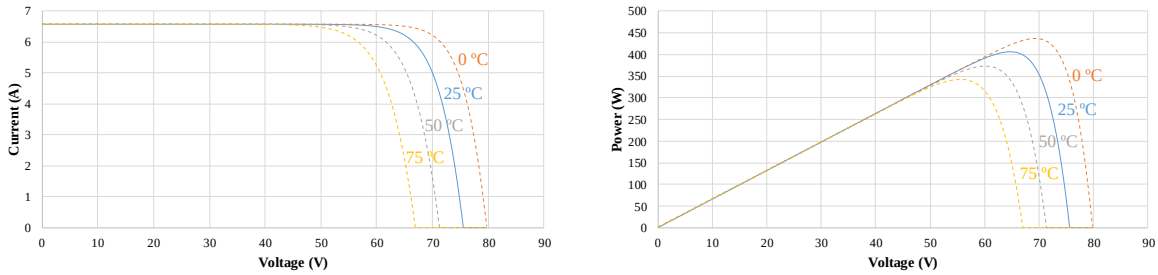

(a) (b)

Figure 2.9 – Influence of the temperature on the waveforms of a solar PV module: (a) I-V curves; (b) P-V curves.

2.4.2.3 Influence of the Shadow

In order to achieve the desired voltage and/or current values, it is recurrent to connect several modules in series and/or parallel in a solar PV installation. However, when a shade falls on a module, it causes a decrease in the performance of the solar PV system. It can be caused by trees, buildings, clouds, power distribution poles, or dust, reducing incident radiation, which can also influence the module's operating temperature. Consequently, the generated voltages and currents will be different, as can be seen in Figure 2.10. In the case of a set of solar PV modules connected in series, the current of the set will be limited by the module with the lowest current value which, most likely, is under the effect of shadow. This reflects in the current with a step waveform as can be seen in Figure 2.10 (a), this originates different peaks of total output power. Figure 2.10 (b) shows 3 points of maximum local power, $LMPP_1$, $LMPP_2$, and $LMPP_3$, and a single point of maximum global power, *GMPP*.

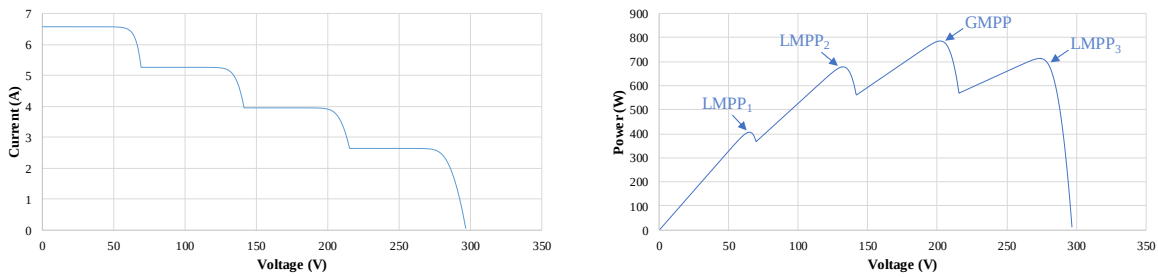

(a) (b)

Figure 2.10 – Influence of shadows on the waveforms from a solar PV module: (a) I-V curves; (b) P-V curves.

These results were obtained in PSIM, considering 4 modules of the 400 W Maxeon 3 solar PV model [87], connected in series, with a bypass diode in parallel to each solar PV module. The solar PV module was maintained at a constant temperature of 25 °C, with an incident radiation value different for each solar PV module.

2.4.3 Solar Photovoltaic Energy in Railway System

Although solar PV systems are quite present in residential and industrial applications, they still do not appear assiduously in the TPS. The first integrations of the solar system with the railway system appeared at railway stations, where the energy produced is consumed directly by the building or by electric cars in the parking lot. However, with the integration of more and larger electric locomotives, the need to upgrade TPS becomes evident.

A comparative study of the economic and technical benefits of integrating a solar PV system in the TPS is presented in [88]. Different connection schemes of the solar PV system are presented and analyzed.

In 2011, 16 000 solar PV modules were installed along a 3.4 km surface railway tunnel in Antwerp, Belgium. Each solar PV module has a maximum power of 245 W, which represents an annual production of 3.3 GWh of energy, enough to feed 4000 locomotives [89]. The total installation area amounts to 50 000 m2, with an estimated decrease of 2400 tons per year in CO_2 emissions into the atmosphere [90].

Germany aims to have a railway system fully powered by renewable energy sources by 2038. As such, there is a project under construction for a solar PV park targeting a total power of 42 MW, with an annual energy forecast of 38 GWh. The energy produced in this park would be used to feed the existing 16.7 Hz railway system in Neumunster [91].

2.5 Conclusions

This chapter covered the electric railway system, the energy storage systems, and the solar PV energy production systems.

Regarding the first topic, the different railway electrification systems were analyzed, with the 25 kV – 50 Hz system being the predominant system in Europe. Nevertheless, with the demand for mobility and the need to introduce more electric locomotives, the weakness of the current TPS is evident. Depending on the locomotives on each railway section, it can exist TPS overloaded while adjacent TPS can be operating at less than nominal power. An easily integrated solution that balances the active powers in each TPS would allow the railway needs to be met in the short term, enabling the integration of more locomotives without the need to resize and install a new TPS.

Regarding energy storage, different technologies that have been integrated into railway systems to store energy from regenerative braking were analyzed. Existing solutions can be implemented on-board or

off-board the railway system. Since the power electronics converters are stationary and connected to the neutral section, ESS solutions with a high value of specific energy or specific power are not a priority. Furthermore, the instants of acceleration and deceleration are of short duration, lasting a few seconds. Consequently, the existing systems were designed to provide high power in a short period of time, not necessarily to store energy for long periods of time. Energy flywheels present interesting characteristics for energy storage in short periods of time, considering the railway traffic, and also presenting robustness and low maintenance. Looking into the integration of renewable energy sources, it was considered that lithium batteries represent the best solution, in order to have a longer-lasting energy capacity. Nevertheless, a hybrid solution with supercapacitors would be best to provide a faster response to the amount of energy required. For the proof of concept, a set of batteries was considered as the storage element.

Finally, the solar PV system is portrayed. In this study, an equivalent model of a solar PV cell is analyzed, having identified its operating principle as a current source. The study continues with the influence of weather on the maximum power available in the solar PV cell. It is concluded that the operating temperature, radiation and shade give rise to different voltage and current values throughout the day. Consequently, over time there will always be an ideal combination between current and voltage to obtain the maximum power.

Chapter 3

Power Converters Topologies and Control Algorithms

3.1 Introduction

Electrical power is an area of research in constant growth. Present in the most diverse applications, the ambition is to develop more compact, lightweight, energy-efficient, and robust solutions. Regarding railway applications, it is possible to identify that one of the major challenges is to develop power electronics solutions for high voltages and power.

This chapter portrays the study and analysis of different topologies of power electronics converters with a view to electric railway applications. The studied solutions focused essentially on their modularity and expandability. Moreover, power electronics converters for high operating power were analyzed to interface with the solar PV system and with the BESS.

Once the best topologies of power electronics converters were analyzed, the algorithms and control techniques necessary for the correct operation of the entire system were studied. The study begins with the analysis of synchronization algorithms, to synchronize the signals generated by the sp-RPC with the fundamental component of the catenary's voltages. In order to guarantee the modularity of the system, maintaining a similar operating power between submodules, different PWM techniques were studied and analyzed to be implemented in the multilevel converters that interface with the ac side. For the control of the output current synthesized by the power electronics converters, different control algorithms were analyzed to identify the most suitable one for implementation. The following topics are related to the solar PV system, analyzing different maximum power point tracking (MPPT) algorithms for the extraction of maximum power, and related to the BESS, exposing different techniques for charging and discharging the BESS.

3.2 Multilevel Power Converter Concept

Multilevel converters (MLC) present themselves as the greatest innovation of recent years in the concept of power electronics converters [92]. The ability to synthesize a ladder output waveform as a function of

the combination of different dc-links creates the MLC concept, widely used in different power electronics applications. The greater the number of dc-links of the MLC, the greater the number of voltage levels that can be synthesized, and, consequently, the output waveform will approach a sinusoid [92]. The main points that characterize the concept of MLC, and which differentiates from conventional two-level power converters topologies, are as follows [92]–[95]:

- Easily extendable due to modular converter substructures. Modularity and expandability allow the creation of redundant operating states, improving system response in case of failures (more fault tolerant);
- Lower harmonic content and more concentrated in the fundamental component and at high frequencies. As illustrated in Figure 3.1: i) the greater the number of levels, the closer the output waveform resembles a sinusoid; ii) the higher frequency harmonic content allows easier filtering;
- Possibility of integrating less bulky passive filters: minimizing implementation costs and system losses, mainly copper and core losses in ferromagnetic elements;
- Possibility of reducing the voltage stress (*dv/dt*) of the power semiconductors. This feature enables the integration of more standard semiconductors with higher commercial stock available and lower costs. Additionally, it allows the mitigation of electromagnetic interference problems caused by high *dv/dt* values when switching semiconductors. Nevertheless, by reducing the *dv/dt* stress is also possible to reduce the galvanic isolation stress;
- Possibility to reduce switching frequencies, minimizing switching losses and semiconductor voltage stress;
- Simpler and faster maintenance service: just exchange the damaged submodule for a functional one;
- Enable the easy integration of renewable energy sources and energy storage systems.

All these features are very attractive, especially for high-voltage power distribution applications. An example of the integration of MLC in high-voltage direct current (HVDC) systems can be seen in [95]–[99]. A distributed control of MLC for HVDC application is proposed in [100] and fault conditions analysis can be found in [101]–[103]. Another major focus of MLC applications lies in solar PV systems [104]–[112] or wind farms onshore [113] and offshore [114]–[117]. The MLC can also interface an energy storage system (ESS) [118]–[125]. Regarding electric mobility, the MLC has great applicability in feeding railway electric systems [126] or operating as an active power conditioner [127], [128] to mitigate power

quality problems in the railway system. Additionally, the MLC concept can be employed in electric vehicles for traction purposes [129], [130] or to interface with an onboard ESS [131], [132]. MLC has also been implemented in marine propulsion [133], [134]. The mentioned characteristics potentiated the integration of MLC for active conditioners to mitigate power quality problems, acting as a static compensator [135]–[140] or distribution STATCOM (DSTATCOM) [141]. Emerging power electronics concepts such as solid-state transformers (SST) have also been exploring the potential of MLC [142]–[146].

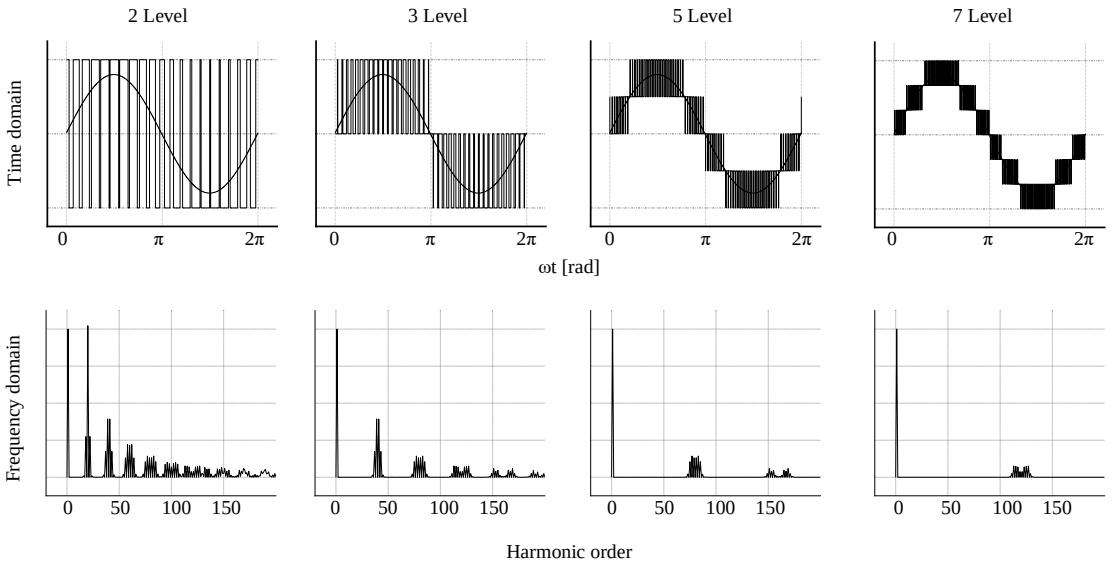

Figure 3.1 – Influence of the voltage levels that a power electronics converter can produce on the quality of the synthesized waveform (adapted from [95]).

In [92] a comparative analysis of five submodule topologies capable of integrating an MLC solution is described, presenting conclusions regarding the allowed operating modes, number of semiconductors and dc-link constitution. In [147] the authors present an analysis of different MLC topologies, highlighting the submodules: neutral-point-clamped (NPC), flying capacitor multilevel converter (FCMC); and cascaded full-bridge (CFB). The applicability of these topologies, as well as the electrical magnitudes of some existing state-of-the-art prototypes developed, are presented.

Akagi, in [148], explains the evolution of the modular multilevel cascaded converter (MMCC) concepts. The terminology adopted by Akagi was MMCC to portray modularity and the multilevel of cascaded power electronics converters. Thus, the study presented by Akagi depicts the analysis, classification, terminology and applications of different MMCC configurations, being each cell composed of a full or half-bridge. Experimental results for a reduced-scale MMCC for an energy storage site and driver engine are also presented, highlighting the good immunity of the system to electromagnetic interference.

The authors of [149] present the evolution of the topologies of the submodules that constitute an MMCC, highlighting the mathematical model of the system. Technical challenges and future trends are also

presented. In [150] the authors intended a hybrid modular and multilevel solution, being based on the combination of submodules of different topologies. An analysis of the evolution of the different cells is also presented. The authors of [151], [152] present a study of the evolution of power electronics solutions for railway applications, highlighting the solutions implemented by different manufacturers, where the submodules of the modular and multilevel systems are based on the SST concept. The evolution of the solutions shows a tendency for the submodules to share the same dc-link, with the output of each submodule being cascaded to the adjacent submodule. Prototypes of the power electronics converters and transformers used in different solutions are also presented and analyzed. Further studies can be found in [152]–[154], where different topologies, configurations, controls, and end applications for MMC are analyzed.

3.2.1 Analysis of Power Semiconductors in the Market

The dc-ac power converters, also known in the literature as inverters, are usually classified according to the constitution of the dc-link: voltage source inverter (VSI) or current source inverter (CSI). In general, the dc-ac power converters have as their main objective the synthetization of an ac component from a dc source, using fully controlled semiconductors. The ac output amplitude and frequency are adjusted from the implemented control algorithms. Regarding the power semiconductors, some examples of technologies can be: i) insulated-gate bipolar transistor (IGBT); ii) metal-oxide-semiconductor field-effect transistor (MOSFET); iii) insulated gate collector transistor (IGCT); etc.

In general, the dc-ac power converters have discrete values in their output, requiring precautions in their implementation to safeguard system integrity [93]. That is, considering that the control of IGBT is based on PWM techniques, the output waveform of the dc-ac power converter will have a resulting frequency equal to or multiple of the switching frequency of each IGBT. Although the output waveform is not sinusoidal, as desired, the frequency of the fundamental component is close to the desired one, as can be seen in Figure 3.1. This characteristic presents some requirements to be met depending on the application.

In the case of VSI, these have high dv/dt output values. In order to smooth the waveform, the load needs to be inductive. Otherwise, with capacitive loads, current spikes would appear [93]. This concludes the need to include an inductive filter between the output of the VSI and the load. In turn, CSI has high di/dt output values. Thus, to smooth the output waveform, the CSI load should be capacitive. Otherwise, with inductive loads, voltage spikes would appear [93]. Thus concluding the need to include a capacitive filter between the output of the CSI and the load.

In order to integrate power electronics converters in high voltage applications, for example, a VSI, it is necessary to increase the amplitude of the dc-link voltage. From a practical point of view, the dc-link voltage should be higher than the peak value of the catenary voltage. As a consequence of increasing the dc-link voltage, larger inductive filters will be required to mitigate the increase in *dv/dt* variations.

Considering the implementation of this type of solution, it is also necessary to take into consideration the semiconductors available in the market. Aspects such as blocking voltages, switching frequencies and stock quantities are important in industrial applications. Emphasizing that semiconductors with high voltages and switching frequencies have limited stock, are more suited to specific applications of limited requirements, and are not very attractive either in research and development or in industry. In turn, semiconductors with medium voltages and switching frequencies present themselves as mature and predominant technology in the market. Table 3.1 illustrates a comparison of the operating characteristics of some semiconductors on the market.

Table 3.1 – Comparative table of power semiconductor modules used in electrified railway systems.

	FZ500R65KE3	FF650R17IE4D_B2	FZ600R17KE4
Semiconductor Technology	IGBT [155]	IGBT [156]	IGBT [157]
No. of semiconductors	2	2	1
Configuration	Parallel	Half-bridge	Single
Voltage (V_{CE})	6 500 V	1 700 V	1 700 V
Current (I_C)	500 A	650 A	600 A
Turn-On delay time	0.64 µs	0.58 µs	0.24 µs
Turn-On rise time	0.18 µs	0.105 µs	0.05 µs
Turn-Off delay time	7.3 µs	1 µs	0.7 µs
Turn-Off fall time	0.4 µs	0.29 µs	0.08 µs

Analyzing the table with examples of semiconductors for railway applications, it can be seen that they have high voltages and currents. In contrast, they have high turn-on and turn-off times when compared to semiconductors for lower-power applications. This makes the switching frequency of these semiconductors limited to a few tens of kHz. Other technologies have been studied and improved by different semiconductor manufacturers, with concepts like 4H-SiC [158], [159] or double implanted MOSFET (DMOSFET) [160] emerging to break the 10 kV barrier. Cree presented a new SiC MOSFET for 10 kV and 240 A, featuring 116 kV/µs transitions during turn-on and 70 kV/µs during turn-off [161]. Another example is a 10 kV and 120 A MOSFET module with a half-bridge configuration for a solid-state

power substation [162]. These modules allowed configuring a switching frequency of 20 kHz, which contributed to 70 % less weight and 50 % less volume compared to a 60 Hz low-frequency transformer.

3.2.2 Multilevel Power Converter Topologies

In the following figures presented in this topic, the IGBT will be used as a power semiconductor due to its predominance in the implementation of high-voltage and high-power applications.

Figure 3.2 illustrates the evolution and emergence of new MLC topologies. The MLC concept emerged in the 1970s, invented and patented by William MacMurray, with the cascaded full-bridge configuration. The same inventor pioneered another approach, where the full-bridges were in parallel, sharing the same dc-link, with low-frequency cascaded transformers at the output of each submodule of the full-bridge [163], [164]. The cascaded full-bridge topology has been matured, and widely used by ABB, featuring a modular and robust structure that is fault tolerant with the addition of bypass switches.

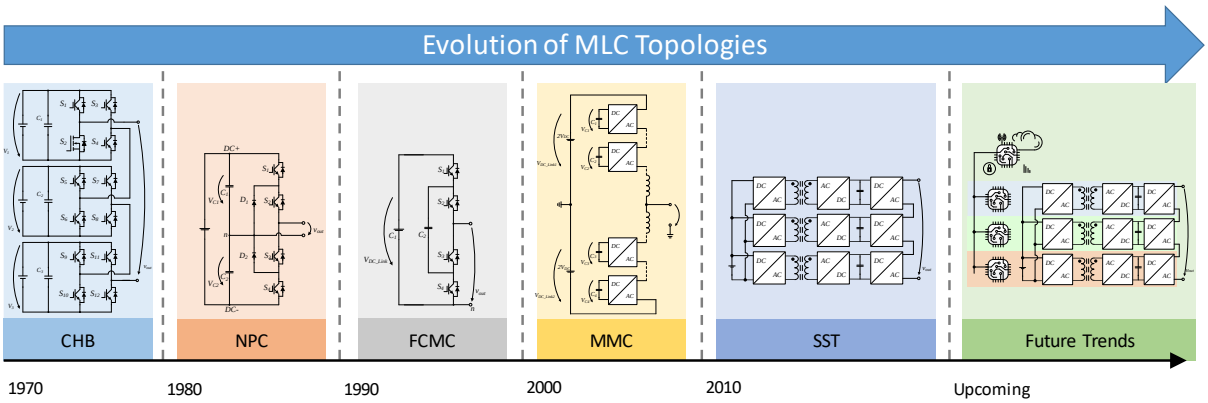

Figure 3.2 – Evolution and the emergence of new MLC topologies.

In 1980, the NPC topology was presented and patented by Baker [165]. NPC topology attracted researchers, becoming best known when, in 1981, Akira Nabae and Hirofumi Akagi presented and experimentally proved its mode of operation [166].

A “multilevel high voltage choppers”, in the literature best known as FCMC topology, was introduced by Meynard and Foch in 1992 [167].

The modular multilevel converter (MMC) topology, emerging in 2002, is a major driver in power electronics for high voltage and high power applications. This concept can be implemented with submodules based on topologies such as: half-bridge [168], full-bridge [168], NPC [169], T-type NPC (TNPC) [169], or FCMC [30]. Despite all the previously mentioned advantages concerning the MLC concept, MMC presents some added challenges such as [98]:

- Sizing of the inductive and capacitive elements: the inductor must be sized to decouple the dc component from ac, as well as minimize the short-circuiting of the dc-link;
- Pre-charging process of the capacitors: whenever the MMC is initialized the capacitors are discharged, requiring a pre-charging mechanism to minimize the inrush current;
- DC-link regulation: the dc-link must be constantly regulated to a reference voltage to allow the correct operation of the MMC, thus requiring several sensors and signal conditioning circuits. The unbalance of dc-link voltages between the different submodules causes the emergence of circulating currents, requiring algorithms and mechanisms to mitigate this problem;
- Ripple in the dc-link: the harmonic spectrum of the dc-link voltage of each submodule will be concentrated in the fundamental frequency and the second-order harmonic. Knowing that the voltage ripple is inversely proportional to the frequency of the fundamental component, this effect is more severe in variable speed applications, namely at start-up and at low motor rotating speeds. As such, capacitors with higher capacity are required, inflating implementation costs;
- Circulating currents: this effect does not affect the ac component of the output voltage and current. However, it increases the root mean square (rms) and peak value of the arm current, consequently increasing the converter losses and the dc-link ripple;
- Fault-tolerance: The MMC is usually implemented with redundant submodules, ready to enter into operation in case of faults. One of the challenges is the decoupling of a damaged submodule and the consequent coupling of an operational one, in a dynamic way, without the emergence of inrush currents. Another challenge is the development of protection mechanisms, namely circuit breakers, capable of shutting down the system in the event of a failure, which is especially important in HVDC applications.

A different approach concerning the MLC concept is the cascading of different power converter topologies capable of synthesizing 5 or more output voltage levels [94]. Different configurations for the MMC using SST can be seen in [151], [153], [170].

System modularity and expandability presented new challenges, particularly in control systems. Knowing that microcontrollers have a limited number of input and output peripherals, the expandability of the system also becomes limited. One solution would be to integrate a Field Programmable Gate Array (FPGA) since it has a large number of configurable input and output peripherals. However, the system would have to be oversized or it would lose modularity [18], [171], [171]. In order to mitigate this disadvantage,

it has been proposed to decentralize the control [172]–[176]. As a future trend, each submodule would have its microcontroller, the slaves, and there would be a communication channel with a central unit, the master. The control will be decentralized. This way, the master would be responsible for managing and configuring the different submodules and distributing the tasks to each of them. Thus, for correct operation, the communication must be fast, not susceptible to interference, synchronized, and robust in case of failures. Possible contributions include the development of algorithms for the management, configuration, and control of each submodule. The hardware is equally important, requiring a balanced solution between parallel communication (fast but with a larger number of connections) and serial communication (slower but with fewer connections).

As the system expands, more voltage sensors, more current sensors, and more communication and monitoring peripherals are needed. As such, and to make a simpler, more compact, and cheaper solution, the development of sensorless control algorithms becomes important [177].

Analyzing the submodules, it becomes evident the assiduous presence of capacitors in the dc-link. It becomes important to minimize bulky and lifetime-limited capacitors by using balancing algorithms or appropriate modulation techniques to extend the lifetime of the components [177].

Analyzing the railway system, high voltages of 25 kV can be identified on the catenaries. In turn, for interfacing a solar PV system and the BESS, the maximum recommended voltages are around 1 kV. Thus, a power electronics solution is required to interface a high-voltage ac system with a low-voltage dc system. With this premise, the SST concept and its constitution are analyzed in the following topics.

3.2.2.1 Solid State Transformer

SST emerges as an interesting concept that, in addition to allowing the creation of isolated sources for each dc-link, also allows for bidirectional power flow [151], [178]. Figure 3.3 shows four groups of SST classification [179]. The first group is classified as single-stage without dc-link or type A (Figure 3.3 (a)). It has high efficiency, simple control, and high feasibility. However, it requires large passive filters as well as topologies that can operate in all four quadrants [179]. The following classification is called two-stage with low-voltage dc-link or type B (Figure 3.3 (b)). This classification is characterized by the addition of a power converter on the secondary side of the transformer. In this way, a low-voltage dc-link is obtained. Despite achieving better control on the low-voltage side, this system requires different algorithms for each block. Nevertheless, the need for bulky filters on the high-voltage side remains [179]. The next group is called two-stage with high-voltage dc-link or type C (Figure 3.3 (c)). In this group, the second conversion stage is added on the high-voltage side. As such, a high-voltage dc-link is obtained. The integration of a

high-voltage solar PV system can be coupled on this dc-link [179]. The last group is called the three-stage with high and low voltage dc-link the type D (Figure 3.3 (d)). In this approach, it is possible to obtain high-voltage ac and dc coupling points and low-voltage ac and dc coupling points. The freedom to use different power electronics converter topologies for each stage increases. The integration of other power sources is easier. However, due to the high number of stages, this system has a lower efficiency as well as more complex control algorithms [179], [180].

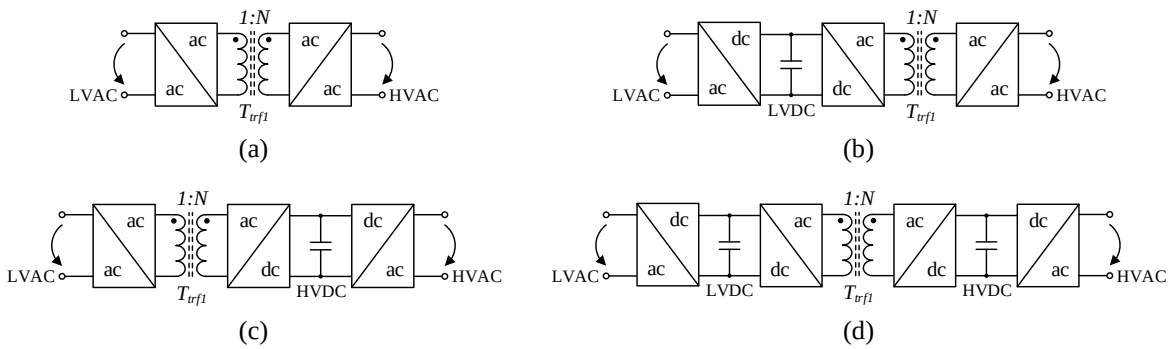

Figure 3.3 – Different classifications of SST considering the power conversion stages: (a) single-stage (type A); (b) two-stage with low voltage dc-link (type B); (c) two-stage with high voltage dc-link (type C); (d) three-stage with high and low voltage dc-link (type D) (based on [179]).

Depending on the operating voltages and currents, sub-modules can be added in series or parallel until the desired operating values are reached [179]. Considering the three-stage classification with high and low-voltage dc-links (type D), a widely used configuration, according to the literature, is illustrated in Figure 3.4. It can be identified modules connected in series on the higher voltage side, and modules connected in parallel on the lower voltage side while maintaining high power ratings. This approach allows for greater modularity of the SST, enabling greater feasibility, redundancy, and quick and simple repair in case of failures. However, with expandability, the complexity of the control algorithms increases [179].

In [142], it is possible to verify an example of SST for a 10 kV/ 1 MW solar PV application. Each submodule is composed of a dual active bridge (DAB) followed by a full-bridge. The primary side of each submodule is connected to a single low voltage dc-link, and the outputs of each submodule are connected in series with the adjacent submodule. Among other features, the following advantages can be highlighted: connection of different submodules to a single dc-link, which allows simplifying the control of the dc-link; integration of the phase-shift technique for power transfer in the high-frequency isolating transformer, minimizing the probability of saturating the ferromagnetic core since the flux density cancels out every two switching cycles as well as allowing for a higher power density in the transformer.

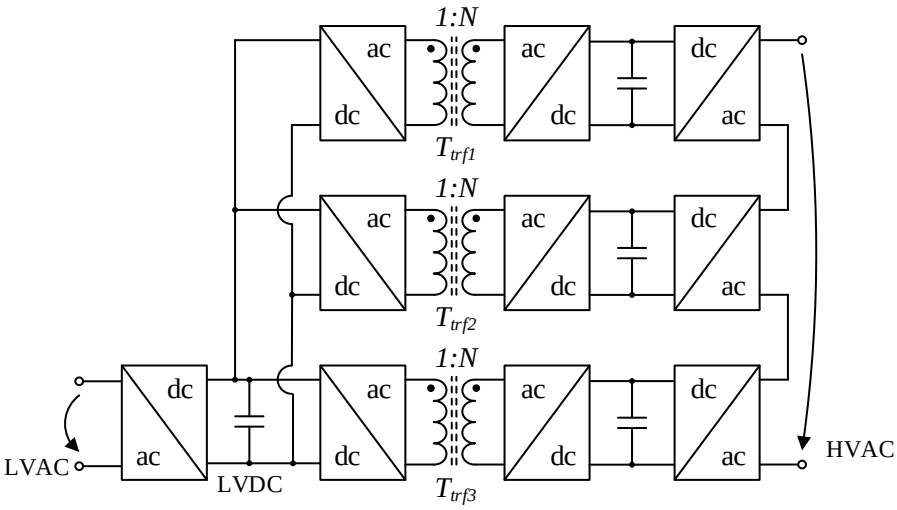

Figure 3.4 – Three stage SST with high and low voltage dc-links.

In the literature there are several studies and reviews concerning SST, highlighting: the modeling of control techniques to balance power between submodules with sensors [181] and current sensorless [182]; different phase shift techniques to control power flow [183], [184]; design for high power [185] and high-voltage applications [146]; techniques to minimize ripple at dc-links and thus reduce capacitors (also reducing volume and costs) [186]; as well as sizing methodologies for the medium and high-frequency transformers that constitute each submodule [187]. The authors of [188] propose a control strategy to avoid inrush currents in the locomotive's SST when passing through neutral sections.

Since the medium or high-frequency transformer plays a crucial role in the correct operation of the SST, it has aroused research interest in the scientific community. The authors of [189] present a methodology to optimize a medium frequency transformer of 400 kVA, 5 kHz as switching frequency, and an efficiency higher than 85 %. This transformer was designed with a view to implementation in railway traction systems. The sizing of a 1 MW transformer is presented in [190], and the methodology is experimentally validated with the performance of a 50 kW transformer with an operating frequency of 5 kHz. Using a Vitroperm500F nano-crystalline material, it was possible to present an experimental efficiency of 99.48 %. Another example is presented in [191], where the transformer was sized to operate with 166 kW, 20 kHz, to interface between 1 kV and 400 V, achieving an efficiency of 99.47 %. The authors of [192] present a transformer design for 100 kW and 10 kW, estimating a transformer efficiency of 97.1 %.

Regarding railway applications, the review studies presented in [151], [193], [194] stand out. Bombardier developed a prototype in 2007 that uses a topology similar to the one shown in Figure 3.4 [195]. The prototype consists of 8 submodules with 500 kW/8 kHz, with the SST operating at a nominal 3 MVA/15 kV. ABB adopted a resonant converter consisting of half-bridge converters to interface with the 1.75 kHz transformer while maintaining the cascaded full-bridge on the ac side [196]. The full-scale

prototype developed consists of 9 submodules, interfacing with a 15 kV catenary at 16.7 Hz with a power rating of 1.2 MVA.

Considering the high-voltage ac and low-voltage dc interfaces, the power electronics converter topologies that can be integrated into each stage are analyzed in the following topics.

3.2.2.2 Full-Bridge Converter

The full-bridge topology consists of 4 IGBT devices and a dc-link. This power converter topology features two IGBT arms, with each arm consisting of 2 IGBT. The output terminals of the power converter are connected to the midpoint of each arm. This configuration characterizes the converter commonly known as the "H-bridge" [168].

Regarding the operating modes, it should be noted that if the dc-link is a voltage source, the IGBT that composes each arm should be driven complementarily to avoid a short-circuit to the dc-link. For this purpose, it is recommended to create a dead-time for the IGBT devices of the same arm. In turn, if the dc-link is constituted by a current source, a path for the current must always be maintained. As such, it is necessary to create an overlap-time of the semiconductors of the same arm [197]. The operating modes considering a dc voltage source on the dc-link are shown in Figure 3.5.

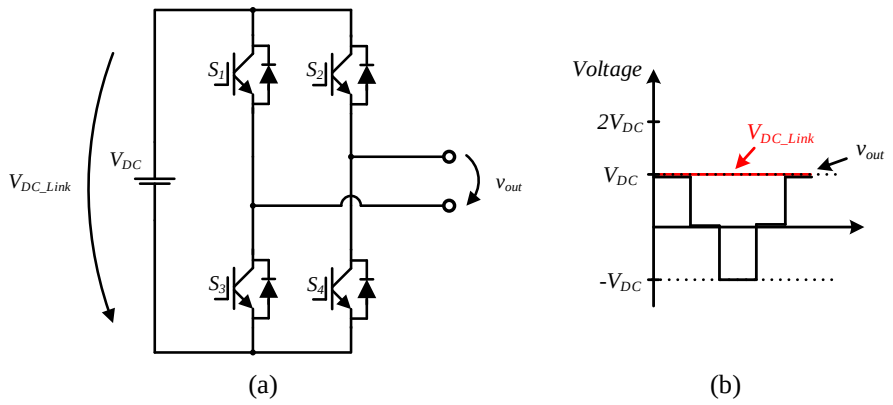

Figure 3.5 – Full-bridge topology: (a) electrical schematic; (b) representation of the voltage in the dc-link, V_{DC_Link}, and the output voltage, v_{out}, of the converter.

Regarding control, with the unipolar modulation technique, it is possible to obtain a resulting output frequency of twice the value of the IGBT switching frequency. This is due to the configuration of two arms in parallel. This characteristic enables the integration of less bulky and cheaper passive filters. Nevertheless, this topology allows the operation in 4 quadrants as well as generating bipolar signals. However, in case of failure of an IGBT, the submodule is inoperable [92], [176]. Table 3.2 shows the operating states for the full-bridge topology.

Table 3.2 – Permitted operating states for the full-bridge topology.

States	1	2	3	4	5	6	7	8	9	10	11	12	13	14	15	16
S_1	0	0	0	1	0	0	1	0	1	1	0	1	1	1	0	1
S_2	0	1	0	1	1	0	0	0	0	0	1	1	1	0	1	1
S_3	0	0	1	0	1	1	0	0	0	1	0	1	0	1	1	1
S_4	0	0	0	0	0	1	0	1	1	0	1	0	1	1	1	1
v_{out}	-	-	-	0	$-V_{DC}$	0	-	-	$+V_{DC}$	-	-	-	-	-	-	-
Condition	**Allowed**									**Destructive**						

Regarding the practical implementation, it is possible to identify the existence of different semiconductors referenced to the same potential which enhances the implementation of simpler and cheaper driver circuits. This topology can generate an output signal with an amplitude equal to the dc-link. However, during the operating states, there will always be two semiconductors in conduction, presenting an output voltage slightly lower than the dc-link voltage, due to the value of the saturation voltage of the IGBT.

3.2.2.3 Cascaded Full-Bridge Converter

Considering the ac high-voltage side, the dc-ac power electronics converter consisting of the cascaded full-bridge can be implemented with *n* submodules [117], [198]. The larger the number of submodules, the higher the output voltage levels and hence the synthesis of a closer to sinusoidal output waveform. Each full-bridge submodule is connected in series with the adjacent submodule, as illustrated in Figure 3.6. In turn, each sub-module has a dedicated dc-link. For proper operation, the total sum of the dc-link voltages of each submodule must be greater than the peak voltage of the ac power grid. Considering a converter consisting of *n* submodules, *4n* fully controlled semiconductors are required.

The cascaded full-bridge power converter can exhibit a symmetric or asymmetric operation mode, depending on the configuration of the dc-link voltages. With the dc-link voltages of each cell equal ($V_1 = V_2 = V_3 = V_{dc}$), the amplitude of the synthesized voltages at the output of each submodule is equal between submodules. Consequently, considering that each submodule allows 3 voltage levels at the output, in the cascaded full-bridge configuration it is possible to obtain *2n+1* levels at the output [98]. For the case presented in Figure 3.6, with 3 submodules (*n=3*), it is possible to obtain 7 voltage levels [94]. Except for the extreme levels, of +3 V_{dc} and -3 V_{dc}, it is possible to obtain redundant states to synthesize the same level. With the correct control algorithm to determine the best operating state, it is possible to maintain the continuous operation of the converter even in case of failures. The greater the redundancy of the system, the greater its robustness.

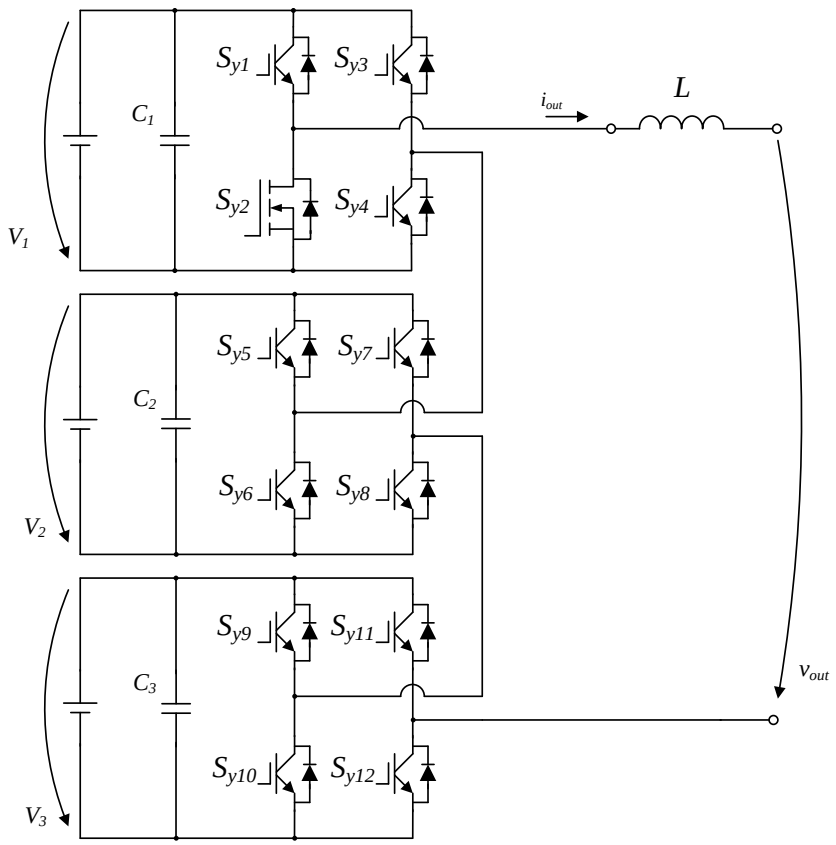

Figure 3.6 – Electric schematic of the cascaded full-bridge power converter.

The other configuration mode, the asymmetric one, involves setting different dc-link voltages between submodules ($V_1 \neq V_2 \neq V_3$). Different configuration proposals appear in the literature, considering the examples of 2^{k-1} and 3^{k-1} [199]. The value of k varies between 1 and n. Considering the configuration of 3^{k-1} and 3 submodules, as illustrated in Figure 3.6, it is necessary to define a voltage V_{dc} for the first submodule ($k=1$). For the second sub-module ($k=2$), the recommended dc-link voltage is 3 V_{dc}. In turn, for the third submodule ($k=3$), the recommended voltage on the dc bus is 9 V_{dc}. Adding up the allowed operating levels it is possible to get 27 levels. In [199] is presented the switching sequence for each level. In order to be able to determine the operating state to synthesize the desired voltage level, control techniques such as space vector modulation are needed. Although it is possible to synthesize more output voltage levels for the same number of submodules, the asymmetric operating mode discards redundant states of operation [39].

In general, this topology needs isolated sources for each dc-link to allow continuous operation, inflating the cost and complexity of implementation [117]. Nevertheless, when the number of output voltage levels increases, the greater the number of fully controlled semiconductors in series, increasing direct conduction losses. For the dimensioning of the amplitude of the output voltages, the saturation voltages of the IGBT devices must be taken into consideration.

In [200] different configurations are analyzed that allow the interface of several arrays of solar PV modules to create a constant power supply for each dc-link that constitutes the cascaded full-bridges. In [117] it is proposed to use a high-frequency transformer with multiple windings to maintain a constant supply on the dc-links of each full-bridge submodule. An ac-dc diode bridge power converter is used in each submodule to maintain a constant voltage at the dc-link. A similar approach for an asymmetric operation is presented in [201]. A static synchronous compensator (STATCOM) based on cascaded full-bridge submodules and using a BESS on each dc-link is analyzed in [148]. Fuzzy logic control is analyzed in [202] for a fifteen-level (seven submodules) cascaded full-bridge converter. Control techniques and different topologies for a cascaded full-bridge for solar PV systems are analyzed in [203]. A current control technique for selective harmonic mitigation using a cascaded full-bridge with a dc-dc power converter on each dc-link is presented in [204]. Considering a cascaded full-bridge operating as a STATCOM, a capacitor voltage balancing control algorithm is presented in [205]. A hybrid solution using full-bridge and half-bridge submodules can be found in [206]. A control algorithm to detect single or multiple open circuit switch faults in cascaded full-bridge is analyzed in [207]

3.2.2.4 Full-Bridge Converter with Cascaded Transformers

The cascaded transformer topology, as mentioned before, emerges as a solution to mitigate the problem of the need for dc power supplies on the dc-link in each submodule. Although it is not a common solution in SST, it was studied for the experimental prototype. Figure 3.7 shows an electrical schematic. Considering a configuration of n submodules, each submodule consists of a full-bridge dc-ac power converter and a transformer. The dc-link of each full-bridge power converter is shared, there is only one dc-link. In turn, the output of each transformer is connected in series with the transformer of the next submodule [208], [209]. The transformers allow isolation between submodules. In turn, since this approach features a single common dc-link, it simplifies the regulation algorithms as well as facilitates the integration of other power systems, namely solar PV systems and BESS. By inserting the different full-bridge converters in parallel to share the same dc-link, it is possible to obtain several IGBT devices referenced to the same voltage potential. Consequently, cheaper driver circuits are obtainable.

Although it allows a simpler dc-link balancing control algorithm, it requires special care in the sizing and control of the ac side to avoid the saturation of the transformers. In order to avoid the magnetic flux having an average value, it is recommended the beginning of operation at 90° or 270°. Thus, the flux density integral from the instant of 90° to 270° has a similar symmetrical value to the integral from 270° to 90°, obtaining a null value at each period [210]. Otherwise, the flux density would have an average value,

which could saturate the ferromagnetic core. This is especially important for ferromagnetic cores that are not laminated and have low flux density values.

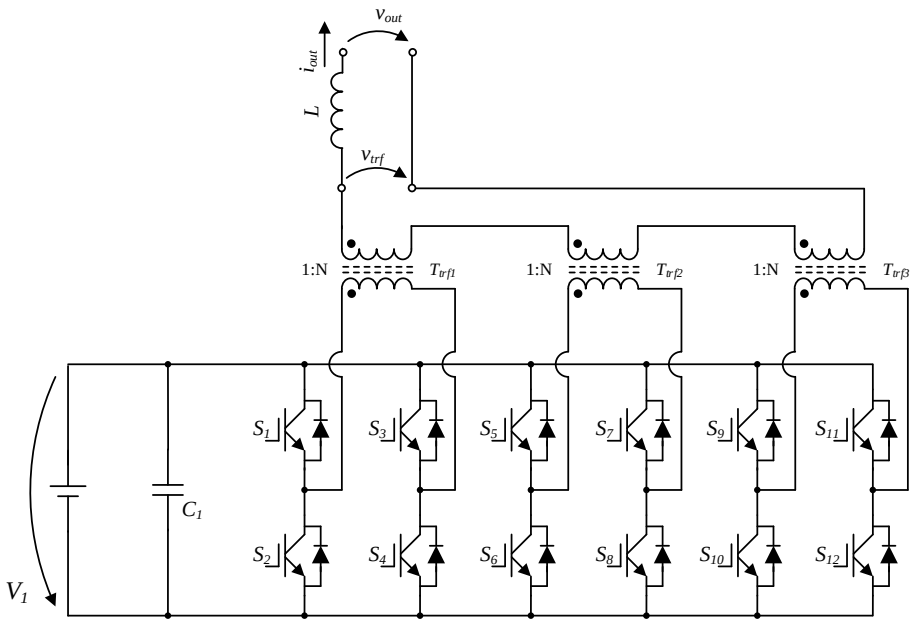

Figure 3.7 – Electrical schematic of the full-bridge with cascaded transformers power converter.

The configuration with cascaded transformers also allows a symmetrical or asymmetrical operating mode. To do this, the transformation ratios of the transformers need to be adjusted. For the symmetric operating mode, the ratio of the transformers is equal to each other. Therefore, the number of levels at the output of the converter with cascaded transformers is obtained by $2n+1$. Considering the 3 submodules ($n=3$) shown in Figure 3.7, 7 different voltage levels are obtained at the output. The states obtained are the same as those obtained with the cascaded full-bridge submodules.

In the asymmetric operating mode, the transformation ratios of the different transformers must be different [211], [212]. The rule of 3^{k-1} can be used to size the ratio of each transformer [211]. Considering a 1:1 ratio for T_{trf1}, 1:3 for T_{trf2} and 1:9 for T_{trf3}, a maximum of 27 different voltage levels can be obtained [211]. An operating mode similar to that obtained with the cascaded full-bridge is obtained by giving up redundant states to obtain more output voltage levels. Consequently, specific control algorithms, such as vector space modulation, are required to determine the operating state that allows for generating the desired voltage level. In [170] is presented the switching pattern obtained considering an MMCC composed of four full-bridge submodules with four transformers with different turns ratios. However, it should be mentioned that this approach causes an unbalance in the operating powers of each submodule. According to [16], the submodule with a lower switching frequency contributes 80 % of the total power transferred. The lower the switching frequency of each submodule, the higher the power. Regarding the power transformers, special attention needs to be paid to their sizing as well as the instant to start the converter.

This topology presents the disadvantage of the semiconductor voltage drop. In [210] it is possible to verify the analysis of a cascaded transformer topology composed of 3 submodules, obtaining a total voltage drop of 19.8 V at the converter output. This voltage drop can be compensated by adjusting the transformer ratio during its sizing. The need for isolating transformers inflates its initial implementation cost. Nevertheless, due to the low-frequency component in the transformers (usually 50 Hz or 60 Hz), they have an increased volume, presenting a low power density. As the number of output voltage levels increases, this solution needs more full-bridge power converters as well as transformers, revealing itself as a bulky and expensive solution [213]. The authors of [212] analyze the influence of the leakage inductance existing in transformers that originates a lag angle and distortion in the output voltage applied to the output filter. This problem can be minimized by using transformers with a reduced dispersion inductance but never fully mitigated

The control for a cascaded transformer with 7 voltage levels and operating as STATCOM can be seen in [141]. A different approach is proposed in [214], where the arm of each full-bridge is shared as the full-bridge arm of the next submodule. This solution allows the use of semiconductors to be reduced. The analysis is done using computer simulations and experimental validation, using low-frequency laminated iron transformers with a switching frequency of 3 kHz. The validation of 27 voltage levels cascaded transformers in asymmetrical operating mode was validated using computer simulations in [211]. The harmonic spectrum of the current from cascaded transformers with seven, nine, eleven, thirteen, and fifteen levels are analyzed based on simulations for different modulation ratios [215]. An example of cascaded transformers with toroidal cores as shunt active power filters are analyzed in [216].

Regarding the sizing of the transformers, to generate a multilevel output voltage with a resulting output frequency higher than the switching frequency, a research gap was found. There is little information for a sizing guideline as well as an experimental validation with grid connection with satisfactory results. The authors of [217] used low-frequency transformers directly connected to loads. In [216] experimental results of cascaded transformers implemented with toroidal cores are presented. However, no sizing methodology is mentioned. The authors of [213] present an analysis of different cascaded transformers in the literature, mentioning that these are susceptible to overshoots and sags in the stairs of the output waveform, contributing to a greater distortion of the waveform. This is why most of the results found in the literature are based on conduction angle [218], [219], or space vector modulation [105], and not the classic sinusoidal PWM control in dc-ac power converters.

3.2.2.5 Dual-Active Bridge Converter

The converter shown in Figure 3.8 consists of two full-bridge power converters, with an isolating transformer connected between them, and is referred to in the literature as a dual-active bridge (DAB). The transformer provides galvanic isolation between the input and output of the DAB. The inputs and outputs can be identified as the dc-link of each full-bridge. The voltages of each dc-link can be adjusted according to the voltage levels of the interfaces to be realized. However, it is recommended that the transformer transformation ratio be similar to the voltage ratio. In this topology, the auxiliary inductor, L_{aux1}, connected in series with each winding, or only on one side, can be identified. These inductors allow the *di/dt* current variation to be limited. The addition of these auxiliary inductors can be optional depending on the desired value and the value obtained for the transformer leakage inductance.

Each full-bridge converter can synthesize up to three voltage levels. By controlling the lag of the waveforms applied to each winding it is possible to control the power flow. In the literature it is possible to find different techniques for DAB [220]–[222], enumerating: single-phase shift, dual-phase shift, triple-phase shift, and extended single-phase shift. These techniques vary in the number of lags to be originated, varying their control complexity.

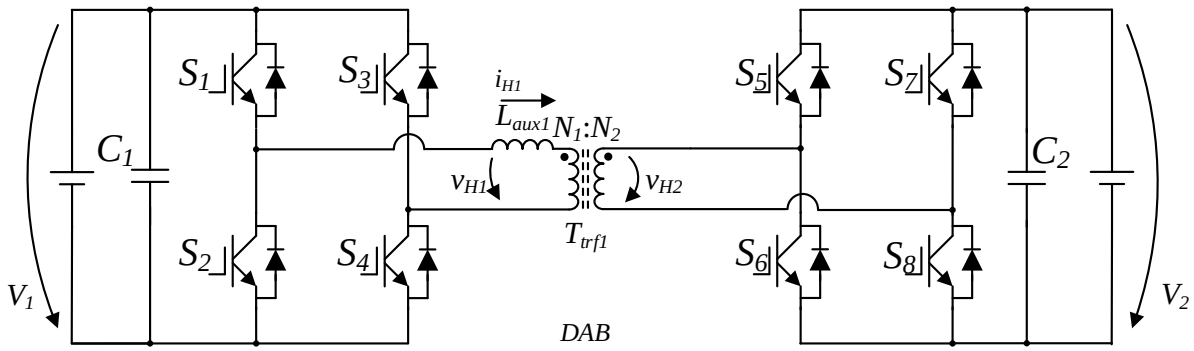

Figure 3.8 – Electrical schematic of the dual-active bridge power converter.

The single-phase shift technique is the simplest control technique. Each full-bridge has a bipolar waveform, as a 50 % duty-cycle. The PWM signals applied to each arm of the full-bridge are shifted by 180°. By adjusting the phase angle, α_1, of the waveforms originating at the output of each full-bridge, the waveforms applied to the transformer windings, it is possible to control the power flow. The typically obtained waveforms on the DAB using the single-phase shift technique are illustrated in Figure 3.9. In [223] they analyze the behavior of the DAB with the gradual increase of the phase-shift. The authors found that the system shows a linearity between the phase shift and transferred power for a phase shift close to 30°. Nevertheless, with the integration of dead-time, it is necessary to compensate for the phase shift to obtain the desired operating value.

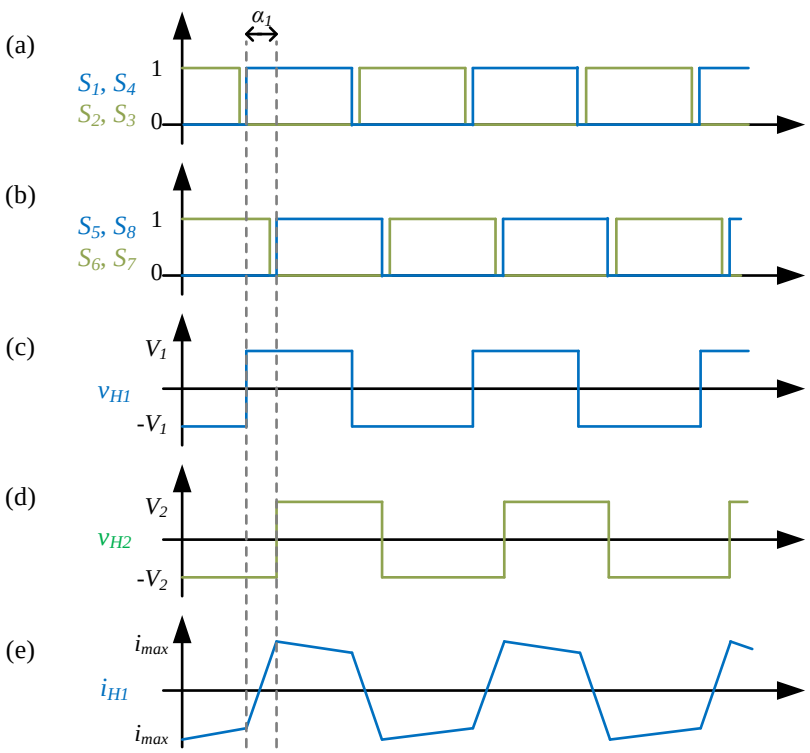

Figure 3.9 – Typical waveforms on the dual-active bridge with the single-phase shift technique: (a) PWM signals for the full-bridge connected to V_1; (b) PWM signals for the full-bridge connected to V_2; (c) voltage on the primary side of T_{trf1}; (d) voltage on the secondary side of T_{trf1}; (e) current on the primary side of T_{trf1}.

The active power transferred by the DAB can be determined according to equation (3.1). It can be seen that the power transferred, P_{trans}, is dependent on the voltages V_1 and V_2, the transformer transformation ratio, N, the operating frequency of the transformer, f_w, and the inductance value, L. The transformation ratio, n, is obtained with the help of equation (3.2), where N_1 is the number of turns in the primary winding, and N_2 is the number of turns in the secondary winding. The value of L represents the total of the auxiliary inductor inductance, L_{aux}, and the transformer leakage inductance, L_{trf}, as exemplified in equation (3.3).

$$P_{trans} = \frac{V_1\, N\, V_2}{360°\, f_w\, L}\left(\alpha_1 - \frac{{\alpha_1}^2}{180°}\right) \tag{3.1}$$

$$N = \frac{N_1}{N_2} \tag{3.2}$$

$$L = L_{aux} + L_{trf} \tag{3.3}$$

The major disadvantage of this technique arises when the power converter is operating with a ratio between *V1* and *V2* different from the *N* ratio for which the transformer was designed. A reactive power component emerges, circulating between full-bridges, not contributing to the transfer of power between the input and output. During this instant, high currents will arise as well as energy losses [223].

3.3 DC-dc Power Converter Topologies for the Solar PV System and BESS

In this topic, the power electronics converters for the interface of the solar PV system and the BESS are analyzed. Unidirectional solutions were analyzed for the solar PV system, while bidirectional solutions were analyzed for the BESS. Since the power electronics converters interfacing with the catenaries already feature galvanic isolation, the power electronics converters analyzed here are uninsulated. As such, the input and output voltages should not be very different. Without a transformer, the ability to raise the voltages is limited by the passive elements in the power converter topology. The presented topologies will be analyzed for the continuous conduction mode of operation.

3.3.1 Unidirectional dc-dc Boost Power Converter

The unidirectional dc-dc boost power converter is also called as "step-up" because of its ability to make available a voltage at the output higher than the voltage at the input [168]. Analyzing Figure 3.10 it is possible to see the constitution of the unidirectional dc-dc boost power converter: one inductor L_1, one IGBT device S_1, one diode D_1 and two capacitors C_1 and C_2. At the output of the power converter are the load R_{Load} and capacitor C_2, used to minimize the output voltage ripple.

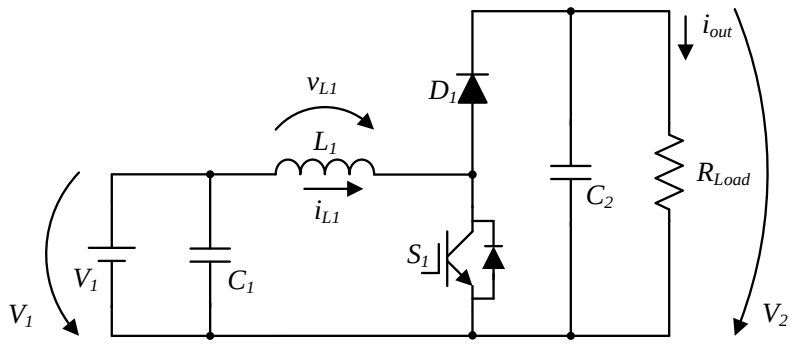

Figure 3.10 – Electrical schematic of the unidirectional dc-dc boost power converter.

When the control is disabled, the capacitor is initially charged with a voltage equal to V_1, via diode D_1. The IGBT S_1 is at the cut-off at this instant. In turn, when the control system is activated, there are two operating modes illustrated in Figure 3.11 [168].

For the first operating mode, illustrated in Figure 3.11 (a), S_1 is activated, diode D_1 becomes inversely biased, and there is no current flow to capacitor C_2 and output. The power supply V_1 is in parallel with L_1, energizing L_1. Consequently, the voltage v_L becomes equal to V_1, and i_{L1} rises linearly. Looking at the output, only C_2 supplies the power to the load [168].

At the instant the IGBT is deactivated, i_L circulates through D_1, and the load is supplied by the energy stored in L_1 and by V_1. C_2 is charged at this instant [168]. This second operating mode is illustrated in Figure 3.11 (b).

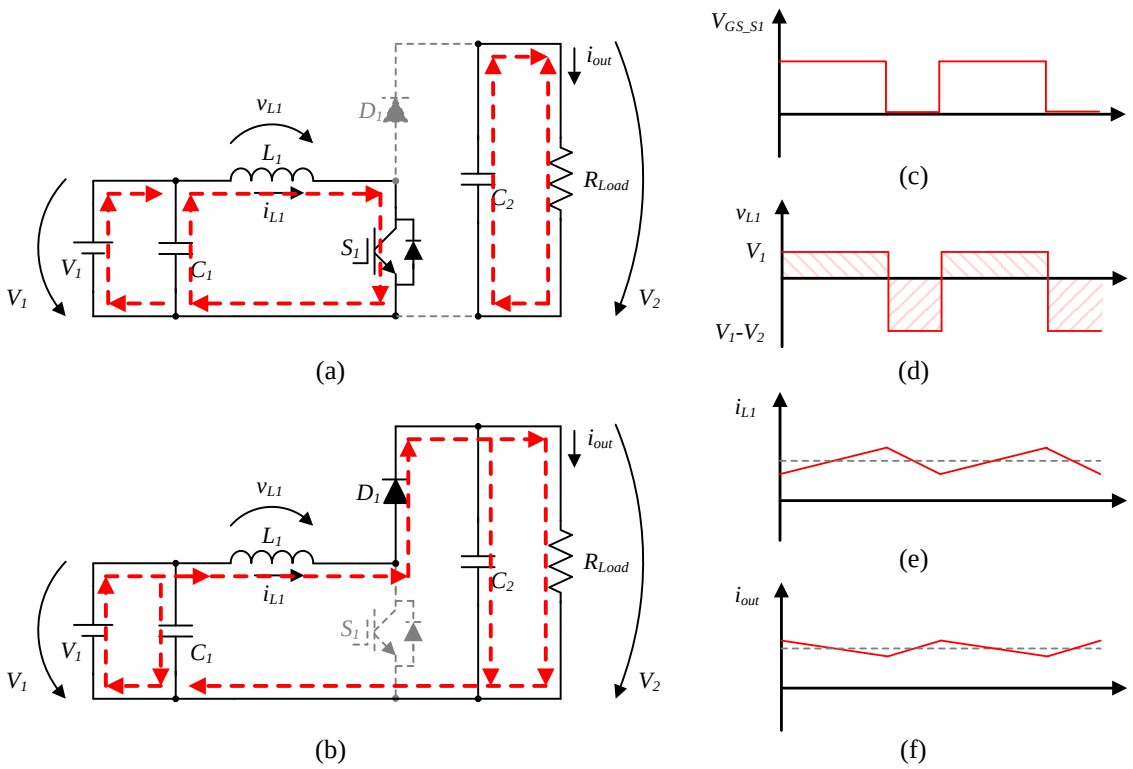

Figure 3.11 – Operating principle and waveforms of the unidirectional dc-dc boost power converter: (a) IGBT S_1 turned-on; (b) IGBT S_1 turned-off; (c) driver signal for S_1; (d) voltage on the inductor L_1; (e) current on the inductor L_1; (f) load current I_2.

Equation (3.4) characterizes the relationship between the V_1 and V_2, for the continuous conduction mode. By maintaining a constant input voltage, V_1, and a constant duty-cycle, D, it is possible to obtain a constant and proportional output voltage V_2 [93].

$$V_2 = \frac{1}{1-D} V_1 \tag{3.4}$$

3.3.2 Unidirectional Interleaved dc-dc Boost Power Converter

The unidirectional interleaved dc-dc boost power converter appears in the literature as an improvement of the conventional unidirectional dc-dc boost topology for high-power applications. By adding more arms, composed of the inductor, diode, and IGBT, it is possible to distribute the current over the different arms. In the literature, they characterize this topology by the number of phases, with each phase consisting of the semiconductor arm and the inductor. In the case of the Figure 3.12, a four-phase interleaved dc-dc boost power converter is illustrated. With the interleaved concept, a lower current semiconductor at a more affordable cost can be included. Moreover, it is possible to decrease the current ripple in the input

of the power converter, and therefore use inductors with lower inductance values [224]. Once the output current presents a lower ripple, the capacitance of the capacitor can also be decreased [225]. By decreasing the current ripple value, more constant power is obtained, which is ideal for both solar PV systems and BESS. Studies in [226], [227] present the relation of the ripple obtained with the increase of the number of arms. Considering a four-phase interleaved converter, similar to the one shown in Figure 3.12, it is possible to obtain a current ripple at least 4 times smaller, in the worst duty-cycle situations.

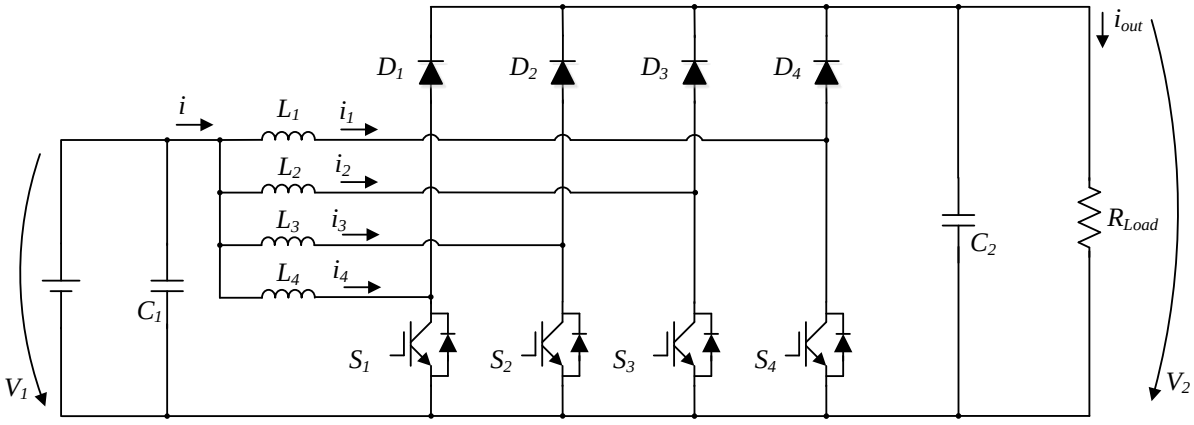

Figure 3.12 – Electrical schematic of the unidirectional interleaved dc-dc power converter.

The operation principle of the converter is similar to the conventional unidirectional dc-dc boost power converter, with the control of the PWM signals for each IGBT arm being shifted 360°/*n* [228]. Being *n* the number of arms, in this case, the phase shift obtained is 90° between each PWM signal. The number of IGBT devices in simultaneous conduction depends on the duty-cycle value. In [229] a four-phase interleaved with four different ranges of duty-cycle value is analyzed.

The unbalance of currents for the different phases can lead to inductor saturation, and uneven thermal stress, and affect the performance of the converter, all of which can result in damage to the power converter [230]. In order to maintain the current balance for each arm, it is recommended to use a closed-loop current control. For that, current sensors in each inductor are required, increasing the implementation cost [226]. The authors in [231] analyze a current sharing technique for a two-phase boost interleaved, while the authors in [232] analyze the performance of a three-phase boost interleaved for a wide range of duty-cycle values using a sensorless current sharing technique for a cheaper solution.

3.3.3 Bidirectional dc-dc Power Converter

The dc-dc bidirectional power converter allows a two-quadrant operation mode: positive voltage and current; positive voltage and negative current [233]. This converter allows to increase or decrease the

voltage, depending on the direction of the power flow. The bidirectional energy mode is a mandatory requirement for interfacing with BESS. In this way, it is possible to store energy or use the stored energy. The topology is illustrated in Figure 3.13, and is usually referred to as a buck-boost bidirectional power converter. V_1 was considered to be the power source with the lowest voltage value, while V_2 has a higher voltage.

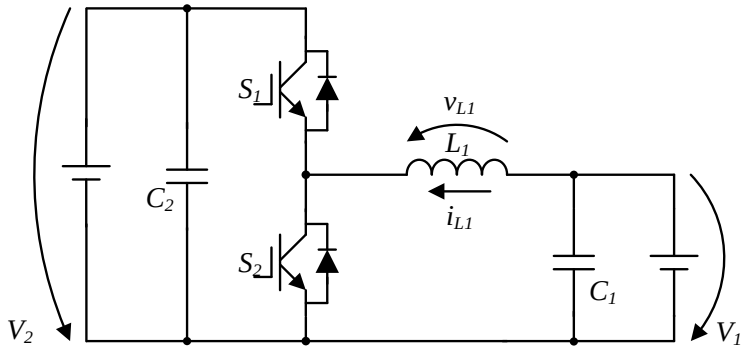

Figure 3.13 – Electrical schematic of the bidirectional dc-dc power converter.

When the bidirectional dc-dc converter operates in boost mode, it sends energy from V_1 to V_2. In turn, when operating in buck mode, the converter sends energy from V_2 to V_1. These two operating modes are discussed next.

Boost Operating Mode

In the boost operation mode, presented in Figure 3.15, the principle of operation is similar to the dc-dc boost converter previously analyzed. In this case, the control is performed with the IGBT S_2, with S_1 deactivated. The free-wheeling diode in the IGBT S_1 is used to provide a path for the current when the S_2 is open. Therefore, the analysis begins when S_2 is turned-on. V_1 supplies L_1, while C_2 maintains a power supply to V_2. When S_2 opens, the free-wheeling diode of S_1 provides a path for the current i_{L1} to circulate to V_2. In this way, energy from V_1 and L_1 is supplied to V_2 and C_2. The free-wheeling diode of S_1 has similar functionality to the diode of D_1 in the boost converter in Figure 3.10.

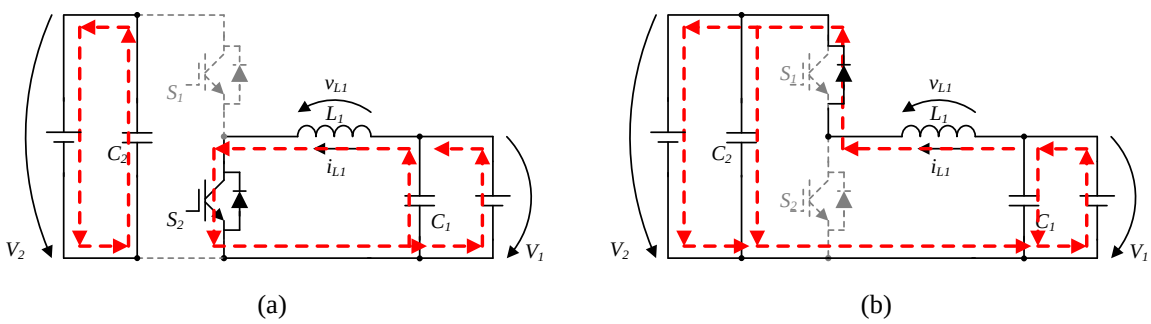

Figure 3.14 – Operating principle of the bidirectional dc-dc power converter during the boost operating mode: (a) IGBT S_2 turned-on; (b) IGBT S_2 turned-off.

Buck Operating Mode

In the buck operating mode, presented in Figure 3.15, the control is done with the IGBT S_1, while S_2 is deactivated. In a dual form, the free-wheeling diode of S_2 is used to maintain a path to i_{L1} even when S_1 is deactivated. Thus, the first step is to analyze the behavior of the circuit when S_1 is activated. The source V_2 will supply energy to all the passive elements in the circuit (C_2 and L_1) as well as the output V_1. As soon as S_1 is turned-off, the free-wheeling diode of S_2 provides a path to i_{L1}, maintaining a constant power supply to C_1 and the load, V_1 [93].

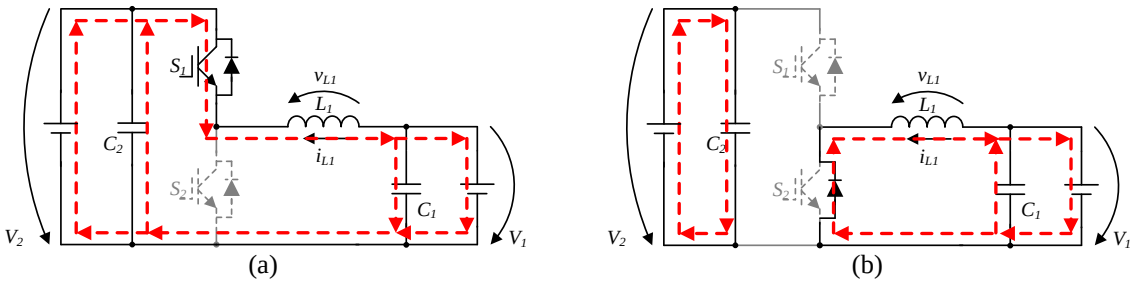

Figure 3.15 – Operating principle of the bidirectional dc-dc power converter during the buck operating mode: (a) IGBT S_1 turned-on; (b) IGBT S_1 turned-off.

Equation (3.5) characterizes the relationship between the V_1 and V_2 for the buck continuous operating mode. By maintaining a constant input voltage value, V_1, and a constant duty-cycle, D, it is possible to obtain a constant and proportional output voltage V_2 [93].

$$V_1 = D\,V_2 \tag{3.5}$$

3.3.4 Bidirectional Interleaved dc-dc Power Converter

The bidirectional interleaved converter consists of adding more semiconductor arms along with the inductor. This concept has the advantages already mentioned for the unidirectional interleaved converter, with the possibility of bidirectional power flow [228]. An electrical schematic of a four-phase bidirectional interleaved dc-dc converter is shown in Figure 3.16.

The operation of the bidirectional interleaved converter can be divided into two modes: boost mode; buck mode. In buck mode, the upper IGBT devices will be controlled, while the lower IGBT devices are turned-off. On the other hand, during the boost mode, the lower IGBT devices will be controlled, with the upper IGBT devices deactivated. The gate signals applied to each arm are out of phase. Considering a 360°/n ratio, where n is the number of arms, for the topology depicted in Figure 3.16, the phase shift obtained is 90° between them [234]. Design guidelines for the current sharing of a two-phase [230] and four-phase [235] interleaved buck converter can be found in the literature. Another approach using a single current sensor for current sharing is analyzed in [236].

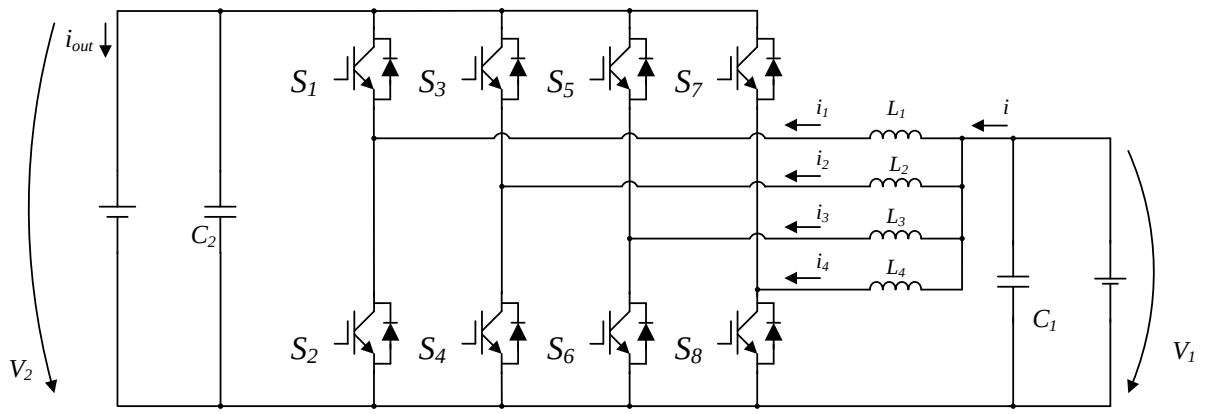

Figure 3.16 – Electrical schematic of the bidirectional interleaved dc-dc power converter.

3.4 Control Algorithms

In this sub-section, different control techniques necessary for the correct operation not only of the simulation models but also of the experimental prototype are analyzed. The study begins with an analysis of the PLL algorithm required for the synchronization of the sp-RPC with the catenary voltages. In order to perform the correct control of each power converter, different current control algorithms are studied. In turn, to guarantee uniformity in the operating powers of each submodule, PWM modulation techniques applied to multilevel converters are analyzed. Regarding BESS, the constant power charge and discharge algorithm is analyzed. In turn, regarding the solar PV system, different algorithms for maximum power extraction are studied

3.4.1 Synchronization Technique with the Catenary Voltage

In order to allow a continuous operation of the sp-RPC when connected to the catenary, the control system must be synchronized with the fundamental component of the voltage in each catenary. With this synchronism, it is possible to control the power factor of the sp-RPC. Analyzing the literature, it is possible to identify several synchronization techniques [237]. This study was focused on the synchronization technique called phase-locked loop (PLL). More specifically, the technique presented by Karimi et al. [237]–[240]. This PLL technique has been used in previous projects, showing good performance.

Briefly, the PLL technique used allows the detection of the phase and amplitude of the fundamental component of the measured signal, resulting in a sinusoidal and in-phase signal. Figure 3.17 shows the representative block diagram of the constitution of the PLL technique used, consisting of a phase detector, a filter, and a voltage-controlled oscillator.

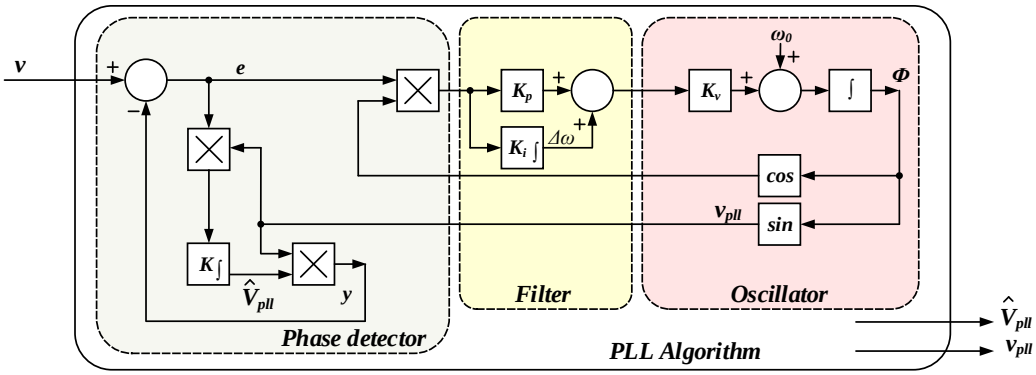

Figure 3.17 – Block diagram of the PLL control algorithm (based on [237]).

The phase detector is responsible for measuring the error between the input signal and the output signal. The resulting signal is used in a low-pass filter that forms the filter block. Finally, the oscillator is responsible for originating an output signal synchronized to the fundamental component of the input signal.

This structure provides access to two signals: v_{pll} and V_{pll}. The v_{pll} signal corresponds to a unitary signal and is synchronized with the fundamental component of the catenary. In turn, V_{pll} represents the amplitude of the input signal. The v_{pll} signal can be used as a reference sinusoidal signal for current control. V_{pll} will allow the amplitude of the reference current to be determined knowing the desired operating power. Moreover, it should also be mentioned that this PLL technique also allows access to a third signal that is offset 90° from v_{pll}. This signal can be used to adjust the sp-RPC power factor if necessary.

For the correct operation of the PLL control algorithm, it is necessary to pay special attention to the existing gains. The parameter K defines the speed of convergence of the amplitude A. K_p and K_v define the speed of convergence of the phase. Finally, K_i and K_v define the speed of frequency convergence.

3.4.2 Current Control Techniques

In this topic, different current control techniques are analyzed. These techniques were analyzed with a view to their implementation in both the computational models and the experimental prototype.

3.4.2.1 Periodic Sampling

The current control technique by periodic sampling is based on the direct comparison between the reference current and the current to be controlled. This technique can be illustrated in Figure 3.18, where it is possible to see a D-type flip-flop operating as a sampling and hold with a fixed frequency. With each clock pulse, the comparison signal is placed on the output of the flip-flop. As such, it can be seen that

the maximum switching frequency will be half the frequency of the clock signal. In this way, it is possible to safeguard the operating limits of the power semiconductors with the correct circuit configuration.

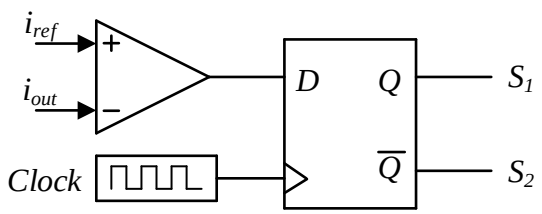

Figure 3.18 – Block diagram of the periodic sampling current control.

Despite its simplicity of implementation and robustness, this control technique has a variable switching frequency. Consequently, the resulting harmonic spectrum is wide, making it difficult to design passive filters capable of eliminating the harmonic content resulting from semiconductor switching.

3.4.2.2 PI Current Control

The PI current control technique aims to minimize the error between the reference current and the current to be controlled. For this, the error originated is used in the proportional and integral controller. Analyzing Figure 3.19 it is possible to see that the PI controller has two gain constants: K_p and K_i. While K_p aims to minimize the instantaneous error, K_i is responsible for minimizing the error on a steady-state. The resulting value from the PI controller is used to synthesize a modulating wave, $v_{Control}$. By comparing this modulating wave with the carrier waves, it is possible to synthesize the PWM signals for the actuation of the power semiconductors.

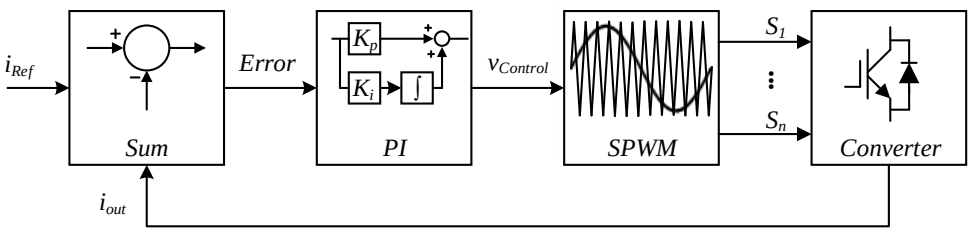

Figure 3.19 – Block diagram of the PI current control with SPWM.

This control technique presents a higher implementation complexity, namely in the analysis and dimensioning of the existing gains. In the literature, there are different analyses for sizing the gains considering the operating conditions. Consequently, the applied gains are usually considered for the nominal operating conditions, presenting a lower performance when the system operates outside this zone. Another disadvantage is the characteristic delay between the signal to be controlled and the reference signal. This delay can be more or less pronounced, depending on the gains. Once will always be an error between the signals, the delay will never be completely extinguished.

On the positive side, since it has a fixed switching frequency, it is possible to correctly size passive filters to mitigate the harmonic content caused by semiconductor switching.

3.4.2.3 Predictive Current Control

The predictive current control technique is based on the electrical model of the system to predict the behavior of the variables to be controlled. This prediction allows a dynamic and fast response in the current control. This concept does not require gain adjustment at the control level, presenting a better system performance regardless of the desired output current waveform. However, it requires a correct analysis of the existing electrical model [98]. A simplified structure of the predictive algorithm and its interaction with the electrical system is shown in Figure 3.20.

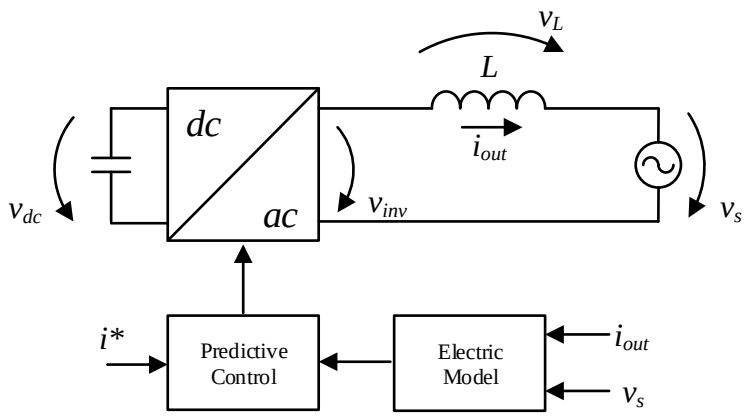

Figure 3.20 – Simplified diagram of the electrical system for the predictive control algorithm.

Considering the multilevel system and the operating voltages of the catenary, the analysis of the control algorithm was performed considering only the coupling inductor. Considering the model in Figure 3.20, the system equation can be deduced according to equation (3.6).

$$v_{inv} = v_L + v_s \tag{3.6}$$

Knowing that the difference between the reference current, $i*$, and the output current, i_{out}, is the error current, i_{error}, the equation (3.7) was deduced by introducing the characteristic equation of the inductor v_L.

$$v_{inv} = L\frac{d(i^* - i_{error})}{dt} + v_s \tag{3.7}$$

In order to cancel the error current portion, it is multiplied by -1 thus obtaining the equation (3.8).

$$v_{inv} = L\frac{di^*}{dt} + L\frac{di_{error}}{dt} + v_s \tag{3.8}$$

For the digital microcontroller to process the equation, it is necessary to convert it to the discrete domain. Applying the forward Euler method [241], [242] with a sampling frequency given by $f_a = 1/T_a$, it is possible to obtain the equation (3.9).

$$v_{inv}[k+1] = v_s[k] + \frac{L}{T_a}(i^*[k] - i^*[k-1] + i_{error}[k] - i_{error}[k-1]) \quad (3.9)$$

Considering that $i_{error}[k]$ defines the difference between $i^*[k]$ and $i_{out}[k]$, equation (3.9) can be simplified to equation (3.10). The resulting value is used to compare with the carrier waves, generated internally in the microcontroller, in order to produce the PWM signals responsible for driving the IGBT devices.

$$v_{inv}[k+1] = v_s[k] + \frac{L}{T_a}(2\, i^*[k] - i^*[k-1] - i_{out}[k] - i_{error}[k-1]) \quad (3.10)$$

3.4.3 PWM Techniques for MLC

In order to control the output current of an MLC, it is necessary to correctly drive the power semiconductors. These PWM signals are originated from the comparison between modulator and carrier waves. The greater the number of voltage levels that the MLC can synthesize, the more complex the implementation of the PWM signals becomes. The number of carrier waves increases with the number of voltage levels generated by the MLC. The arrangement of the carrier waves as well as the sequence of the generated signals will affect the performance of the MLC.

Barros et al. present in [243] a study and analysis of different PWM techniques applied to MLC. The analysis is done for: i) level shift PWM technique; ii) phase shift carrier; iii) hybrid carrier. For each group, the different variants are also analyzed to minimize the circulating currents between submodules, lower the harmonic content and increase the balance of operating powers between submodules. The preferred techniques for each MLC topology are also identified. Considering the results presented as well as the concept of using ac-side cascaded full-bridge converters, the phase-shift carrier technique is the most suitable.

The phase-shift carrier technique shifts the carrier waveforms horizontally. All carrier waves have the same amplitude, frequency, and mean value. They in turn present a phase shift between them of 2π/n as represented in Figure 3.21. The value of n is adjusted by considering the number of arms that the MLC topology presents.

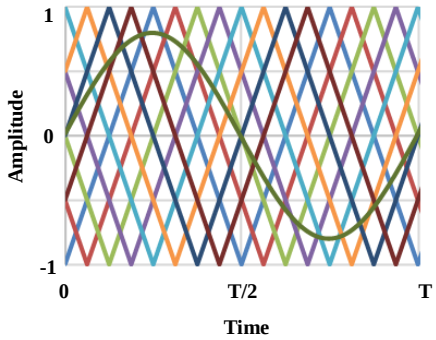

Figure 3.21 – Illustration of the carrier and modulation waveforms for the phase-shift carrier technique.

Considering several cascaded full-bridges, with this control technique it is possible to impose a similar operating power between each full-bridge. In this way, the concept of modularity is maintained. Analyzing its implementation in a microcontroller, there are solutions on the market, as is the case of Texas Instruments, whose microcontrollers present dedicated peripherals to perform the desired horizontal displacement [243], [244].

3.4.4 BESS Control Algorithms

In order to preserve the lifetime of the batteries, it is necessary to study and analyze different control techniques for charging and discharging the batteries. It is therefore recommended to analyze the datasheet provided by the manufacturer of the batteries that will constitute the BESS.

In the literature, several algorithms can be used for charging and discharging the BESS, including [245]–[248]: i) the constant current algorithm; ii) the constant voltage algorithm; iii) and the constant current followed by the constant voltage algorithm; iv) pulse-charging; v) reflex charging. These algorithms, varying the battery technology, are the most recommended to preserve the health of the batteries. However, considering the application of the railway system, where the BESS must store the available energy or make the necessary energy available, the analysis focused on the control algorithms where they present constant power.

The constant power charge and discharge method consists of applying constant power during these processes. For this, the control algorithm must control the charging/discharging current considering the reference power value as well as the battery's voltage. During the discharge process, the voltage will decrease, requiring an increase in the discharge current to maintain the power constant. In turn, during the charging process, the voltage will increase, causing the operating current to decrease. When the battery reaches its maximum voltage, a constant voltage must be maintained until the current shows a residual value [248]. Consequently, during this final stage of charge, the power varies linearly with the variation in charge current. The charging process is represented in Figure 3.22.

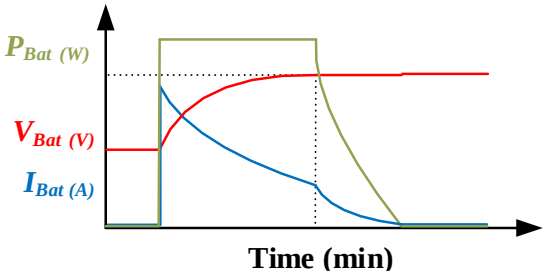

Figure 3.22 – Evolution of the voltage, V_{Bat}, and current, I_{Bat}, of the battery during a constant power, P_{Bat}, charging control algorithm.

3.4.5 MPPT Control Algorithms

Ideally, the solar PV module should always operate at maximum power. However, due to weather conditions (solar radiation, temperature, and shade), the MPP changes successively during the day. Therefore, it becomes necessary to implement a control algorithm capable of detecting the MPP and to impose that the power electronics converter operates at that point every instant. This control algorithm is called the maximum power point tracker (MPPT).

In the literature, there are several MPPT control algorithms [249]. These vary essentially in the complexity and cost of implementation (need for auxiliary circuits or sensors), in the convergence speed, the stability, and the performance obtained. There are also hybrid solutions to increase the robustness of the MPPT algorithm to any type of disturbance.

3.4.5.1 Constant Voltage

The MPPT algorithm based on the constant voltage method works on the principle of linearity between the open circuit voltage of the solar PV module and the voltage at the MPP. This relationship is represented in the equation (3.11). The proportionality constant K_1 is obtained empirically and supplied by the manufacturer, with values between 0.7 and 0.8 [249], [250]. Knowing the value of K_1 and periodically measuring the value of the open circuit voltage, it is possible to stipulate the ideal value to obtain the MPP voltage.

$$V_{MPP} = K_1 V_{OC} \tag{3.11}$$

In order to measure the open circuit voltage, an additional circuit is required to periodically disconnect the solar PV modules. Besides the inflated implementation cost, there is a momentary interruption in energy production. One solution to mitigate this problem is to use *pilot cells* to find the open circuit voltage value. However, this control algorithm is based on an approximation of the system, with the value of K_1 being obtained at the factory, not accounting for the degradation of the PV solar module. As such, the solar PV module and the power electronics converter will never operate at MPP.

3.4.5.2 Constant Current

The MPPT algorithm based on the constant current method has a similar operating principle as the constant voltage method. As such, there is likewise a linear relationship between the short-circuit current and the current in the MPP, as shown in the equation (3.12). The proportionality constant K_2 is determined empirically and provided by the manufacturer, with values ranging from 0.78 to 0.92 [249]. By knowing the value of K_2 and periodically measuring the short-circuit current, it is possible to stipulate the optimal value to obtain the MPP current.

$$I_{MPP} = K_2 I_{SC} \tag{3.12}$$

Similar to the constant voltage method, an auxiliary circuit is required to interrupt the connection of the solar PV modules to the power electronics converter and measure the short-circuit current. Consequently, this method leads to additional costs as well as a decrease in performance.

3.4.5.3 Perturbation & Observation

The MPPT based on the Perturbation and Observation (P&O) technique is a widely used algorithm in the literature [250]. This method has as its working principle the periodic perturbation and observation of the power variation obtained, thus, performed periodically. As such, it can be seen that the P&O MPPT algorithm will always oscillate around the MPP, causing the extracted power to oscillate around the MPP. Depending on the control platform, perturbations with smaller increments can be performed to minimize the oscillation. However, this solution decreases the speed of convergence of the system. This algorithm has a deficiency in finding the MPP in events of sudden variations in weather conditions. A correct configuration of the parameters of this control algorithm will allow a better response. Hybrid solutions with variable increments can be found to mitigate the associated problems.

Figure 3.23 depicted the flowchart of the P&O MPPT algorithm [250]. Analyzing the algorithm, one can see that initially, after acquiring the voltage and current values, the power value of the solar PV module is determined. Next, it is verified whether the operating power has increased or decreased. Depending on the power variation obtained, the voltage variation is checked in the same way. Considering the true conditions, a perturbation in the reference variable is performed, increasing or decreasing. The values are then saved for comparison in the next interaction. It should be mentioned that the increased sign, positive or negative, must be adjusted considering the variable to be controlled (directly in the duty-cycle, in the current, or the voltage).

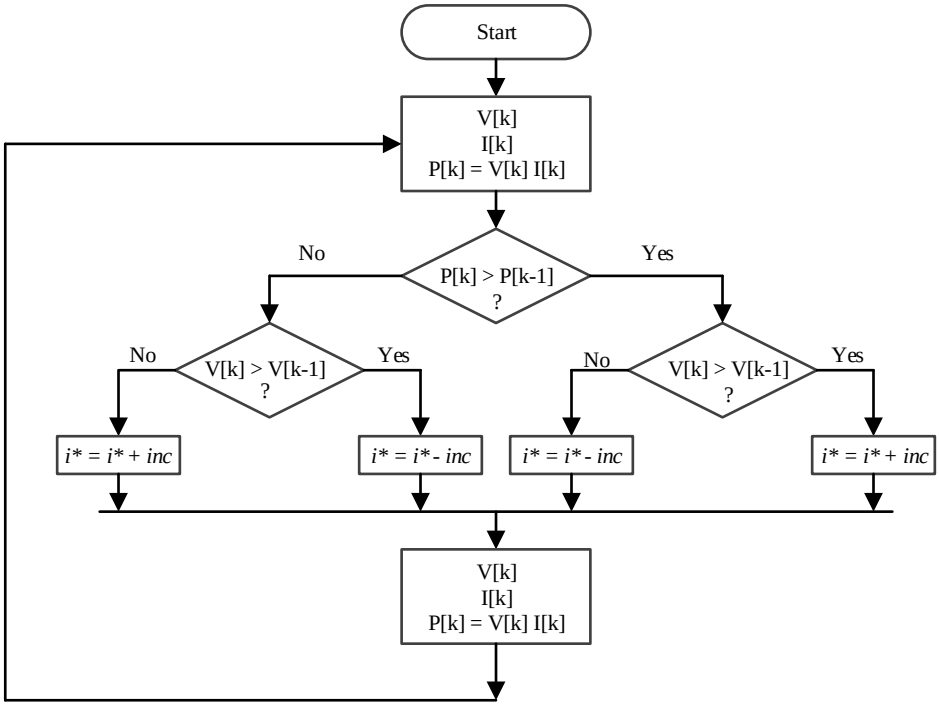

Figure 3.23 – Flowchart of the P&O MPPT control algorithm.

3.4.5.4 Incremental Conductance

The MPPT algorithm based on the incremental conductance technique is based on the characteristic curve of the solar PV module [250]. It determines the derivative of the power versus voltage at each instant to ascertain the location of the MPP. That is, if the derivative is positive, the MPPT algorithm is to the left of the MPP. On the other hand, if the derivative is negative, the MPPT algorithm is to the right of the MPP. If the derivative has a zero value, the MPPT algorithm is at MPP. Table 3.3 shows the three cases to be analyzed.

Table 3.3 – Summary of the power behavior with the incremental conductance MPPT control algorithm.

Condition	Working Point
$\frac{dP}{dV} = 0$	On the MPP
$\frac{dP}{dV} > 0 \Leftrightarrow \frac{\Delta I}{\Delta V} > -\frac{I}{V}$	In the left of the MPP
$\frac{dP}{dV} < 0 \Leftrightarrow \frac{\Delta I}{\Delta V} < -\frac{I}{V}$	In the right of the MPP

To determine the operating point it is necessary to calculate the derivative of the power with the voltage, obtaining the equation (3.13).

$$\frac{dP}{dV} = \frac{d(VI)}{dV} = V\frac{dI}{dV} + I = I + V\frac{\Delta I}{\Delta V} \tag{3.13}$$

The next step is to equalize the ratio between the derivative of the power with the derivative of the voltage to zero. By comparing the instantaneous conductance with the incremental conductance, it is possible to verify that it is MPP, as shown in the equation (3.14).

$$\frac{dP}{dV} = 0 \Leftrightarrow I + V\frac{\Delta I}{\Delta V} = 0 \Leftrightarrow \frac{\Delta I}{\Delta V} = -\frac{I}{V} \tag{3.14}$$

If the condition presented in equation (3.14) is verified, the system is at MPP. Otherwise, it is necessary to identify on which side of the MPP the operating point is, based on the condition presented in Table 3.3, and converge to the MPP.

Figure 3.24 shows the flowchart of the incremental conductance-based MPPT algorithm [250]. Analyzing the algorithm, it is possible to see that initially, after acquiring the voltage and current values, the voltage and current variations to the previous interaction are determined. The next step is to verify if it is at MPP, checking if there was no change in the voltage and current variations. If so, the variables are saved for the next interaction. Otherwise, it is necessary to verify the location of the operating point and converge to the MPP. It should be mentioned that the increment signal, positive or negative, must be adjusted considering the variable to be controlled (directly in the duty-cycle, in the current, or the voltage).

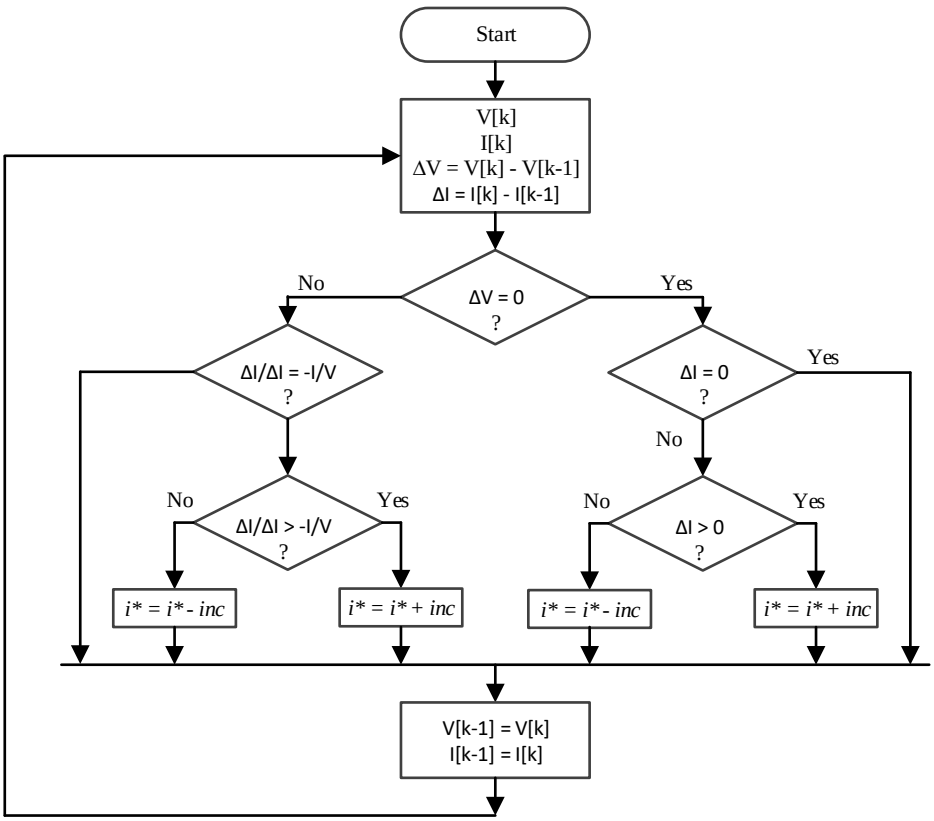

Figure 3.24 – Flowchart of the incremental conductance MPPT algorithm.

3.4.5.5 Hill Climbing

The MPPT algorithm based on the Hill Climbing method has emerged as one of the first MPPT algorithms, serving as the base structure for the previously presented algorithms. The principle of operation involves determining the top of the hill of the P-V curve. This top can be identified if the direction of movement is always upward [251].

In Figure 3.25 is represented the flowchart of the MPPT algorithm based on Hill Climbing. Analyzing the algorithm, it can be seen that initially, after acquiring the voltage and current values, it is checked if there was an increase in power. If so, the perturbation is performed in the same direction. Otherwise, the disturbance is performed in the previous direction. The variables are saved at the end for comparison in the next interaction [251].

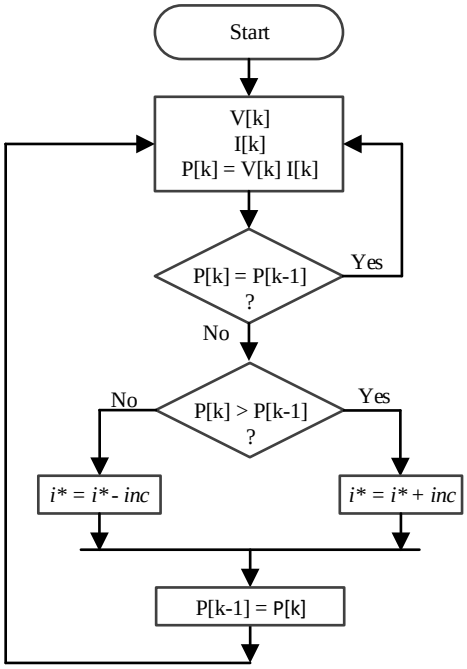

Figure 3.25 – Flow diagram of the hill climbing MPPT algorithm.

3.4.5.6 Fuzzy Logic Control

The MPPT algorithm based on the fuzzy logic control (FLC) method presents three analysis steps: fuzzification, inference, and defuzzification [250], [252]. This structure is exemplified in Figure 3.26. In contrast to previous algorithms, where they present only two logical values, the fuzzy logic control MPPT algorithm can present multiple values. These logic values can have different analysis steps, providing a fast response and accuracy in MPP detection.

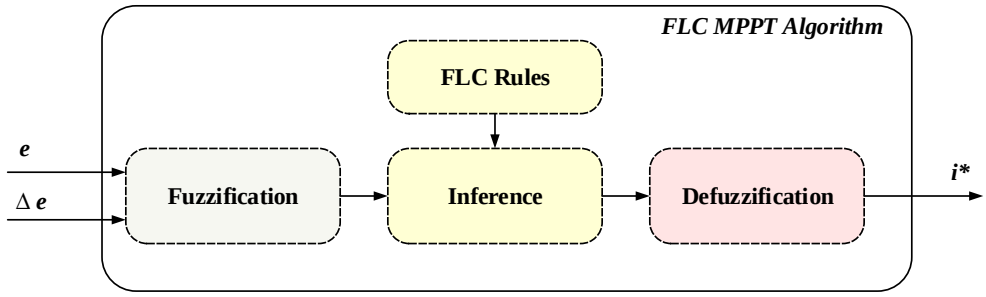

Figure 3.26 – Block diagram of the fuzzy logic MPPT algorithm.

For the first fuzzy step, the FLC MPPT algorithm needs the value determined by equation (3.15). For the determination of the error, *e[k]*, either the equation (3.16) or the equation (3.17) can be used [252].

$$\Delta e[k] = e[k] - e[k-1] \tag{3.15}$$

$$e[k] = \frac{P_{pv}[k] - P_{pv}[k-1]}{V_{pv}[k] - V_{pv}[k-1]} \tag{3.16}$$

$$e[k] = \frac{P_{pv}[k] - P_{pv}[k-1]}{I_{pv}[k] - I_{pv}[k-1]} \tag{3.17}$$

Once the equations are determined, the value is classified according to its sign and amplitude. The classification can vary depending on the number of categories considered for the algorithm. In the inference process, the input variables are subjected to the rules of the FLC algorithm. An example of the analysis performed for 5 categories is shown in Table 3.4. The analysis variables can be identified as: NB - Negative Big; NS - Negative Small; ZE - Zero; PS - Positive Small; PB - Positive Big.

Table 3.4 – Rules for the FLC MPPT control algorithm.

		$\Delta e[k]$				
		NB	NS	ZE	PS	PB
$e[k]$	NB	ZE	ZE	NB	NB	NB
	NS	ZE	ZE	NS	NS	NS
	ZE	NS	ZE	ZE	ZE	PS
	PS	PS	PS	PS	ZE	ZE
	PB	PB	PB	PB	ZE	ZE

In the final process, of defuzzification, the control variable is updated according to the analysis result of the inference process.

3.5 Conclusions

In this research work, it was possible to identify the different technological trends for the railway system in the short and medium-term, with concepts that are easy to adapt to the traditional railway system. In turn, there are innovative concepts that require a transport line totally independent of the traditional system to enhance its application. Thus it is expected that these concepts only have greater interest for

the railway system in the long-term use. In addition, it was possible to ascertain the need to increase the capacity of overhead contact lines to enable the integration of more and larger electric locomotives in the railway system. To this end, different approaches have been explored, since the implementation of cooperative strategies such as the integration of local energy sources or energy storage locations. Considering the emerging concepts, the need for power electronics solutions that allow for meeting the requirements of the rail system becomes evident. From the point of view of applicability, it was possible to ascertain that the modular and multilevel solutions, the MMCC, will play an important role in the railway systems.

In this chapter, an analysis of different power electronics converter topologies for integration into the railway system was performed. Due to the limitations in the semiconductor operating voltages and powers as well as the high voltages of the railway system, a modular and multilevel solution is required. With the modularity of the system, it is possible to expand the number of sub-modules to meet the desired operating conditions. However, in addition to easier maintenance and redundancy of operating states for increased robustness, it allows for reduced voltage stress on the semiconductors. With this analysis, it was possible to identify a power electronics converter topology, based on an SST, capable of meeting the desired requirements. The SST allows interfacing with high ac voltages, while also enabling a low-voltage common dc-link. The common low-voltage dc-link presents some interesting characteristics for the research project. In addition to facilitating the interface with a solar PV system and a BESS, it allows the implementation of simpler control algorithms. With the perspective of implementing an experimental prototype the topology of full-bridge converters with cascaded transformers was analyzed. This topology allows the implementation of a common dc-link, as well as the realization of a multilevel interface for the ac-link (the catenary). The simplified structure also allows for the centralization of the control algorithms using a single microcontroller, taking into consideration the number of PWM signals required.

Following the analysis of electronics converter topologies, the best solutions for interfacing with the solar PV system and the BESS were analyzed. Considering the operating powers and the no need for galvanic isolation, the interleaved dc-dc topologies were chosen. By increasing the number of phases in the converter, it is possible to divide the currents between the different arms. Consequently, a smaller current ripple at the inverter input is obtained, which can decrease the passive filter size. For the interface of the solar PV system a four-phase interleaved unidirectional converter was chosen, while for the interface with the BESS, a four-phase interleaved bidirectional converter was chosen. For the development of the experimental prototype, a simpler solution of only one phase was chosen for both cases.

Given different types of power electronics converters and interfaces, different control techniques and algorithms to be implemented were also analyzed. For the interface with the ac catenary, an algorithm that allows synchronization with the fundamental component of the voltage was studied. This algorithm presents two output signals, a sinusoidal signal with unitary amplitude and a second signal that represents the maximum voltage amplitude. These two signals are necessary for the correct determination of the converter reference currents. Following this, different current control algorithms were also analyzed, verifying that the predictive algorithm, due to the non-dependence on gain adjustment, is the most suitable for the current control of the ac side. In turn, for the dc side, due to its easy implementation and replication for the different phases of the interleaved converters, the PI control was chosen. However, given the practical implementation and the limitation in the number of PWM signal peripherals, the period sampling algorithm was adopted.

Concerning the PWM techniques, special focus was given to the techniques to be integrated into multilevel converters. Considering the modular concept, different PWM techniques were studied. With this study it was possible to contribute a paper, concluding that the PSC technique allows for maintaining a balanced power in the different submodules. Nevertheless, considering a practical implementation, the horizontal shift of the carrier waves with the PSC PWM technique is simpler on Texas Instruments microcontrollers.

Finally, different control algorithms to be integrated into the BESS and the solar PV system are presented. Considering the BESS, and since the sp-RPC always operates with a reference power, the constant power battery charging technique was analyzed. In turn, to maintain a maximum power extraction from the solar PV modules, different MPPT algorithms were analyzed. With the developed analysis it was found that the performance of the MPPT algorithm is dependent on the convergence speed as well as the stability of the system. The perturbation & observation algorithm and the incremental conductance algorithm are the most widely used in the literature. While one oscillates around the MPP, the other uses the curve of power versus voltage to determine the MPP. Thus, the incremental conductance algorithm was chosen for analysis and preliminary simulations of the system.

Chapter 4

Proposed System, Operation Principle and Simulation Results

4.1 Introduction

This chapter analyzes the performance of the proposed dynamic control for an sp-RPC system with the possibility of interfacing with a solar PV system and/or with a BESS. For this validation, the nominal operating conditions of a railway system were considered, and a modular and multilevel solution based on SST was integrated to interface with the high-voltage ac catenary. In turn, for both the solar PV system and the BESS, an interleaved converter topology was chosen, to reduce the semiconductors current stress. The proposed control algorithm intends to provide dynamic control in the railway systems, balancing the powers of each TPS.

In the second section of this chapter, simulation results are also presented based on a simpler topology used in the developed laboratory prototype. This topology shares some characteristics of the topology implemented for the real system. Regarding the high-voltage ac side, it was decided to implement a dc-ac power converter with cascade transformers. For each side, the system has three submodules connected in cascade and sharing the same dc-link. The concept of modularity and multilevel is also used. In turn, a unidirectional dc-dc boost and bidirectional dc-dc power converters were chosen for the solar PV system and for the BESS. The architecture's similarities allowed a migration and adaptation of the proposed algorithm to the reduced-scale simulation model. Consequently, with the validation of computer simulations, it was possible to migrate the code developed in C language and adapt it to the digital control platform used in the experimental prototype for subsequent validation.

At the end of the chapter, a quantitative analysis and discussion of the system performance in the different operating modes is carried out.

4.2 Proposed sp-RPC Topology based on SST

In order to validate the control algorithm proposed for the sp-RPC with interface with the solar PV system and the BESS, a computer simulation model was developed. It was intended that the simulation model would be able to respond to the requirements of a real application, considering the power levels and operating voltages and currents. Therefore, modularity and multilevel concepts were used for the high-voltage ac catenary side. In turn, for interface with the solar PV system and the BESS, since they present low voltages and high currents, interleaved topologies with several arms in parallel were chosen. The proposed topology is shown in Figure 4.1. Different submodules connected in series were used for the ac side. Thus, a common low-voltage dc side can be identified, which facilitates energy exchange and minimizes the complexity of the control algorithms. In order to provide isolation, the DAB topology was integrated into each submodule. The DAB integrated into each submodule is responsible for the exchange of energy between the common dc-link and the submodule high-voltage dc-link. Nevertheless, the transformation ratio used in the high-frequency transformer of the SST allows the creation of a common low-voltage dc-link and the creation of a dedicated high-voltage dc-link for each submodule. In this way, the number of submodules used can be adjusted as a function of the transformation ratio. For a better understanding of the explanation, the power converter that is connected to the *x*-side was called *spRPCx*. In turn, the power electronics converter that is connected to the *y*-side was called *spRPCy*.

Regarding the interface with the solar PV system, a four-phase unidirectional interleaved boost dc-dc power converter was chosen. In turn, for the BESS, the four-phase bidirectional interleaved dc-dc topology was chosen. In this way, it is possible to obtain a relatively interface with low voltage, with the high currents being divided by the different arms that constitute the converters. In this way, it is possible not only to minimize the current ripple but also respond to acceptable current limits for the fully controllable power semiconductors available on the market.

The used topology must consider the requirements of a real application. Thus, the main parameters of the operating conditions of the sp-RPC, the solar PV system, the BESS, as well as the rest of the railway system, are presented in Table 4.1. For the developed simulation model, the average nominal power for the *spRPCx*, P_{spRPCx}, and the *spRPCy*, P_{spRPCy}, of 2.5 MW, for the solar PV system, P_{PV}, of 1.1 MW, and the BESS, P_{BESS}, of 1 MW was considered. Regarding the dc-link, a nominal voltage of 1 kV was considered on the common dc-link, v_{dc}, and a voltage of 7 kV on the dedicated dc-link of each submodule, v_{dc_xk}, and v_{dc_yk}, being *k* the number of the submodule of the *x*-side or *y*-side. The value of 1 kV was defined to obtain a voltage value on the low-voltage common dc-link. In this way, it would be possible to implement a solar PV system and a BESS with lower interface voltages, without increasing the number of

elements in series. Moreover, as it is a common dc-link with different power converters connected, it needs capacitors with high capacities, being in the market solutions with a nominal voltage value close to 1 kV. Regarding the high-voltage dc-link in each submodule, this value was defined considering the number of submodules and the peak value of the catenary voltage. A modulation index of around 80 % was also considered.

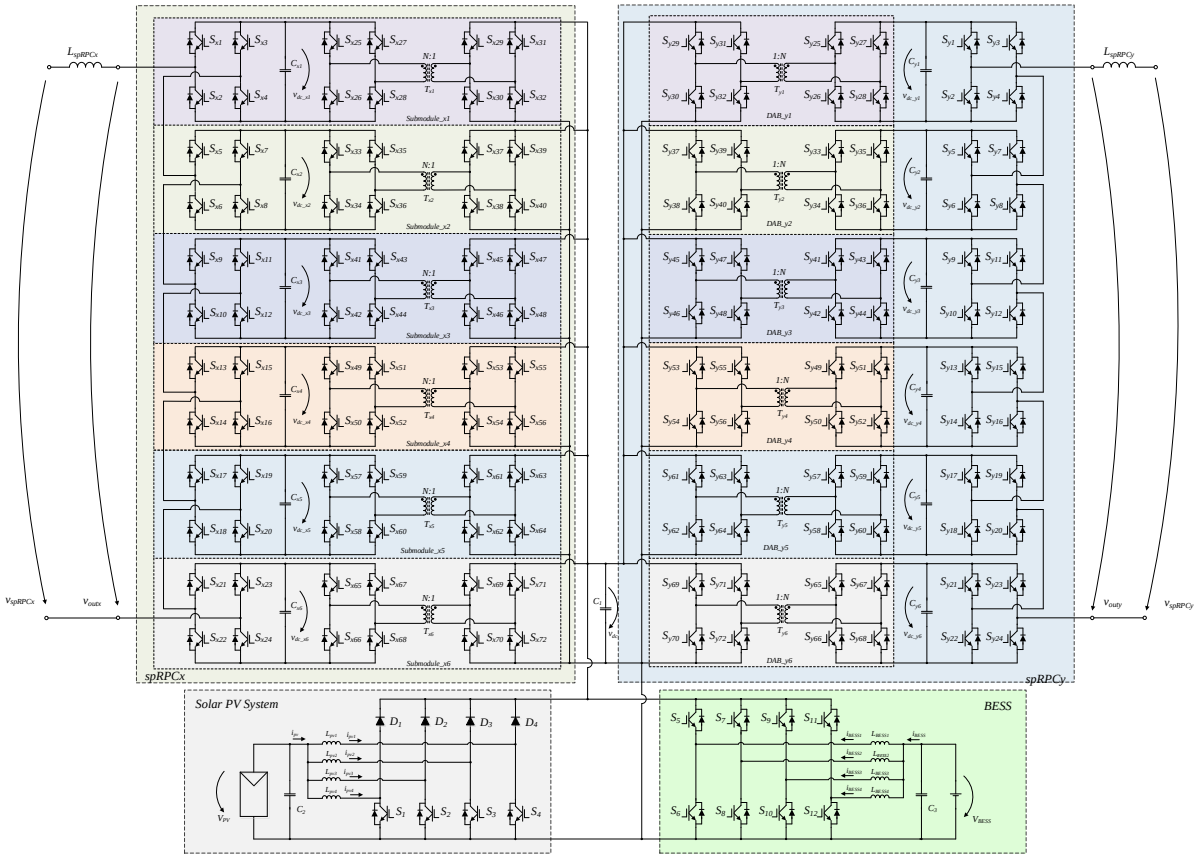

Figure 4.1 – Electrical schematic of the proposed topology for the sp-RPC with interface for the solar PV system and BESS.

Table 4.1 – Main parameters of the topology.

	Variable	Minimum	Nominal	Maximum	unit
sp-RPC active power	P_{spRPCx}, P_{spRPCy}		2.5		MW
Solar PV system power	P_{PV}			1.23	MW
BESS power	P_{BESS}			1	MW
Common dc-link voltage	V_{dc}		1		kV
Submodule high-voltage dc-link voltage	V_{dc_x1}, V_{dc_x2}, V_{dc_x3}, V_{dc_x4}, V_{dc_x5}, V_{dc_x6}, V_{dc_y1}, V_{dc_y2}, V_{dc_y3}, V_{dc_y4}, V_{dc_y5}, V_{dc_y6}		7		kV
TPS voltage	v_{PGx}, v_{PGy}		25		kV
Solar PV system voltage	V_{PV}		733	831	V
BESS voltage	V_{BESS}	550	726	814	V
Sp-RPC current	i_{spRPCx}, i_{spRPCy}		100		A
Solar PV system current	I_{PV}		1520	1645	A
BESS current	I_{BESS}	1229	1377	1818	A
Communication frequency	f_{s_PG}		5		Hz
Sampling frequency	f_s		50		kHz
Switching frequency sp-RPC	f_{sw_spRPC}, $f_{sw_spRPC_DAB}$		5		kHz
Switching frequency for PV and BESS	f_{sw_PV}, f_{sw_BESS}		20		kHz

Regarding the operating frequency values, it should be mentioned that the update frequency of the average operating power values of the TPS, f_{s_PG}, is 5 Hz, using a sampling frequency, f_s, of 50 kHz for the local variables of the sp-RPC. In turn, a switching frequency of 5 kHz was considered for each submodule of *spRPCx* and *spRPCy*, f_{sw_spRPC}, as well as for the DAB that constitutes the SST, $f_{sw_spRPC_DAB}$. Regarding the dc-dc converters of the solar PV system and BESS, a frequency of 20 kHz was considered, $f_{sw_spRPC_PV}$ and f_{sw_BESS}.

The frequency of 5 Hz was considered acceptable to validate the propagation delay in the communications channel. Furthermore, for a 3 second simulation with electric locomotive disturbances every 1 second, the 0.2 second period allows for the analysis of the sp-RPC performance after some interactions, converging to the steady-state operation. Regarding the remaining values, since they had already been considered in other previous simulation models as well as during the analysis of each converter in its initial phase, they were migrated to the final simulation model.

Table 4.2 shows some of the values considered for the different components that compose the simulation model of the sp-RPC topology based on SST.

Table 4.2 – Main parameters of the electric components used on the sp-RPC topology based on SST.

	Variable	Value	Unit
Line impedance inductors	L_{PGzx}, L_{PGzy}, $L_{spRPCzx}$, $L_{spRPCzx}$,	2.5 (250[#1])	mH (mΩ)
Coupling inductor	L_{spRPCx}, L_{spRPCy}	50 (10[#1])	mH (mΩ)
Inductor for the PV	L_{pv1}, L_{pv2}, L_{pv3}, L_{pv4}	100 (100[#1])	µH (mΩ)
Inductor for the BESS	L_{BESS1}, L_{BESS2}, L_{BESS3}, L_{BESS4}	20 (100[#1])	µH (mΩ)
Capacitance on the dc-link	C_1	200 (10[#1])	mF (mΩ)
Capacitance on the dc-link	C_{x1}, C_{x2}, C_{x3}, C_{x4}, C_{x5}, C_{x6}, C_{y1}, C_{y2}, C_{y3}, C_{y4}, C_{y5}, C_{y6}	10 (10[#1])	mF (mΩ)
Open-circuit voltage on the BESS	V_{BESS_0}	550	V
Capacitor of the BESS model	C_{BESS}	36 (3.6[#2])	F
Internal series resistor of the BESS	R_{BESS_ESR}	100	mΩ

[#1] Considered as internal series resistance for each component;
[#2] Considered for simulation with regenerative braking to validate de transition between the charging and discharging process for the same simulation time.

4.3 Control Algorithm Proposed for the sp-RPC based on SST

For the correct functioning of the sp-RPC it is necessary to constantly monitor the different variables of the system. The sp-RPC controller has real-time access to the local variables, and access to the active

power in each TPS in intervals of 0.2 s (f_{s_PG} = 5 Hz). Due to the inherent concept, the sp-RPC will have to conciliate the instantaneous monitoring of the operating variables of the power electronics converters, with periodic monitoring, caused by the time delay of sending information, of the active power of each TPS. In this way, throughout this topic, all the implemented algorithms are presented to provide a continuous operation of the sp-RPC. This topic starts by analyzing the different variables to be controlled, the interaction between different control algorithms, the determination of the reference values for each power electronics converter, and the control signals for the power semiconductors.

Figure 4.2 shows a simplified electrical schematic of the proposed topology for the integration of a full-scale sp-RPC. In the represented electrical diagram, it is possible to verify not only the constitution of each power electronics converter but also the measurement points of the different variables, both currents, and voltages.

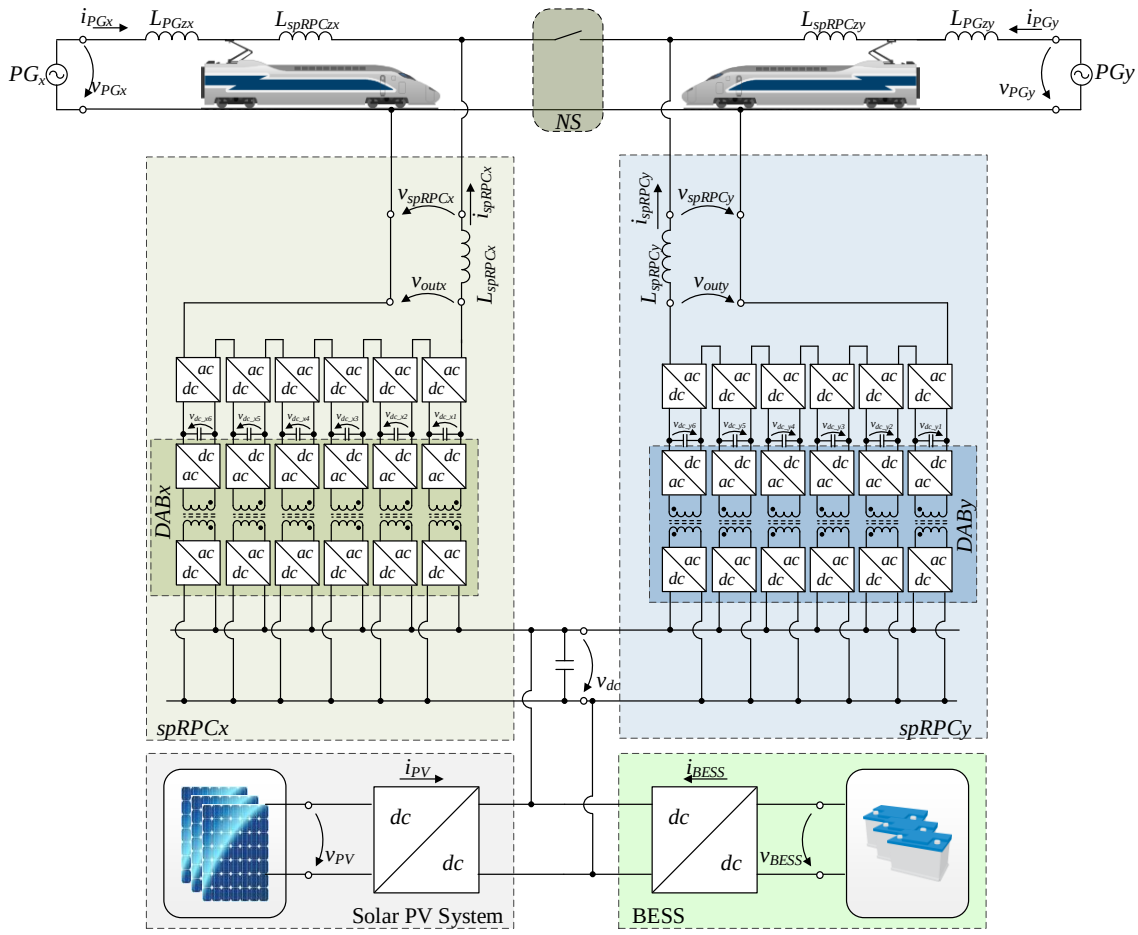

Figure 4.2 – Simplified schematic of the proposed topology for the sp-RPC, highlighting the measurement points for the variables involved in the control algorithms.

For the correct operation of sp-RPC, the entire algorithm must present a given sequence of data processing, as well as identify the interaction of variables between different blocks of data processing. Figure 4.3 shows the main implemented control algorithms, highlighting the input and output variables

of each one. Nevertheless, it is possible to verify a sequence of data processing, starting with the acquisition of instantaneous voltage and current values from different points of the sp-RPC, going through to determine the average values of both voltage and power required. Based on the combination of average and instantaneous values with specific control functions, it is possible to determine the operating reference powers for each sp-RPC subsystem, whether interfacing with the railway system, with the *spRPCx* and *spRPCy*, with the solar PV system, P_{PV}, or the BESS, P_{BESS}. These values are later used to adjust the control signals to minimize operating errors compared to the reference values.

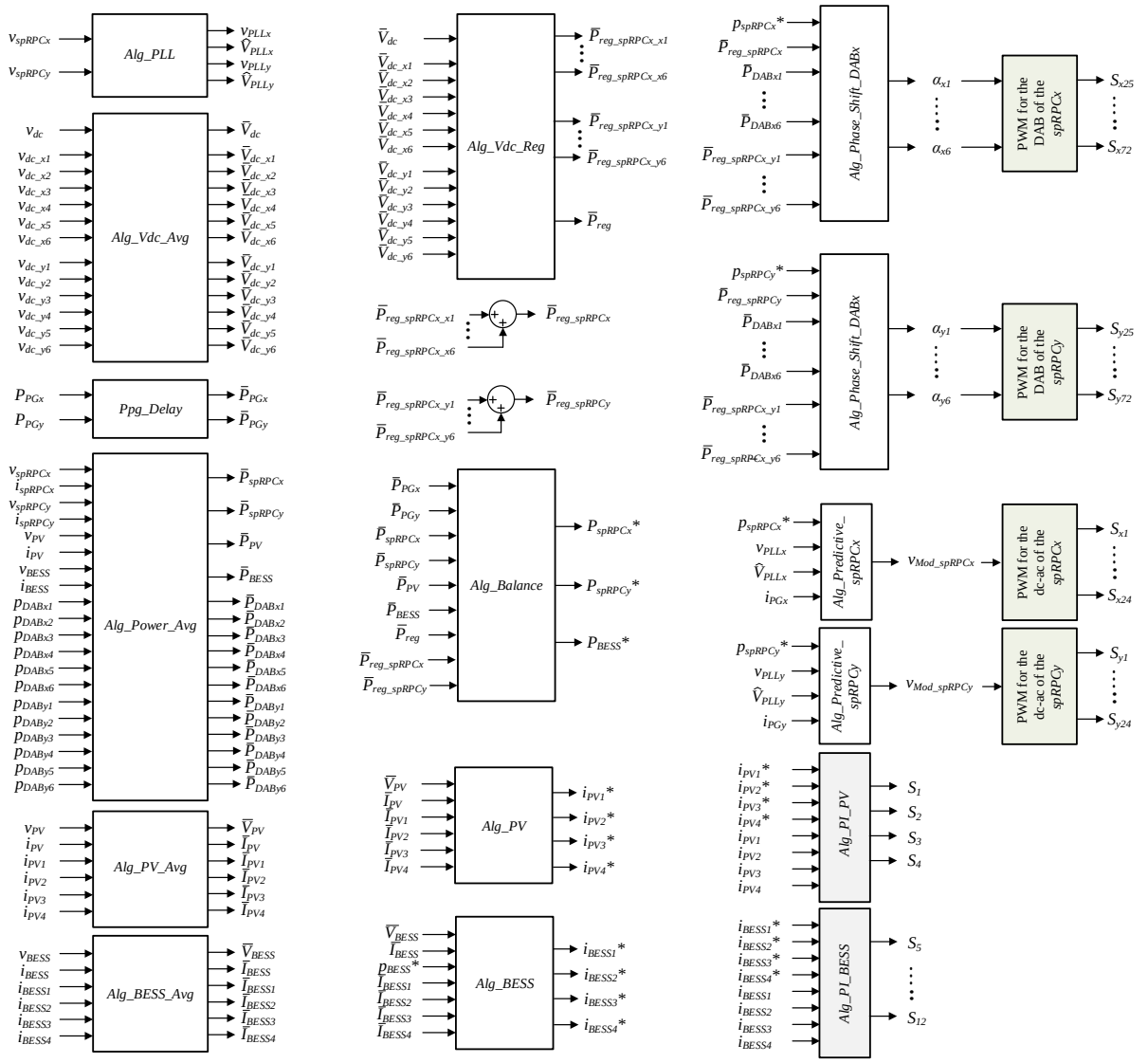

Figure 4.3 – Block diagram of all the control algorithms implemented for the proposed sp-RPC.

For the correct functioning of the implemented algorithm, it is necessary to initially determine the average values of voltage and power. This way, the control algorithm *Alg_Vdc_Avg* is responsible for determining the average values of the voltages in the different dc-link that compose the sp-RPC. In turn, the control algorithms *Alg_Power_Avg*, *Alg_PV_avg,* and *Alg_BESS_avg* are responsible for determining the active powers of each submodule of power electronics converters, the average values of the solar PV system

and the average values of the BESS. Regarding the control algorithm *Ppg_Delay*, it is responsible for generating the delay of the active power values of each TPS. Finally, as the last control block for the input variables, there is the PLL control algorithm, *Alg_PLL*, responsible for synchronizing the system with the fundamental component of the voltage of each catenary.

Once all the instantaneous input variables have been processed, it is necessary to define the operating reference values for each power electronics converter. In this way, based on the *Alg_Vdc_Reg* function, one starts by determining the regulating power to keep the voltages of the dc-links regulated. The sum of the regulating power for *spRPCx*, *Preg_spRPCx*, and for *spRPCy*, *Preg_spRPCy*, are later used in the control algorithm *Alg_Balance*. This block is responsible for managing and determining the reference active power values for the different power electronics converters. On the other hand, the solar PV system operating power is determined by the MPPT algorithm that is implemented in the *Alg_PV* function. Finally, *Alg_BESS* is responsible for controlling the charging and discharging process of the BESS based on the reference power P_{BESS}*.

Once all the operating reference values have been determined, it is necessary to activate the different power semiconductors that compose the power electronics converters, based on the modulation technique used for each one. That is, for the DAB the control is done by the phase shift technique, with the control algorithm *Alg_Phase_Shift_DABx* being responsible for generating the phase angles for each DAB that constitutes the *spRPCx*, while the *Alg_Phase_Shift_DABy* is responsible for generating the phase angles for each DAB that constitutes the *spRPCy*. These values are later used for the direct drive of semiconductors Sx25 to Sx72 of *spRPCx* and Sy25 to Sy72 of *spRPCy*. For the power converters that are connected to the catenary, a predictive control algorithm is used to determine a modulator wave for the PWM signals. In this way, the *Alg_Predictive_spRPCx* function is responsible for generating a modulating wave v_{Mod_spRPCx}, while *Alg_Preditice_spRPCy* is responsible for generating a modulating wave v_{Mod_spRPCy}. These modulating waves are later compared with carrier waves for the activation of semiconductors Sx1 to Sx24 of *spRPCx* and semiconductors Sy1 to Sy24 of *spRPCy*. It should be mentioned that to impose a better power balance between submodules, the phase-shift carrier PWM technique was implemented. Regarding the solar PV system, to control each current of the 4-arm interleaved unidirectional dc-dc boost power converter, a PI algorithm is used for each reference current, this control algorithm is implemented in the *Alg_PI_PV* function. Analogously, the *Alg_PI_BESS* function presents a similar functionality for the BESS power electronics converter.

Regarding the control algorithm implemented in the *Alg_BESS* block, it is responsible for managing the operating state of the BESS, charge, or discharge, depending on the state of charge of the batteries. The

implemented algorithm is represented in Figure 4.4 through a flowchart. Analyzing the figure, it is possible to verify that the first stage of operation involves determining the maximum and minimum limits of operation. Once defined, the state of charge of the battery is checked. If the battery is fully charged, the charging flag *_Charging* is disabled, and the discharge flag *_Discharging* is enabled. If the first situation does not occur, the control algorithm will check whether the battery is completely discharged. If so, *_Charging* is enabled and *_Discharging* is disabled. If one of these conditions is verified, the BESS control algorithm is disabled, disabling the *En_BESS_Ctrl* flag. If these two situations are false, a hysteresis margin has been defined so that the battery is charged again when the voltage is less than 80 % of the maximum value or is discharged again when the voltage is greater than 20 % of the minimum value. In this way, undesirable state transitions are avoided, and these limits can be adjusted depending on rail traffic or battery manufacturer recommendations. Once the state of charge of the batteries has been verified, the desired state of operation is verified. That is, if $P_{BESS}*$ is positive and the batteries are not completely discharged allowing their discharge, i.e. with *_Discharging* activated, the *En_BESS_Ctrl* flag is activated again. On the other hand, if $P_{BESS}*$ is negative and the batteries are not fully charged allowing charging, that is, with *_Charging* activated, the *En_BESS_Ctrl* flag is activated again. The *En_BESS_Ctrl* flag is later used to add or not add the $P_{BESS}*$ portion to the sp-RPC operating state.

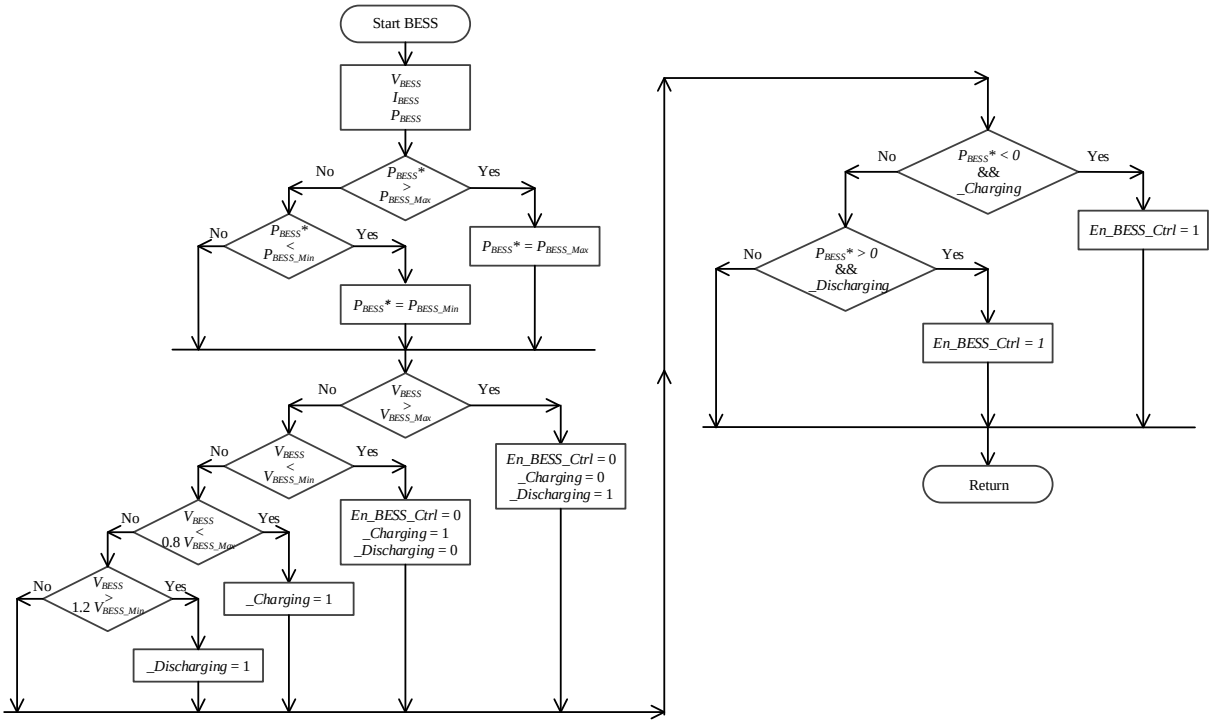

Figure 4.4 – Flowchart of the control algorithm implemented on the BESS.

For the sp-RPC to be able to synthesize the desired output current, the voltages on the dc-links must present a minimum value. This value depends not only on the peak voltage of the catenary but also on the topology of the power electronics converter. In this specific case, it is necessary to consider the

combination of the different voltage values of each submodule that constitutes the sp-RPC, and the total value must exceed the peak voltage of the catenary. Thus, the control algorithm *Alg_Vdc_Reg* is responsible for determining the necessary regulating power value for voltage regulation of each capacitor of the different dc-links. Considering this premise, it is necessary to proceed with the regulation of all the dc-links that composes the sp-RPC.

Initially considering the common dc-link, it is necessary to determine the average voltage value, proceeding in this way with the implementation of a sliding window average. Making the difference between the desired voltage reference value and the average value obtained, the voltage error is obtained. The *V_dc_error* portion is used with a PI controller to determine the final regulating power *Preg*. The representative block diagram of the algorithm implemented for regulating the dc-link voltage is shown in Figure 4.5.

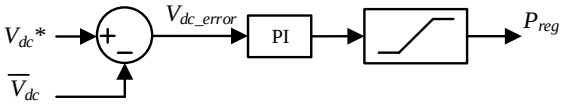

Figure 4.5 – Block diagram of the control algorithm responsible to regulate the voltage on the common dc-link.

Regarding the capacitors that compose each DAB submodule, it is necessary to apply the same methodology for their regulation. Figure 4.6 shows a block diagram illustrating the algorithm performed for the regulation of the dc-link of each DAB that composes the *spRPCx*. The sum of each plot is then used to determine the reference active power of *spRPCx*. The same methodology is replicated for *spRPCy*.

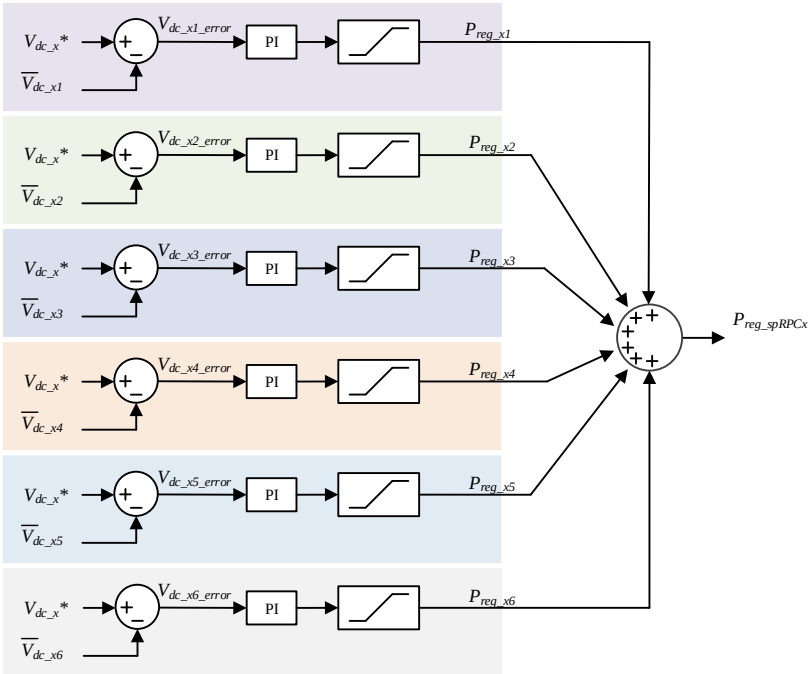

Figure 4.6 – Block diagram of the control algorithm responsible to regulate the different dc-link voltages on the *spRPCx*.

Once the *spRPCx* total operating active power has been determined, it is necessary to determine the reference active power for each submodule, to maintain not only the regulation of the dc-link but essentially impose an equal power distribution between submodules. In this way, the power value is defined as a function of the number of existing submodules, dividing P_{spRPCx} by *N*. The resulting portion is then added to the regulating power of each submodule, thus creating a reference active power. The operating active power of each submodule is then compared with the respective reference active power, resulting in an error value. This value is used in a PI controller to generate a phase angle capable of minimizing the error obtained.

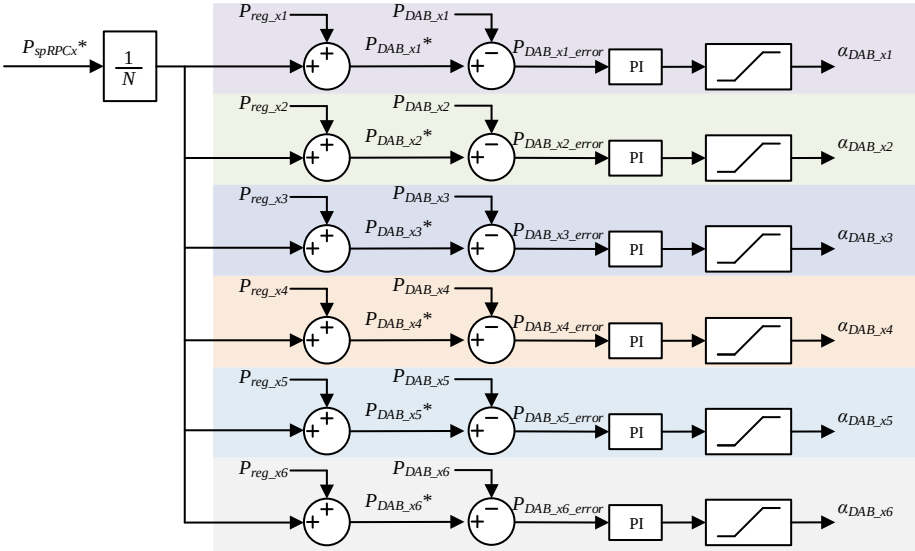

Figure 4.7 – Block diagram of the control algorithm responsible to balance de power between the different submodules of the *spRPCx*.

Once the acquisition of the different input signals, their processing, and different algorithms has been verified, the constitution of the *Alg_Balance()* control block is presented below. In this control block, all the algorithms necessary for defining the operating reference values of each power electronics converter are implemented to balance the average active powers of each TPS. Nevertheless, the correct determination of these reference values will allow a continuous operation of the system, keeping the voltages of different dc-link regulated, as well as allowing greater robustness of the system to any variation or disturbance of the system.

For the correct dynamic operation of the system, it is necessary to continuously acquire the active power values on each side of the TPS. That is, the average value of the TPS on the *x*-side, P_{PGx}, and on the *y*-side, P_{PGy}. Due to the distance from the TPS to the sp-RPC, these parameters are updated periodically. In this way, the determination of the average value of the operating power between the two TPS, P_{avg}, represented in equation (4.1), is affected by the time of sending this information. Thus, a time interval of 200 ms was considered for updating the operating conditions, to validate the simulation model.

$$P_{avg} = (P_{PGx} + P_{PGy})/2 \tag{4.1}$$

Once the P_{avg} value has been determined, it is necessary to determine the desired energy transfer between TPS, P_{trans}. That is, if it is intended to absorb energy from the TPS on the *x*-side and inject it into the *y*-side, or vice versa. For this, equation (4.2) is used, being necessary to determine the active power of the *spRPCy* on the *y*-side, P_{spRPCy}. By adding P_{PGy} to P_{spRPCy} and subtracting the value of P_{avg}, it is possible to verify the intended energy flow. If a positive result is obtained, the power flow is carried out from the *x*-side TPS to the *y*-side TPS. Otherwise, the energy flow is carried out oppositely.

$$P_{trans} = -P_{avg} + P_{PGy} + P_{spRPCy} \tag{4.2}$$

In case the sp-RPC has an interface with the BESS, it is possible to use the stored energy to minimize the dependence on the TPS. In this way, and as represented in equation (4.3), the reference power of the batteries, $P_{BESS}*$, is determined as the difference of the active power of each TPS, P_{PGx} P_{PGy}, with the average power coming from the solar PV system. If the solar PV system does not exist or the operation is disabled, the P_{PV} value is null. As a protection mechanism, the reference value is always limited to the maximum allowable power and dimensioned for each subsystem. In the case of $P_{BESS}*$ it is 1 MW, and the P_{PV} value is determined by the MPPT control algorithm integrated in the system, and this value varies throughout the day.

$$P_{BESS}{}^{*} = (P_{PGx} + P_{PGy} - P_{PV}) \tag{4.3}$$

Once the P_{trans} and $P_{BESS}*$ values are determined, it remains to define the average operating powers for *spRPCx* and *spRPCy*, $P_{spRPCx}*$ and $P_{spRPCy}*$ respectively. For this, it was considered that *spRPCx* would be responsible for performing an initial perturbation, and *spRPCy* always operated with a constant average operating power. Equation (4.4) is used to determine the value of $P_{spRPCx}*$, while equation (4.5) is used for the $P_{spRPCy}*$.

$$P_{spRPCx}{}^{*} = -P_{trans} + P_{PV} - P_{BESS} \tag{4.4}$$

$$P_{spRPCy}{}^{*} = P_{trans} \tag{4.5}$$

These values presented are limited to the maximum and minimum values desired for the operating powers of each power converter, *spRPCx,* and *spRPCy.* Once limited, the portion of the regulating powers used for the regulation of the dc-links that constitutes the full sp-RPC system, as represented in equation (4.6), is subsequently added. If the losses are significant, a greater initial limitation is recommended so that the final reference values for the operating powers do not exceed the nominal values considered for the power in a steady-state.

$$P_{spRPCx}{}^{*} = P_{spRPCx}{}^{*} - (P_{reg} + P_{reg_{spRPCx}} - P_{reg_spRPCy}) \tag{4.6}$$

4.4 Simulation Results of the sp-RPC based on SST

In this topic, the different simulation results obtained are presented, considering the real-scale simulation model of sp-RPC. This analysis considered the different operating modes, as well as the different operating conditions caused by the loads. Regarding the operating modes, the performance of the system with and without the integration of the solar PV system and/or the BESS in the sp-RPC was analyzed. In turn, the analysis of the robustness of the system was also analyzed considering different operating conditions of the loads, considering operating inputs and outputs, load transients, and regenerative braking.

For a comparative analysis of the performance of the sp-RPC, the different loads considered are presented in Figure 4.8, highlighting the imposed operating conditions. The analysis of each figure is presented in the following topics:

- In Figure 4.8 (a) the load on the *x*-side presents an average active power P_{Loadx} = 0.998 MW, while the load on the *y*-side presents P_{Loady} = 6.12 MW. Regarding the currents, it is possible to verify that i_{PGx} presents an amplitude of 56.54 A, while i_{PGy} presents an amplitude of 357.2 A;

- In Figure 4.8 (b) the load on the *x*-side presents an average active power P_{Loadx} = 0.998 MW, while the load on the *y*-side presents P_{Loady} = -3.88 MW. Regarding the currents, it is possible to verify that i_{PGx} presents an amplitude of 56.54 A, while i_{PGy} presents an amplitude of 228.4 A;

- In Figure 4.8 (c) the load on the *x*-side presents an average active power P_{Loadx} = 0.998 MW, while the load on the *y*-side presents P_{Loady} = 4.12 MW. Regarding the currents, it is possible to verify that i_{PGx} presents an amplitude of 56.54 A, while i_{PGy} presents an amplitude of 243 A;

- In Figure 4.8 (d) the load on the *x*-side presents an average active power P_{Loadx} = 2.99 MW, while the load on the *y*-side presents P_{Loady} = 0 W. Regarding the currents, it is possible to verify that i_{PGx} presents an amplitude of 169.4 A, while i_{PGy} presents an amplitude of 0 A;

- In Figure 4.8 (e) the load on the *x*-side presents an average active power P_{Loadx} = 2.99 MW, while the load on the *y*-side presents P_{Loady} = 0.999 MW. Regarding the currents, it is possible to verify that i_{PGx} presents an amplitude of 169.4 A, while i_{PGy} presents an amplitude of 56.54 A;

- In Figure 4.8 (f) the load on the *x*-side presents an average active power P_{Loadx} = 2.00 MW, while the load on the *y*-side presents P_{Loady} = 0.99 MW. Regarding the currents, it is possible to verify that i_{PGx} presents an amplitude of 113 A, while i_{PGy} presents an amplitude of 56.54 A.

For a better analysis, two case scenarios were considered: scenario A; and scenario B. Case scenario A has three instants with different locomotive consumption, being characterized by the regenerative braking event. Thus, each moment of disturbance is identified in the moments: i) P_{Loadx} = 0.998 MW and P_{Loady} = 6.12 MW; ii) P_{Loadx} = 0.998 MW and P_{Loady} = -3.88 MW; and iii) P_{Loadx} = 0.998 MW and P_{Loady} = 4.12 MW. On the other hand, case scenario B also has three instants with different train consumption, being characterized by positive consumption of energy. Thus, each moment of disturbance is identified in the moments: i) P_{Loadx} = 2.99 MW and P_{Loady} = 0 W; ii) P_{Loadx} = 2.99 MW and P_{Loady} = 0.999 MW; and iii) P_{Loadx} = 2.00 MW and P_{Loady} = 0.99 MW. Each scenario is analyzed in more detail in the following topics.

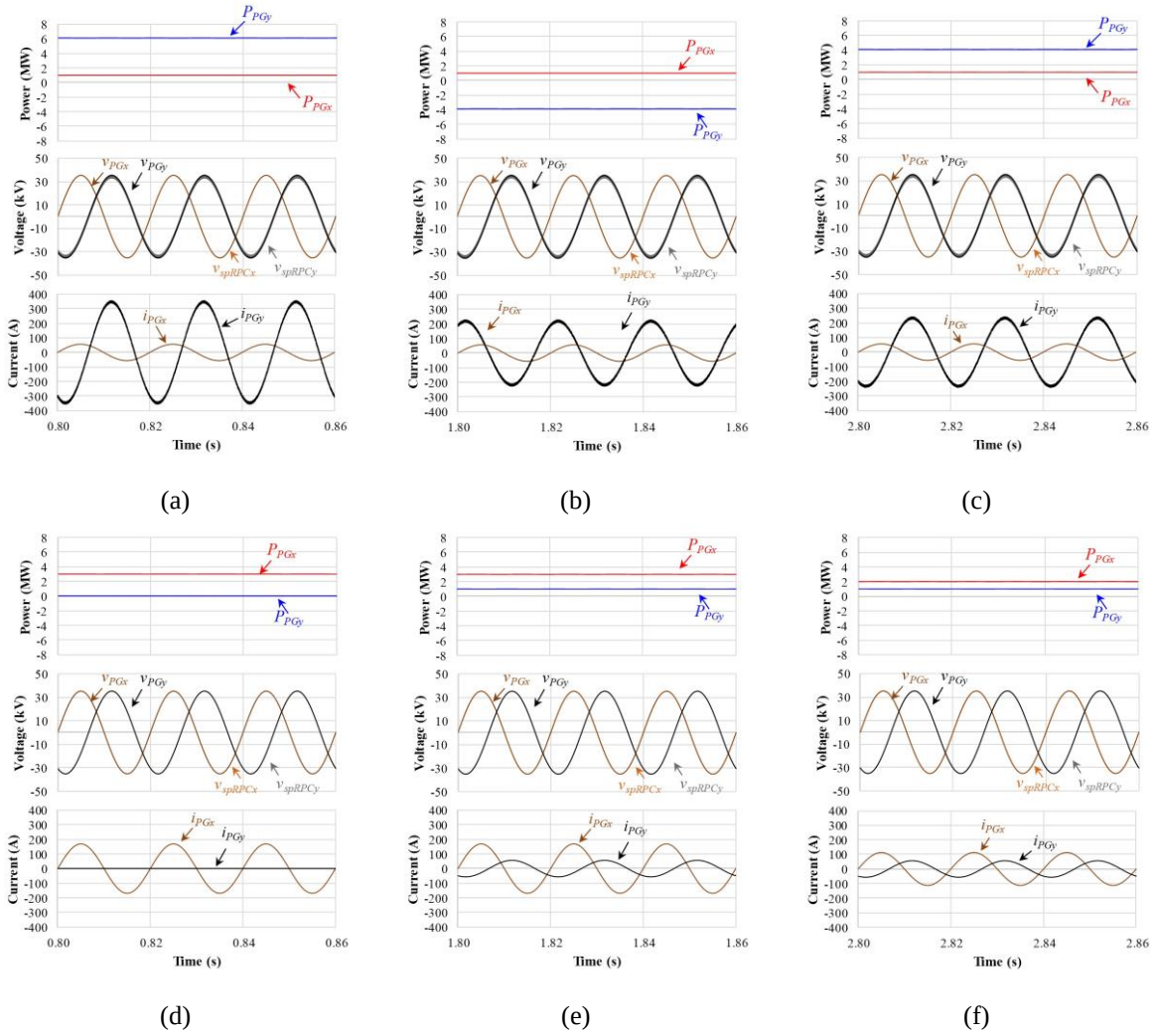

Figure 4.8 – Simulation results of the power in each TPS, P_{PGx} and P_{PGy}, the voltages, v_{PGx}, v_{PGy}, v_{spRPCx} and v_{spRPCy}, and currents, i_{PGx} and i_{PGy}, for different load conditions: (a) P_{Loadx} = 0.998 MW and P_{Loady} = 6.12 MW; (b) P_{Loadx} = 0.998 MW and P_{Loady} = -3.88 MW; (c) P_{Loadx} = 0.998 MW and P_{Loady} = 4.12 MW; (d) P_{Loadx} = 2.99 MW and P_{Loady} = 0 MW; (e) P_{Loadx} = 2.99 MW and P_{Loady} = 0.99 MW; and (f) P_{Loadx} = 2.00 MW and P_{Loady} = 0.99 MW.

4.4.1 Simulation Result of the sp-RPC based on SST with Dynamic Control

Case Scenario A

This topic focuses on the analysis of the sp-RPC for case scenario A, when the solar PV system and the BESS are disabled, as can be seen in Figure 4.9. In Figure 4.9 (a) it is possible to verify that P_{Loadx} and P_{Loady} initially present different values, causing an unbalance in the active powers P_{PGx} and P_{PGy}. At time instant 0.4 s the proposed control algorithm is activated, being able to verify that P_{PGx} and P_{PGy} converge to an average value of 3.6 MW. At instant 1 s, the locomotive on the *y*-side starts to brake (P_{Loady} < 0), causing a new unbalance between the values of P_{PGx} and P_{PGy}. When the control algorithm updates the reference values for the sp-RPC, it is possible to verify that P_{PGx} and P_{PGy} converge to an average value of -1.4 MW. Finally, at the instant 2 s, the locomotive on the *y*-side start to accelerate (P_{Loady} > 0 W), and P_{PGy} varies again. As soon as the reference values for the sp-RPC are updated, it is possible to verify that the average values of P_{PGx} and P_{PGy} converge to an average value of 2.6 MW.

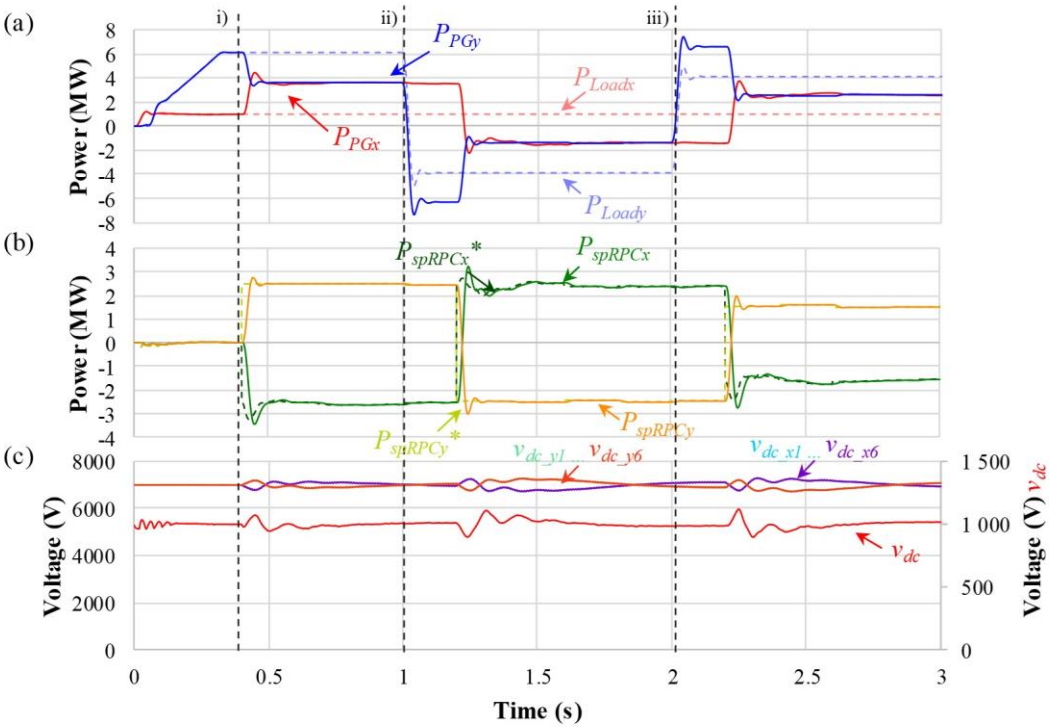

Figure 4.9 – Simulation results of the evolution of active powers and voltages over time, for the real scale sp-RPC during the case scenario A: (a) load active power, P_{Loadx} and P_{Loady}, and TPS active power, P_{PGx} and P_{PGy}; (b) sp-RPC active power, P_{spRPCx} and P_{spRPCy}, as well as the reference values, $P_{spRPCx*}$ and $P_{spRPCy*}$; (c) common dc-link voltage, v_{dc}, and dc-link voltages on each submodule, v_{dc_x1} to v_{dc_x6}, and v_{dc_y1} to v_{dc_y6}.

In Figure 4.9 (b) it is possible to see that the powers P_{spRPCx} and P_{spRPCy} always follow the reference values P_{spRPCx}* and P_{spRPCy}*. Figure 4.9 (c) shows the variation of the dc voltage on the different dc-links over time. Regarding the common dc-link, it is possible to verify that the v_{dc} remains regulated to an

average value of 1 kV. In turn, the remaining dc voltages that compose each submodule, from v_{dc_x1} to v_{dc_x6} and from v_{dc_y1} to v_{dc_y6}, are also regulated to an average value of 7 kV.

Figure 4.10 presents a greater detail of the system operation between the time interval from 0.3 s to 0.6 s. In Figure 4.10 (a) it is possible to verify the voltages of each TPS, v_{PGx} and v_{PGy}, as well as the voltages on each side of the sp-RPC, v_{spRPCx} and v_{spRPCy}. Moreover, it is possible to check the dc-link voltages from v_{dc_x1} to v_{dc_x6} and from v_{dc_y1} to v_{dc_y6}, showing an initial disturbance caused by the start of the operation, but maintaining a constant desired average value of 7 kV. In Figure 4.10 (b) the voltages v_{outx} and v_{outy} are presented, being able to verify the 13 voltage levels generated by the modular power converter based on SST. Nevertheless, it is also possible to see that despite the initial perturbation, v_{dc} remains regulated at a value of 1 kV. Finally, by analyzing Figure 4.10 (c), it is possible to verify that as soon as the sp-RPC starts operating, synthesizing i_{spRPCx} and i_{spRPCy}, it was possible to equalize the amplitudes of the i_{PGx} and i_{PGy}.

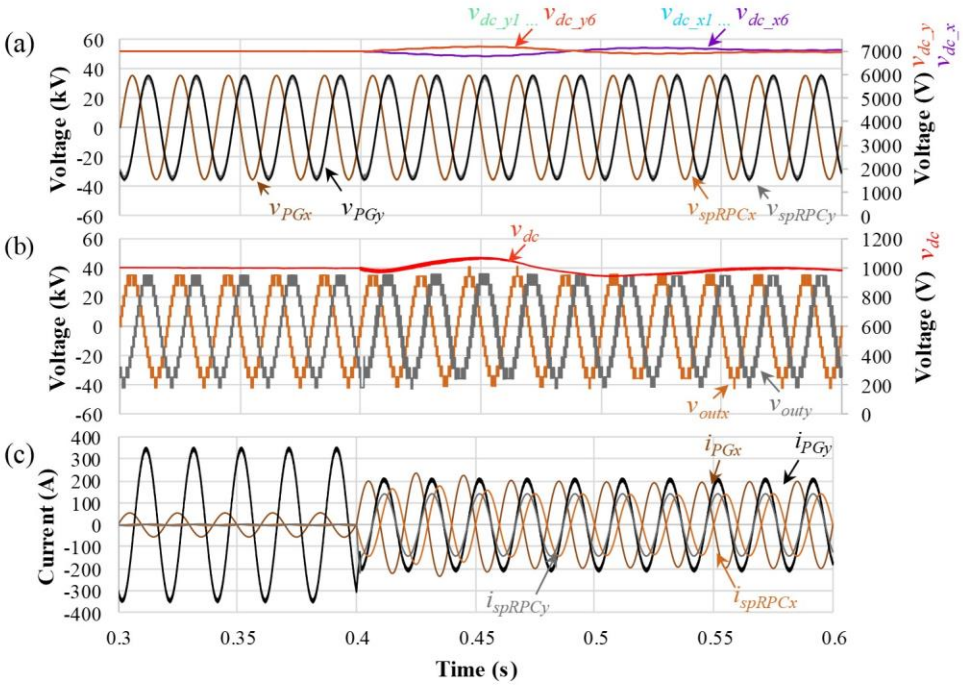

Figure 4.10 – Detailed simulation results, during the time interval from 0.3 s to 0.6 s, for the real scale sp-RPC during the case scenario A: (a) TPS voltages, v_{PGx} and v_{PGy}, the output voltages of the *spRPCx* and *spRPCy*, v_{spRPCx} and v_{spRPCy}, and voltages on the dc-link of each submodule, v_{dc_x1} to v_{dc_x6}, and v_{dc_y1} to v_{dc_y6}; (b) the multilevel voltage of the sp-RPC, v_{outx} and v_{outy}, and the voltage of the common dc-link voltage, v_{dc}; (c) TPS currents, i_{PGx} and i_{PGy}, and the output currents of the sp-RPC, i_{spRPCx} and i_{spRPCy}.

Continuing with the analysis, it is possible to verify in more detail in Figure 4.11 the operation of the system between the time interval from 0.95 s to 1.25 s, representative of event *ii)* of Figure 4.9. Figure 4.11 (a) it is possible to verify the voltages of each TPS, v_{PGx} and v_{PGy}, as well as the voltages on each side of the sp-RPC, v_{spRPCx} and v_{spRPCy}. Moreover, it is possible to see that v_{dc_x6} has an average

value of 7.02 kV, while v_{dc_y6} has an average value of 6.99 kV during this interval. The remaining voltages have similar values of the dc-link on the same side. In Figure 4.11 (b) the voltages v_{outx} and v_{outy} are displayed, as well as it is also possible to see that v_{dc} shows an average value of 1.0 kV during this interval. Finally, by analyzing Figure 4.11 (c), it is possible to verify that until the instant 1 s, the amplitudes of i_{PGx} and i_{PGy} were almost similar, obtaining a maximum amplitude value of 205.5 A and 213.0 A. At this time, i_{spRPCx} has a maximum value of 148.4 A, while i_{spRPCy} has a maximum value of 142.6 A. However, with the locomotive on the *y*-side starting regenerative braking ($P_{Loady} < 0$), the amplitude of i_{PGy} increases to a maximum value of 364.8 A, and a new unbalance appears. At instant 1.2 s, the proposed control algorithm updates the operation reference values, as can be seen with the amplitude change of the i_{spRPCx} and i_{spRPCy}, being able to verify that i_{PGx} and i_{PGy} converge again to similar amplitude values.

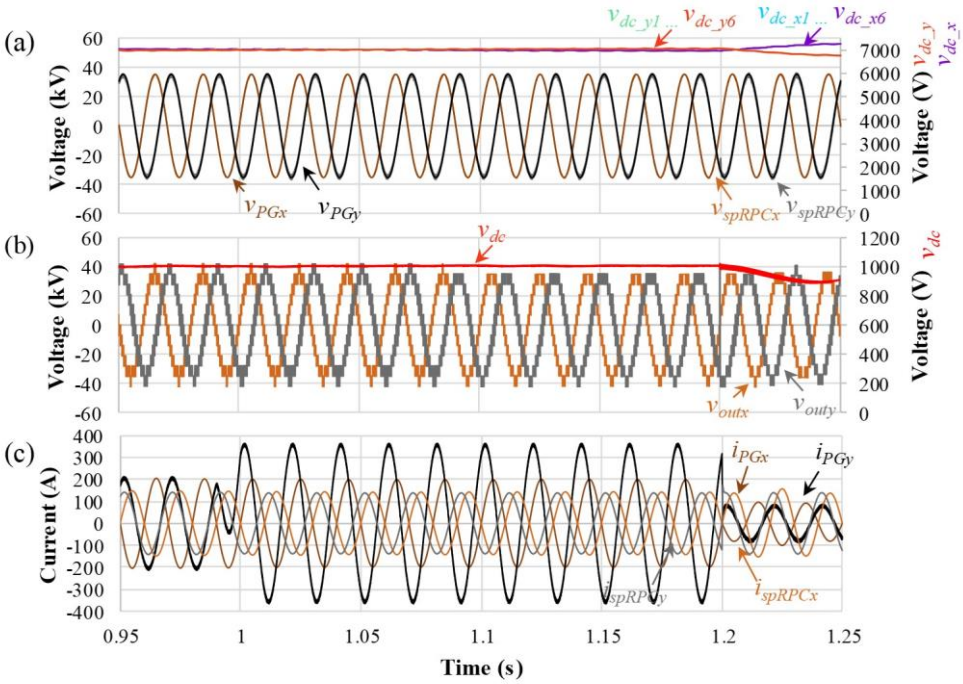

Figure 4.11 – Detailed simulation results, during the time interval from 0.95 s to 1.25 s, for the real scale sp-RPC during the case scenario A: (a) TPS voltages, v_{PGx} and v_{PGy}, the output voltages of the *spRPCx* and *spRPCy*, v_{spRPCx} and v_{spRPCy}, and voltages on the dc-link of each submodule, v_{dc_x1} to v_{dc_x6}, and v_{dc_y1} to v_{dc_y6}; (b) the multilevel voltage of the sp-RPC, v_{outx} and v_{outy}, and the voltage of the common dc-link voltage, v_{dc}; (c) TPS currents, i_{PGx} and i_{PGy}, and the output currents of the sp-RPC, i_{spRPCx} and i_{spRPCy}.

Figure 4.12 shows the simulation results during the time interval from 1.95 s to 2.25 s, representative of event *iii)* of Figure 4.9. Figure 4.12 (a) it is possible to verify the voltages of each TPS, v_{PGx} and v_{PGy}, as well as the voltages on each side of the sp-RPC, v_{spRPCx} and v_{spRPCy}. Moreover, it is possible to see that v_{dc_x6} has an average value of 7.06 kV, while v_{dc_y6} has an average value of 6.94 kV during this interval. The remaining voltages have similar values of the dc-link on the same side. In Figure 4.12 (b) the voltages

v_{outx} and v_{outy} are displayed, as well as it is also possible to see that v_{dc} shows an average value of 0.99 kV during this interval. Finally, by analyzing Figure 4.12 (c), it is possible to verify that until the instant 2 s, the amplitudes of i_{PGx} and i_{PGy} were similar, obtaining a maximum value of 81.15 A and 85.51 A, respectively. At this time, i_{spRPCx} has a maximum value of 137 A, while i_{spRPCy} has a maximum value of 68.61 A. However, with the locomotive on the *y*-side starting to accelerate, varying the $P_{Loadx} > 0$, i_{PGx} increases to a maximum amplitude value of 381 A, and a new unbalance appears. At the time instant 2.1 s, the proposed control algorithm updates the operation reference values, as can be seen with the amplitude change of the i_{spRPCx} and i_{spRPCy}, being able to verify that i_{PGx} and i_{PGy} converge again to similar amplitude values.

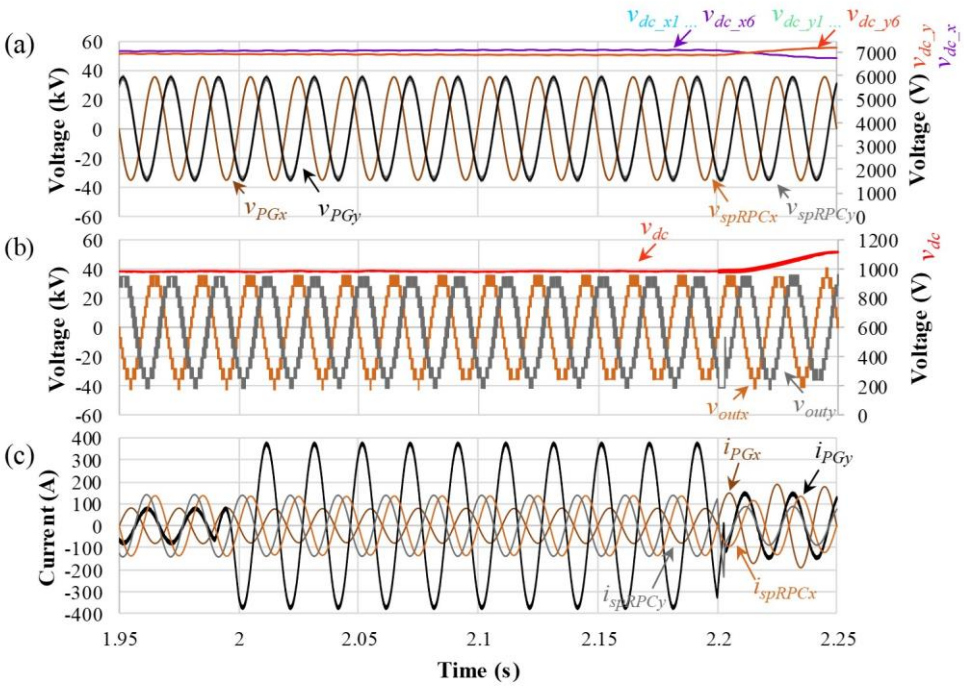

Figure 4.12 – Detailed simulation results, during the time interval from 1.95 s to 2.25 s, for the real scale sp-RPC during the case scenario A: (a) TPS voltages, v_{PGx} and v_{PGy}, the output voltages of the *spRPCx* and *spRPCy*, v_{spRPCx} and v_{spRPCy}, and voltages on the dc-link of each submodule, v_{dc_x1} to v_{dc_x6}, and v_{dc_y1} to v_{dc_y6}; (b) the multilevel voltage of the sp-RPC, v_{outx} and v_{outy}, and the voltage of the common dc-link voltage, v_{dc}; (c) TPS currents, i_{PGx} and i_{PGy}, and the output currents of the sp-RPC, i_{spRPCx} and i_{spRPCy}.

Finally, the final result is presented in Figure 4.13 during the time interval from 2.9 s to 3 s, when the system is in steady-state operation. Figure 4.13 (a) it is possible to verify the voltages of each TPS, v_{PGx} and v_{PGy}, as well as the voltages on each side of the sp-RPC, v_{spRPCx} and v_{spRPCy}. Moreover, it is possible to see that v_{dc_x6} has an average value of 6.95 kV, while v_{dc_y6} has an average value of 7.07 kV during this interval. The remaining voltages have similar values of the dc-link on the same side. In Figure 4.13 (b) the voltages v_{outx} and v_{outy} are displayed, as well as it is also possible to see that v_{dc} shows an average value of 1.02 kV during this interval. Finally, by analyzing Figure 4.13 (c), it is possible to verify that i_{PGx}

and i_{PGy} have a similar amplitude value, obtaining a maximum amplitude of 146.3 A and 155 A, respectively. At this time, i_{spRPCx} has a maximum value of 89.74 A, while i_{spRPCy} has a maximum value of 87.46 A.

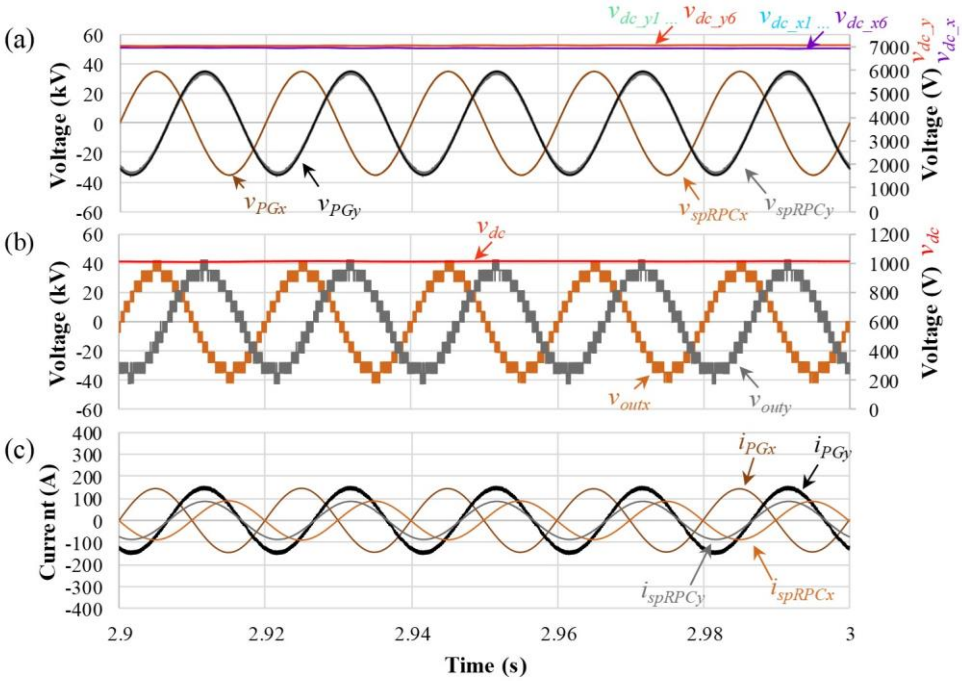

Figure 4.13 – Detailed simulation results, during the time interval from 2.9 s to 3 s, for the real scale sp-RPC during the case scenario A: (a) TPS voltages, v_{PGx} and v_{PGy}, the output voltages of the *spRPCx* and *spRPCy*, v_{spRPCx} and v_{spRPCy}, and voltages on the dc-link of each submodule, v_{dc_x1} to v_{dc_x6}, and v_{dc_y1} to v_{dc_y6}; (b) the multilevel voltage of the sp-RPC, v_{outx} and v_{outy}, and the voltage of the common dc-link voltage, v_{dc}; (c) TPS currents, i_{PGx} and i_{PGy}, and the output currents of the sp-RPC, i_{spRPCx} and i_{spRPCy}.

Case Scenario B

This topic focuses on the analysis of the sp-RPC for case scenario B, when the solar PV system and the BESS are disabled, as can be seen in Figure 4.14. In Figure 4.14 (a) it is possible to verify that P_{Loadx} and P_{Loady} initially present different values, causing an unbalance in the active powers P_{PGx} and P_{PGy}. At 0.4 s the proposed control algorithm is activated, being able to verify that P_{PGx} and P_{PGy} converge to an average value of 1.5 MW. At instant 1 s, an electric locomotive is added to the *y*-side, increasing P_{PGy}. As a consequence, a new unbalance between the values of P_{PGx} and P_{PGy} appears. When the control algorithm updates the reference values for the sp-RPC, it is possible to verify that P_{PGx} and P_{PGy} converge to an average value of 2 MW. Finally, at the instant 2 s, the locomotive on the *x*-side decreases the P_{Loadx} consumption, causing a new unbalance. As soon as the reference values are updated, it is possible to verify that the average values of P_{PGx} and P_{PGy} converge to an average value of 1.5 MW. In Figure 4.14 (b) it is possible to see that the powers P_{spRPCx} and P_{spRPCy} always follow the reference values P_{spRPCx}* and P_{spRPCy}*. Figure 4.14 (c) shows the variation of the dc voltage on the different dc-

links over time. Regarding the common dc-link, it is possible to verify that the v_{dc} remains regulated to an average value of 1 kV. In turn, the remaining dc voltages that compose each submodule, from v_{dc_x1} to v_{dc_x6} and from v_{dc_y1} to v_{dc_y6}, are also regulated to an average value of 7 kV. The detailed performance analysis of the sp-RPC based on SST for case scenario B can be found in Appendix A.

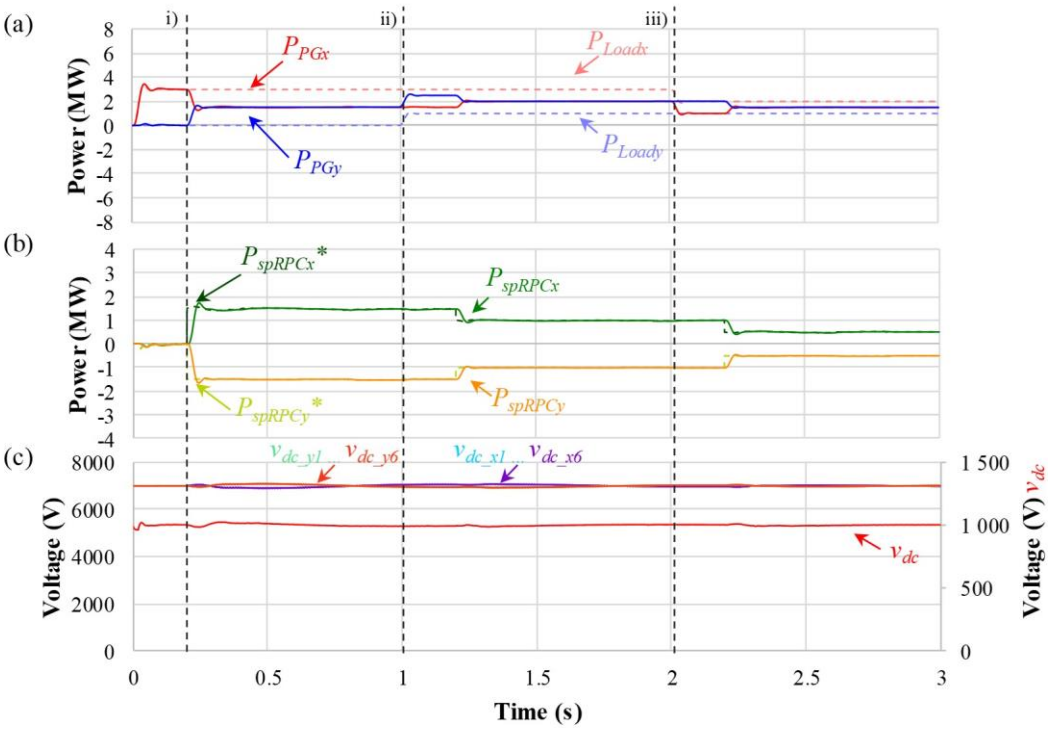

Figure 4.14 – Simulation results of the evolution of active powers and voltages over time, for the real scale sp-RPC during the case scenario B: (a) load active power, P_{Loadx} and P_{Loady}, and TPS active power, P_{PGx} and P_{PGy}; (b) sp-RPC active power, P_{spRPCx} and P_{spRPCy}, as well as the reference values, P_{spRPCx}* and P_{spRPCy}*; (c) common dc-link voltage, v_{dc}, and dc-link voltages on each submodule, v_{dc_x1} to v_{dc_x6}, and v_{dc_y1} to v_{dc_y6}.

4.4.2 Simulation Result of the sp-RPC based on SST and Solar PV System with Dynamic Control

Case Scenario A

This topic focuses on the analysis of the sp-RPC with the solar PV system for case scenario A, as can be seen in Figure 4.15. In Figure 4.15 (a) it is possible to verify that P_{Loadx} and P_{Loady} initially present different values, causing an unbalance in the active powers P_{PGx} and P_{PGy}. At 0.4 s the proposed control algorithm is activated, being able to verify that P_{PGx} converges to an average value of 2.58 MW, while P_{PGy} converges to an average value of 3.63 MW. At instant 1 s, the locomotive on the *y*-side starts to brake (P_{Loady} < 0), causing a new unbalance between the values of P_{PGx} and P_{PGy}. When the control algorithm updates the reference values for the sp-RPC, it is possible to verify that P_{PGx} and P_{PGy} converge to an average value of -2 MW. Finally, at the instant 2 s, the locomotive on the *y*-side start to accelerate

(P_{Loady} > 0 W), and P_{PGy} varies again. As soon as the reference values for the sp-RPC are updated, it is possible to verify that the average values of P_{PGx} and P_{PGy} converge to an average value of 2 MW. In Figure 4.15 (b) it is possible to see that the powers P_{spRPCx} and P_{spRPCy} always follow the reference values P_{spRPCx}* and P_{spRPCy}*. Figure 4.15 (c) shows the evolution of the P_{PV}, keeping a maximum extraction of 1.22 MW over time. Figure 4.15 (d) shows the variation of the dc voltage on the different dc-links over time. Regarding the common dc-link, it is possible to verify that the v_{dc} remains regulated to an average value of 1 kV. In turn, the remaining dc voltages that compose each submodule, from v_{dc_x1} to v_{dc_x6} and from v_{dc_y1} to v_{dc_y6}, are also regulated to an average value of 7 kV. The detailed performance analysis of the sp-RPC based on SST with the solar PV system for case scenario A can be found in Appendix B.

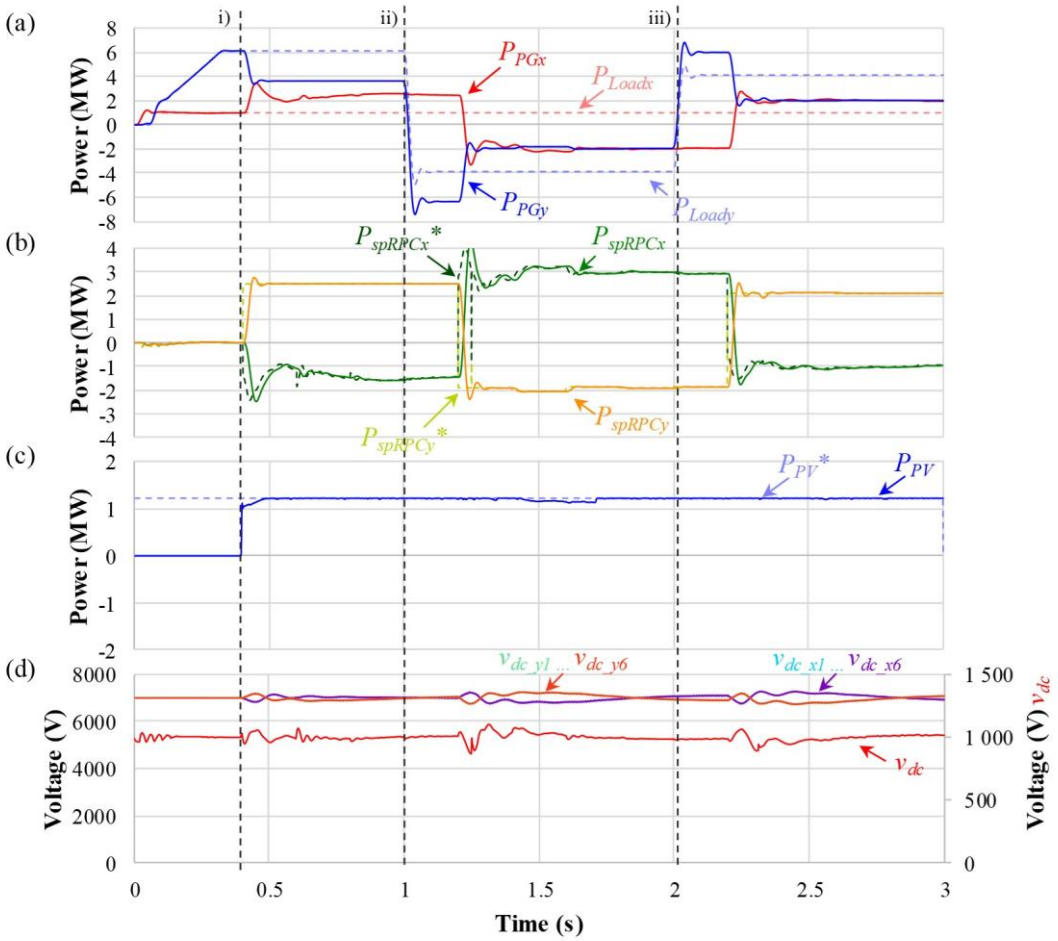

Figure 4.15 – Simulation results of the evolution of active powers and voltages over time, for the real scale sp-RPC with the solar PV system during the case scenario A: (a) load active power, P_{Loadx} and P_{Loady}, and TPS active power, P_{PGx} and P_{PGy}; (b) sp-RPC active powers, P_{spRPCx} and P_{spRPCy}, as well as the reference values, P_{spRPCx}* and P_{spRPCy}*; (c) solar PV system active power and the maximum power value, P_{PV} and P_{PV}*; (d) variation of the common dc-link voltage, v_{dc}, variation of the voltage of the dc-link on each submodule, v_{dc_x1} to v_{dc_x6}, and v_{dc_y1} to v_{dc_y6}.

Case Scenario B

This topic focuses on the analysis of the sp-RPC with the solar PV system for case scenario B, as can be seen in Figure 4.16. In Figure 4.16 (a) it is possible to verify that P_{Loadx} and P_{Loady} initially present different values, causing an unbalance in the active powers P_{PGx} and P_{PGy}. At 0.4 s the proposed control algorithm is activated, being able to verify that P_{PGx} and P_{PGy} converge to an average value of 1 MW. At instant 1 s, an electric locomotive is added to the *y*-side, increasing P_{PGy}. As a consequence, a new unbalance between the values of P_{PGx} and P_{PGy} appears. When the control algorithm updates the reference values for the sp-RPC, it is possible to verify that P_{PGx} and P_{PGy} converge to similar values, presenting an average value of 1.4 MW. Finally, at the instant 2 s, the locomotive on the *x*-side decreases the P_{Loadx} consumption, causing a new unbalance. As soon as the reference values are updated, it is possible to verify that the average values of P_{PGx} and P_{PGy} converge again, presenting an average value of 0.9 MW.

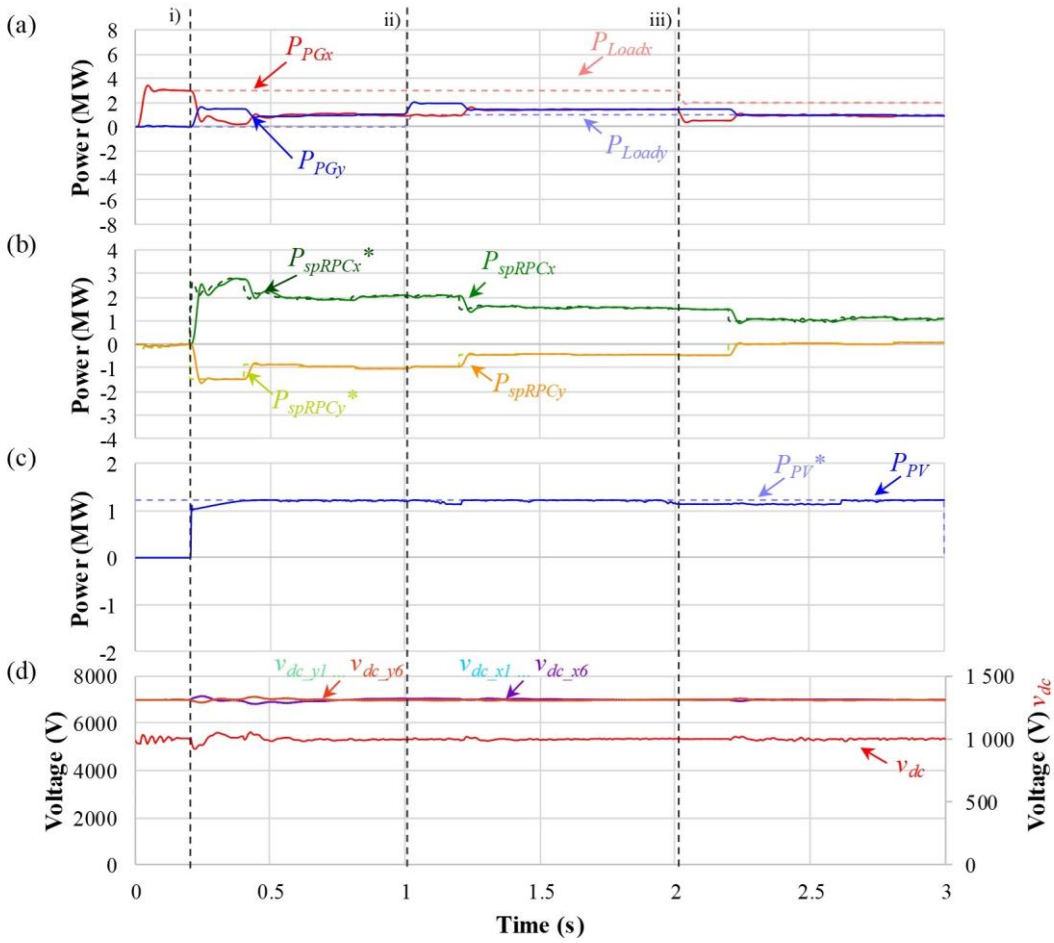

Figure 4.16 – Simulation results of the evolution of active powers and voltages over time, for the real scale sp-RPC with the solar PV system during the case scenario B: (a) load active power, P_{Loadx} and P_{Loady}, and TPS active power, P_{PGx} and P_{PGy}; (b) sp-RPC active powers, P_{spRPCx} and P_{spRPCy}, as well as the reference values, P_{spRPCx}* and P_{spRPCy}*; (c) solar PV system active power and the maximum power value, P_{PV} and P_{PV}*; (d) variation of the common dc-link voltage, v_{dc}, variation of the voltage of the dc-link on each submodule, v_{dc_x1} to v_{dc_x6}, and v_{dc_y1} to v_{dc_y6}.

In Figure 4.16 (b) it is possible to see that the powers P_{spRPCx} and P_{spRPCy} always follow the reference values P_{spRPCx}* and P_{spRPCy}*. Figure 4.16 (c) shows the evolution of the P_{PV}, keeping a maximum extraction of 1.22 MW over time. Figure 4.16 (d) shows the variation of the dc voltage on the different dc-links over time. Regarding the common dc-link, it is possible to verify that the v_{dc} remains regulated to an average value of 1 kV. In turn, the remaining dc voltages that compose each submodule, from v_{dc_x1} to v_{dc_x6} and from v_{dc_y1} to v_{dc_y6}, are also regulated to an average value of 7 kV. The detailed performance analysis of the sp-RPC based on SST with the solar PV system for case scenario B can be found in Appendix B.

4.4.3 Simulation Result of the sp-RPC based on SST and BESS with Dynamic Control

Case Scenario A

This topic focuses on the analysis of the sp-RPC with the BESS for case scenario A, as can be seen in Figure 4.17. In Figure 4.17 (a) it is possible to verify that P_{Loadx} and P_{Loady} initially present different values, causing an unbalance in the active powers P_{PGx} and P_{PGy}. At 0.4 s the proposed control algorithm is activated, being able to verify that P_{PGx} converges to an average value of 2.79 MW, while P_{PGy} converges to an average value of 3.63 MW, during the time that the BESS is discharging. At instant 1 s, the locomotive on the *y*-side starts to brake (P_{Loady} < 0), causing a new unbalance between the values of P_{PGx} and P_{PGy}. When the control algorithm updates the reference values for the sp-RPC, it is possible to verify that P_{PGx} and P_{PGy} present an average value of -0.61 MW and -1.36 MW, respectively, during the time that the BESS is charging. Finally, at the instant 2 s, the locomotive on the *y*-side start to accelerate (P_{Loady} > 0 W), and P_{PGy} varies again. As soon as the reference values for the sp-RPC are updated, it is possible to verify that the average values of P_{PGx} and P_{PGy} converge again, presenting an average value of 2.43 MW and 1.9 MW, during the time that the BESS is charging. In Figure 4.17 (b) it is possible to see that the powers P_{spRPCx} and P_{spRPCy} always follow the reference values P_{spRPCx}* and P_{spRPCy}*. Figure 4.17 (c) shows the evolution of the P_{BESS}, being able to identify the instants in which the BESS are fully loaded or unloaded. Figure 4.17 (d) shows the variation of the dc voltage on the different dc-links over time. Regarding the common dc-link, it is possible to verify that the v_{dc} remains regulated to an average value of 1 kV. In turn, the remaining dc voltages that compose each submodule, from v_{dc_x1} to v_{dc_x6} and from v_{dc_y1} to v_{dc_y6}, are also regulated to an average value of 7 kV. The detailed performance analysis of the sp-RPC based on SST with the BESS for case scenario A can be found in Appendix C.

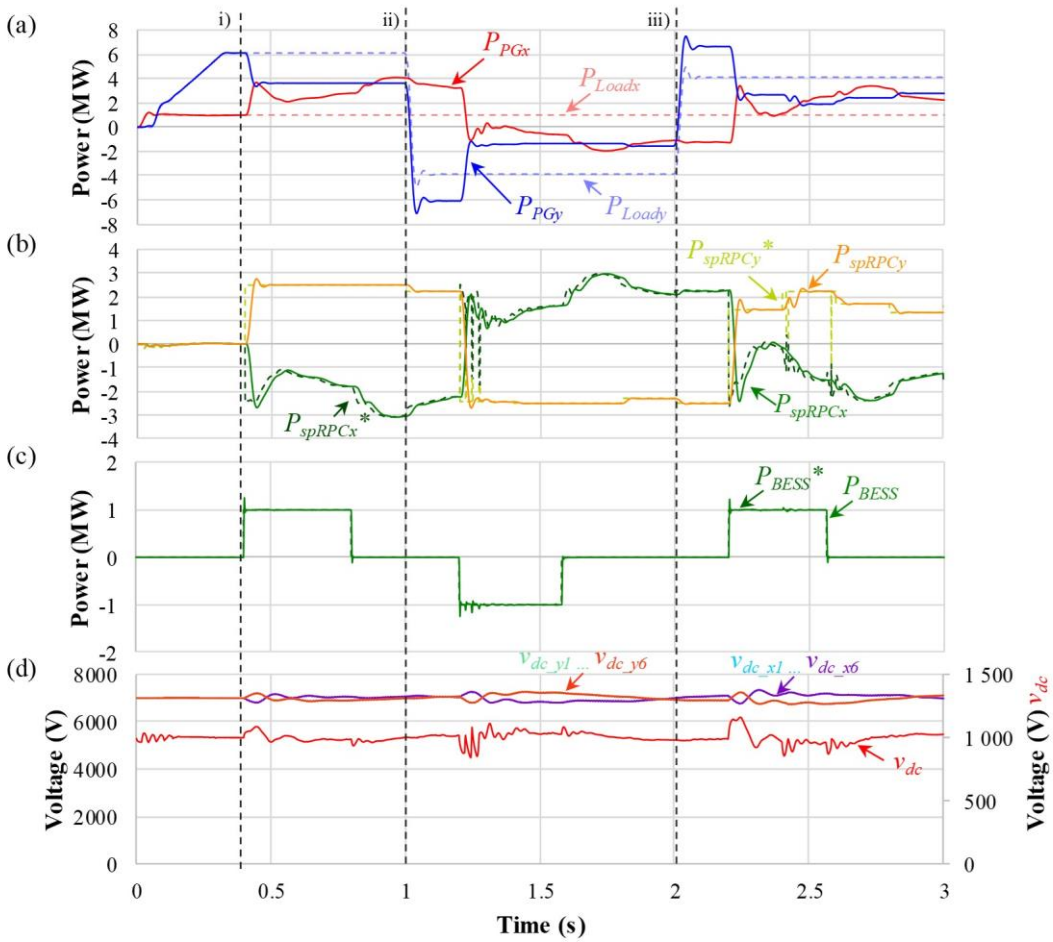

Figure 4.17 – Simulation results of the evolution of active powers and voltages over time, for the real scale sp-RPC with the BESS during the case scenario A: (a) load active power, P_{Loadx} and P_{Loady}, and TPS active power, P_{PGx} and P_{PGy}; (b) sp-RPC active powers, P_{spRPCx} and P_{spRPCy}, as well as the reference values, P_{spRPCx}* and P_{spRPCy}*; (c) BESS active power and references value, P_{BESS} and P_{BESS}*; (d) variation of the common dc-link voltage, v_{dc}, variation of the voltage of the dc-link on each submodule, v_{dc_x1} to v_{dc_x6}, and v_{dc_y1} to v_{dc_y6}.

Case Scenario B

This topic focuses on the analysis of the sp-RPC with the BESS for case scenario B, as can be seen in Figure 4.18. In Figure 4.18 (a) it is possible to verify that P_{Loadx} and P_{Loady} initially present different values, causing an unbalance in the active powers P_{PGx} and P_{PGy}. At 0.4 s the proposed control algorithm is activated, being able to verify that P_{PGx} and P_{PGy} converge to an average value of 1.11 MW. At instant 1 s, an electric locomotive is added to the *y*-side, increasing P_{PGy}. As a consequence, a new unbalance between the values of P_{PGx} and P_{PGy} appears. When the control algorithm updates the reference values for the sp-RPC, it is possible to verify that P_{PGx} and P_{PGy} converge to an average of 1.55 MW. Finally, at the instant 3 s, the locomotive on the *x*-side decreases the P_{Loadx} consumption, causing a new unbalance. As soon as the reference values are updated, it is possible to verify that the average values of P_{PGx} and P_{PGy} converge to an average value of 1 MW. In Figure 4.18 (b) it is possible to see that the powers P_{spRPCx} and P_{spRPCy} always follow the reference values P_{spRPCx}* and P_{spRPCy}*. Figure 4.18 (c) shows

the evolution of the P_{BESS}, keeping an average value of 1 MW over time. Figure 4.18 (d) shows the variation of the dc voltage on the different dc-links over time. Regarding the common dc-link, it is possible to verify that the v_{dc} remains regulated to an average value of 1 kV. In turn, the remaining dc voltages that compose each submodule, from v_{dc_x1} to v_{dc_x6} and from v_{dc_y1} to v_{dc_y6}, are also regulated to an average value of 7 kV. The detailed performance analysis of the sp-RPC based on SST with the BESS for case scenario B can be found in Appendix C.

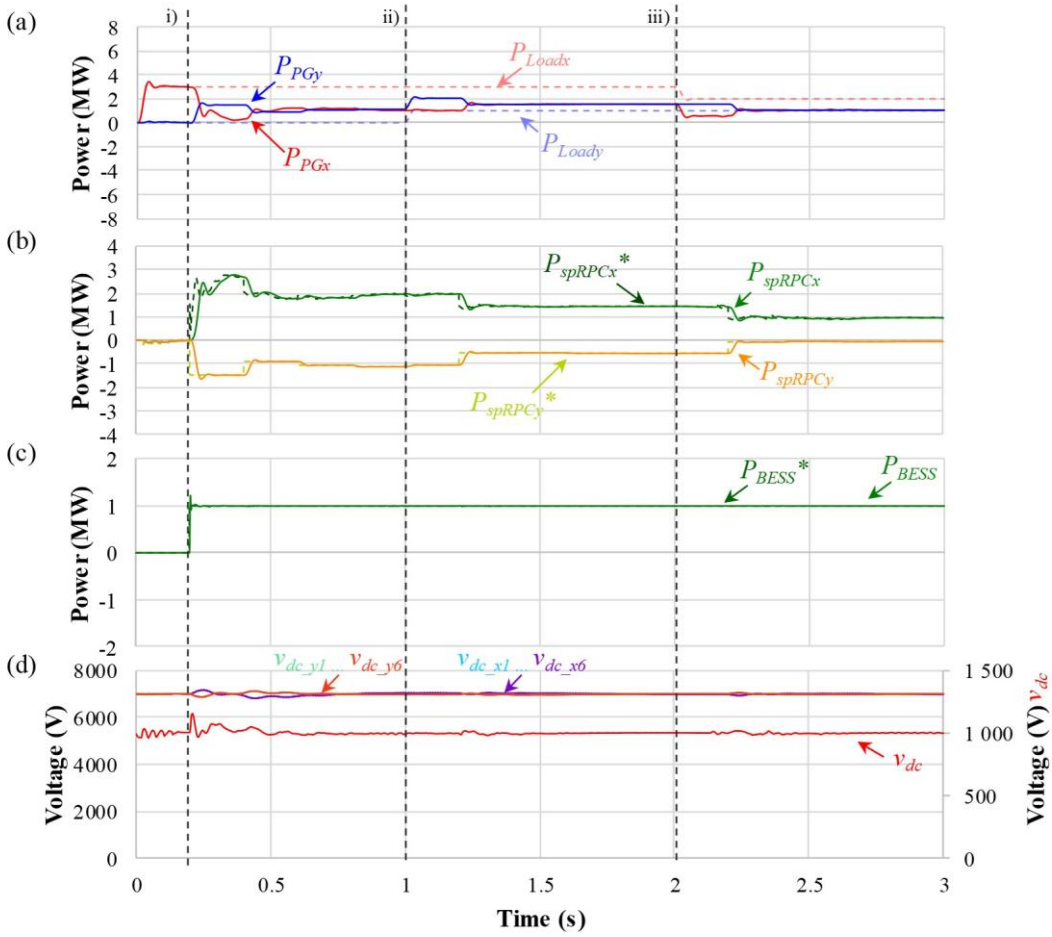

Figure 4.18 – Simulation results of the evolution of active powers and voltages over time, for the real scale sp-RPC with the BESS during the case scenario A: (a) load active power, P_{Loadx} and P_{Loady}, and TPS active power, P_{PGx} and P_{PGy}; (b) sp-RPC active powers, P_{spRPCx} and P_{spRPCy}, as well as the reference values, P_{spRPCx}* and P_{spRPCy}*; (c) BESS active power and references value, P_{BESS} and P_{BESS}*; (d) variation of the common dc-link voltage, v_{dc}, variation of the voltage of the dc-link on each submodule, v_{dc_x1} to v_{dc_x6}, and v_{dc_y1} to v_{dc_y6}.

4.4.4 Simulation Result of the sp-RPC based on SST with Solar PV System and BESS with Dynamic Control

Case Scenario A

This topic focuses on the analysis of the sp-RPC with the solar PV system and BESS for case scenario A, as can be seen in Figure 4.19. In Figure 4.19 (a) it is possible to verify that P_{Loadx} and P_{Loady} initially

present different values, causing an unbalance in the active powers P_{PGx} and P_{PGy}. At 0.4 s the proposed control algorithm is activated, being able to verify that P_{PGx} converges to an average value of 1.68 MW, while P_{PGy} converges to an average value of 3.63 MW, during the time that the BESS is discharging. At instant 1 s, the locomotive on the *y*-side starts to brake (P_{Loady} < 0), causing a new unbalance between the values of P_{PGx} and P_{PGy}. When the control algorithm updates the reference values for the sp-RPC, it is possible to verify that P_{PGx} and P_{PGy} present an average value of -1.27 MW and -1.36 MW, respectively, during the time that the BESS is charging. Finally, at the instant 2 s, the locomotive on the *y*-side start to accelerate (P_{Loady} > 0 W), and P_{PGy} varies again. As soon as the reference values for the sp-RPC are updated, it is possible to verify that the average values of P_{PGx} and P_{PGy} converge again, presenting an average value of 1.92 MW and 1.62 MW, during the time that the BESS is charging.

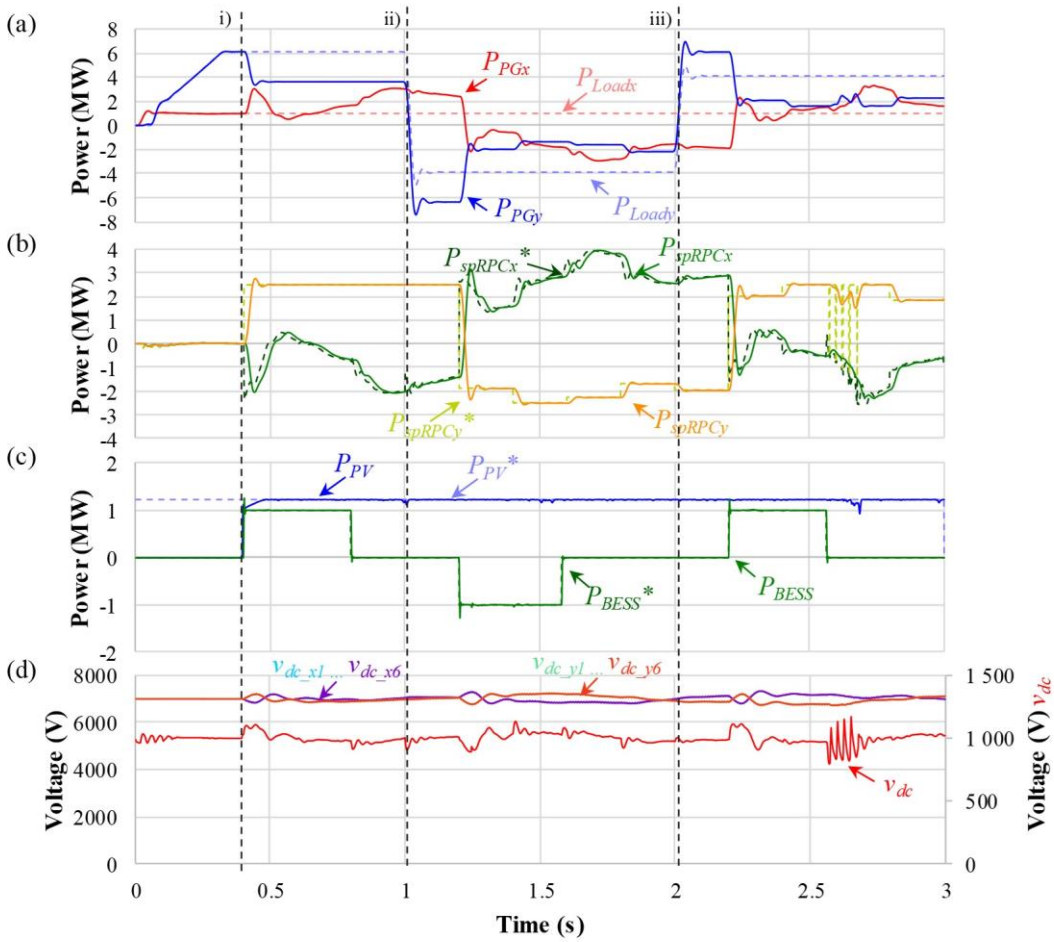

Figure 4.19 – Simulation results of the evolution of active powers and voltages over time, for the real scale sp-RPC with the solar PV system and BESS during the case scenario A: (a) load active power, P_{Loadx} and P_{Loady}, and TPS active power, P_{PGx} and P_{PGy}; (b) sp-RPC active powers, P_{spRPCx} and P_{spRPCy}, as well as the reference values, P_{spRPCx}* and P_{spRPCy}*; (c) solar PV system, the BESS active powers and references value for the BESS, P_{PV}, P_{BESS} and P_{BESS}*; (d) variation of the common dc-link voltage, v_{dc}, variation of the voltage of the dc-link on each submodule, v_{dc_x1} to v_{dc_x6}, and v_{dc_y1} to v_{dc_y6}.

In Figure 4.19 (b) it is possible to see that the powers P_{spRPCx} and P_{spRPCy} always follow the reference values P_{spRPCx}* and P_{spRPCy}*. Figure 4.19 (c) shows the evolution of the P_{PV}, keeping a maximum

extraction of 1.22 MW over time. Regarding the BESS; it is also possible to identify the instants in which are fully charged or discharged. Figure 4.19 (d) shows the variation of the dc voltage on the different dc-links over time. Regarding the common dc-link, it is possible to verify that the v_{dc} remains regulated to an average value of 1 kV. In turn, the remaining dc voltages that compose each submodule, from v_{dc_x1} to v_{dc_x6} and from v_{dc_y1} to v_{dc_y6}, are also regulated to an average value of 7 kV. The detailed performance analysis of the sp-RPC based on SST with the solar PV system and BESS for the case scenario A can be found in Appendix D.

Case Scenario B

This topic focuses on the analysis of the sp-RPC with the solar PV system and BESS for case scenario B, as can be seen in Figure 4.20. In Figure 4.20 (a) it is possible to verify that P_{Loadx} and P_{Loady} initially present different values, causing an unbalance in the active powers P_{PGx} and P_{PGy}. At 0.4 s the proposed control algorithm is activated, being able to verify that P_{PGx} converges to an average value of 0.3 MW, while P_{PGy} converges to a value average of 0.78 MW. At instant 1 s there is a disturbance in the system, being able to verify that there is a new unbalance between the values of P_{PGx} and P_{PGy}. When the control algorithm updates the reference values for the sp-RPC, it is possible to verify that P_{PGx} and P_{PGy} converge to an average value of 0.99 MW. Finally, at the instant 3 s, P_{Loady} varies again and, as soon as the reference values are updated, it is possible to verify that the average values of P_{PGx} and P_{PGy} converge to an average value of 0.6 MW. In Figure 4.20 (b) it is possible to see that the powers P_{spRPCx} and P_{spRPCy} always follow the reference values P_{spRPCx}* and P_{spRPCy}*. Figure 4.20 (c) shows the evolution of the P_{PV}, keeping a maximum extraction of 1.22 MW over time. Regarding the BESS; it is possible to verify the evolution of P_{BESS} over time, providing only the necessary power to minimize the average active power between P_{PGx} and P_{PGy}. Figure 4.20 (d) shows the variation of the dc voltage on the different dc-links over time. Regarding the common dc-link, it is possible to verify that the v_{dc} remains regulated to an average value of 1 kV. In turn, the remaining dc voltages that compose each submodule, from v_{dc_x1} to v_{dc_x6} and from v_{dc_y1} to v_{dc_y6}, are also regulated to an average value of 7 kV. The detailed performance analysis of the sp-RPC based on SST with the solar PV system and BESS for case scenario B can be found in Appendix D.

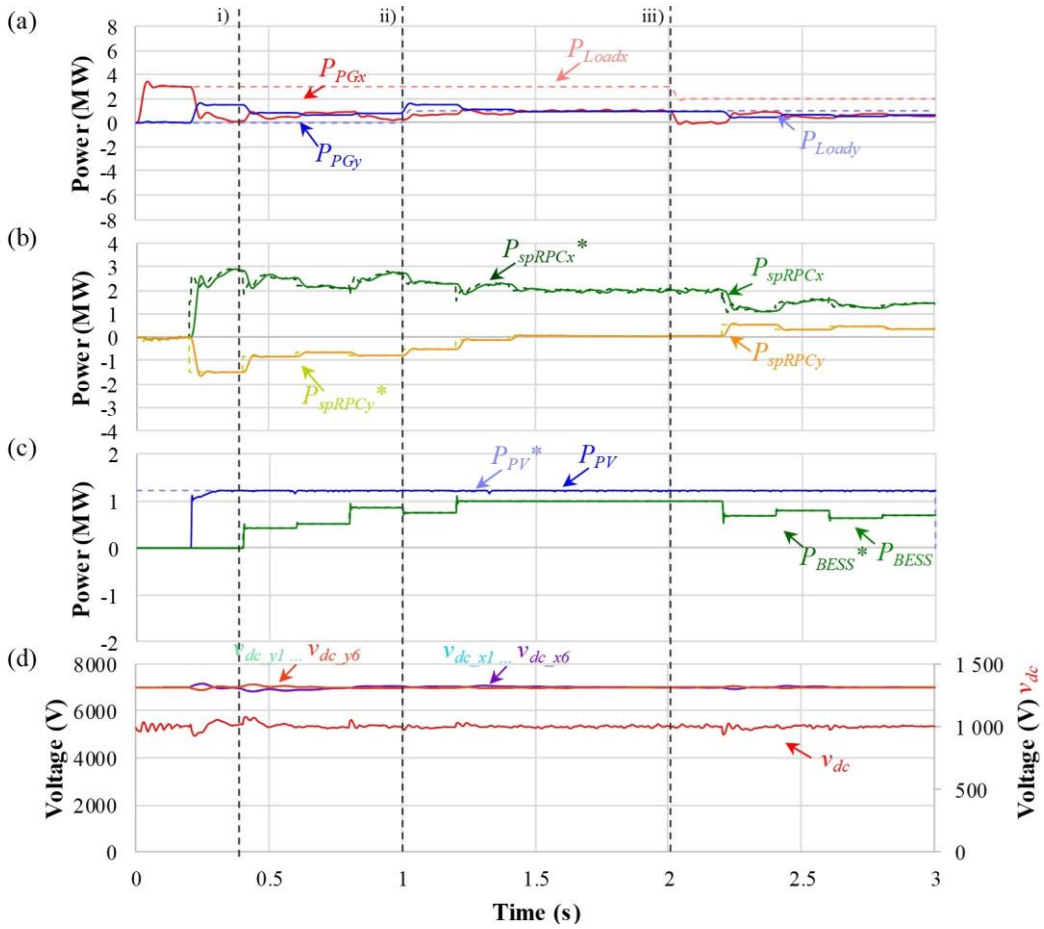

Figure 4.20 – Simulation results of the evolution of active powers and voltages over time, for the real scale sp-RPC with the solar PV system and BESS during the case scenario B: (a) load active power, P_{Loadx} and P_{Loady}, and TPS active power, P_{PGx} and P_{PGy}; (b) sp-RPC active powers, P_{spRPCx} and P_{spRPCy}, as well as the reference values, P_{spRPCx}* and P_{spRPCy}*; (c) solar PV system, the BESS active powers and references value for the BESS, P_{PV}, P_{BESS} and P_{BESS}*; (d) variation of the common dc-link voltage, v_{dc}, variation of the voltage of the dc-link on each submodule, v_{dc_x1} to v_{dc_x6}, and v_{dc_y1} to v_{dc_y6}.

4.4.5 Performance Analyses of the sp-RPC Based on Simulation Results

This topic serves as a critical analysis and discussion of the simulation results obtained, presenting quantitative data on the performance of the real-scale, developed, simulation model. These data essentially portray the ability to balance the active power in each TPS.

For the quantitative analysis, it is necessary to implement a methodology, quantifies the percentage value of active power unbalance in operation in each TPS. Thus, the values before and after the activation of the implemented control algorithms were measured. With the aid of the methodology implemented in [243], it was possible to quantify the performance of the sp-RPC. The quantitative analysis is based on equation (4.7). Initially, the maximum absolute value of the difference between P_{PG} and P_{avg} is determined, where P_{PG} represents the operating power of one side of the TPS, either side *x*-side or *y*-side, and P_{avg} represents the average value of the operating power of the two TPS. The maximum value

determined is then divided by P_{avg} to determine the unbalance. Multiplying the result by 100, it is possible to obtain the percentage value of the unbalance.

$$Imbalance_{\%} = \frac{\left|P_{PG} - P_{avg}\right|_{Max}}{P_{avg}} \times 100 \text{ [in \%]} \tag{4.7}$$

Table 4.3 shows the average values of the operating powers of each TPS for different initial load conditions (with the sp-RPC disconnected). The average active power between the two TPS when the sp-RPC is disabled, P_{PG_off}, is also shown. Analyzing the data, it is possible to verify that the greater the difference in the value of the connected load, the greater the unbalance caused by each TPS, as expected. Nevertheless, to mention that the system unbalance varies from values of 33.3 % to 169.3 %.

Table 4.3 – Average values of the operating powers and unbalanced values for different load conditions when the sp-RPC is disabled.

Figure	P_{Loadx}	P_{Loady}	P_{PV}	P_{BESS}	P_{PGx}	P_{PGy}	P_{PG_off}	Unbalance
	kW	kW	kW	kW	kW	kW	kW	%
Figure 4.8 (a)	998	6119	0	0	999	6119	3559	71.9
Figure 4.8 (b)	998	-3884	0	0	999	-3884	-1442	169.3
Figure 4.8 (c)	998	4122	0	0	999	4122	2560	61.0
Figure 4.8 (d)	2990	0	0	0	2990	0	1495	100
Figure 4.8 (e)	2990	998	0	0	2990	999	1994	49.9
Figure 4.8 (f)	2000	998	0	0	1996	999	1497	33.3

Analyzing the remaining electrical quantities of the system, under the same operating conditions, it is possible to verify that the side with the highest load also causes a voltage drop. This phenomenon can be verified by analyzing Table 4.4, concluding that the greater the load, the greater the voltage drop at the connection point of sp-RPC, v_{spRPCx} and v_{spRPCy}. Additionally, to highlight the existing unbalance in the current values of the i_{PGx} and i_{PGy}.

Table 4.4 – Currents and voltages rms values for different load conditions when the sp-RPC is disabled.

P_{Loadx}	P_{Loady}	P_{PV}	P_{BESS}	i_{PGx}	i_{PGy}	i_{spRPCx}	i_{spRPCy}	v_{PGx}	v_{PGy}	v_{spRPCx}	v_{spRPCy}
kW	kW	kW	kW	rms (A)	rms (A)	rms (A)	rms (A)	rms (V)	rms (V)	rms (V)	rms (V)
998	6119	0	0	39.97	245.8	-	-	24992	24982	24982	24940
998	-3884	0	0	39.97	155	-	-	24992	25018	24982	25081
998	4122	0	0	39.97	165.4	-	-	24994	24985	24984	24968
2990	0			119.8	0	-	-	24984	25002	24954	25002
2990	998	0	0	119.8	399.8	-	-	24984	24998	24954	24988
2000	998	0	0	79.9	399.8	-	-	24990	24997	24970	24987

Table 4.5 shows the values obtained from the active powers when the sp-RPC is enabled (being the solar PV system and BESS disabled). Analyzing the obtained data, it is possible to conclude that the proposed algorithm manages to mitigate the initial unbalance, decreasing to values below 1.86 % in the existing operating conditions. Nevertheless, it was possible to verify that with the start of the operation of the sp-RPC, the average value of the active power between the two TPS increased, P_{PG_on}. That is, and for the

case P_{Loadx} = 2 MW and P_{Loady} = 998 kW initially the average value of the two TPS with the sp-RPC disabled, P_{PG_off}, was 1497 kW, changing to 1501 kW when the sp-RPC was enabled, P_{PG_on}. The inclusion of sp-RPC reflected an increase of 0.2 %, $P_{PG_\%inc}$, in the active power of the two TPS. The same phenomenon occurs in the remaining operating conditions

Table 4.5 – Average values of the operating powers and unbalanced values for different load conditions when the sp-RPC is enabled (solar PV system and BESS are disabled).

P_{Loadx}	P_{Loady}	P_{PV}	P_{BESS}	P_{PGx}	P_{PGy}	P_{spRPCx}	P_{spRPCy}	P_{PG_on}	$P_{PG_\%inc}$	Unbalance
kW	kW	kW	kW	kW	kW	kW	kW	kW	%	%
998	6119	0	0	3612	3626	-2608	2507	3619.3	1.7	0.19
998	-3884	0	0	-1419	-1367	2424	2507	-1393	-3.4	1.86
998	4122	0	0	2565	2565	-1564	1534	2565	0.2	0
2990	0	0	0	1513	1521	1484	-1520	1517	1.5	0.29
2990	998	0	0	2003	2013	993	-1014	2008	0.7	0.25
2000	998	0	0	1496	1506	502	-506	1501	0.2	0.33

Regarding the voltage and current values, presented in Table 4.6, it was possible to verify that in the side where the sp-RPC injects energy, the voltage at the coupling point, v_{spRPCx} and v_{spRPCy}, increases slightly. On the other hand, on the side with the highest load coupled, the voltage drop is minimized. Nevertheless, to highlight the balancing capability of the sp-RPC, imposing similar i_{PGx} and i_{PGy} rms values.

Table 4.6 – Currents and voltages rms values for different load conditions when the sp-RPC is enabled (solar PV system and BESS are disabled).

P_{Loadx}	P_{Loady}	P_{PV}	P_{BESS}	i_{PGx}	i_{PGy}	i_{spRPCx}	i_{spRPCy}	v_{PGx}	v_{PGy}	v_{spRPCx}	v_{spRPCy}
kW	kW	kW	kW	rms (A)	rms (A)	rms (A)	rms (A)	rms (V)	rms (V)	rms (V)	rms (V)
998	6119	0	0	144	143	105	100	24983	24990	24923	25013
998	-3884	0	0	56.9	63.5	97.0	100	25004	25005	25043	25014
998	4122	0	0	102	104	62.4	61.4	24987	24992	24950	25000
2990	0	0	0	60.6	60.9	59.3	60.9	24991	24996	24992	24966
2990	998	0	0	80.1	80.6	39.8	40.6	24990	24993	24981	24966
2000	998	0	0	59.9	60.3	20.2	20.4	24992	24995	24985	24978

Table 4.7 shows the active power values obtained when the sp-RPC is in operation together with the solar PV system (BESS is disabled). Analyzing the obtained data, it is possible to conclude that the proposed algorithm manages to mitigate the initially existing unbalance, decreasing to values below 16.8 % in the existing operating conditions. Nevertheless, it was possible to verify that with the sp-RPC operating with the solar PV system, the average value of the power between the two TPS decreased. For example, for the case P_{Loadx} = 2 MW and P_{Loady} = 998 kW, initially the average value of the two TPS with the sp-RPC disabled, P_{PG_off}, was 1497 kW, changing to 918 kW when the sp-RPC was enabled, P_{PG_on}. The operation of the sp-RPC with the solar PV system, with P_{PV} = 1228 kW, reflected a decrease of -35.2 %, $P_{PG_\%inc}$, in the average operating power of the two TPS. Moreover, it is noticeable that if the P_{PV} increases, the dependence on the TPS would decrease, so that the power converter losses would be

compensated locally, with the excess of energy being injected into the catenary. Thus, reducing the average value of the power of the two TPS.

Table 4.7 – Average values of the operating powers and unbalanced values for different load conditions when the sp-RPC and the solar PV system are enabled (BESS is disabled).

P_{Loadx}	P_{Loady}	P_{PV}	P_{BESS}	P_{PGx}	P_{PGy}	P_{spRPCx}	P_{spRPCy}	P_{PG_on}	$P_{PG_\%inc}$	Unbalance
kW	kW	kW	kW	kW	kW	kW	kW	kW	%	%
998	6119	1224	0	2584	3630	-1582	2507	3107	-12.7	16.8
998	-3884	1224	0	-1990	-1954	2997	-1917	-1972	36.7	0.90
998	4122	1227	0	1971	2021	-972	2102	1996	-22	1.25
2990	0	1221	0	934	1031	2060	-1029	982	-34.3	4.94
2990	998	1211	0	1447	1433	1548	-433	1440	-27.8	0.47
2000	998	1228	0	917	919	1081	809	918	-38.7	0.1

Regarding the voltage and current values, presented in Table 4.8, it was possible to verify that on the side where the sp-RPC injects energy, the voltage at the coupling point increases slightly. On the other hand, on the side with the highest load coupled, the voltage drop is minimized. Nevertheless, to highlight the balancing capability of the sp-RPC, imposing similar i_{PGx} and i_{PGy} rms values, and with the aid of the solar PV system was possible to decrease rms values in each TPS.

Table 4.8 – Currents and voltages rms values for different load conditions when the sp-RPC and the solar PV system are enabled (BESS is disabled).

P_{Loadx}	P_{Loady}	P_{PV}	P_{BESS}	i_{PGx}	i_{PGy}	i_{spRPCx}	i_{spRPCy}	v_{PGx}	v_{PGy}	v_{spRPCx}	v_{spRPCy}
kW	kW	kW	kW	rms (A)	rms (A)	rms (A)	rms (A)	rms (V)	rms (V)	rms (V)	rms (V)
998	6119	1224	0	104	146	63.6	100	24987	24988	24948	25000
998	-3884	1224	0	79.5	81.2	120	76.7	25006	25007	25059	25026
998	4122	1227	0	78.4	81.0	38.5	84.2	24990	24993	24966	25007
2990	0	1221	0	37.1	41.3	82.9	41.3	24994	24997	25004	24982
2990	998	1211	0	58.1	57.4	61.9	17.5	24991	24996	24994	24978
2000	998	1228	0	36.7	36.8	43.4	39.3	24994	24998	24999	24992

Table 4.9 shows the active power values obtained when the sp-RPC is in operation together with the BESS (with the solar PV system disabled). Analyzing the obtained data, it is possible to conclude that the proposed algorithm manages to mitigate the initial unbalances, decreasing to values below 54.8 % in the existing operating conditions. Nevertheless, it was possible to verify that with the entry into operation of the sp-RPC, the average value of the power between the two TPS decreased in general. That is, exemplifying for the case P_{Loadx} = 2 MW and P_{Loady} = 998 kW, initially, the average value of the two TPS with the sp-RPC disabled, P_{PG_off}, was 1497 kW, changing to 1043 kW when the sp-RPC was enabled, P_{PG_on}. The operation of the sp-RPC together with the BESS, with P_{BESS} = 1000 kW, reflected a decrease of -30.3 %, $P_{PG_\%inc}$, in the average operating power of the two TPS.

Table 4.9 – Average values of the operating powers and unbalanced values for different load conditions when the sp-RPC and the BESS are enabled (solar PV system is disabled).

P_{Loadx}	P_{Loady}	P_{PV}	P_{BESS}	P_{PGx}	P_{PGy}	P_{spRPCx}	P_{spRPCy}	P_{PG_on}	$P_{PG_\%inc}$	Unbalance
kW	kW	kW	kW	kW	kW	kW	kW	kW	%	%
998	6119	0	1000	2627	3629	-1927	2506	3128	-12.1	16
998	-3884	0	-1000	-397	-1359	1398	-2519	-878	-39.1	54.8
998	4122	0	1000	2133	2104	-1133	2050	2118	-17.3	0.69
2990	0		1000	1110	1111	1885	-1108	1110	-25.7	0.06
2990	998	0	1000	1545	1554	1450	-553	1549	-22.3	0.3
2000	998	0	1000	1037	1049	1037	1049	1043	-30.3	0.62

Regarding the voltage and current values, presented in Table 4.10, it was possible to verify that on the side where the sp-RPC injects energy, the voltage at the coupling point increases slightly. On the other hand, on the side with the highest load coupled, the voltage drop is minimized. Nevertheless, to highlight the balancing capability of the sp-RPC, imposing similar i_{PGx} and i_{PGy} rms values, and with the aid of the BESS was also possible to decrease rms values in each TPS.

Table 4.10 – Currents and voltages rms values for different load conditions when the sp-RPC and the BESS are enabled (solar PV system is disabled).

P_{Loadx}	P_{Loady}	P_{PV}	P_{BESS}	i_{PGx}	i_{PGy}	i_{spRPCx}	i_{spRPCy}	v_{PGx}	v_{PGy}	v_{spRPCx}	v_{spRPCy}
kW	kW	kW	kW	rms (A)	rms (A)	rms (A)	rms (A)	rms (V)	rms (V)	rms (V)	rms (V)
998	6119	0	1000	105	145	65.3	100	24988	24987	24948	24992
998	-3884	0	-1000	16.0	54.6	55.9	101	2500	25006	25020	25028
998	4122	0	1000	85.3	84.3	45.4	81.0	24990	24993	24960	25012
2990	0		1000	43	45.0	76.9	45.0	24995	24996	25004	24975
2990	998	0	1000	61.8	62.2	58.2	22.3	24991	24995	24991	24977
2000	998	0	1000	41.6	42	38.5	2.74	24993	24997	24996	24988

Finally, Table 4.11 shows the active power values obtained when the sp-RPC is fully operational together with the solar PV system and BESS. Analyzing the data obtained, it is possible to conclude that the proposed algorithm manages to mitigate the initially existing unbalances, decreasing to values below 42.8 % in the existing operating conditions. Nevertheless, it is possible to verify that with the sp-RPC operating input, the average value of the power between the two TPS generally decreases. That is, exemplifying for the case P_{Loadx} = 2 MW and P_{Loady} = 998 kW, initially, the average value of the two TPS with the sp-RPC deactivated, P_{PG_off}, was 1497 kW, changing to 602 W when the sp-RPC started to work, P_{PG_on}. The start-up of the sp-RPC together with the BESS, with P_{BESS} = 659 kW, and the solar PV system, P_{PV} = 1222 kW, reflected in a decrease of -59.8 %, $P_{PG_\%inc}$, in the average operating power of the two TPS power.

Table 4.11 – Average values of the operating powers and unbalanced values for different load conditions when the sp-RPC, the solar PV system and the BESS are enabled.

P_{Loadx}	P_{Loady}	P_{PV}	P_{BESS}	P_{PGx}	P_{PGy}	P_{spRPCx}	P_{spRPCy}	P_{PG_on}	$P_{PG_\%inc}$	Unbalance
kW	kW	kW	kW	kW	kW	kW	kW	kW	%	%
998	6119	1227	1000	1454	3629	-454	2505	2541	-28.6	42.8
998	-3884	1223	-1000	-1465	-1423	2470	-2457	-1444	0.1	1.47
998	4122	1227	1000	1450	1621	-451	2505	1536	-40	5.56
2990	0	1225	701	632	610	2369	-609	621	-58.5	1.76
2990	998	1227	1000	989	958	2010	41.4	973	-51.2	1.58
2000	998	1222	659	601	603	1399	397	602	-59.8	0.18

Regarding the voltage and current values, presented in Table 4.12 it was possible to verify that on the side where the sp-RPC injects energy, the voltage at the coupling point increases slightly. On the other hand, on the side with the highest load coupled, the voltage drop is minimized. Nevertheless, to highlight the balancing capability of the sp-RPC, imposing similar i_{PGx} and i_{PGy} rms values, and with the aid of the solar PV system and with the BESS was possible to decrease rms values in each TPS.

Table 4.12 – Currents and voltages rms values for different load conditions when the sp-RPC, the solar PV system and the BESS are enabled.

P_{Loadx}	P_{Loady}	P_{PV}	P_{BESS}	i_{PGx}	i_{PGy}	i_{spRPCx}	i_{spRPCy}	v_{PGx}	v_{PGy}	v_{spRPCx}	v_{spRPCy}
kW	kW	kW	kW	rms (A)	rms (A)	rms (A)	rms (A)	rms (V)	rms (V)	rms (V)	rms (V)
998	6119	1227	1000	58.2	145	18.3	100	24993	24987	24977	24992
998	-3884	1223	-1000	58.4	57.1	98.4	98.4	25003	25007	25046	25026
998	4122	1227	1000	58.1	65	18.2	100	24993	24995	24766	25019
2990	0	1225	701	25.3	24.5	94.7	24.5	24995	24999	25013	24989
2990	998	1227	1000	39.7	38.4	80.2	2.49	24995	24997	25006	24991
2000	998	1222	659	25	23.9	55.1	16.27	24995	24999	25005	25000

4.5 Control Algorithm and sp-RPC Reduced-Scale Prototype used for Simulation Validation

In order to confirm the algorithms' performance in real data acquisition and environment, the development of a reduced-scale laboratory prototype was intended. Due to implementation complexity, available time and resources, a different topology was chosen, always maintaining the feature of the common dc-link between the different ports of the power electronics converter. Thus, and also considering the modularity of the system, the topology of full-bridge power converter with cascade transformers was chosen, as shown in Figure 4.21. Thus, it would be possible to add more submodules, maintaining the common connection point between them, and the output of each converter would be connected in cascade, thus increasing the number of output voltage levels. In turn, regarding the solar PV system, the unidirectional boost topology was considered. On the other hand, for the BESS, the bidirectional dc-dc topology was considered. Since this simulation was used to support the analysis of the reduced-scale sp-RPC prototype, some requirements and limitations were taken into consideration, as presented in

Table 4.13. The nominal active power for the *spRPCx*, P_{spRPCx}, and the *spRPCy*, P_{spRPCy}, was reduced to 1.5 kW, as well as a maximum power of 1 kW for the solar PV system and BESS. Regarding the common dc-link, considering an sp-RPC with three cascaded modules, a nominal voltage of 90 V was considered.

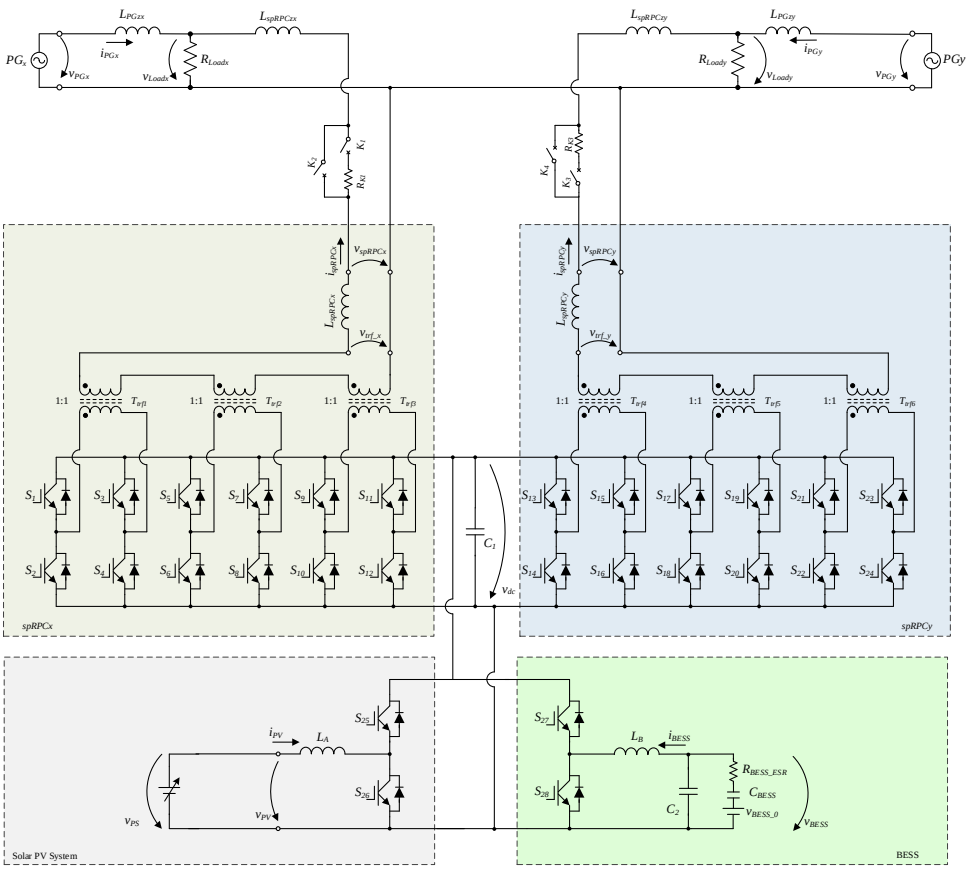

Figure 4.21 – Electrical schematic of the reduced-scale sp-RPC implemented in simulation based on the laboratory prototype.

Table 4.13 – Main parameters considered for the reduced-scale sp-RPC simulation model.

	Variable	Minimum	Nominal	Maximum	unit
sp RPC active power	P_{spRPCx}, P_{spRPCy}		1.5		kW
Solar PV system power	P_{PV}			1	kW
BESS power	P_{BESS}			1	kW
Common dc-link voltage	V_{dc}	80	90	135	V
TPS and sp-RPC voltages	v_{PGx}, v_{PGy}, v_{spRPCx}, v_{spRPCy}	92	115	138	V
Solar PV system voltage	V_{PV}	50	68	85	V
BESS voltage	V_{BESS}	47.5	60.8	70.3	V
Sp-RPC current	i_{spRPCx}, i_{spRPCy}		18	23	A
Solar PV system current	I_{PV}		18	19	A
BESS current	I_{BESS}		18	23	A
Communication frequency	f_{s_PG}		5		Hz
Sampling frequency	f_s		50		kHz
Switching frequency sp-RPC	f_{sw_spRPC} (unipolar)		1		kHz
Switching frequency for PV and BESS	f_{sw_PV}, f_{sw_BESS}		25		kHz

In order to create a computational model similar to the implemented laboratory prototype, different characteristics presented in Table 4.14 were considered. Regarding the inductors, the existing inductors in the laboratory were considered as well as the inductors implemented exclusively for the laboratory prototype. In either case, an inductor series resistance value was also considered or stipulated. Regarding the dc-link, the number of capacitors and the nominal value used in the experimental prototype were also considered, stipulating an equivalent series resistance, thus causing losses in the system and the need to regulate the bus. Regarding the BESS, the minimum voltage value of the batteries was considered and the remaining values of the equivalent model stipulated considering the capacity of the batteries and the simulation time. That is, considering the simulation time, a reduced value for C_{BESS} was considered to be perceptible in the steps of BESS operation. In turn, for an analysis of a continuous operation of the BESS and in a steady-state, a higher C_{BESS} value was considered. Regarding the IGBT devices, the internal characteristics provided by the manufacturer of the IGBT module used were considered. In turn, for the model of transformers, a different computational model was considered for each one of them, considering the values obtained experimentally. These values are presented in Chapter 5, on the topic *5.3.3.4 Final Analysis and Comparison Between Transformers*.

Table 4.14 – Main parameters of the electric components used on the sp-RPC reduced-scale simulation model system.

	Variable	Value	Unit
Line impedance inductors	L_{PGzx}, L_{PGzy}, $L_{spRPCzx}$, $L_{spRPCzx}$,	2 (145[#1])	mH (mΩ)
Coupling inductor	L_{spRPCx}, L_{spRPCy}	4.3396 (128[#1])	mH (mΩ)
Inductor for the PV	L_A	1 (100[#1])	mH (mΩ)
Inductor for the BESS	L_B	1 (100[#1])	mH (mΩ)
Capacitance on the dc-link	C1	13 (100[#1])	mF (mΩ)
Open-circuit voltage on the BESS	V_{BESS_0}	47.5	V
Capacitor of the BESS model	C_{BESS}	9 0.9[#2]	F
Internal series resistor of the BESS	R_{BESS_ESR}	100	mΩ
Saturation voltage of the IGBT module		1.75	V
Transistor resistance of the IGBT module		8.1	mΩ
Reverse diode threshold voltage of the IGBT module		2.2	V
Reverse diode resistance of the IGBT module		9	mΩ

[#1] Considered as internal series resistance for each component;
[#2] Considered for simulation with regenerative braking to validate de transition between the charging and discharging process for the same simulation time.

Since this topology presents a very similar structure to the one presented in topic 4.2 Proposed sp-RPC Topology based on SST, the migration of the algorithm presented in 4.3 Control Algorithm Proposed for the sp-RPC based on SST to this computational model was simple, requiring small adjustments. Namely, since this topology only has a single dc-link, only the control algorithm shown in Figure 4.5 was considered, disregarding the flowcharts in Figure 4.6 and Figure 4.7. Consequently, the final control equation is adapted thus considering equation (4.8) for *spRPCx* and equation (4.9) for *spRPCy*. All upstream algorithms were used.

$$P_{spRPCx}{}^{*} = -P_{trans} + P_{PV} - P_{BESS} - P_{reg} \tag{4.8}$$

$$P_{spRPCy}{}^{*} = P_{trans} \tag{4.9}$$

4.6 Reduced-Scale Prototype Simulations Results

In this topic, the different simulation results obtained with the reduced-scale model of sp-RPC are presented. This analysis considered the different operating modes, as well as the different operating conditions imposed by the loads. Regarding the operating modes, the performance of the system with and without the integration of the solar PV system and/or the BESS in the sp-RPC was analyzed. In turn, the analysis of the robustness of the system was also analyzed considering different operating conditions of the loads, considering operating inputs and outputs, load transients and regenerative braking.

For a comparative analysis of the performance of the sp-RPC, the different loads considered are presented in Figure 4.22, highlighting the imposed operating conditions. The analysis of each figure is presented in the following topics:

- In Figure 4.22 (a) the load on the *x*-side presents an average active power P_{Loadx} = 1033.9 W (R_{Loadx} = 12.6 Ω), while the load on the *y*-side presents P_{Loady} = 0 W (R_{Loady} = ∞ Ω). Regarding the currents, it is possible to verify that i_{PGx} presents an amplitude of 12.73 A, while i_{PGy} presents an amplitude of 0 A;
- In Figure 4.22 (b) the load on the *x*-side presents an average active power P_{Loadx} = 1033.9 W (R_{Loadx} = 12.6 Ω), while the load on the *y*-side presents P_{Loady} = 1995.7 W (R_{Loady} = 6.4 Ω). Regarding the currents, it is possible to verify that i_{PGx} presents an amplitude of 0 A, while i_{PGy} presents an amplitude of 18.75 A;
- In Figure 4.22 (c) the load on the *x*-side presents an average active power P_{Loadx} = 1033.9 W (R_{Loadx} = 12.6 Ω), while the load on the *y*-side presents P_{Loady} = 1519.1 W (R_{Loady} = 8.5 Ω).

Regarding the currents, it is possible to verify that i_{PGx} presents an amplitude of 0 A, while i_{PGy} presents an amplitude of 24.68 A;

- In Figure 4.22 (d) the load on the *x*-side presents an average active power P_{Loadx} = 0 W (R_{Loadx} = ∞ Ω), while the load on the *y*-side presents P_{Loady} = 1519.1 W (R_{Loady} = 8.5 Ω). Regarding the currents, it is possible to verify that i_{PGx} presents an amplitude of 12.74 A, while i_{PGy} presents an amplitude of 18.74 A;
- In Figure 4.22 (e) the load on the *x*-side presents an average active power P_{Loadx} = 0 W (R_{Loadx} = ∞ Ω), while the load on the *y*-side presents P_{Loady} = 1995.7 W (R_{Loady} = 6.4 Ω). Regarding the currents, it is possible to verify that i_{PGx} presents an amplitude of 12.74 A, while i_{PGy} presents an amplitude of 24.68 A;
- In Figure 4.22 (f) the load on the *x*-side presents an average active power P_{Loadx} = 1033.9 W (R_{Loadx} = 12.6 Ω), while the load on the *y*-side presents P_{Loady} = -2881.5 W (with a constant reference of -3 kW). Regarding the currents, it is possible to verify that i_{PGx} presents an amplitude of 12.73 A, while i_{PGy} presents an amplitude of 35.88 A.

For a better analysis, three case scenarios were considered: scenario A; scenario B and scenario C. Case scenario A has four instants with a locomotive always on the *x*-side. Thus, each moment of disturbance is identified in the moments: i) P_{Loadx} = 1033.9 W and P_{Loady} = 0 W; ii) P_{Loadx} = 1033.9 W and P_{Loady} = 1519.1 W; iii) P_{Loadx} = 1033.9 W and P_{Loady} = 1995.7 W; and iv) P_{Loadx} = 1033.9 W and P_{Loady} = 1519.1 W. Regarding the case scenario B, also has four instants with different train consumption, with a locomotive always on the *y*-side. Thus, each moment of disturbance is identified in the moments: i) P_{Loadx} = 0 W and P_{Loady} = 1519.1 W; ii) P_{Loadx} = 1033.9 W and P_{Loady} = 1519.1 W; iii) P_{Loadx} = 0 W and P_{Loady} = 1519.1 W; and iv) P_{Loadx} = 0 W and P_{Loady} = 1995.7 W. Finally, the case scenario C was considered for the analysis of regenerative braking, presenting only three instants: i) P_{Loadx} = 1033.9 W and P_{Loady} = 1995.7 W; ii) P_{Loadx} = 1033.9 W and P_{Loady} = -2881.5 W; iii) and P_{Loadx} = 1033.9 W and P_{Loady} = 1519.1 W.

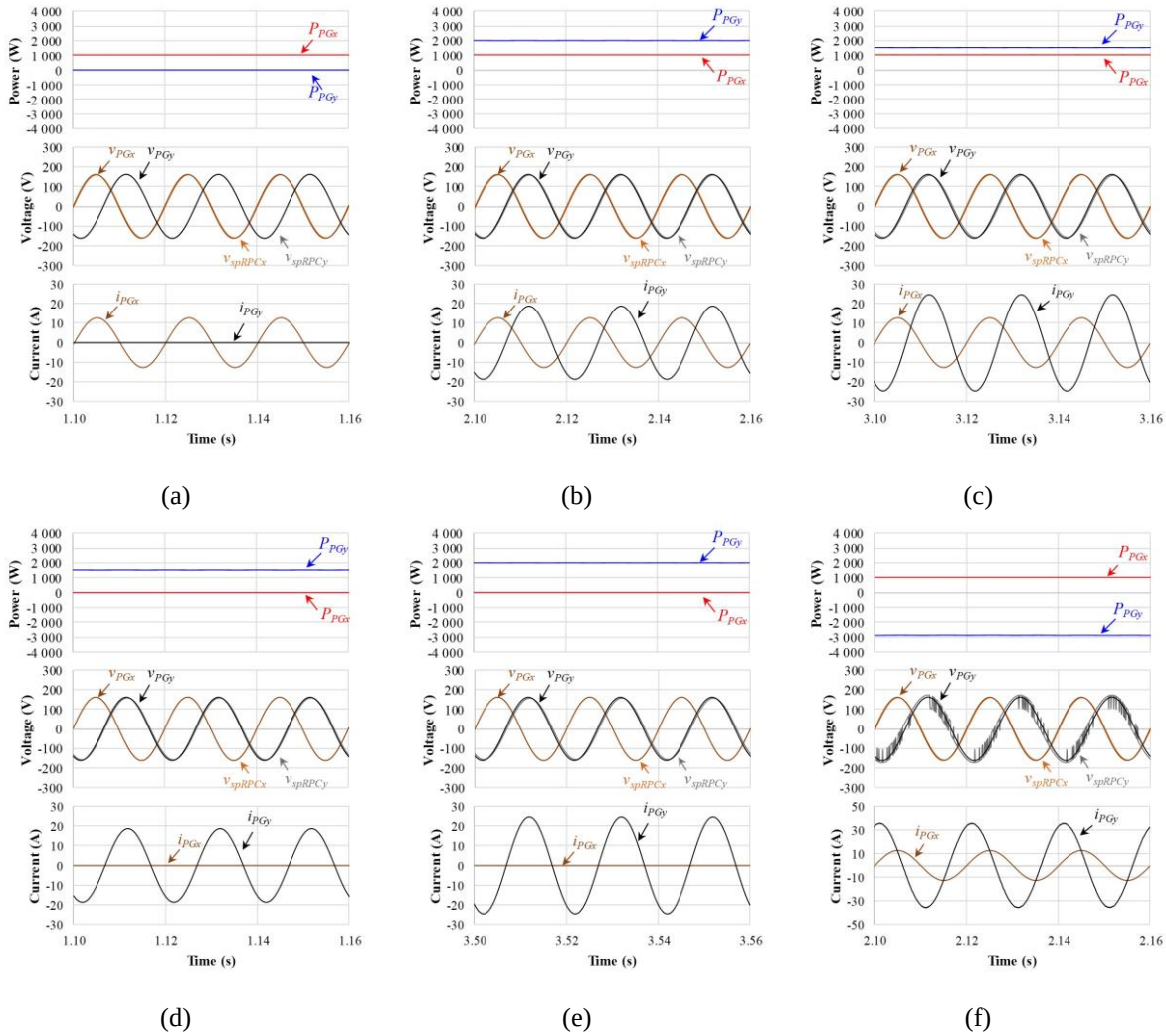

Figure 4.22 – Simulation results of the power in each TPS, P_{PGx} and P_{PGy}, the voltages, v_{PGx}, v_{PGy}, v_{spRPCx} and v_{spRPCy}, and currents, i_{PGx} and i_{PGy}, for different load conditions: (a) P_{Loadx} = 1033.9 W and P_{Loady} = 0 W; (b) P_{Loadx} = 1033.9 W and P_{Loady} = 1995.7 W; (c) P_{Loadx} = 1033.9 W and P_{Loady} = 1519.1 W; (d) P_{Loadx} = 0 W and P_{Loady} = 1519.1 W; (e) P_{Loadx} = 0 W and R_{Loady} = 1995.7 W; and (f) P_{Loadx} = 1033.9 W and P_{Loady} = -2881.5 W.

4.6.1 Simulation Result of the Reduced-Scale Prototype sp-RPC with Dynamic Control

Case Scenario A

This topic focuses on the analysis of the reduced-scale prototype sp-RPC for case scenario A, with the solar PV system and the BESS disabled, as can be seen in Figure 4.23. In Figure 4.23 (a) it is possible to verify that P_{Loadx} and P_{Loady} initially present different values, causing an unbalance in the active powers P_{PGx} and P_{PGy}. At 0.5 s the proposed control algorithm is activated, being able to verify that P_{PGx} and P_{PGy} converge to an average value of 605 W. At instant 1.4 s, an electric locomotive is added to the *y*-side, increasing P_{PGy}. As a consequence, a new unbalance between the values of P_{PGx} and P_{PGy} appears. When the control algorithm updates the reference values for the sp-RPC, it is possible to verify that P_{PGx} and P_{PGy} converge to an average value of 1311 W. At instant 2.45 s, the consumption of the

locomotives on the *y*-side increases, originating a new unbalance between the values of P_{PGx} and P_{PGy}. Once again, as soon as the reference values are updated, it is possible to verify that the average values of P_{PGx} and P_{PGy} converge to an average value of 1601 W. Finally, at the instant 3.2 s, P_{Loady} decreases, verifying that, despite the initial perturbation, the values of P_{PGx} and P_{PGy} converge to an average value of 1311 W. In Figure 4.23 (b) it is possible to see that the powers P_{spRPCx} and P_{spRPCy} always follow the reference values P_{spRPCx}* and P_{spRPCy}*. Figure 4.23 (c) shows the variation of v_{dc} along the disturbances, being able to identify its initial pre-charge, the instant when the control is enabled, and its correct operation maintaining a practically constant voltage over time, and within the expected values, despite disturbances.

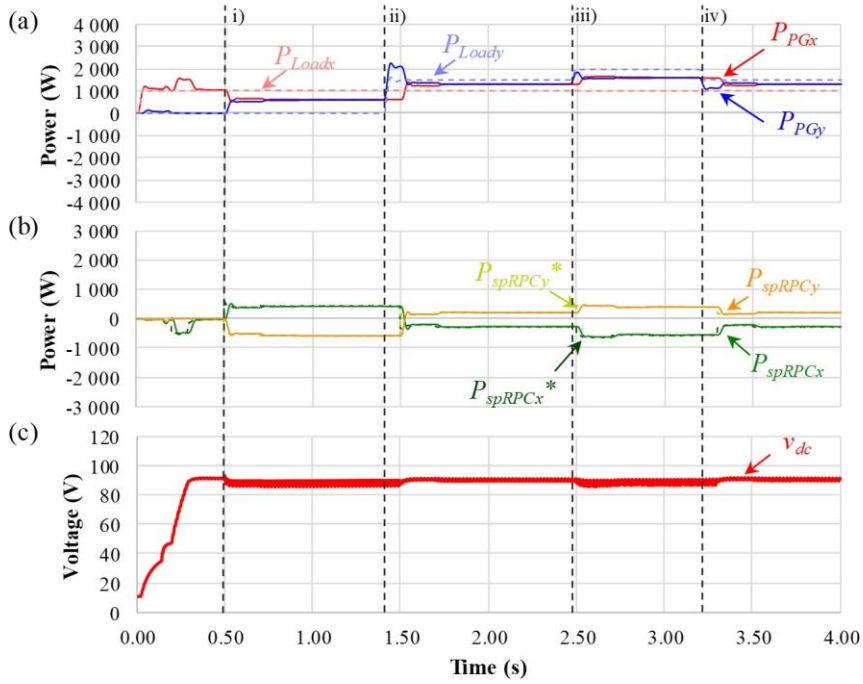

Figure 4.23 – Simulation results of the evolution of active powers and voltages over time, for the reduced-scale sp-RPC during the case scenario A: (a) load active power, P_{Loadx} and P_{Loady}, and TPS active power, P_{PGx} and P_{PGy}; (b) sp-RPC active power, P_{spRPCx} and P_{spRPCy}, and the reference values, P_{spRPCx}* and P_{spRPCy}*; (c) variation of the dc-link voltage, v_{dc}.

Figure 4.24 presents a greater detail of the system operation during the time interval from 0.46 s to 0.56 s, representative of event i) of Figure 4.23. In Figure 4.24 (a) it is possible to verify the voltages of each TPS, v_{PGx} and v_{PGy}, as well as the voltages on each side of the sp-RPC, v_{spRPCx} and v_{spRPCy}. Moreover, it is possible to check v_{dc}, showing an initial disturbance caused by the start of operation, but maintaining a constant desired average value. In Figure 4.24 (b) the voltages v_{trfx} and v_{trfy} are presented, being able to verify the different voltage levels generated by the power converter with cascade transformers. Finally, by analyzing Figure 4.24 (c), it is possible to verify that as soon as the sp-RPC starts operating, synthesizing i_{spRPCx} and i_{spRPCy}, allows balancing the amplitudes of the i_{PGx} and i_{PGy}.

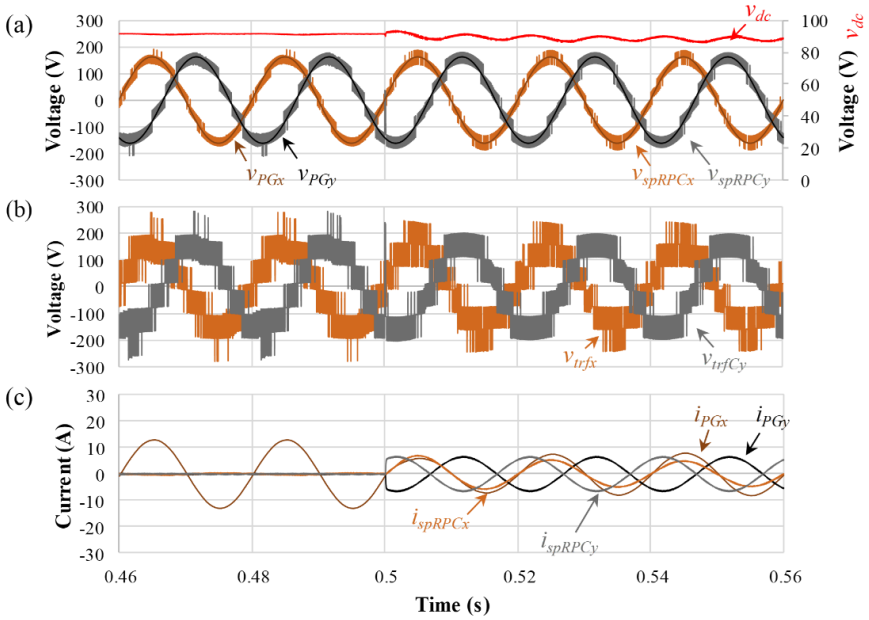

Figure 4.24 – Detailed simulation results, during the time interval from 0.46 s to 0.56 s, for the reduced-scale sp-RPC during the case scenario A: (a) TPS voltages, v_{PGx} and v_{PGy}, the output voltages of the *spRPCx* and *spRPCy*, v_{spRPCx} and v_{spRPCy}, and dc-link voltage, v_{dc}; (b) the output voltages of the cascaded transformers, v_{trfx} and v_{trfy}; (c) TPS currents, i_{PGx} and i_{PGy}, and the sp-RPC output currents, i_{spRPCx} and i_{spRPCy}.

Continuing with the analysis, it is possible to verify in more detail in Figure 4.25 the operation of the system during the time interval from 1.35 s to 1.65 s, representative of event *ii)* of Figure 4.23. Figure 4.25 (a) it is possible to verify the voltages of each TPS, v_{PGx} and v_{PGy}, as well as the voltages on each side of the sp-RPC, v_{spRPCx} and v_{spRPCy}. Moreover, it is possible to see that v_{dc} has an average value of 89.3 V during this interval. In Figure 4.25 (b) the voltages v_{trfx} and v_{trfy} are displayed. Finally, by analyzing Figure 4.25 (c), it is possible to verify that until the instant 1.4 s, the amplitudes of i_{PGx} and i_{PGy} were similar, obtaining a maximum value of 7.49 A and 7.56 A, respectively. At this time, i_{spRPCx} has a maximum value of 5.56 A, while i_{spRPCy} has a maximum value of 7.57 A. However, with the increase of P_{Loady}, i_{PGy} increases to a maximum amplitude value of 26.0 A and a new unbalance appears. At instant 1.5 s, the proposed control algorithm updates the operation references, as can be seen with the amplitude change of the i_{spRPCx} and i_{spRPCy}, being able to verify that i_{PGx} and i_{PGy} converge again to similar amplitude values.

Figure 4.26 shows the simulation results during the time interval from 2.4 s to 2.7 s, representative of event *iii)* of Figure 4.23. Figure 4.26 (a) it is possible to verify the voltages of each TPS, v_{PGx} and v_{PGy}, as well as the voltages on each side of the sp-RPC, v_{spRPCx} and v_{spRPCy}. Moreover, it is possible to see that v_{dc} has an average value of 88.8 V during this interval. In Figure 4.26 (b) the voltages v_{trfx} and v_{trfy} are displayed. Finally, by analyzing Figure 4.26 (c), it is possible to verify that until the instant 2.45 s, the amplitudes of i_{PGx} and i_{PGy} were similar, obtaining a maximum value of 16.0 A and 16.2 A, respectively. At this time, i_{spRPCx} has a maximum value of 3.79 A, while i_{spRPCy} has a maximum value of 2.71 A.

However, with the increase of P_{Loady}, i_{PGy} increases to a maximum amplitude value of 22.17 A, and a new unbalance appears. At the time instant 2.5 s, the proposed control algorithm updates the operation reference values, as can be seen with the amplitude change of the i_{spRPCx} and i_{spRPCy}, being able to verify that i_{PGx} and i_{PGy} converge again to similar amplitude values.

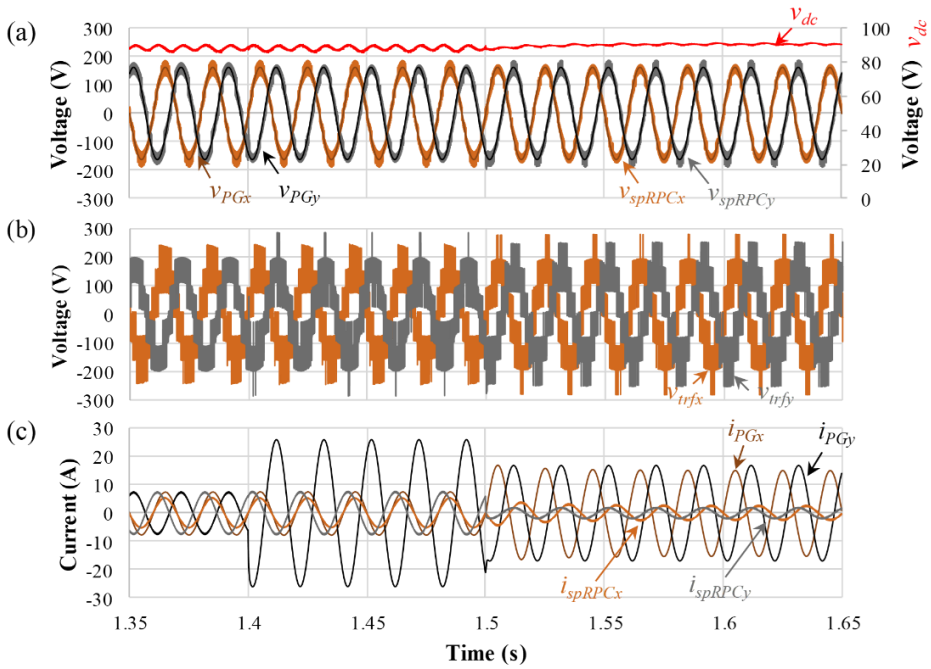

Figure 4.25 – Detailed simulation results, during the time interval from 1.35 s to 1.65 s, for the reduced-scale sp-RPC during the case scenario A: (a) TPS voltages, v_{PGx} and v_{PGy}, the output voltages of the *spRPCx* and *spRPCy*, v_{spRPCx} and v_{spRPCy}, and dc-link voltage, v_{dc}; (b) the output voltages of the cascaded transformers, v_{trfx} and v_{trfy}; (c) TPS currents, i_{PGx} and i_{PGy}, and the sp-RPC output currents, i_{spRPCx} and i_{spRPCy}.

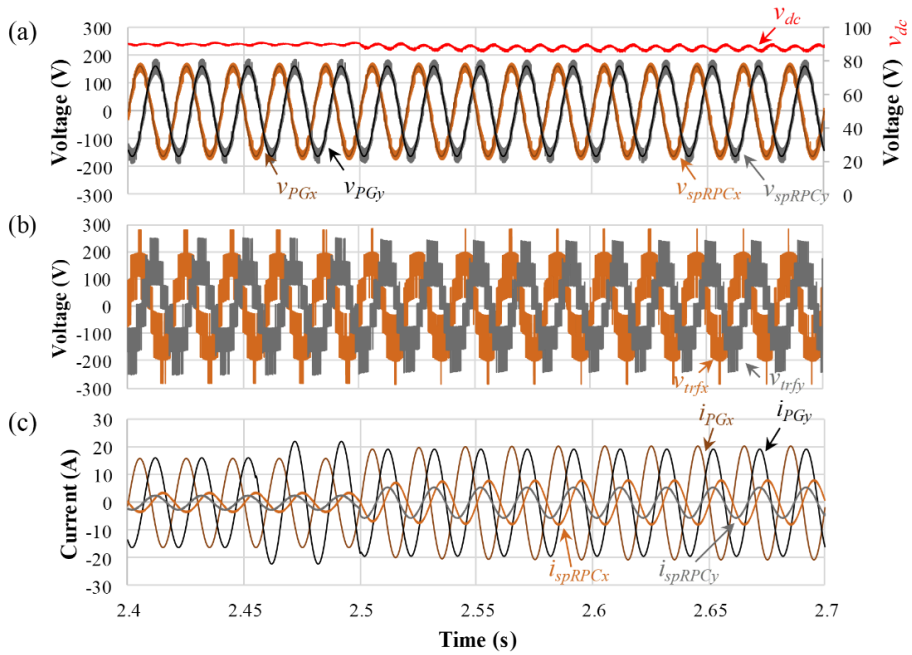

Figure 4.26 – Detailed simulation results, during the time interval from 2.4 s to 2.7 s, for the reduced-scale sp-RPC during the case scenario A: (a) TPS voltages, v_{PGx} and v_{PGy}, the output voltages of the *spRPCx* and *spRPCy*, v_{spRPCx} and v_{spRPCy}, and dc-link voltage, v_{dc}; (b) the output voltages of the cascaded transformers, v_{trfx} and v_{trfy}; (c) TPS currents, i_{PGx} and i_{PGy}, and the sp-RPC output currents, i_{spRPCx} and i_{spRPCy}.

Figure 4.27 shows the simulation results during the time interval from 3.1 s to 3.4 s, representative of event *iv)* of Figure 4.23. Figure 4.27 (a) it is possible to verify the voltages of each TPS, v_{PGx} and v_{PGy}, as well as the voltages on each side of the sp-RPC, v_{spRPCx} and v_{spRPCy}. Moreover, it is possible to see that v_{dc} has an average value of 89.4 V during this interval. In Figure 4.27 (b) the voltages v_{trfx} and v_{trfy} are displayed. Finally, by analyzing Figure 4.27 (c), it is possible to verify that until the instant 3.15 s, the amplitudes of i_{PGx} and i_{PGy} were similar, obtaining a maximum amplitude value of 19.6 A and 19.9 A, respectively. At this time, i_{spRPCx} has a maximum value of 7.43 A, while i_{spRPCy} has a maximum value of 5.12 A. However, with the decrease of P_{Loady}, i_{PGy} decreases to a maximum value of 13.94 A and a new unbalance appears. At instant 3.3 s, the proposed control algorithm updates the operation reference values, as can be seen with the amplitude change of the i_{spRPCx} and i_{spRPCy}, being able to verify that i_{PGx} and i_{PGy} converge again to similar amplitude values.

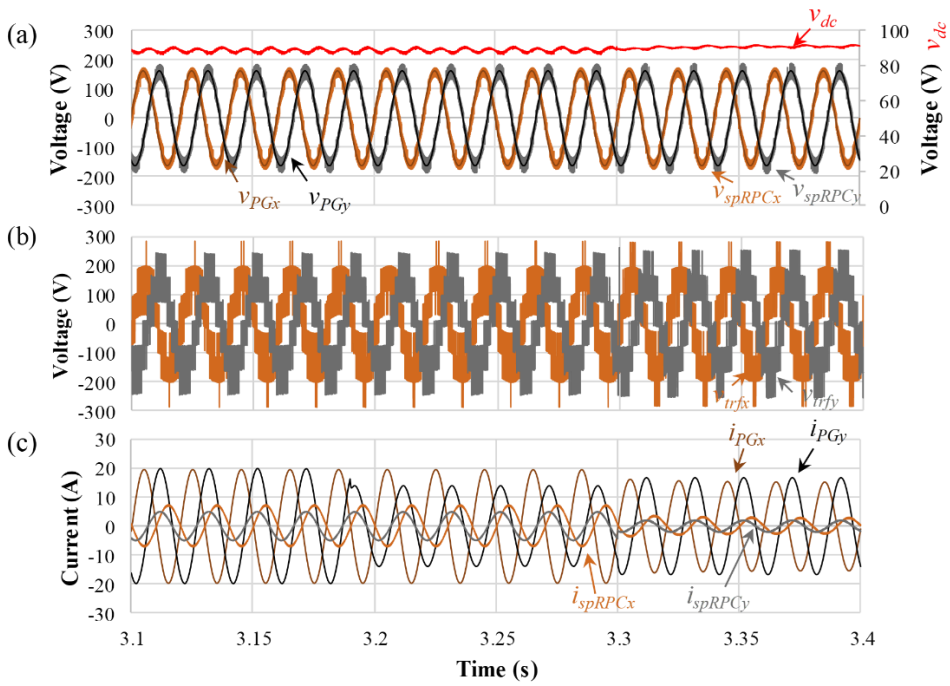

Figure 4.27 – Detailed simulation results, during the time interval from 3.1 s to 3.4 s, for the reduced-scale sp-RPC during the case scenario A: (a) TPS voltages, v_{PGx} and v_{PGy}, the output voltages of the *spRPCx* and *spRPCy*, v_{spRPCx} and v_{spRPCy}, and dc-link voltage, v_{dc}; (b) the output voltages of the cascaded transformers, v_{trfx} and v_{trfy}; (c) TPS currents, i_{PGx} and i_{PGy}, and the sp-RPC output currents, i_{spRPCx} and i_{spRPCy}.

The final result is presented in Figure 4.28 during the time interval from 3.9 s to 4 s, when the system is in steady-state operation. Figure 4.28 (a) it is possible to verify the voltages of each TPS, v_{PGx} and v_{PGy}, as well as the voltages on each side of the sp-RPC, v_{spRPCx} and v_{spRPCy}. Nevertheless, it can be seen that v_{dc} has an average value of 90.5 V during this interval. In Figure 4.28 (b) the voltages v_{trfx} and v_{trfy} are displayed. Finally, by analyzing Figure 4.28 (c), it is possible to verify that i_{PGx} and i_{PGy} have a similar amplitude value, obtaining a maximum amplitude value of 16.0 A and 16.2 A, respectively. At this time, i_{spRPCx} has a maximum value of 3.86 A, while i_{spRPCy} has a maximum value of 2.72 A.

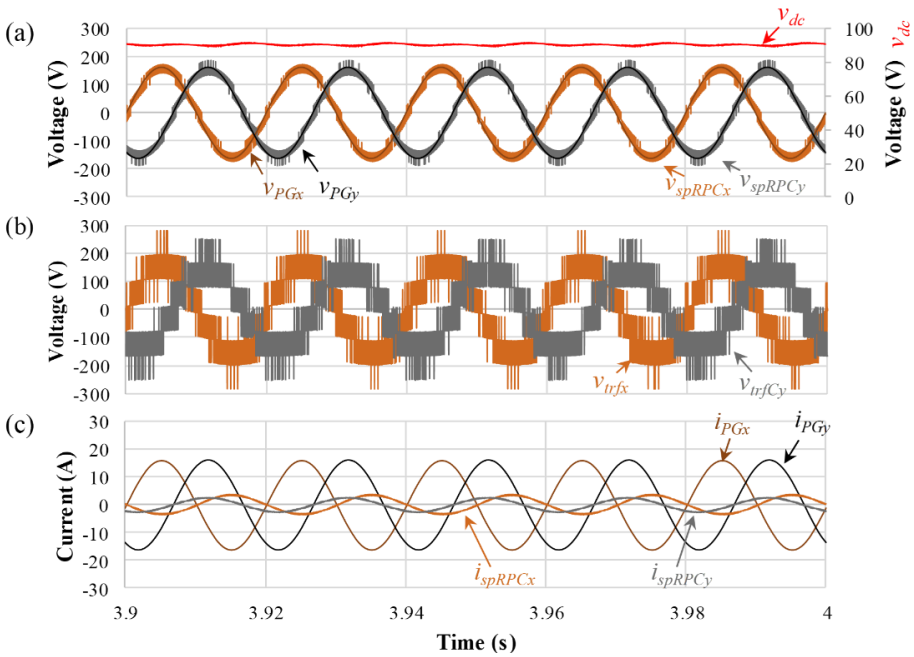

Figure 4.28 – Detailed simulation results, during the time interval from 3.9 s to 4 s, for the reduced-scale sp-RPC during the case scenario A: (a) TPS voltages, v_{PGx} and v_{PGy}, the output voltages of the *spRPCx* and *spRPCy*, v_{spRPCx} and v_{spRPCy}, and dc-link voltage, v_{dc}; (b) the output voltages of the cascaded transformers, v_{trfx} and v_{trfy}; (c) TPS currents, i_{PGx} and i_{PGy}, and the sp-RPC output currents, i_{spRPCx} and i_{spRPCy}.

Case Scenario B

This topic focuses on the analysis of the reduced-scale prototype sp-RPC for case scenario B, with the solar PV system and the BESS disabled, as can be seen in Figure 4.29. In Figure 4.29 (a) it is possible to verify that P_{Loadx} and P_{Loady} initially present different values, causing an unbalance in the active powers P_{PGx} and P_{PGy}. At 0.5 s the proposed control algorithm is activated, being able to verify that P_{PGx} and P_{PGy} converge to an average value of 924 W. At instant 1.4 s there is a disturbance in the system, being able to verify that there is a new unbalance between the values of P_{PGx} and P_{PGy}. When the control algorithm updates the reference values for the sp-RPC, it is possible to verify that P_{PGx} and P_{PGy} converge to an average value of 1310 W. At instant 2.45 s a new disturbance is originated, being able to verify a new divergence of the values between P_{PGx} and P_{PGy}. Once again, as soon the reference values are updated, it is possible to verify that the average values of P_{PGx} and P_{PGy} converge to an average value of 933 W. Finally, at the instant 3.2 s, P_{Loady} varies and, as soon as the reference values are updated, it is possible to verify that the average values of P_{PGx} and P_{PGy} converge to an average value of 1272 W. In Figure 4.29 (b) it is possible to see that the powers P_{spRPCx} and P_{spRPCy} always follow the reference values P_{spRPCx}* and P_{spRPCy}*. Figure 4.29 (c) shows the variation of the dc voltage of the common dc-link along the disturbances, being able to identify its initial pre-charge, the instant the control is enabled, and its correct operation maintaining a practically constant voltage over time, and within the expected values, despite disturbances. The detailed performance analysis of the reduced-scale sp-RPC for case scenario B can be found in Appendix E.

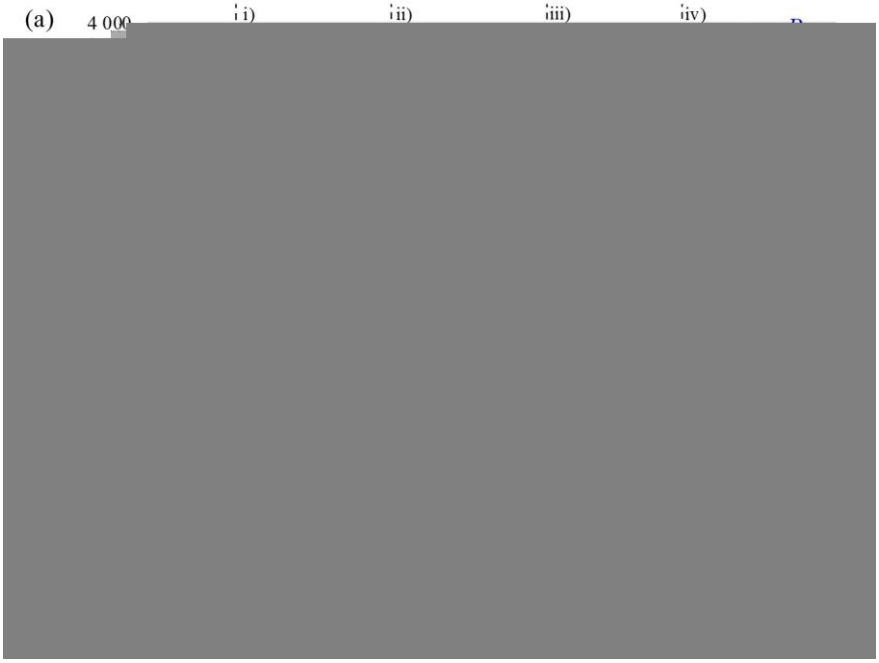

Figure 4.29 – Simulation results of the evolution of active powers and voltages over time, for the reduced-scale sp-RPC during the case scenario B: (a) load active power, P_{Loadx} and P_{Loady}, and TPS active power, P_{PGx} and P_{PGy}; (b) sp-RPC active power, P_{spRPCx} and P_{spRPCy}, and the reference values, P_{spRPCx}* and P_{spRPCy}*; (c) variation of the dc-link voltage, v_{dc}.

Case Scenario C

This topic focuses on the analysis of the reduced-scale prototype sp-RPC for case scenario C, with the solar PV system and the BESS disabled, as can be seen in Figure 4.30. In Figure 4.30 (a) it is possible to verify that P_{Loadx} and P_{Loady} initially present different values, causing an unbalance in the active powers P_{PGx} and P_{PGy}. At 0.5 s the proposed control algorithm is activated, being able to verify that P_{PGx} and P_{PGy} converge to an average value of 1632 W. At instant 1.5 s there is a disturbance in the system, with the load on the y-side creating a regenerative braking event, being able to verify that there is a new unbalance between the values of P_{PGx} and P_{PGy}. When the control algorithm updates the reference values for the sp-RPC, it is possible to verify that P_{PGx} and P_{PGy} present an average value of -914.1 W and -735.7 W, respectively. Finally, at the instant 3.2 s, P_{Loady} varies and, as soon as the reference values are updated. It is possible to verify that the average values of P_{PGx} and P_{PGy} converge to an average value of 1323 W. In Figure 4.30 (b) it is possible to see that the powers P_{spRPCx} and P_{spRPCy} always follow the reference values P_{spRPCx}* and P_{spRPCy}*. Figure 4.30 (c) shows the variation of the dc voltage of the common dc-link along the disturbances, being able to identify its initial pre-charge, the instant when the control is enabled, and its correct operation maintaining a practically constant voltage over time, and within the expected values, despite disturbances. The detailed performance analysis of the reduced-scale sp-RPC for case scenario C can be found in Appendix E.

Finally, the final result is presented in Figure Ap. B.4 during the instant 2.9 s to 3 s of Figure 4.15, when the system is in steady-state operation. Figure Ap. B.4 (a) it is possible to verify the voltages of each TPS, v_{PGx} and v_{PGy}, as well as the voltages on each side of the sp-RPC, v_{spRPCx} and v_{spRPCy}. Moreover, it is possible to see that v_{dc_x6} has an average value of 6.95 kV, while v_{dc_y6} has an average value of 7.06 kV during this interval. The remaining voltages have similar values of the dc-link on the same side. Analyzing Figure Ap. B.4 (b), it is possible to verify that i_{PGx} and i_{PGy} presents a similar amplitude value, obtaining a maximum amplitude value of 112 A and 123.4 A, respectively. At this time, i_{spRPCx} has a maximum value of 55.41 A, while i_{spRPCy} has a maximum value of 119.5 A. Nevertheless, it is also possible to see that despite the perturbation, v_{dc} shows an average value of 1.02 kV during this interval. Finally, Figure Ap. B.4 (c) shows that the solar PV system maintains a constant operation, been possible to measure an average value of 778.5 V on v_{PV} and 1575.9 A on i_{PV}.

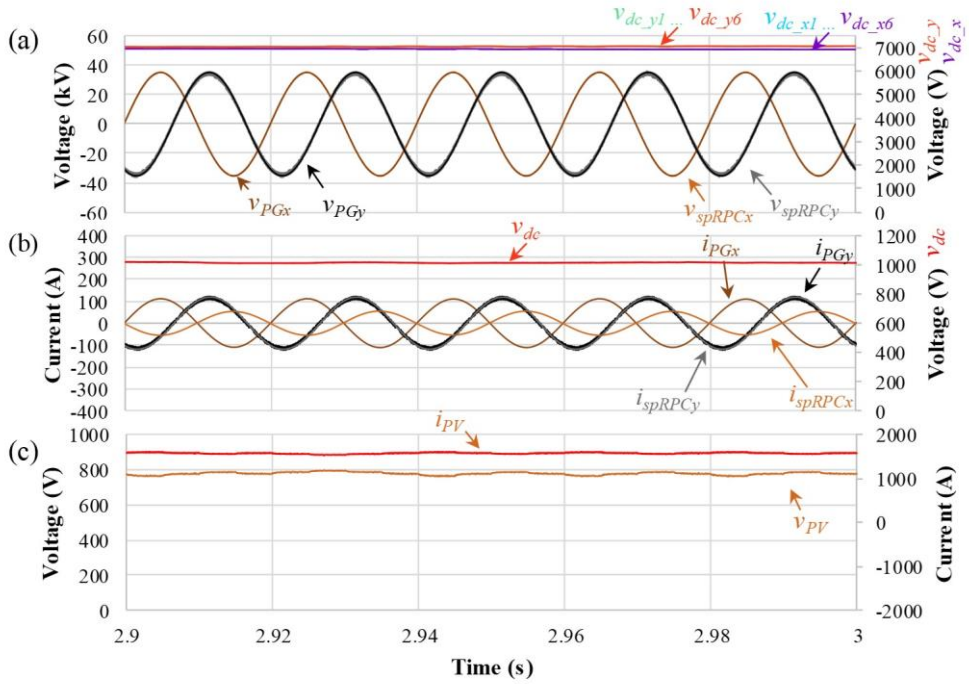

Figure Ap. B.4 – Detailed simulation results, during the time interval from 2.9 s to 3 s, for the real scale sp-RPC with the solar PV system during the case scenario A: (a) the voltages on each TPS, v_{PGx} and v_{PGy}, the output voltages of the *spRPCx* and *spRPCy*, v_{spRPCx} and v_{spRPCy}, and voltages on the dc-link of each submodule, v_{dc_x1} to v_{dc_x6}, and v_{dc_y1} to v_{dc_y6}; (b) the currents on each TPS, i_{PGx} and i_{PGy}, and the output currents of the sp-RPC, i_{spRPCx} and i_{spRPCy}, and the voltage of the common dc-link voltage, v_{dc}; (c) voltage and current on the solar PV system, v_{PV} and i_{PV}.

Case Scenario B

In the following simulation results the operation of the sp-RPC with the solar PV system enabled and the BESS disabled, representative of the results presented in Figure 4.16, is analyzed in more detail.

Figure Ap. B.5 presents a greater detail of the system operation during the time interval from 0.3 s to 0.6 s of Figure 4.16. In Figure Ap. B.5 (a) it is possible to verify the voltages of each TPS, v_{PGx} and v_{PGy}, as well as the voltages on each side of the sp-RPC, v_{spRPCx} and v_{spRPCy}. Moreover, it is possible to check the dc-link voltages from v_{dc_x1} to v_{dc_x6} and from v_{dc_y1} to v_{dc_y1}, showing an initial disturbance caused by the start of operation, but maintaining a constant desired average value of 7 kV. In Figure Ap. B.5 (b) it is possible to verify that as soon as the sp-RPC starts operating, synthesizing i_{spRPCx} and i_{spRPCy}, it was possible to equalize the amplitudes of the i_{PGx} and i_{PGy}. Nevertheless, it is also possible to see that despite the initial perturbation, v_{dc} remains regulated at a value of 1 kV. Finally, by analyzing Figure Ap. B.5 (c), it is possible to verify the beginning of operation of the solar PV system, with the MPPT control algorithm searching for the MPP, being possible to see that v_{PV} converge to an average value of 810.7 V, while i_{PV} converge to an average value of 1477.0 A.

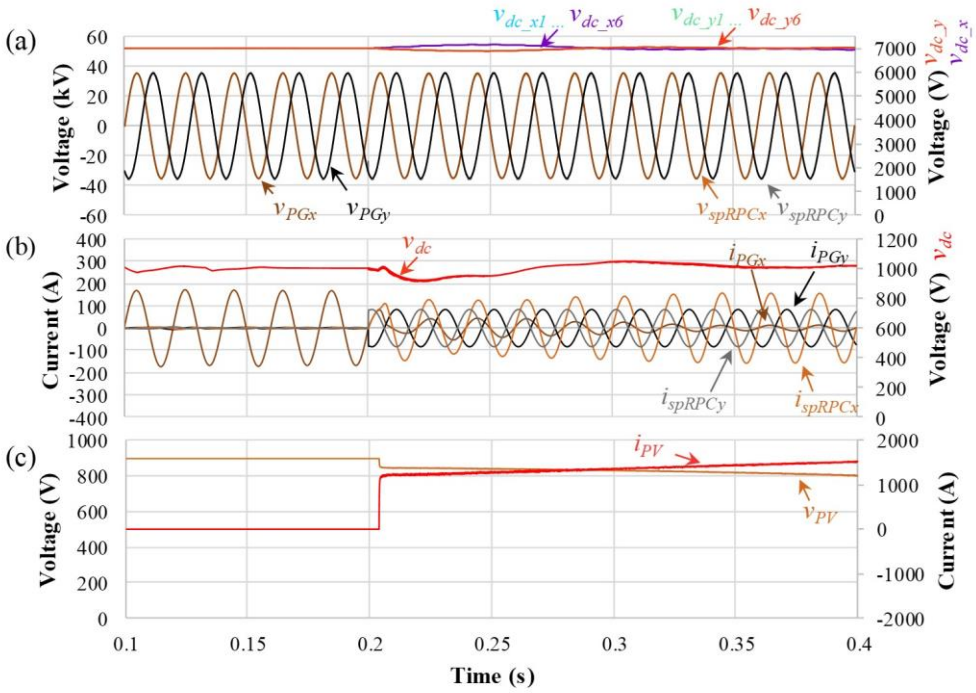

Figure Ap. B.5 – Detailed simulation results, during the time interval from 0.3 s to 0.6 s, for the real scale sp-RPC with the solar PV system during the case scenario B: (a) the voltages on each TPS, v_{PGx} and v_{PGy}, the output voltages of the *spRPCx* and *spRPCy*, v_{spRPCx} and v_{spRPCy}, and voltages on the dc-link of each submodule, v_{dc_x1} to v_{dc_x6}, and v_{dc_y1} to v_{dc_y6}; (b) the currents on each TPS, i_{PGx} and i_{PGy}, and the output currents of the sp-RPC, i_{spRPCx} and i_{spRPCy}., and the voltage of the common dc-link voltage, v_{dc}; (c) voltage and current on the solar PV system, v_{PV} and i_{PV}.

Continuing with the analysis, it is possible to verify in more detail in Figure Ap. B.6 the operation of the system between the time instants from 0.95 s to 1.25 s, representative of event *ii)* of Figure 4.16.

Figure Ap. B.6 (a) it is possible to verify the voltages of each TPS, v_{PGx} and v_{PGy}, as well as the voltages on each side of the sp-RPC, v_{spRPCx} and v_{spRPCy}. Moreover, it is possible to see that v_{dc_x6} has an average value of 7.04 kV, while v_{dc_y6} has an average value of 6.99 kV during this interval. The remaining voltages have similar values of the dc-link on the same side. Analyzing Figure Ap. B.6 (b), it is possible to verify that until the instant 1 s, the amplitudes of i_{PGx} and i_{PGy} were similar, obtaining a maximum value of 51.33 A and 58.75 A, respectively. At this time, i_{spRPCx} has a maximum value of 118.6 A, while i_{spRPCy} has a maximum value of 58.89 A. However, with the variation of R_{Loady}, starting regenerative braking, i_{PGy} increases to a maximum amplitude value of 115.2 A and a new unbalance appears. At instant 1.1 s, the proposed control algorithm updates the operation reference values, as can be seen with the amplitude change of the i_{spRPCx} and i_{spRPCy}, being able to verify that i_{PGx} and i_{PGy} converge again to similar amplitude values. Nevertheless, it is also possible to see that despite the perturbation, v_{dc} shows an average value of 1.00 kV during this interval. Finally, Figure Ap. B.6 (c) shows that the solar PV system maintains a constant operation, been possible to measure an average value of 741 V on v_{PV} and 1615.7 A on i_{PV}.

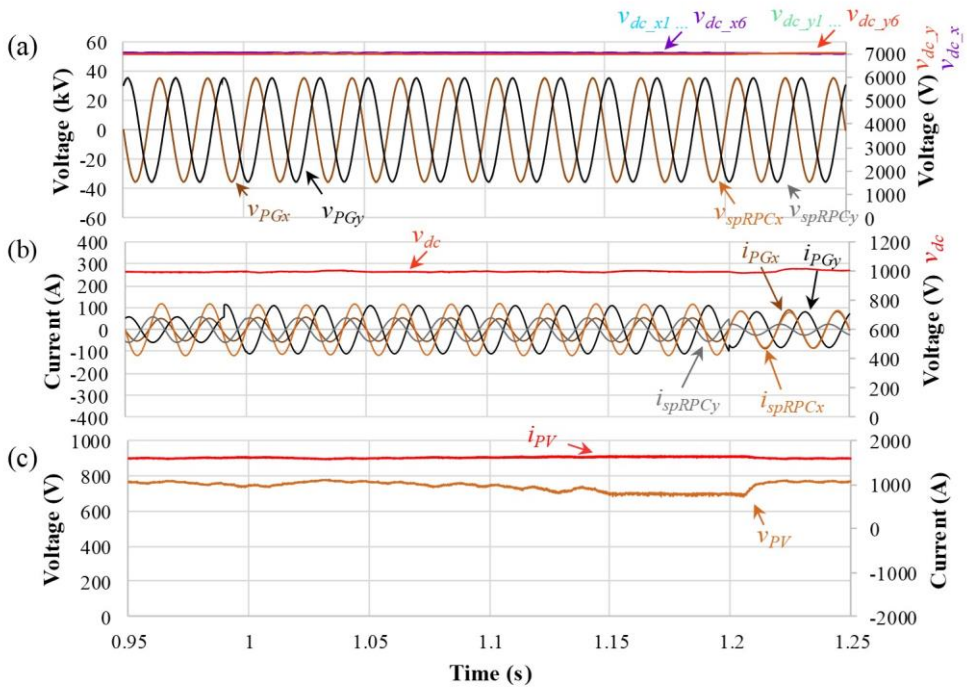

Figure Ap. B.6 – Detailed simulation results, during the time interval from 0.95 s to 1.25 s, for the real scale sp-RPC with the solar PV system during the case scenario B: (a) the voltages on each TPS, v_{PGx} and v_{PGy}, the output voltages of the *spRPCx* and *spRPCy*, v_{spRPCx} and v_{spRPCy}, and voltages on the dc-link of each submodule, v_{dc_x1} to v_{dc_x6}, and v_{dc_y1} to v_{dc_y6}; (b) the currents on each TPS, i_{PGx} and i_{PGy}, and the output currents of the sp-RPC, i_{spRPCx} and i_{spRPCy}., and the voltage of the common dc-link voltage, v_{dc}; (c) voltage and current on the solar PV system, v_{PV} and i_{PV}.

Figure Ap. B.7 shows the simulation results during time instants from 1.95 s to 2.25 s, representative of event *iii)* of the Figure 4.16. Figure Ap. B.7 (a) it is possible to verify the voltages of each TPS, v_{PGx} and

v_{PGy}, as well as the voltages on each side of the sp-RPC, v_{spRPCx} and v_{spRPCy}. Moreover, it is possible to see that v_{dc_x6} has an average value of 6.99 kV, while v_{dc_y6} has an average value of 7.02 kV during this interval. The remaining voltages have similar values of the dc-link on the same side. Analyzing Figure Ap. B.7 (b), it is possible to verify that until the instant 2 s, the amplitudes of i_{PGx} and i_{PGy} were similar, obtaining a maximum value of 82.79 A and 81.49 A, respectively. At this time, i_{spRPCx} has a maximum value of 87.12 A, while i_{spRPCy} has a maximum value of 25.04 A. However, with the variation of R_{Loadx}, i_{PGx} decreases to a maximum amplitude value of 29.96 A and a new unbalance appears. At instant 2.1 s, the proposed control algorithm updates the operation reference values, as can be seen with the amplitude change of the i_{spRPCx} and i_{spRPCy}, being able to verify that i_{PGx} and i_{PGy} converge again to similar amplitude values. Nevertheless, it is also possible to see that despite the perturbation, v_{dc} shows an average value of 1 kV during this interval. Finally, Figure Ap. B.7 (c) shows that the solar PV system maintains a constant operation, been possible to measure an average value of 703.7 V on v_{PV} and 1636.2 A on i_{PV}.

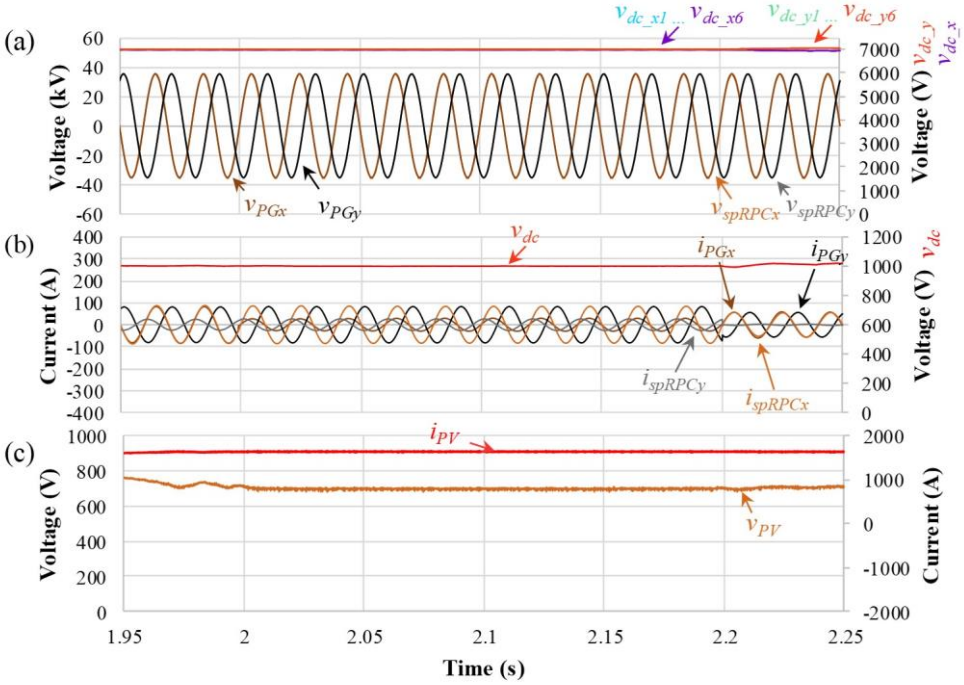

Figure Ap. B.7 – Detailed simulation results, during the time interval from 1.95 s to 2.25 s, for the real scale sp-RPC with the solar PV system during the case scenario B: (a) the voltages on each TPS, v_{PGx} and v_{PGy}, the output voltages of the *spRPCx* and *spRPCy*, v_{spRPCx} and v_{spRPCy}, and voltages on the dc-link of each submodule, v_{dc_x1} to v_{dc_x6}, and v_{dc_y1} to v_{dc_y6}; (b) the currents on each TPS, i_{PGx} and i_{PGy}, and the output currents of the sp-RPC, i_{spRPCx} and i_{spRPCy}., and the voltage of the common dc-link voltage, v_{dc}; (c) voltage and current on the solar PV system, v_{PV} and i_{PV}.

Finally, the final result is presented in Figure Ap. B.8 during the instant 2.9 s to 3 s of Figure 4.16, when the system is in steady-state operation. Figure Ap. B.8 (a) it is possible to verify the voltages of each TPS, v_{PGx} and v_{PGy}, as well as the voltages on each side of the sp-RPC, v_{spRPCx} and v_{spRPCy}. Moreover, it is

possible to see that v_{dc_x6} has an average value of 6.99 kV, while v_{dc_y6} has an average value of 7.00 kV during this interval. The remaining voltages have similar values of the dc-link on the same side. Analyzing Figure Ap. B.8 (b), it is possible to verify that i_{PGx} and i_{PGy} presents a similar amplitude value, obtaining a maximum amplitude value of 55.37 A and 52.54 A, respectively. At this time, i_{spRPCx} has a maximum value of 62.55 A, while i_{spRPCy} has a maximum value of 5.6 A. Nevertheless, it is also possible to see that despite the perturbation, v_{dc} shows an average value of 1 kV during this interval. Finally, Figure Ap. B.8 (c) shows that the solar PV system maintains a constant operation, been possible to measure an average value of 780.3 V on v_{PV} and 1573.4 A on i_{PV}.

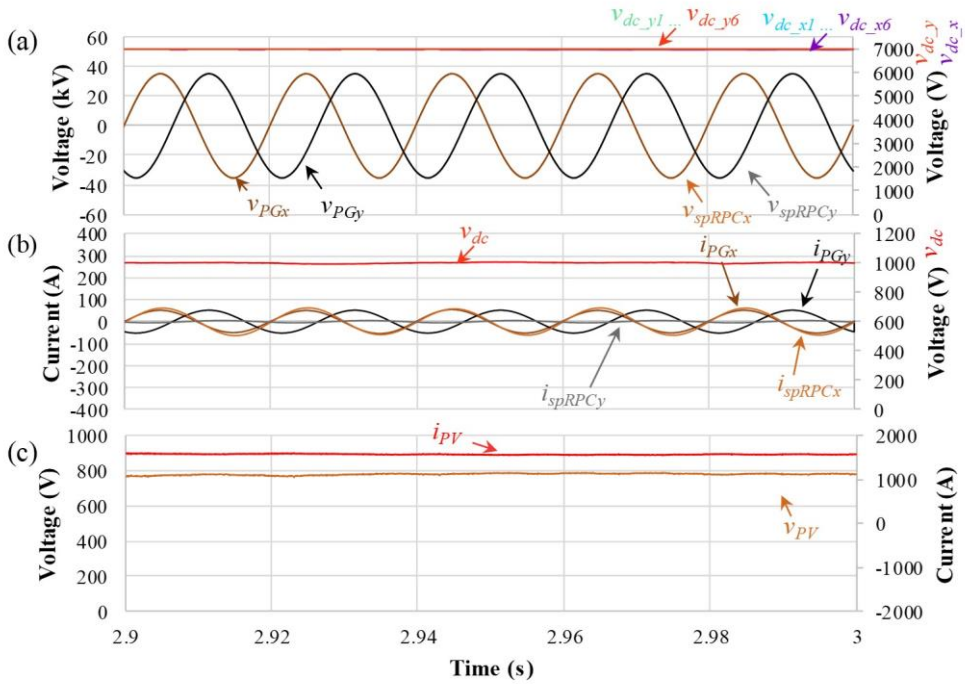

Figure Ap. B.8 – Detailed simulation results, during the time interval from 2.9 s to 3 s, for the real scale sp-RPC with the solar PV system during the case scenario B: (a) the voltages on each TPS, v_{PGx} and v_{PGy}, the output voltages of the *spRPCx* and *spRPCy*, v_{spRPCx} and v_{spRPCy}, and voltages on the dc-link of each submodule, v_{dc_x1} to v_{dc_x6}, and v_{dc_y1} to v_{dc_y6}; (b) the currents on each TPS, i_{PGx} and i_{PGy}, and the output currents of the sp-RPC, i_{spRPCx} and i_{spRPCy}., and the voltage of the common dc-link voltage, v_{dc}; (c) voltage and current on the solar PV system, v_{PV} and i_{PV}.

Appendix C
Detailed Simulation Result of the sp-RPC based on SST and BESS with Dynamic Control

Case Scenario A

In the following simulation results the operation of the sp-RPC with the BESS enabled and the solar PV system disabled, representative of the results presented in Figure 4.17, is analyzed in more detail.

Figure Ap. C.1 presents a greater detail of the system operation during the time interval from 0.3 s to 0.6 s of Figure 4.17. In Figure Ap. C.1 (a) it is possible to verify the voltages of each TPS, v_{PGx} and v_{PGy}, as well as the voltages on each side of the sp-RPC, v_{spRPCx} and v_{spRPCy}. Moreover, it is possible to check the dc-link voltages from v_{dc_x1} to v_{dc_x6} and from v_{dc_y1} to v_{dc_y1}, showing an initial disturbance caused by the start of operation, but maintaining a constant desired average value of 7 kV. In Figure Ap. C.1 (b) it is possible to verify that as soon as the sp-RPC starts operating, synthesizing i_{spRPCx} and i_{spRPCy}, it was possible to equalize the amplitudes of the i_{PGx} and i_{PGy}. Nevertheless, it is also possible to see that despite the initial perturbation, v_{dc} remains regulated at a value of 1 kV. Finally, by analyzing Figure Ap. C.1 (c), it is possible to verify the beginning of operation of the BESS, being possible to see that v_{BESS} converge to an average value of 733.8 V, while i_{BESS} converge to an average value of 1370.4 A, at 0.4 s, reaching a value of 656.7 V and 1525.2 A at 0.6 s, respectively.

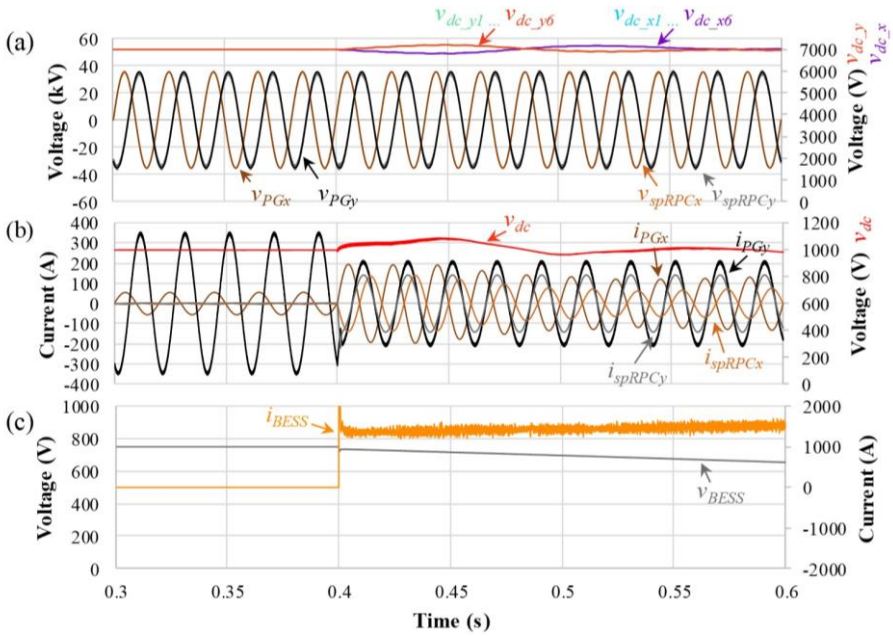

Figure Ap. C.1 – Detailed simulation results, during the time interval from 0.3 s to 0.6 s, for the real scale sp-RPC with the BESS during the case scenario A: (a) the voltages on each TPS, v_{PGx} and v_{PGy}, the output voltages of the *spRPCx* and *spRPCy*, v_{spRPCx} and v_{spRPCy}, and voltages on the dc-link of each submodule, v_{dc_x1} to v_{dc_x6}, and v_{dc_y1} to v_{dc_y6}; (b) the currents on each TPS, i_{PGx} and i_{PGy}, and the output currents of the sp-RPC, i_{spRPCx} and i_{spRPCy}., and the voltage of the common dc-link voltage, v_{dc}; (c) voltage and current on the BESS, v_{BESS} and i_{BESS}.

Figure Ap. C.2 shows the simulation results during time instants from 0.65 s to 0.95 s of Figure 4.17, when the BESS is fully discharged. Figure Ap. C.2 (a) it is possible to verify the voltages of each TPS, v_{PGx} and v_{PGy}, as well as the voltages on each side of the sp-RPC, v_{spRPCx} and v_{spRPCy}. Moreover, it is possible to see that v_{dc_x6} has an average value of 7.04 kV, while v_{dc_y6} has an average value of 6.90 kV during this interval. The remaining voltages have similar values of the dc-link on the same side. Analyzing Figure Ap. C.2 (b), it is possible to verify that until the instant 0.8 s, the amplitudes of i_{PGx} and i_{PGy} presents a maximum value of 158.3 A and 213.2 A, respectively. At this time, i_{spRPCx} has a maximum value of 102.5 A, while i_{spRPCy} has a maximum value of 142.4 A. However, at 0.81 s with the BESS fully discharged, the active power from each TPS starts to increase, increasing the amplitudes of each current. Nevertheless, it is also possible to see that despite the perturbation, v_{dc} shows an average value of 0.97 kV during this interval. Finally, Figure Ap. C.2 (c) shows that the BESS reach the value of 559.8 V on v_{BESS} and 1936 A on i_{BESS}., is fully discharged, being disabled.

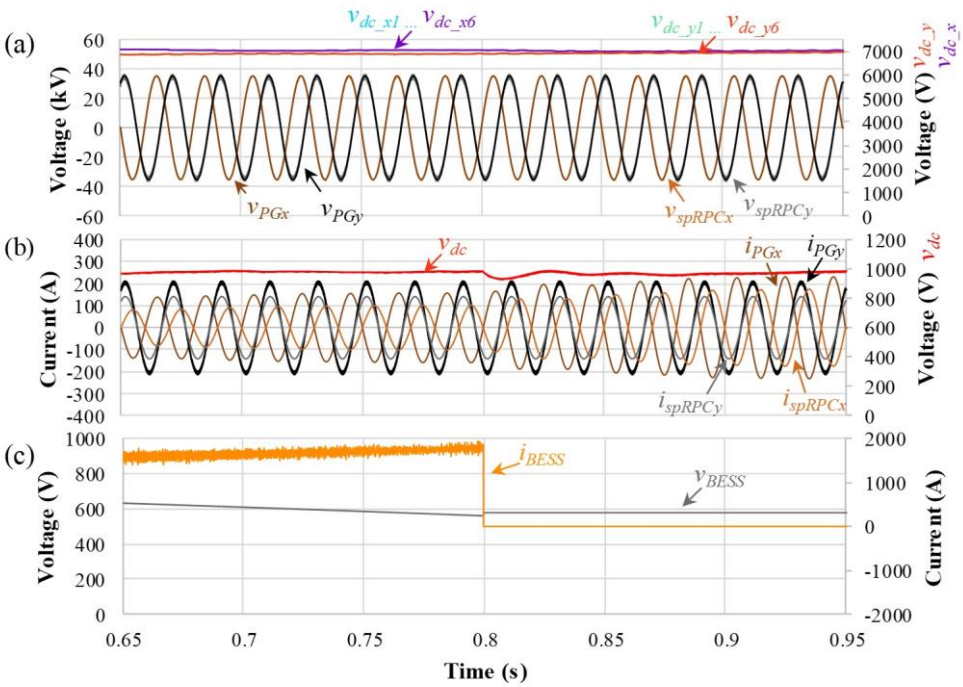

Figure Ap. C.2 – Detailed simulation results, during the time interval from 0.3 s to 0.6 s, for the real scale sp-RPC with the BESS during the case scenario A: (a) the voltages on each TPS, v_{PGx} and v_{PGy}, the output voltages of the *spRPCx* and *spRPCy*, v_{spRPCx} and v_{spRPCy}, and voltages on the dc-link of each submodule, v_{dc_x1} to v_{dc_x6}, and v_{dc_y1} to v_{dc_y6}; (b) the currents on each TPS, i_{PGx} and i_{PGy}, and the output currents of the sp-RPC, i_{spRPCx} and i_{spRPCy}., and the voltage of the common dc-link voltage, v_{dc}; (c) voltage and current on the BESS, v_{BESS} and i_{BESS}.

Continuing with the analysis, it is possible to verify in more detail in Figure Ap. C.3 the operation of the system between the time instants from 0.95 s to 1.25 s, representative of event *ii)* of the Figure 4.17. Figure Ap. C.3 (a) it is possible to verify the voltages of each TPS, v_{PGx} and v_{PGy}, as well as the voltages on each side of the sp-RPC, v_{spRPCx} and v_{spRPCy}. Moreover, it is possible to see that v_{dc_x6} has an average

value of 7.08 kV, while v_{dc_y6} has an average value of 7 kV during this interval. The remaining voltages have similar values of the dc-link on the same side. Analyzing Figure Ap. C.3 (b), it is possible to verify that until the instant 1 s, the amplitudes of i_{PGx} and i_{PGy} were similar, obtaining a maximum value of 230.9 A and 213.1 A, respectively. At this time, i_{spRPCx} has a maximum value of 175.4 A, while i_{spRPCy} has a maximum value of 142.4 A. However, with the variation of R_{Loady}, starting regenerative braking, i_{PGy} increases to a maximum amplitude value of 352.3 A and a new unbalance appears. At instant 1.1 s, the proposed control algorithm updates the operation reference values, as can be seen with the amplitude change of the i_{spRPCx} and i_{spRPCy}, being able to verify that i_{PGx} and i_{PGy} converge again to similar amplitude values. Nevertheless, it is also possible to see that despite the perturbation, v_{dc} shows an average value of 0.99 kV during this interval. Finally, Figure Ap. C.3 (c) shows that with the regenerative braking, the BESS starts to charge, presenting an average value of 611.4 V on v_{BESS} and -1647.9 A on i_{BESS}.

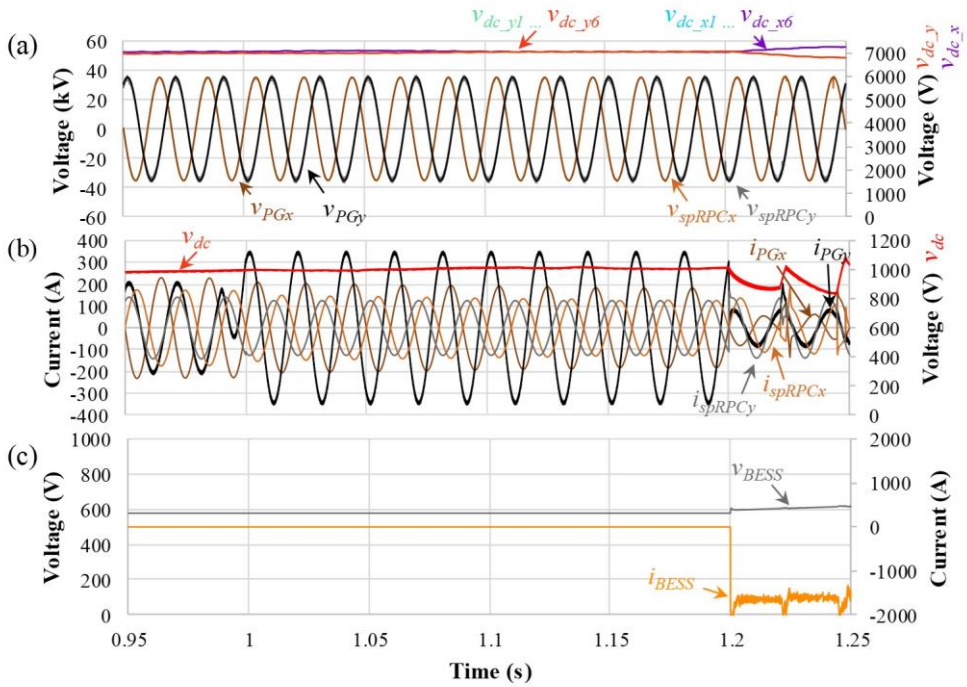

Figure Ap. C.3 – Detailed simulation results, during the time interval from 0.95 s to 1.25 s, for the real scale sp-RPC with the BESS during the case scenario A: (a) the voltages on each TPS, v_{PGx} and v_{PGy}, the output voltages of the *spRPCx* and *spRPCy*, v_{spRPCx} and v_{spRPCy}, and voltages on the dc-link of each submodule, v_{dc_x1} to v_{dc_x6}, and v_{dc_y1} to v_{dc_y6}; (b) the currents on each TPS, i_{PGx} and i_{PGy}, and the output currents of the sp-RPC, i_{spRPCx} and i_{spRPCy}., and the voltage of the common dc-link voltage, v_{dc}; (c) voltage and current on the BESS, v_{BESS} and i_{BESS}.

Figure Ap. C.4 shows the simulation results during time instants from 1.55 s to 1.85 s of Figure 4.17, when the BESS is fully charged. Figure Ap. C.4 (a) it is possible to verify the voltages of each TPS, v_{PGx} and v_{PGy}, as well as the voltages on each side of the sp-RPC, v_{spRPCx} and v_{spRPCy}. Moreover, it is possible to see that v_{dc_x6} has an average value of 6.86 kV, while v_{dc_y6} has an average value of 7.12 kV during

this interval. The remaining voltages have similar values of the dc-link on the same side. Analyzing Figure Ap. C.4 (b), it is possible to verify that until the instant 1.6 s, the amplitudes of i_{PGx} and i_{PGy} presents a maximum value of 36.07 A and 86.25 A, respectively. At this time, i_{spRPCx} has a maximum value of 93.02 A, while i_{spRPCy} has a maximum value of 143.0 A. However, at 0.81 s with the BESS fully discharged, the active power from each TPS starts to increase, increasing the amplitudes of each current. Nevertheless, it is also possible to see that despite the perturbation, v_{dc} shows an average value of 1.02 kV during this interval. Finally, Figure Ap. C.4 (c) shows that when the BESS reach the value of 747.1 V on v_{BESS} and -1336.3 A on i_{BESS}., is fully charged, being disabled.

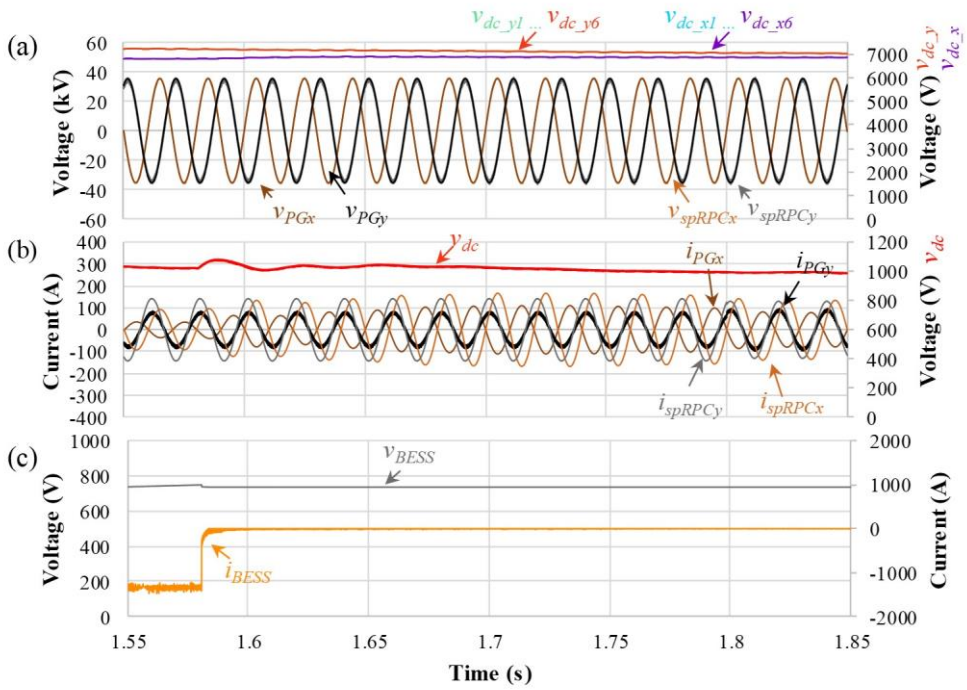

Figure Ap. C.4 – Detailed simulation results, during the time interval from 0.95 s to 1.25 s, for the real scale sp-RPC with the BESS during the case scenario A: (a) the voltages on each TPS, v_{PGx} and v_{PGy}, the output voltages of the *spRPCx* and *spRPCy*, v_{spRPCx} and v_{spRPCy}, and voltages on the dc-link of each submodule, v_{dc_x1} to v_{dc_x6}, and v_{dc_y1} to v_{dc_y6}; (b) the currents on each TPS, i_{PGx} and i_{PGy}, and the output currents of the sp-RPC, i_{spRPCx} and i_{spRPCy}., and the voltage of the common dc-link voltage, v_{dc}; (c) voltage and current on the BESS, v_{BESS} and i_{BESS}.

Figure Ap. C.5 shows the simulation results during time instants from 1.95 s to 2.25 s, representative of event *iii)* of Figure 4.17. Figure Ap. C.5 (a) it is possible to verify the voltages of each TPS, v_{PGx} and v_{PGy}, as well as the voltages on each side of the sp-RPC, v_{spRPCx} and v_{spRPCy}. Moreover, it is possible to see that v_{dc_x6} has an average value of 7.00 kV, while v_{dc_y6} has an average value of 7.02 kV during this interval. The remaining voltages have similar values of the dc-link on the same side. Analyzing Figure Ap. C.5 (b), it is possible to verify that until the instant 2 s, the amplitudes of i_{PGx} and i_{PGy} presents a maximum value of 64.01 A and 97.33 A, respectively. At this time, i_{spRPCx} has a maximum value of 119.7 A, while i_{spRPCy} has a maximum value of 131.1 A. However, with the variation of R_{Loadx}, i_{PGx}

increases to a maximum amplitude value of 384.5 A and a new unbalance appears. At instant 2.1 s, the proposed control algorithm updates the operation reference values, as can be seen with the amplitude change of the i_{spRPCx} and i_{spRPCy}, being able to verify that i_{PGx} and i_{PGy} converge again to similar amplitude values. Nevertheless, it is also possible to see that despite the perturbation, v_{dc} shows an average value of 1 kV during this interval. Finally, Figure Ap. C.5 (c) shows that with a new acceleration from R_{Loady}, BESS starts to discharge, presenting an average value of 704.2 V on v_{BESS} and 1421.4 A on i_{BESS}.

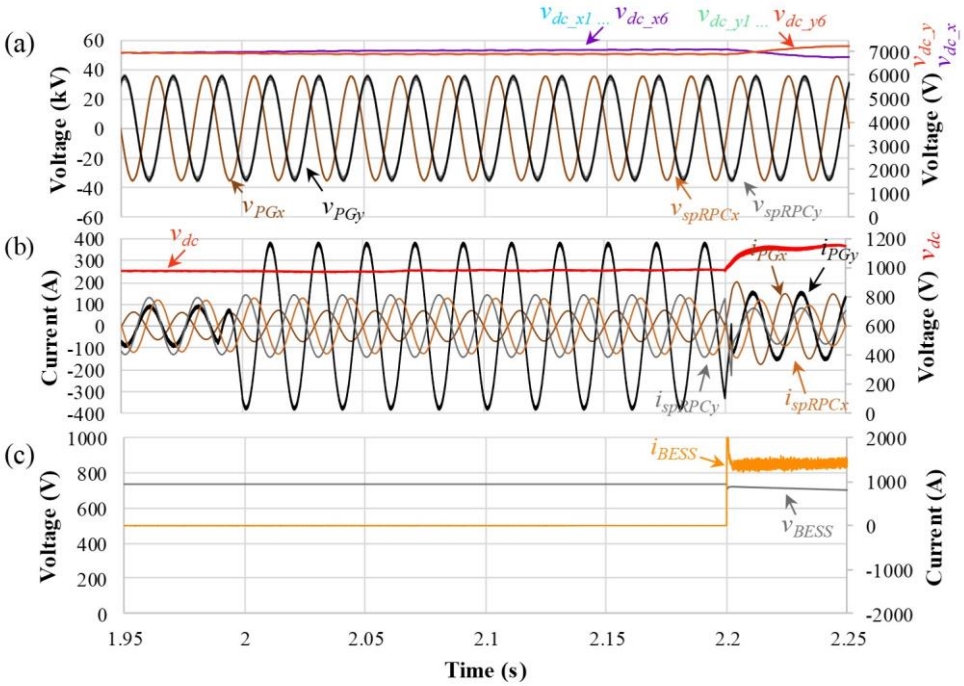

Figure Ap. C.5 – Detailed simulation results, during the time interval from 1.95 s to 2.25 s, for the real scale sp-RPC with the BESS during the case scenario A: (a) the voltages on each TPS, v_{PGx} and v_{PGy}, the output voltages of the *spRPCx* and *spRPCy*, v_{spRPCx} and v_{spRPCy}, and voltages on the dc-link of each submodule, v_{dc_x1} to v_{dc_x6}, and v_{dc_y1} to v_{dc_y6}; (b) the currents on each TPS, i_{PGx} and i_{PGy}, and the output currents of the sp-RPC, i_{spRPCx} and i_{spRPCy}., and the voltage of the common dc-link voltage, v_{dc}; (c) voltage and current on the BESS, v_{BESS} and i_{BESS}.

Figure Ap. C.6 shows the simulation results during time instants from 2.3 s to 2.6 s of Figure 4.17. Figure Ap. C.6 (a) it is possible to verify the voltages of each TPS, v_{PGx} and v_{PGy}, as well as the voltages on each side of the sp-RPC, v_{spRPCx} and v_{spRPCy}. Moreover, it is possible to see that v_{dc_x6} has an average value of 7.20 kV, while v_{dc_y6} has an average value of 6.79 kV during this interval. The remaining voltages have similar values of the dc-link on the same side. Analyzing Figure Ap. C.6 (b), it is possible to verify that until the instant 2.55 s, the amplitudes of i_{PGx} and i_{PGy} were similar, obtaining a maximum value of 136.4 A and 126.7 A, respectively. At this time, i_{spRPCx} has a maximum value of 77.74 A, while i_{spRPCy} has a maximum value of 126.9 A. However, at 2.56 s with the BESS fully discharged, the active power from each TPS starts to increase, increasing the amplitudes of each current. Nevertheless, it is also

possible to see that despite the perturbation, v_{dc} shows an average value of 0.96 kV during this interval. Finally, Figure Ap. C.6 (c) shows that the BESS reach the value of 559.8 V on v_{BESS} and 1838.9 A on i_{BESS}, is fully discharged, being disabled.

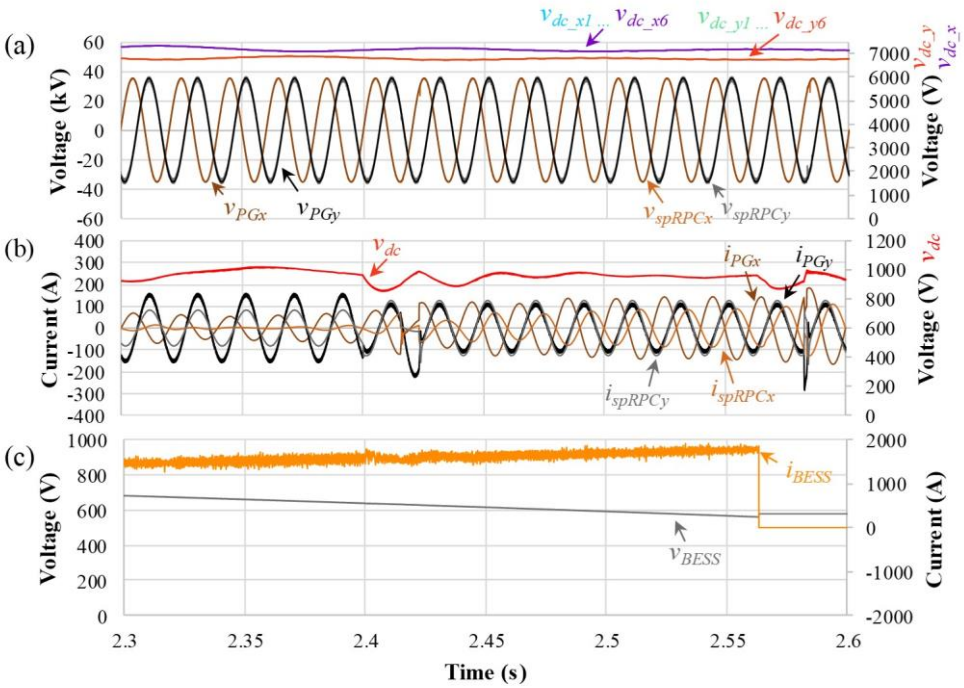

Figure Ap. C.6 – Detailed simulation results, during the time interval from 2.3 s to 2.6 s, for the real scale sp-RPC with the BESS during the case scenario A: (a) the voltages on each TPS, v_{PGx} and v_{PGy}, the output voltages of the *spRPCx* and *spRPCy*, v_{spRPCx} and v_{spRPCy}, and voltages on the dc-link of each submodule, v_{dc_x1} to v_{dc_x6}, and v_{dc_y1} to v_{dc_y6}; (b) the currents on each TPS, i_{PGx} and i_{PGy}, and the output currents of the sp-RPC, i_{spRPCx} and i_{spRPCy}., and the voltage of the common dc-link voltage, v_{dc}; (c) voltage and current on the BESS, v_{BESS} and i_{BESS}.

Finally, the final result is presented in Figure Ap. C.7 during the instant 2.9 s to 3 s of Figure 4.17, when the system is in steady-state operation. Figure Ap. C.7 (a) it is possible to verify the voltages of each TPS, v_{PGx} and v_{PGy}, as well as the voltages on each side of the sp-RPC, v_{spRPCx} and v_{spRPCy}. Moreover, it is possible to see that v_{dc_x6} has an average value of 7 kV, while v_{dc_y6} has an average value of 7.10 kV during this interval. The remaining voltages have similar values of the dc-link on the same side. Analyzing Figure Ap. C.7 (b), it is possible to verify that i_{PGx} and i_{PGy} presents a similar amplitude value, obtaining a maximum amplitude value of 135.0 A and 166.6 A, respectively. At this time, i_{spRPCx} has a maximum value of 77.59 A, while i_{spRPCy} has a maximum value of 76.31 A. Nevertheless, it is also possible to see that despite the perturbation, v_{dc} shows an average value of 1.03 kV during this interval. Finally, Figure Ap. C.7 (c) shows that the BESS fully discharged, presenting an average value of 578.5 V on v_{BESS} and 0 A on i_{BESS}.

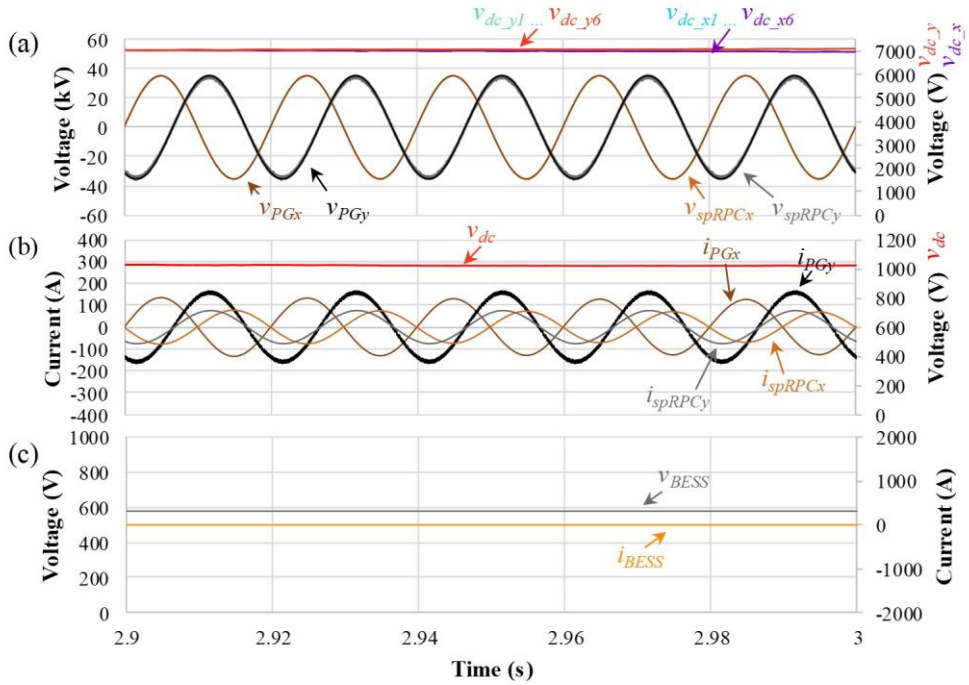

Figure Ap. C.7 – Detailed simulation results, during the time interval from 2.9 s to 3 s, for the real scale sp-RPC with the BESS during the case scenario A: (a) the voltages on each TPS, v_{PGx} and v_{PGy}, the output voltages of the *spRPCx* and *spRPCy*, v_{spRPCx} and v_{spRPCy}, and voltages on the dc-link of each submodule, v_{dc_x1} to v_{dc_x6}, and v_{dc_y1} to v_{dc_y6}; (b) the currents on each TPS, i_{PGx} and i_{PGy}, and the output currents of the sp-RPC, i_{spRPCx} and i_{spRPCy}., and the voltage of the common dc-link voltage, v_{dc}; (c) voltage and current on the BESS, v_{BESS} and i_{BESS}.

Case Scenario B

In the following simulation results the operation of the sp-RPC with the BESS enabled and the solar PV system disabled, representative of the results presented in Figure 4.18, is analyzed in more detail.

Figure Ap. C.8 a greater detail of the system operation during the time interval from 0.3 s to 0.6 s of Figure 4.18. In Figure Ap. C.8 (a) it is possible to verify the voltages of each TPS, v_{PGx} and v_{PGy}, as well as the voltages on each side of the sp-RPC, v_{spRPCx} and v_{spRPCy}. Moreover, it is possible to check the dc-link voltages from v_{dc_x1} to v_{dc_x6} and from v_{dc_y1} to v_{dc_y1}, showing an initial disturbance caused by the start of operation, but maintaining a constant desired average value of 7 kV. In Figure Ap. C.8 (b) it is possible to verify that as soon as the sp-RPC starts operating, synthesizing i_{spRPCx} and i_{spRPCy}, it was possible to equalize the amplitudes of the i_{PGx} and i_{PGy}. Nevertheless, it is also possible to see that despite the initial perturbation, v_{dc} remains regulated at a value of 1 kV. Finally, by analyzing Figure Ap. C.8 (c), it is possible to verify the beginning of operation of the BESS, being possible to see that v_{BESS} converges to an average value of 735.2V, while i_{BESS} converges to an average value of 1381.1 A.

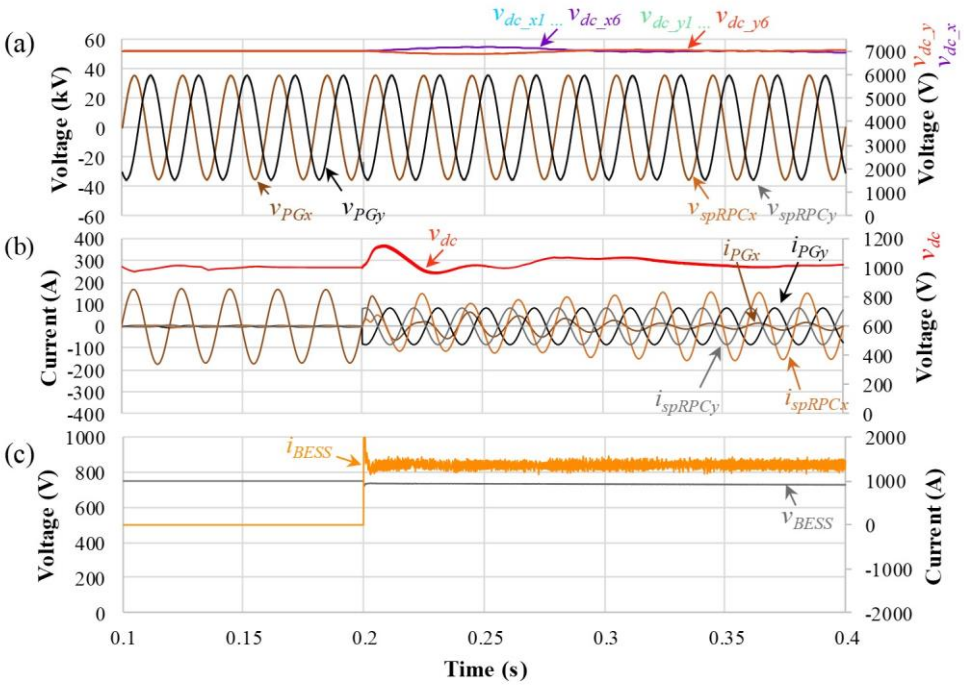

Figure Ap. C.8 – Detailed simulation results, during the time interval from 0.3 s to 0.6 s, for the real scale sp-RPC with the BESS during the case scenario B: (a) the voltages on each TPS, v_{PGx} and v_{PGy}, the output voltages of the *spRPCx* and *spRPCy*, v_{spRPCx} and v_{spRPCy}, and voltages on the dc-link of each submodule, v_{dc_x1} to v_{dc_x6}, and v_{dc_y1} to v_{dc_y6}; (b) the currents on each TPS, i_{PGx} and i_{PGy}, and the output currents of the sp-RPC, i_{spRPCx} and i_{spRPCy}., and the voltage of the common dc-link voltage, v_{dc}; (c) voltage and current on the BESS, v_{BESS} and i_{BESS}.

Continuing with the analysis, it is possible to verify in more detail in Figure Ap. C.9 the operation of the system between the time instants from 0.95 s to 1.25 s, representative of event *ii)* of Figure 4.18. Figure Ap. C.9 (a) it is possible to verify the voltages of each TPS, v_{PGx} and v_{PGy}, as well as the voltages on each side of the sp-RPC, v_{spRPCx} and v_{spRPCy}. Moreover, it is possible to see that v_{dc_x6} has an average value of 7.04 kV, while v_{dc_y6} has an average value of 6.97 kV during this interval. The remaining voltages have similar values of the dc-link on the same side. Analyzing Figure Ap. C.9 (b), it is possible to verify that until the instant 1 s, the amplitudes of i_{PGx} and i_{PGy} were similar, obtaining a maximum value of 57.8 A and 63.93 A, respectively. At this time, i_{spRPCx} has a maximum value of 112 A, while i_{spRPCy} has a maximum value of 63.97 A. However, with the variation of R_{Loady}, starting regenerative braking, i_{PGy} increases to a maximum amplitude value of 120.3 A and a new unbalance appears. At instant 1.1 s, the proposed control algorithm updates the operation reference values, as can be seen with the amplitude change of the i_{spRPCx} and i_{spRPCy}, being able to verify that i_{PGx} and i_{PGy} converge again to similar amplitude values. Nevertheless, it is also possible to see that despite the perturbation, v_{dc} shows an average value of 1.00 kV during this interval. Finally, Figure Ap. C.9 (c) shows that the BESS maintains a constant operation, been possible to measure an average value of 700.9 V on v_{BESS} and 1426.7 A on i_{BESS}.

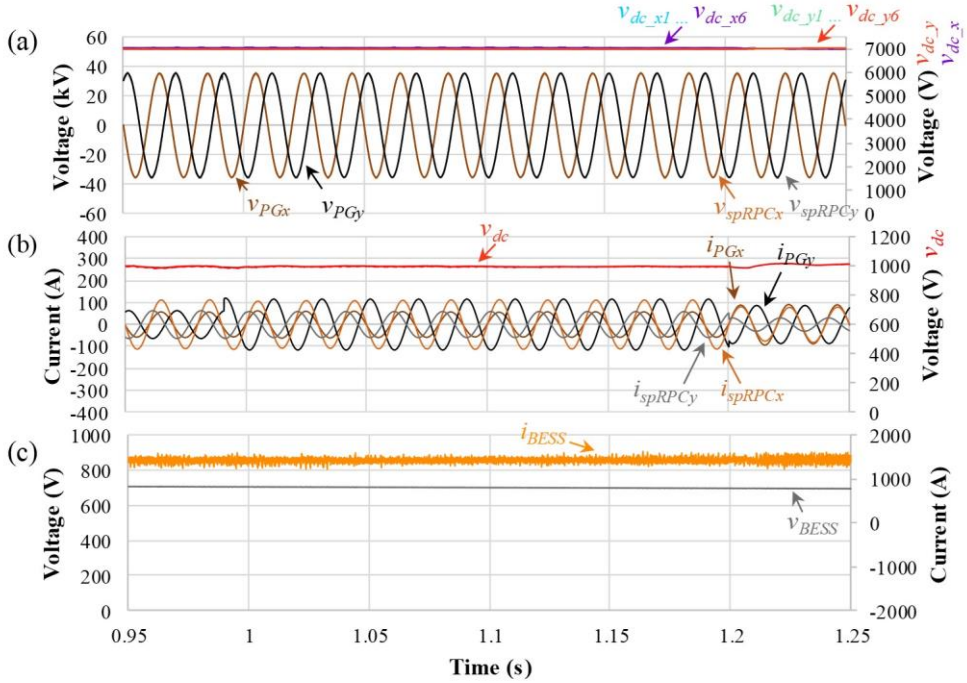

Figure Ap. C.9 – Detailed simulation results, during the time interval from 0.95 s to 1.25 s, for the real scale sp-RPC with the BESS during the case scenario B: (a) the voltages on each TPS, v_{PGx} and v_{PGy}, the output voltages of the *spRPCx* and *spRPCy*, v_{spRPCx} and v_{spRPCy}, and voltages on the dc-link of each submodule, v_{dc_x1} to v_{dc_x6}, and v_{dc_y1} to v_{dc_y6}; (b) the currents on each TPS, i_{PGx} and i_{PGy}, and the output currents of the sp-RPC, i_{spRPCx} and i_{spRPCy}., and the voltage of the common dc-link voltage, v_{dc}; (c) voltage and current on the BESS, v_{BESS} and i_{BESS}.

Figure Ap. C.10 shows the simulation results during time instants from 1.95 s to 2.25 s, representative of event *iii)* of Figure 4.18. Figure Ap. C.10 (a) it is possible to verify the voltages of each TPS, v_{PGx} and v_{PGy}, as well as the voltages on each side of the sp-RPC, v_{spRPCx} and v_{spRPCy}. Moreover, it is possible to see that v_{dc_x6} has an average value of 6.96 kV, while v_{dc_y6} has an average value of 7.02 kV during this interval. The remaining voltages have similar values of the dc-link on the same side. Analyzing Figure Ap. C.10 (b), it is possible to verify that until the instant 2 s, the amplitudes of i_{PGx} and i_{PGy} were similar, obtaining a maximum value of 87.75 A and 88.31 A, respectively. At this time, i_{spRPCx} has a maximum value of 82.13 A, while i_{spRPCy} has a maximum value of 31.82 A. However, with the variation of R_{Loadx}, i_{PGx} decreases to a maximum amplitude value of 33.36 A and a new unbalance appears. At instant 2.1 s, the proposed control algorithm updates the operation reference values, as can be seen with the amplitude change of the i_{spRPCx} and i_{spRPCy}, being able to verify that i_{PGx} and i_{PGy} converge again to similar amplitude values. Nevertheless, it is also possible to see that despite the perturbation, v_{dc} shows an average value of 1 kV during this interval. Finally, Figure Ap. C.10 (c) shows that the BESS maintains a constant operation, been possible to measure an average value of 659.1 V on v_{BESS} and 1516.9 A on i_{BESS}.

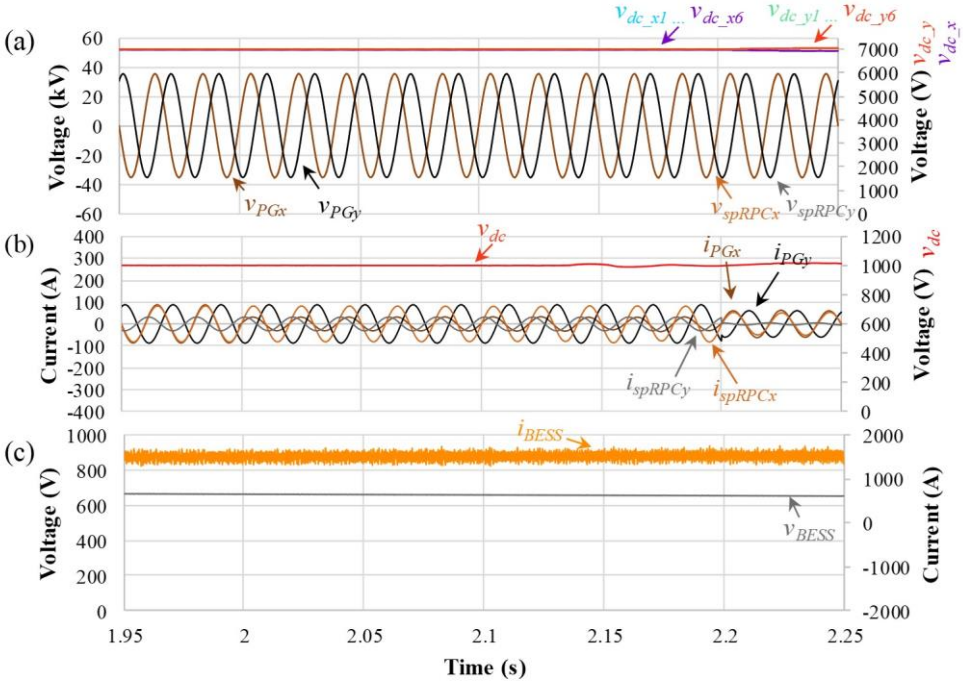

Figure Ap. C.10 – Detailed simulation results, during the time interval from 1.95 s to 2.25 s, for the real scale sp-RPC with the BESS during the case scenario B: (a) the voltages on each TPS, v_{PGx} and v_{PGy}, the output voltages of the *spRPCx* and *spRPCy*, v_{spRPCx} and v_{spRPCy}, and voltages on the dc-link of each submodule, v_{dc_x1} to v_{dc_x6}, and v_{dc_y1} to v_{dc_y6}; (b) the currents on each TPS, i_{PGx} and i_{PGy}, and the output currents of the sp-RPC, i_{spRPCx} and i_{spRPCy}., and the voltage of the common dc-link voltage, v_{dc}; (c) voltage and current on the BESS, v_{BESS} and i_{BESS}.

Finally, the final result is presented in Figure Ap. C.11 during the instant 2.9 s to 3 s of Figure 4.18, when the system is in steady-state operation. Figure Ap. C.11 (a) it is possible to verify the voltages of each TPS, v_{PGx} and v_{PGy}, as well as the voltages on each side of the sp-RPC, v_{spRPCx} and v_{spRPCy}. Moreover, it is possible to see that v_{dc_x6} has an average value of 6.98 kV, while v_{dc_y6} has an average value of 7.00 kV during this interval. The remaining voltages have similar values of the dc-link on the same side. Analyzing Figure Ap. C.11 (b), it is possible to verify that i_{PGx} and i_{PGy} presents a similar amplitude value, obtaining a maximum amplitude value of 59.66 A and 59.87 A, respectively. At this time, i_{spRPCx} has a maximum value of 55.23 A, while i_{spRPCy} has a maximum value of 4.29 A. Nevertheless, it is also possible to see that despite the perturbation, v_{dc} shows an average value of 1 kV during this interval. Finally, Figure Ap. C.11 (c) shows that the BESS maintains a constant operation, been possible to measure an average value of 621.4 V on v_{BESS} and 1609.4 A on i_{BESS}.

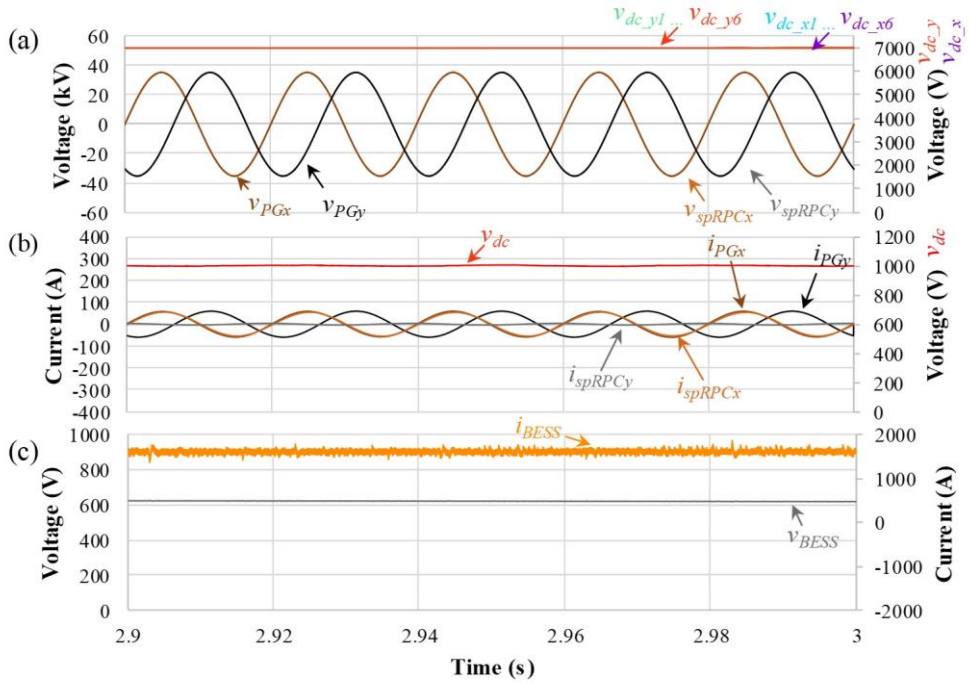

Figure Ap. C.11 – Detailed simulation results, during the time interval from 2.9 s to 3 s, for the real scale sp-RPC with the BESS during the case scenario B: (a) the voltages on each TPS, v_{PGx} and v_{PGy}, the output voltages of the *spRPCx* and *spRPCy*, v_{spRPCx} and v_{spRPCy}, and voltages on the dc-link of each submodule, v_{dc_x1} to v_{dc_x6}, and v_{dc_y1} to v_{dc_y6}; (b) the currents on each TPS, i_{PGx} and i_{PGy}, and the output currents of the sp-RPC, i_{spRPCx} and i_{spRPCy}., and the voltage of the common dc-link voltage, v_{dc}; (c) voltage and current on the BESS, v_{BESS} and i_{BESS}.

Appendix D
Detailed Simulation Result of the sp-RPC based on SST with Solar PV System and BESS with Dynamic Control

Case Scenario A

In the following simulation results the operation of the sp-RPC with the solar PV system and BESS enabled, representative of the results presented in Figure 4.19, is analyzed in more detail.

Figure Ap. D.1 presents a greater detail of the system operation during the time interval from 0.3 s to 0.6 s of Figure 4.19. In Figure Ap. D.1 (a) it is possible to verify the voltages of each TPS, v_{PGx} and v_{PGy}, as well as the voltages on each side of the sp-RPC, v_{spRPCx} and v_{spRPCy}. Moreover, it is possible to check the dc-link voltages from v_{dc_x1} to v_{dc_x6} and from v_{dc_y1} to v_{dc_y1}, showing an initial disturbance caused by the start of operation, but maintaining a constant desired average value of 7 kV.

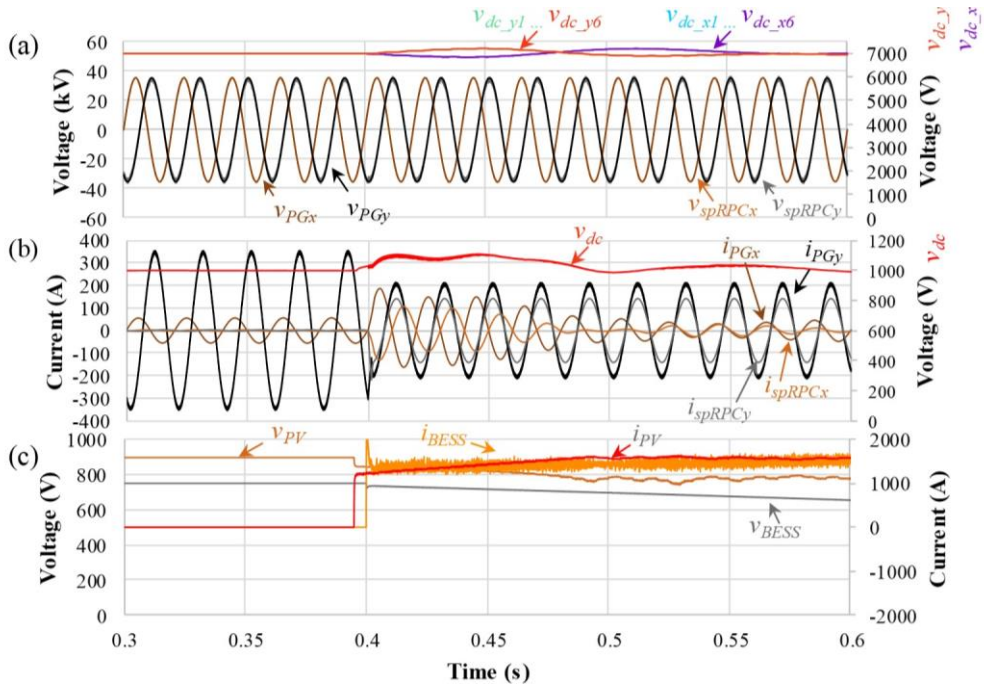

Figure Ap. D.1 – Detailed simulation results, during the time interval from 0.3 s to 0.6 s, for the real scale sp-RPC with the solar PV system and BESS during the case scenario A: (a) the voltages on each TPS, v_{PGx} and v_{PGy}, the output voltages of the *spRPCx* and *spRPCy*, v_{spRPCx} and v_{spRPCy}, and voltages on the dc-link of each submodule, v_{dc_x1} to v_{dc_x6}, and v_{dc_y1} to v_{dc_y6}; (b) the currents on each TPS, i_{PGx} and i_{PGy}, and the output currents of the sp-RPC, i_{spRPCx} and i_{spRPCy}., and the voltage of the common dc-link voltage, v_{dc}; (c) voltage and current on the BESS, v_{BESS} and i_{BESS}, and on the solar PV system, v_{PV} and i_{PV}.

In Figure Ap. D.1 (b) it is possible to verify that as soon as the sp-RPC starts operating, synthesizing i_{spRPCx} and i_{spRPCy}, it was possible to equalize the amplitudes of the i_{PGx} and i_{PGy}. Nevertheless, it is also possible to see that despite the initial perturbation, v_{dc} remains regulated at a value of 1 kV. Finally, by analyzing Figure Ap. D.1 (c), it is possible to verify the beginning of operation of the BESS, being possible

to see that v_{BESS} converge to an average value of 733.6 V, while i_{BESS} converge to an average value of 1433.7 A, at 0.4 s, reaching a value of 656.7 V and 1531.1 A, respectively, at 0.6 s. Regarding the solar PV system, is possible to measure an average value of 789.3 V and 1552.8 A for the v_{PV} and i_{PV}.

Figure Ap. D.2 shows the simulation results during time instants from 0.65 s to 0.95 s of Figure 4.19. Figure Ap. D.2 (a) it is possible to verify the voltages of each TPS, v_{PGx} and v_{PGy}, as well as the voltages on each side of the sp-RPC, v_{spRPCx} and v_{spRPCy}. Moreover, it is possible to see that v_{dc_x6} has an average value of 6.98 kV, while v_{dc_y6} has an average value of 6.89 kV during this interval. The remaining voltages have similar values of the dc-link on the same side.

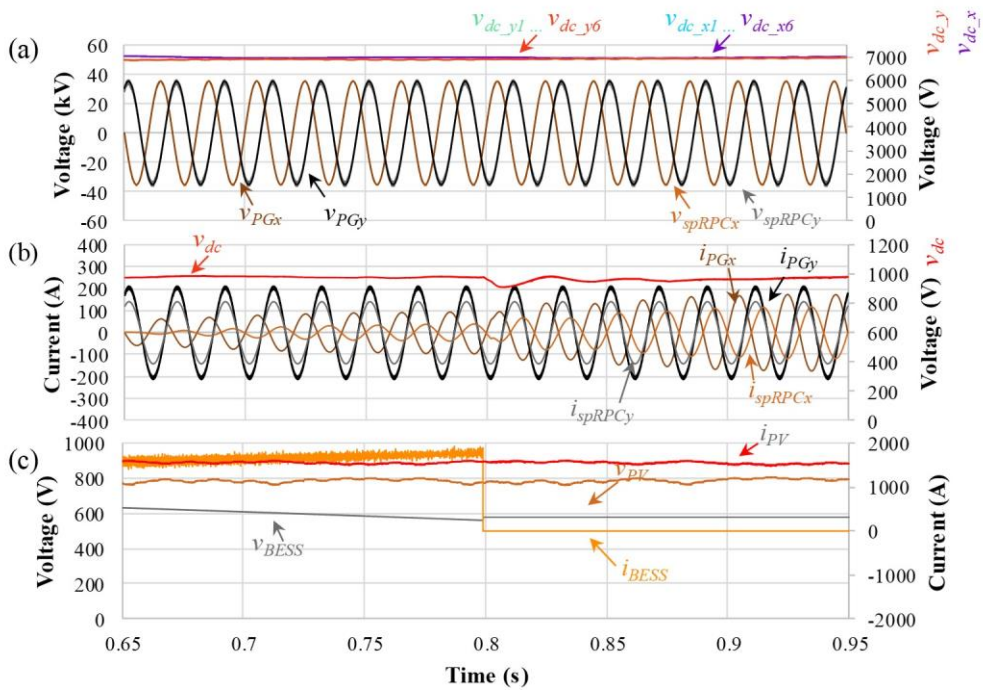

Figure Ap. D.2 – Detailed simulation results, during the time interval from 0.65 s to 0.95 s, for the real scale sp-RPC with the solar PV system and BESS during the case scenario A: (a) the voltages on each TPS, v_{PGx} and v_{PGy}, the output voltages of the *spRPCx* and *spRPCy*, v_{spRPCx} and v_{spRPCy}, and voltages on the dc-link of each submodule, v_{dc_x1} to v_{dc_x6}, and v_{dc_y1} to v_{dc_y6}; (b) the currents on each TPS, i_{PGx} and i_{PGy}, and the output currents of the sp-RPC, i_{spRPCx} and i_{spRPCy}., and the voltage of the common dc-link voltage, v_{dc}; (c) voltage and current on the BESS, v_{BESS} and i_{BESS}, and on the solar PV system, v_{PV} and i_{PV}.

Analyzing Figure Ap. D.2 (b), it is possible to verify that until the instant 0.8 s, the amplitudes of i_{PGx} and i_{PGy} present a maximum value of 115.6 A and 213.0 A, respectively. At this time, i_{spRPCx} has a maximum value of 58.1 A, while i_{spRPCy} has a maximum value of 142.4 A. However, at 0.81 s with the BESS fully discharged, the active power from each TPS starts to increase, increasing the amplitudes of each current. Nevertheless, it is also possible to see that despite the perturbation, v_{dc} shows an average value of 0.97 kV during this interval. Finally, Figure Ap. D.2 (c) shows that the solar PV system maintains a constant operation, been possible to measure an average value of 559.6 V on v_{PV} and 1876.1 A on i_{PV}.

Nevertheless, it is also possible to see that when the BESS reaches the value of 754.9 V on v_{BESS} and 1943.4 A on i_{BESS}., is fully discharged, being disabled.

Continuing with the analysis, it is possible to verify in more detail in Figure Ap. D.3 the operation of the system between the time instants from 0.95 s to 1.25 s, representative of event *ii)* of Figure 4.19. Figure Ap. D.3 (a) it is possible to verify the voltages of each TPS, v_{PGx} and v_{PGy}, as well as the voltages on each side of the sp-RPC, v_{spRPCx} and v_{spRPCy}. Moreover, it is possible to see that v_{dc_x6} has an average value of 7.1 kV, while v_{dc_y6} has an average value of 6.98 kV during this interval. The remaining voltages have similar values of the dc-link on the same side.

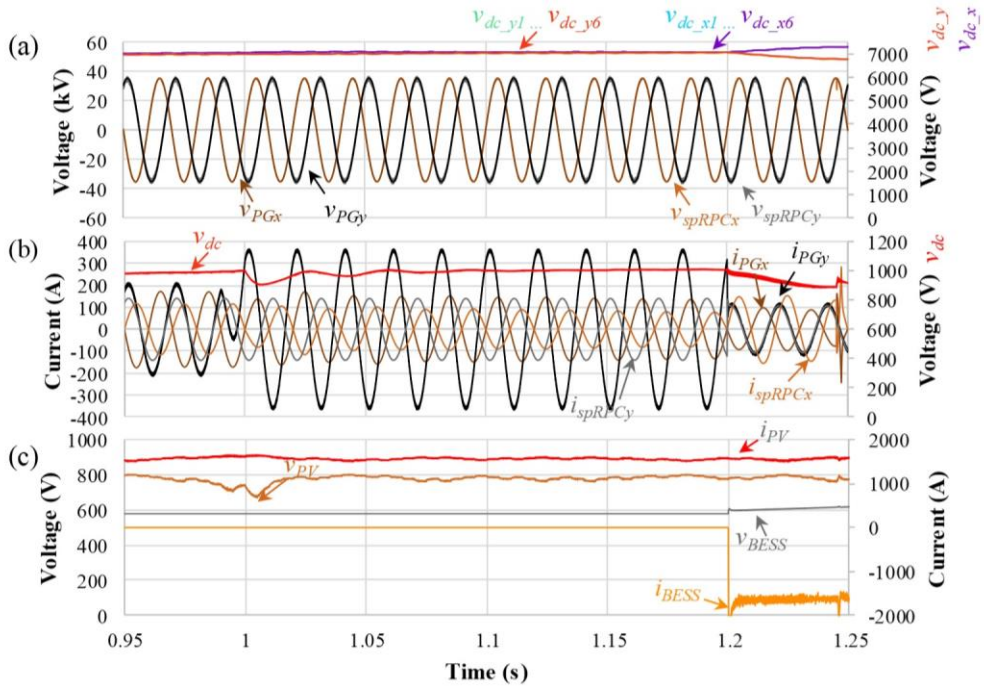

Figure Ap. D.3 – Detailed simulation results, during the time interval from 0.95 s to 1.25 s, for the real scale sp-RPC with the solar PV system and BESS during the case scenario A: (a) the voltages on each TPS, v_{PGx} and v_{PGy}, the output voltages of the *spRPCx* and *spRPCy*, v_{spRPCx} and v_{spRPCy}, and voltages on the dc-link of each submodule, v_{dc_x1} to v_{dc_x6}, and v_{dc_y1} to v_{dc_y6}; (b) the currents on each TPS, i_{PGx} and i_{PGy}, and the output currents of the sp-RPC, i_{spRPCx} and i_{spRPCy}., and the voltage of the common dc-link voltage, v_{dc}; (c) voltage and current on the BESS, v_{BESS} and i_{BESS}, and on the solar PV system, v_{PV} and i_{PV}.

Analyzing Figure Ap. D.3 (b), it is possible to verify that until the instant 1 s, the amplitudes of i_{PGx} and i_{PGy} were similar, obtaining a maximum value of 198.1 A and 212.9 A, respectively. At this time, i_{spRPCx} has a maximum value of 142.4 A, while i_{spRPCy} has a maximum value of 142.6 A. However, with the variation of R_{Loady}, starting regenerative braking, i_{PGy} increases to a maximum amplitude value of 366.9 A and a new unbalance appears. At instant 1.1 s, the proposed control algorithm updates the operation reference values, as can be seen with the amplitude change of the i_{spRPCx} and i_{spRPCy}, being able to verify that i_{PGx} and i_{PGy} converge again to similar amplitude values. Nevertheless, it is also possible to see that despite the perturbation, v_{dc} shows an average value of 0.98 kV during this interval. Finally,

Figure Ap. D.3 (c) shows that the solar PV system maintains a constant operation, been possible to measure an average value of 683.7 V on v_{PV} and 1640.2 A on i_{PV}. Nevertheless, it is also possible to see that with the regenerative braking, the BESS starts to charge, presenting an average value of 618.2 V on v_{BESS} and -1709.5 A on i_{BESS}.

Figure Ap. D.4 shows the simulation results during time instants from 1.55 s to 1.85 s in Figure 4.19. Figure Ap. D.4 (a) it is possible to verify the voltages of each TPS, v_{PGx} and v_{PGy}, as well as the voltages on each side of the sp-RPC, v_{spRPCx} and v_{spRPCy}. Moreover, it is possible to see that v_{dc_x6} has an average value of 6.82 kV, while v_{dc_y6} has an average value of 7.15 kV during this interval. The remaining voltages have similar values of the dc-link on the same side.

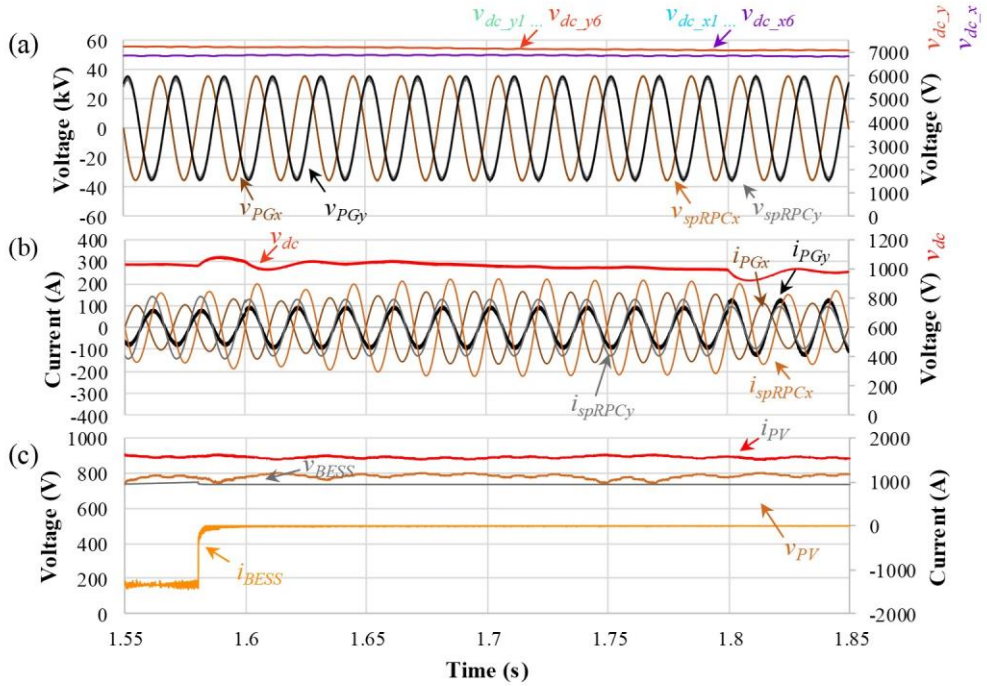

Figure Ap. D.4 – Detailed simulation results, during the time interval from 1.55 s to 1.85 s, for the real scale sp-RPC with the solar PV system and BESS during the case scenario A: (a) the voltages on each TPS, v_{PGx} and v_{PGy}, the output voltages of the *spRPCx* and *spRPCy*, v_{spRPCx} and v_{spRPCy}, and voltages on the dc-link of each submodule, v_{dc_x1} to v_{dc_x6}, and v_{dc_y1} to v_{dc_y6}; (b) the currents on each TPS, i_{PGx} and i_{PGy}, and the output currents of the sp-RPC, i_{spRPCx} and i_{spRPCy}., and the voltage of the common dc-link voltage, v_{dc}; (c) voltage and current on the BESS, v_{BESS} and i_{BESS}, and on the solar PV system, v_{PV} and i_{PV}.

Analyzing Figure Ap. D.4 (b), it is possible to verify that until the instant 1.6 s, the amplitudes of i_{PGx} and i_{PGy} present a maximum value of 89.89 A and 85.13 A, respectively. At this time, i_{spRPCx} has a maximum value of 150.8 A, while i_{spRPCy} has a maximum value of 143 A. However, at 0.81 s with the BESS fully discharged, the active power from each TPS starts to increase, increasing the amplitudes of each current. Nevertheless, it is also possible to see that despite the perturbation, v_{dc} shows an average value of 1.02 kV during this interval. Finally, Figure Ap. D.4 (c) shows that the solar PV system maintains a constant

operation, been possible to measure an average value of 707.1 V on v_{PV} and 1635.2 A on i_{PV}. Nevertheless, it is also possible to see that when the BESS reaches the value of 750.3 V on v_{BESS} and -1415.2 A on i_{BESS}., is fully discharged, being disabled.

Figure Ap. D.5 shows the simulation results during time instants from 1.95 s to 2.25 s, representative of event *iii)* of Figure 4.19. Figure Ap. D.5 (a) it is possible to verify the voltages of each TPS, v_{PGx} and v_{PGy}, as well as the voltages on each side of the sp-RPC, v_{spRPCx} and v_{spRPCy}. Moreover, it is possible to see that v_{dc_x6} has an average value of 7.05 kV, while v_{dc_y6} has an average value of 6.92 kV during this interval. The remaining voltages have similar values of the dc-link on the same side.

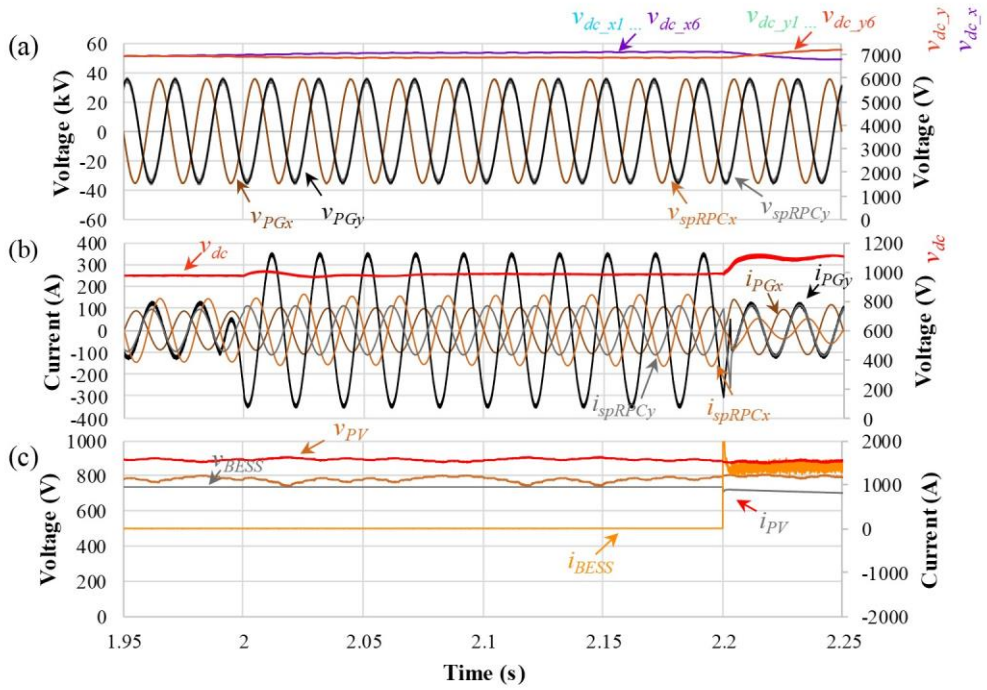

Figure Ap. D.5 – Detailed simulation results, during the time interval from 1.95 s to 2.25 s, for the real scale sp-RPC with the solar PV system and BESS during the case scenario A: (a) the voltages on each TPS, v_{PGx} and v_{PGy}, the output voltages of the *spRPCx* and *spRPCy*, v_{spRPCx} and v_{spRPCy}, and voltages on the dc-link of each submodule, v_{dc_x1} to v_{dc_x6}, and v_{dc_y1} to v_{dc_y6}; (b) the currents on each TPS, i_{PGx} and i_{PGy}, and the output currents of the sp-RPC, i_{spRPCx} and i_{spRPCy}., and the voltage of the common dc-link voltage, v_{dc}; (c) voltage and current on the BESS, v_{BESS} and i_{BESS}, and on the solar PV system, v_{PV} and i_{PV}.

Analyzing Figure Ap. D.5 (b), it is possible to verify that until the instant 2 s, the amplitudes of i_{PGx} and i_{PGy} were similar, obtaining a maximum value of 76.94 A and 118.3 A, respectively. At this time, i_{spRPCx} has a maximum value of 131.9 A, while i_{spRPCy} has a maximum value of 109.4 A. However, with the variation of R_{Loadx}, i_{PGx} increases to a maximum amplitude value of 367.5 A and a new unbalance appears. At instant 2.1 s, the proposed control algorithm updates the operation reference values, as can be seen with the amplitude change of the i_{spRPCx} and i_{spRPCy}, being able to verify that i_{PGx} and i_{PGy} converge again to similar amplitude values. Nevertheless, it is also possible to see that despite the

perturbation, v_{dc} shows an average value of 1.00 kV during this interval. Finally, Figure Ap. D.5 (c) shows that the solar PV system maintains a constant operation, been possible to measure an average value of 741.2 V on v_{PV} and 1620.9 A on i_{PV}. Nevertheless, it is also possible to see that with the regenerative braking, the BESS starts to charge, presenting an average value of 700.8 V on v_{BESS} and 1608.7 A on i_{BESS}.

Figure Ap. D.6 shows the simulation results during time instants from 2.3 s to 2.6 s in Figure 4.19. Figure Ap. D.6 (a) it is possible to verify the voltages of each TPS, v_{PGx} and v_{PGy}, as well as the voltages on each side of the sp-RPC, v_{spRPCx} and v_{spRPCy}. Moreover, it is possible to see that v_{dc_x6} has an average value of 7.22 kV, while v_{dc_y6} has an average value of 6.78 kV during this interval. The remaining voltages have similar values of the dc-link on the same side.

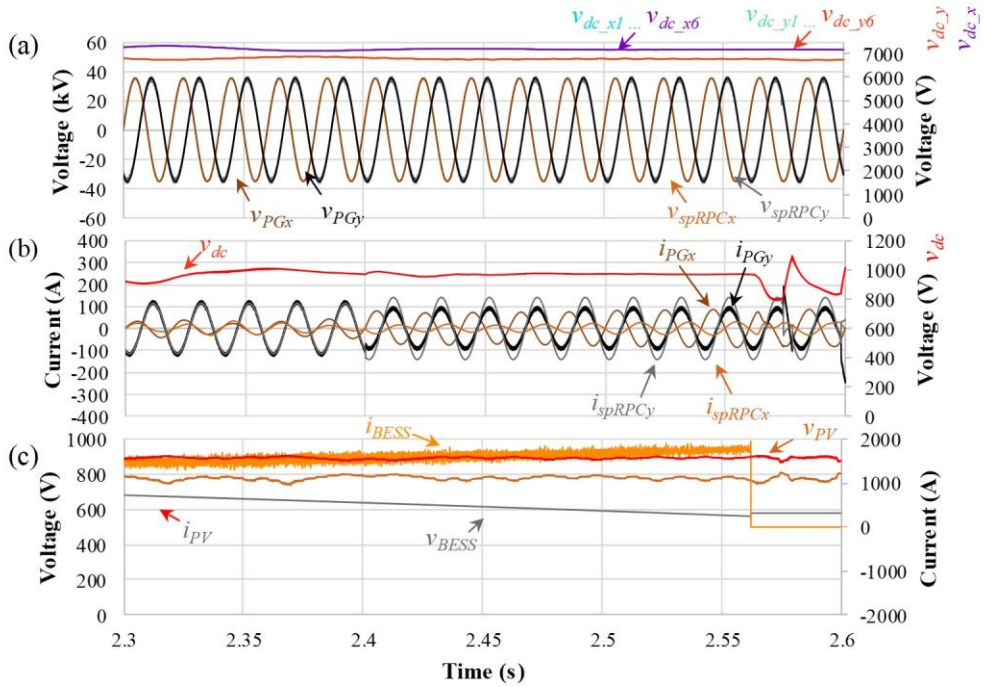

Figure Ap. D.6 – Detailed simulation results, during the time interval from 1.95 s to 2.25 s, for the real scale sp-RPC with the solar PV system and BESS during the case scenario A: (a) the voltages on each TPS, v_{PGx} and v_{PGy}, the output voltages of the *spRPCx* and *spRPCy*, v_{spRPCx} and v_{spRPCy}, and voltages on the dc-link of each submodule, v_{dc_x1} to v_{dc_x6}, and v_{dc_y1} to v_{dc_y6}; (b) the currents on each TPS, i_{PGx} and i_{PGy}, and the output currents of the sp-RPC, i_{spRPCx} and i_{spRPCy}., and the voltage of the common dc-link voltage, v_{dc}; (c) voltage and current on the BESS, v_{BESS} and i_{BESS}, and on the solar PV system, v_{PV} and i_{PV}.

Analyzing Figure Ap. D.6 (b), it is possible to verify that until the instant 2.55 s, the amplitudes of i_{PGx} and i_{PGy} were similar, obtaining a maximum value of 99.88 A and 100.6 A, respectively. At this time, i_{spRPCx} has a maximum value of 40.91 A, while i_{spRPCy} has a maximum value of 142.1 A. However, at 2.56 s with the BESS fully discharged, the active power from each TPS starts to increase, increasing the amplitudes of each current. Nevertheless, it is also possible to see that despite the perturbation, v_{dc} shows an average value of 0.96 kV during this interval. Finally, Figure Ap. D.6 (c) shows that the solar PV

system maintains a constant operation, been possible to measure an average value of 669.6 V on v_{PV} and 1641.6 A on i_{PV}. Nevertheless, it is also possible to see that the BESS reaches the value of 559.6 V on v_{BESS} and 1942.4 A on i_{BESS}, is fully discharged, being disabled.

Finally, the final result is presented in Figure Ap. D.7 during the instant 2.9 s to 3 s of Figure 4.19, when the system is in steady-state operation. Figure Ap. D.7 (a) it is possible to verify the voltages of each TPS, v_{PGx} and v_{PGy}, as well as the voltages on each side of the sp-RPC, v_{spRPCx} and v_{spRPCy}. Moreover, it is possible to see that v_{dc_x6} has an average value of 7.03 kV, while v_{dc_y6} has an average value of 7.13 kV during this interval. The remaining voltages have similar values of the dc-link on the same side.

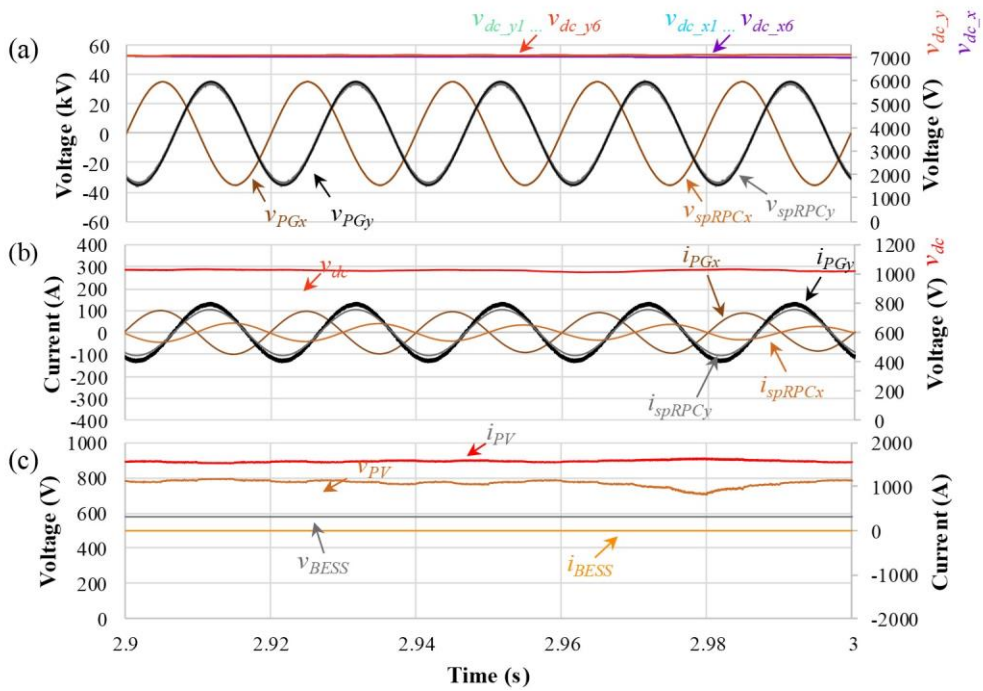

Figure Ap. D.7 – Detailed simulation results, during the time interval from 2.9 s to 3 s, for the real scale sp-RPC with the solar PV system and BESS during the case scenario A: (a) the voltages on each TPS, v_{PGx} and v_{PGy}, the output voltages of the *spRPCx* and *spRPCy*, v_{spRPCx} and v_{spRPCy}, and voltages on the dc-link of each submodule, v_{dc_x1} to v_{dc_x6}, and v_{dc_y1} to v_{dc_y6}; (b) the currents on each TPS, i_{PGx} and i_{PGy}, and the output currents of the sp-RPC, i_{spRPCx} and i_{spRPCy}., and the voltage of the common dc-link voltage, v_{dc}; (c) voltage and current on the BESS, v_{BESS} and i_{BESS}, and on the solar PV system, v_{PV} and i_{PV}.

Analyzing Figure Ap. D.7 (b), it is possible to verify that i_{PGx} and i_{PGy} present a maximum amplitude value of 94.79 A and 155.5 A, respectively. At this time, i_{spRPCx} has a maximum value of 40.89 A, while i_{spRPCy} has a maximum value of 87.35 A. Nevertheless, it is also possible to see that despite the perturbation, v_{dc} shows an average value of 1.03 kV during this interval. Finally, Figure Ap. D.7 (c) shows that the solar PV system maintains a constant operation, been possible to measure an average value of 716.5 V on v_{PV} and 1633 A on i_{PV}. Nevertheless, it is also possible to see that the BESS is fully discharged and disabled, presenting an average value of 579.0 V on v_{BESS} and 0 A on i_{BESS}.

Case Scenario B

In the following images, the operation of the sp-RPC with the solar PV system and BESS enabled, representative of the results presented in Figure 4.20 is analyzed in more detail.

Figure Ap. D.8 presents a greater detail of the system operation during the time interval from 0.35 s to 0.65 s of Figure 4.20, being the BESS activated at 0.4 s. In Figure Ap. D.8 (a) it is possible to verify the voltages of each TPS, v_{PGx} and v_{PGy}, as well as the voltages on each side of the sp-RPC, v_{spRPCx} and v_{spRPCy}. Moreover, it is possible to check the dc-link voltages from v_{dc_x1} to v_{dc_x6} and from v_{dc_y1} to v_{dc_y1}, showing an initial disturbance caused by the start of operation of the BESS, but maintaining a constant desired average value of 7 kV. In Figure Ap. D.8 (b) it is possible to verify that as soon as the BESS and the solar PV system are enabled, the sp-RPC starts to synthesize i_{spRPCx} and i_{spRPCy}, equalizing the amplitudes of the i_{PGx} and i_{PGy}. Nevertheless, it is also possible to see that despite the initial perturbation, v_{dc} remains regulated at a value of 1 kV. Finally, by analyzing Figure Ap. D.8 (c), it is possible to verify the beginning of operation of the BESS, being possible to see that v_{BESS} converges to an average value of 744 V, while i_{BESS} converges to an average value of 573.9 A, at 0.41 s, reaching a value of 738.9 V and 700.4 A, respectively, at 0.65 s. Regarding the solar PV system, is possible to measure an average value of 743.3 V and 1572.5 A for the v_{PV} and i_{PV}.

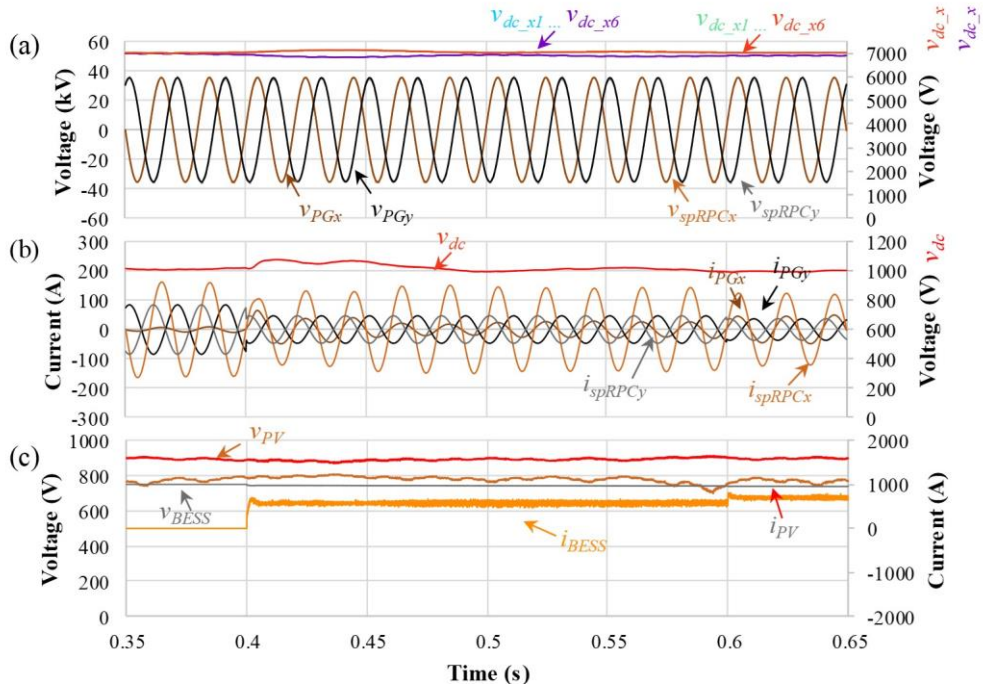

Figure Ap. D.8 – Detailed simulation results, during the time interval from 0.35 s to 0.65 s, for the real scale sp-RPC with the solar PV system and BESS during the case scenario B: (a) the voltages on each TPS, v_{PGx} and v_{PGy}, the output voltages of the *spRPCx* and *spRPCy*, v_{spRPCx} and v_{spRPCy}, and voltages on the dc-link of each submodule, v_{dc_x1} to v_{dc_x6}, and v_{dc_y1} to v_{dc_y6}; (b) the currents on each TPS, i_{PGx} and i_{PGy}, and the output currents of the sp-RPC, i_{spRPCx} and i_{spRPCy}., and the voltage of the common dc-link voltage, v_{dc}; (c) voltage and current on the BESS, v_{BESS} and i_{BESS}, and on the solar PV system, v_{PV} and i_{PV}.

Continuing with the analysis, it is possible to verify in more detail in Figure Ap. D.9 the operation of the system between the time instants from 0.95 s to 1.25 s, representative of event *ii)* of Figure 4.20. Figure Ap. D.9 (a) it is possible to verify the voltages of each TPS, v_{PGx} and v_{PGy}, as well as the voltages on each side of the sp-RPC, v_{spRPCx} and v_{spRPCy}. Moreover, it is possible to see that v_{dc_x6} has an average value of 7.03 kV, while v_{dc_y6} has an average value of 6.98 kV during this interval. The remaining voltages have similar values of the dc-link on the same side.

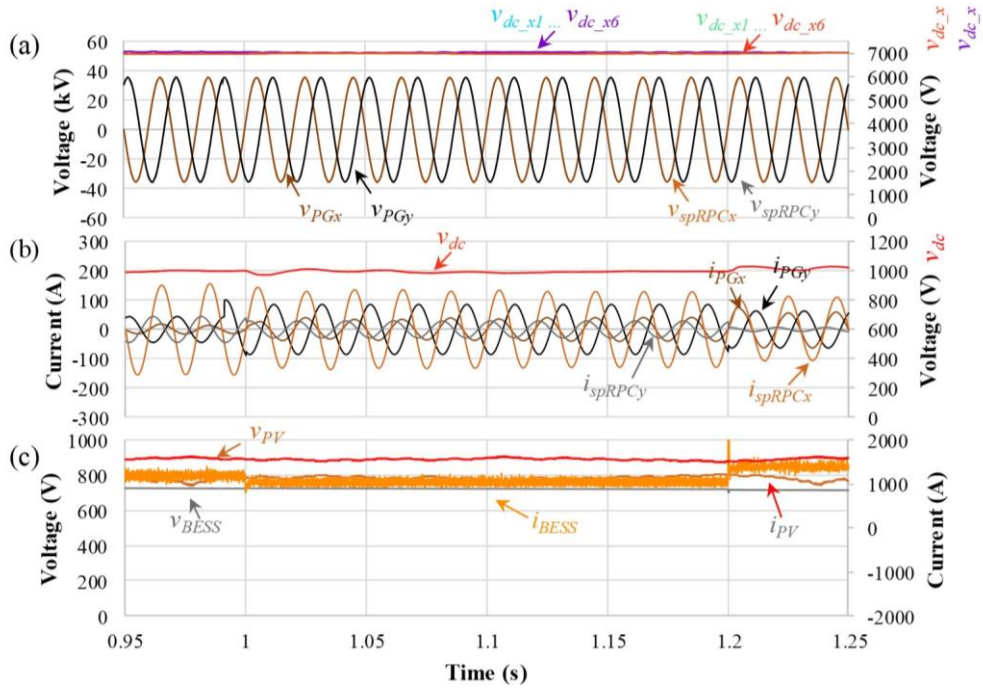

Figure Ap. D.9 – Detailed simulation results, during the time interval from 0.95 s to 1.25 s, for the real scale sp-RPC with the solar PV system and BESS during the case scenario B: (a) the voltages on each TPS, v_{PGx} and v_{PGy}, the output voltages of the *spRPCx* and *spRPCy*, v_{spRPCx} and v_{spRPCy}, and voltages on the dc-link of each submodule, v_{dc_x1} to v_{dc_x6}, and v_{dc_y1} to v_{dc_y6}; (b) the currents on each TPS, i_{PGx} and i_{PGy}, and the output currents of the sp-RPC, i_{spRPCx} and i_{spRPCy}., and the voltage of the common dc-link voltage, v_{dc}; (c) voltage and current on the BESS, v_{BESS} and i_{BESS}, and on the solar PV system, v_{PV} and i_{PV}.

Analyzing Figure Ap. D.9 (b), it is possible to verify that until the instant 1 s, the amplitudes of i_{PGx} and i_{PGy} presented a maximum value of 19.01 A and 44.50 A, respectively. At this time, i_{spRPCx} has a maximum value of 151.2 A, while i_{spRPCy} has a maximum value of 44.55 A. However, with the variation of R_{Loady}, starting regenerative braking, i_{PGy} increases to a maximum amplitude value of 92.04 A and a new unbalance appears. At instant 1.1 s, the proposed control algorithm updates the operation reference values, as can be seen with the amplitude change of the i_{spRPCx} and i_{spRPCy}, being able to verify that i_{PGx} and i_{PGy} converge again to similar amplitude values. Nevertheless, it is also possible to see that despite the perturbation, v_{dc} shows an average value of 1.00 kV during this interval. Finally, Figure Ap. D.9 (c) shows that the PV maintains a constant operation, been possible to measure an average value of 782.3 V on v_{PV} and 1565.1 A on i_{PV}. Regarding the BESS, it is possible to see that presents a small oscillation

due to the regulation of the voltages on the dc-links. However, at 1.25 s v_{BESS} presents an average value of 714.8 V while i_{BESS} presents an average value of 1398.9 A.

Figure Ap. D.10 shows the simulation results during time instants from 1.95 s to 2.25 s, representative of the event *iii)* of Figure 4.20. Figure Ap. D.10 (a) it is possible to verify the voltages of each TPS, v_{PGx} and v_{PGy}, as well as the voltages on each side of the sp-RPC, v_{spRPCx} and v_{spRPCy}. Moreover, it is possible to see that v_{dc_x6} has an average value of 6.99 kV, while v_{dc_y6} has an average value of 7.02 kV during this interval. The remaining voltages have similar values of the dc-link on the same side.

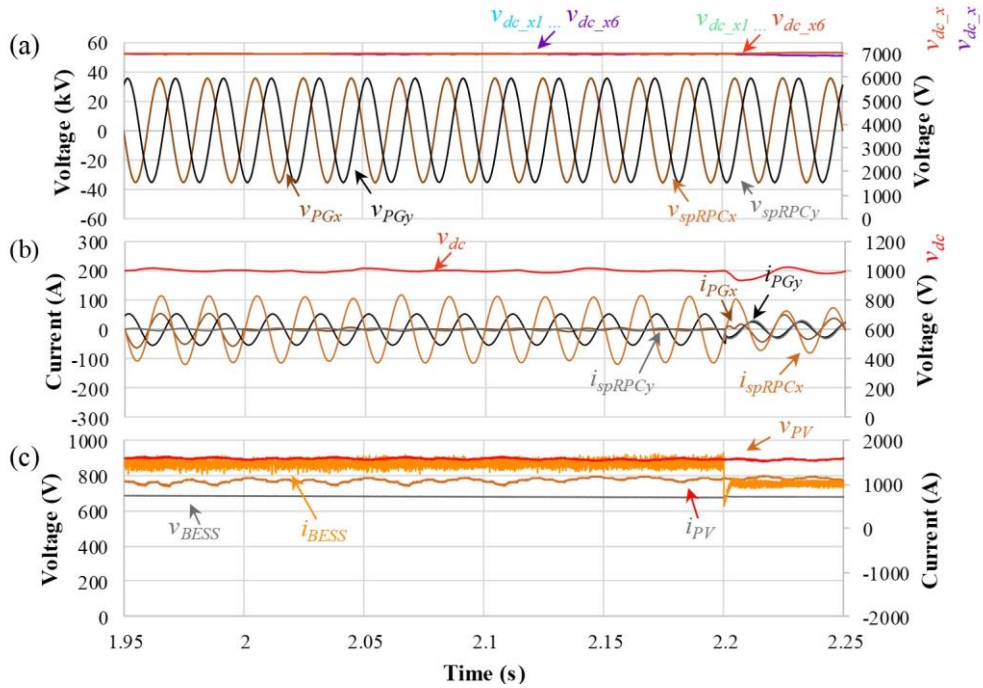

Figure Ap. D.10 – Detailed simulation results, during the time interval from 1.95 s to 2.25 s, for the real scale sp-RPC with the solar PV system and BESS during the case scenario B: (a) the voltages on each TPS, v_{PGx} and v_{PGy}, the output voltages of the *spRPCx* and *spRPCy*, v_{spRPCx} and v_{spRPCy}, and voltages on the dc-link of each submodule, v_{dc_x1} to v_{dc_x6}, and v_{dc_y1} to v_{dc_y6}; (b) the currents on each TPS, i_{PGx} and i_{PGy}, and the output currents of the sp-RPC, i_{spRPCx} and i_{spRPCy}., and the voltage of the common dc-link voltage, v_{dc}; (c) voltage and current on the BESS, v_{BESS} and i_{BESS}, and on the solar PV system, v_{PV} and i_{PV}.

Analyzing Figure Ap. D.10 (b), it is possible to verify that until the instant 2 s, the amplitudes of i_{PGx} and i_{PGy} were similar, obtaining a maximum value of 54.76 A and 54.09 A, respectively. At this time, i_{spRPCx} has a maximum value of 115.4 A, while i_{spRPCy} has a maximum value of 4.08 A. However, with the variation of R_{Loadx}, i_{PGx} decreases to a maximum amplitude value of 6.37 A and a new unbalance appears. At instant 2.1 s, the proposed control algorithm updates the operation reference values, as can be seen with the amplitude change of the i_{spRPCx} and i_{spRPCy}, being able to verify that i_{PGx} and i_{PGy} converge again to similar amplitude values. Finally, Figure Ap. D.10 (c) shows that the solar PV system and the BESS maintains a constant operation. By measuring the average values was possible to obtain 774.1 V on the v_{PV} and 1581.9 A on the i_{PV}. Regarding the BESS, was possible to obtain an average

value of 681 V on the v_{BESS} and 1468.7 A on the i_{BESS}, from 1.95 s to 2.2 s, charging to 671.3 V on the v_{BESS} and 1196.6 A on the i_{BESS}, from 2.24 s to 2.25 s

Finally, the final result is presented in Figure Ap. D.11 during the instant 2.9 s to 3 s of Figure 4.20, when the system is in steady-state operation. Figure Ap. D.11 (a) it is possible to verify the voltages of each TPS, v_{PGx} and v_{PGy}, as well as the voltages on each side of the sp-RPC, v_{spRPCx} and v_{spRPCy}. Moreover, it is possible to see that v_{dc_x6} has an average value of 7.00 kV, while v_{dc_y6} has an average value of 7 kV during this interval. The remaining voltages have similar values of the dc-link on the same side.

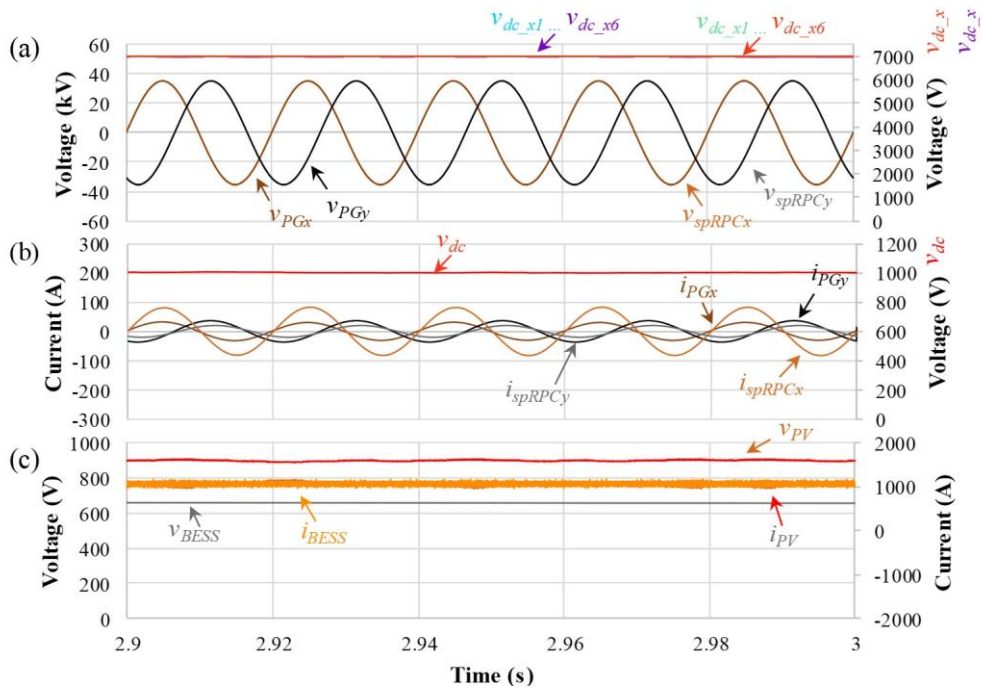

Figure Ap. D.11 – Detailed simulation results, during the time interval from 2.9 s to 3 s, for the real scale sp-RPC with the solar PV system and BESS during the case scenario B: (a) the voltages on each TPS, v_{PGx} and v_{PGy}, the output voltages of the *spRPCx* and *spRPCy*, v_{spRPCx} and v_{spRPCy}, and voltages on the dc-link of each submodule, v_{dc_x1} to v_{dc_x6}, and v_{dc_y1} to v_{dc_y6}; (b) the currents on each TPS, i_{PGx} and i_{PGy}, and the output currents of the sp-RPC, i_{spRPCx} and i_{spRPCy}., and the voltage of the common dc-link voltage, v_{dc}; (c) voltage and current on the BESS, v_{BESS} and i_{BESS}, and on the solar PV system, v_{PV} and i_{PV}.

Analyzing Figure Ap. D.11 (b), it is possible to verify that i_{PGx} and i_{PGy} present a similar amplitude value, obtaining a maximum amplitude value of 32.69 A and 37.02 A, respectively. At this time, i_{spRPCx} has a maximum value of 82.99 A, while i_{spRPCy} has a maximum value of 20.62 A. Nevertheless, it is also possible to see that despite the perturbation, v_{dc} shows an average value of 1 kV during this interval. Finally, Figure Ap. D.11 (c) shows that the solar PV system and the BESS maintains a constant operation. By measuring the average values was possible to obtain 765.6 V on the v_{PV} and 1595.9 A on the i_{PV}, while for the BESS, was possible to obtain 657.9 V on the v_{BESS} and 1063.3 A on the i_{BESS}.

Appendix E
Detailed Simulation Result of the Reduced-Scale Prototype sp-RPC with Dynamic Control

Case Scenario B

In the following simulation results the operation of the reduced-scale sp-RPC with the solar PV system and BESS disabled, representative of the results presented in Figure 4.29, is analyzed in more detail.

Figure Ap. E.1 presents a greater detail of the system operation during the time interval from 0.46 s to 0.56 s of Figure 4.29. In Figure Ap. E.1 (a) it is possible to verify the voltages of each TPS, v_{PGx} and v_{PGy}, as well as the voltages on each side of the sp-RPC, v_{spRPCx} and v_{spRPCy}. Moreover, it is possible to check v_{dc}, showing an initial disturbance caused by the start of operation, but maintaining a constant desired average value. In Figure Ap. E.1 (b) the voltages v_{trfx} and v_{trfy} are presented, being able to verify the different voltage levels generated by the power converter with cascade transformers. Finally, by analyzing Figure Ap. E.1 (c), it is possible to verify that as soon as the sp-RPC starts operating, synthesizing i_{spRPCx} and i_{spRPCy}, allows balancing the amplitudes of the i_{PGx} and i_{PGy}.

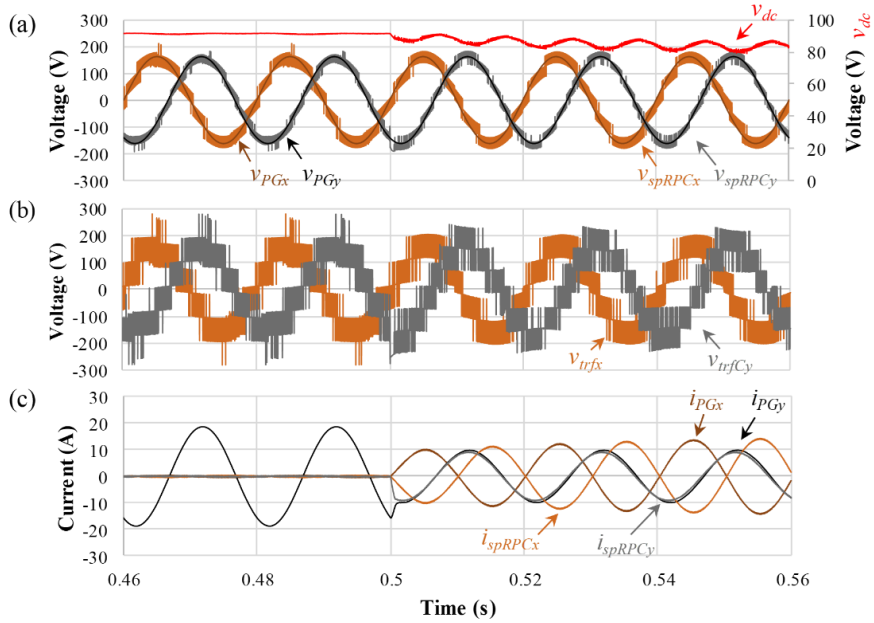

Figure Ap. E.1 – Detailed simulation results, during the time interval from 0.46 s to 0.56 s, for the reduced-scale sp-RPC during the case scenario B: (a) the voltages on each TPS, v_{PGx} and v_{PGy}, the output voltages of the *spRPCx* and *spRPCy*, v_{spRPCx} and v_{spRPCy}, and dc-link voltage, v_{dc}; (b) the output voltages of the cascaded transformers, v_{trfx} and v_{trfy}; (c) the currents on each TPS, i_{PGx} and i_{PGy}, and the output currents of the sp-RPC, i_{spRPCx} and i_{spRPCy}.

Continuing with the analysis, it is possible to verify in more detail in Figure Ap. E.2 the operation of the system between the time interval from 1.35 s to 1.65 s, representative of event *ii)* of Figure 4.29. Figure Ap. E.2 (a) it is possible to verify the voltages of each TPS, v_{PGx} and v_{PGy}, as well as the voltages on each side of the sp-RPC, v_{spRPCx} and v_{spRPCy}. Moreover, it is possible to see that v_{dc} has an average

- To increase the capacitance on the PCB, it is recommended to place the power line close to the ground plane, with a dielectric thickness of approximately 5 mils ;
- The return path signal should be initially analyzed, considering the trace shape and the impedance [276], [278]–[280]. It is also recommended to place a ground plane close to the signal track to minimize noise [281]. If there is any restriction in the ground planes or the number of layers, ensure a signal return path as close as possible, without copper plane breaks, such as vias, other signals, or components in the path to the sent signal [275]. The total inductance will be reduced by the mutual inductance [278];
- Different routing techniques for general purposes used can be found in [275] and in [278] dedicated to OpAmp integrated circuits;
- High-frequency signals should be terminated with an impedance at the end of the line to minimize signal reflection [275]: different termination techniques can be found in [274], [278];
- For each integrated circuit, a decoupling capacitor as close as possible to each supply pin was used [274], [282];
- For each capacitor, it is recommended to add an individual via to the ground plane, to reduce the return path and consequently the inductance [274];
- For general purpose used it is recommended to use a bypass capacitor of 100 Ð for mid frequencies, the use of a capacitor of 10 Ð or 1 Ð for high frequencies, and the use of a capacitor of 1 μF or 10 μF for low frequencies: the use of different values could help to suppress different frequencies in the power line [283];
- Decoupling capacitors with different capacities were used in the voltage regulators as well as in the power inputs of each PCB [274]: the capacitor with a smaller capacitor value should be placed as closely as possible to the voltage pin [284];
- Use of capacitor with a reduced effective series resistance (ESR) value [274], [283];
- Once the differential signals are sensitive to differences between the pair, the routing of these differential signals should be as close as possible [284]: the length of the path is a critical issue once the two signal should arrive at the same time at the next circuit [285] and should keep a minimum distance to other track signals of 30 mils and for a minimum distance of 50 mils of the clock or periodic signals [275];

- Due to the limitation of implementing a 4-layer PCB, the gridding technique was used on the 2-layer PCB: placing vias from the top to bottom layers as many physically possible for the traces with the same power signal [276];
- Each layer was used with predominantly different track layouts (for example, the paths on the top layer running vertically and the traces on the bottom layer running horizontally), to avoid breaking the surrounding ground planes as well as to avoid the crosstalk [276];
- A star-shaped and single-point distribution of feeds was preferably chosen, despite the use of more wire length [276];
- It is recommended to use ferrites beads between the ground planes of digital circuits from the ground planes of analog circuits, as well as at the input of each PCB power supply connection to minimize the noise from the external power supply [274];
- Arrangement of different circuits with different functionalities in different locations on the PCB: Analog circuits away from digital circuits, switching voltage regulators and power sources away from other circuits [274], [275], [278];
- For the signals and a frequency lower than 20 kHz, it is recommended to separate the digital circuit from the analog circuits by 20 H, being the H distance between the signal and the ground plane [286];
- Considering the PCB boundary lines and space limitations, the space between signal lines should be increased whenever possible to avoid the phenomenon of crosstalk [274], [275], [287], [288]: authors of [289] indicate that using the 3 W rule the crosstalk is reduced to 70 % and with the 10 W rule the reduction reaches 98 %. The 3 W rule advises the use of a minimum distance between the center of two parallel tracks of 3 times the width (W) of the track.
- Each signal via should be added a GND via together in order to decrease the impedance [275], [277], [290], [291];
- In [292] can be found information regarding the track width or the clearances considering the operating current and voltages;

Appendix J
Theoretical Analysis of the Cascaded Transformer

Theoretical Study of the T_{trf_f} Ferrite Transformer at 50 V

This topic describes the theoretical analysis of the T_{trf_f} ferrite transformer, considering the parameters presented in Table 5.8. Thus, considering the number of turns, the length of the cable and an MPL of 44 cm, with the aid of the equation (5.19) it was possible to determine a value of L_P and L_S of 148 μH and a value of L_M of 309 mH. The determined values were transported to the simulation model. A full-bridge dc-ac power converter was coupled to the primary winding of the transformer model. The power converter is operating with open-loop unipolar sPWM modulation, with a modulation index of 80 % and a voltage on the dc-link of 50 V. A resistor of 13.3 Ω was coupled to the output of the transformer so that a maximum current of 3.8 A is applied when the maximum 50 V is applied. The results obtained are shown in Figure Ap. J.1.

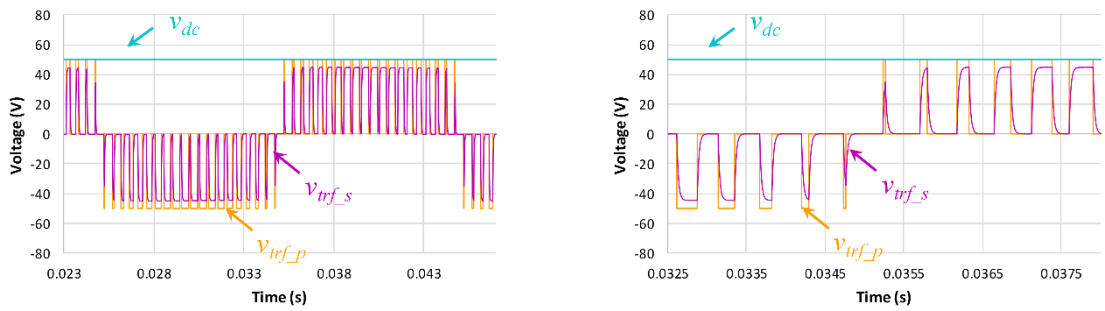

(a) (b)

Figure Ap. J.1 – Simulation result of the computational model developed for the handmade ferrite transformer based on theoretical values.

Theoretical Study of the T_{trf_fp} Primarsec Ferrite Transformer at 90 V

This topic describes the theoretical analysis of the T_{trf_fp} Primarsec ferrite transformer, considering the parameters presented in Table 5.8. The values of L_P and L_S were stipulated to be 1070 μH and the value of L_M to be 965 mH. As expected, and since this new transformer has a winding that is almost 52 % longer, the inductance value obtained is high. Migrating the theoretical values to the simulation model, the voltage on the dc-link was also updated to 90 V and a resistive load of 8.1 Ω to obtain a maximum current of 11.1 A for a power of 1 kVA. Analyzing the simulation results presented in Figure Ap. J.2, it was possible to verify that the output voltage presents a distorted waveform, not following the variation in step obtained in the primary winding of the transformer. Since the primary winding has a high wire length and has been fully wound, the secondary winding has been wound on top. As such, because the magnetic

coupling between turns is not ideal, the leakage impedances present a high value, causing the output voltage to present a greater distortion.

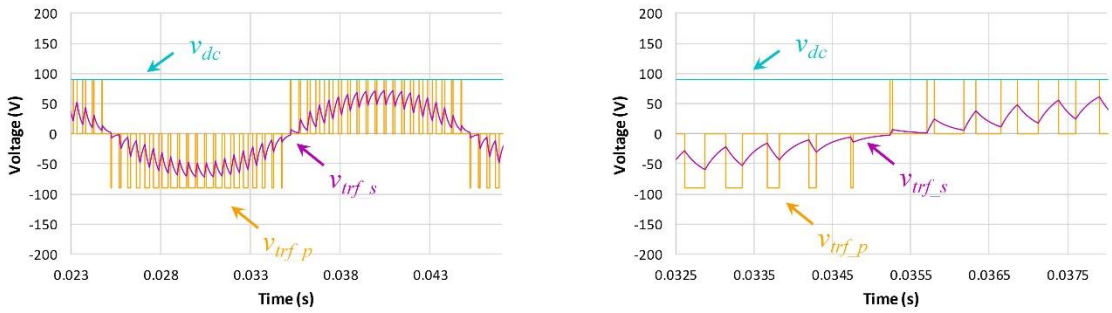

(a) (b)

Figure Ap. J.2 – Simulation result of the computational model developed for the Primarsec ferrite transformer based on real measured values and experimental tests.

Theoretical Study of the T_{trf_a} Amorphous Transformer at 90 V

This topic describes the theoretical analysis of the T_{trf_a} amorphous transformer, considering the parameters presented in Table 5.8. Considering the number of turns, the length of the cable, and an MPL of 34 cm, with the aid of the equation it was possible to determine a value of L_P and L_S of 80.4 μH and a value of L_M of 255 mH. The determined values were transported to the simulation model. A full-bridge dc-ac power converter was coupled to the primary winding of the transformer model. The power converter is operating with open-loop unipolar sPWM modulation, with a modulation index of 80 % and a voltage on the dc-link of 90 V. A resistor of 6.5 Ω was coupled to the output of the transformer. The results obtained are shown in Figure Ap. J.3.

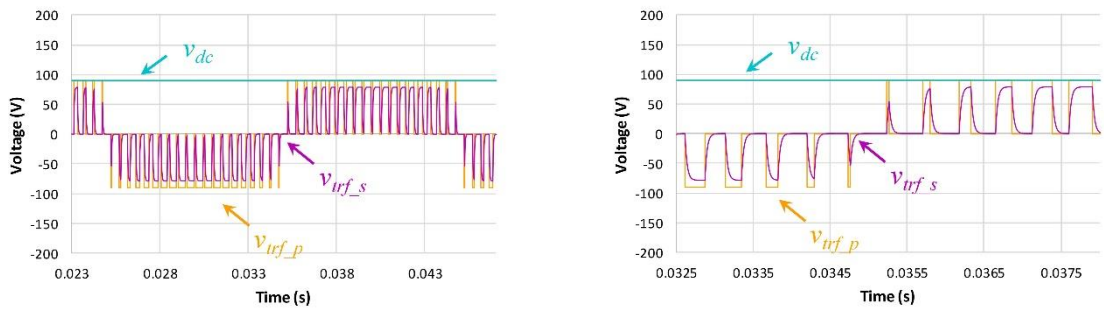

(a) (b)

Figure Ap. J.3 – Simulation result of the computational model developed for the handmade amorphous transformer (T_{trf_a}) based on theoretical values.

Appendix K
Experimental Analysis of the Implemented Transformer for the Cascaded Transformer Topology

Figure Ap. K.1 shows the experimental results obtained with the different transformers, analyzing the current performance with the applied voltage. Analyzing the figures, the result obtained with the ferrite transformer stands out, as can be seen in Figure Ap. K.1 (b) and in Figure Ap. K.1 (f). This phenomenon is due to the high L_P value of the transformer. In order to minimize this effect, it is necessary to couple an inductor with a much higher impedance value to decouple the transformer output voltages from the load voltage. Regarding the other transformers, it is possible to obtain a pulsed output voltage and current.

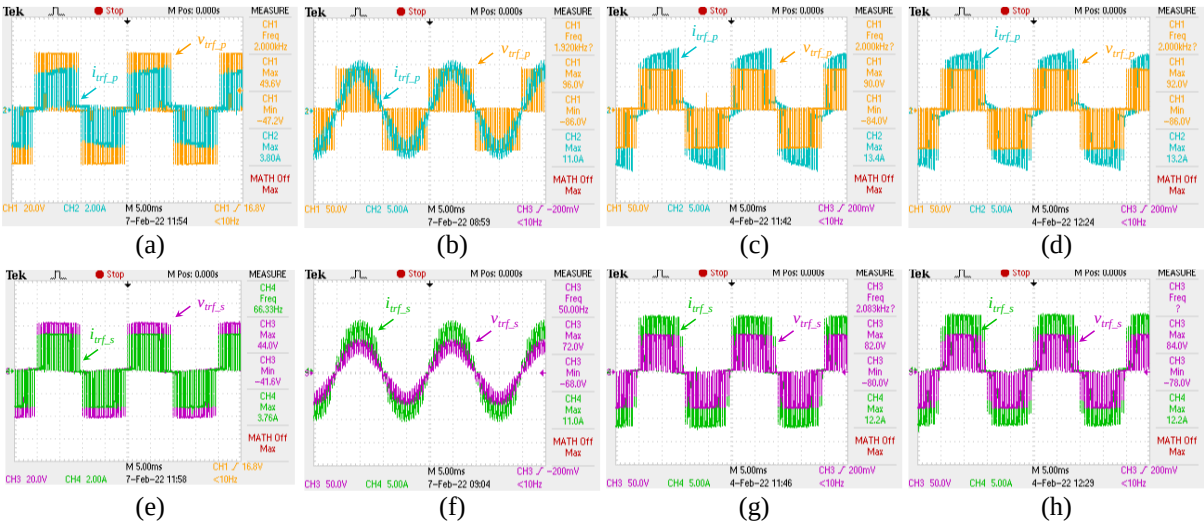

Figure Ap. K.1 – Experimental results of the primary voltage of the transformers (v_{trf_p}) and primary current (i_{trf_p}), with a resistive load of 6.5 Ω (no coupling inductor): (a) T_{trf_f}; (b) T_{trf_fp}; (c) T_{trf_a}; (d) T_{trf1}; (e) T_{trf_f}; (f) T_{trf_fp}; (g) T_{trf_a}; (h) T_{trf1}.

Since the T_{trf_f} transformer presents this phenomenon more evident, a simulation was carried out to compare the output voltages with and without the coupling inductor between the transformer and load. Figure Ap. K.2 shows the simulation results obtained. It is proved that with the insertion of the inductor, it was possible to minimize the distortion previously identified. Analyzing Figure Ap. K.2 (a), and with more detail in Figure Ap. K.2 (c), it is possible to verify a similar result with the waveforms of both current and voltage distorted. In turn, with the insertion of an inductor, it is possible to obtain the desired pulsed waveforms, as shown in Figure Ap. K.2 (b), and with more detail in Figure Ap. K.2 (d).

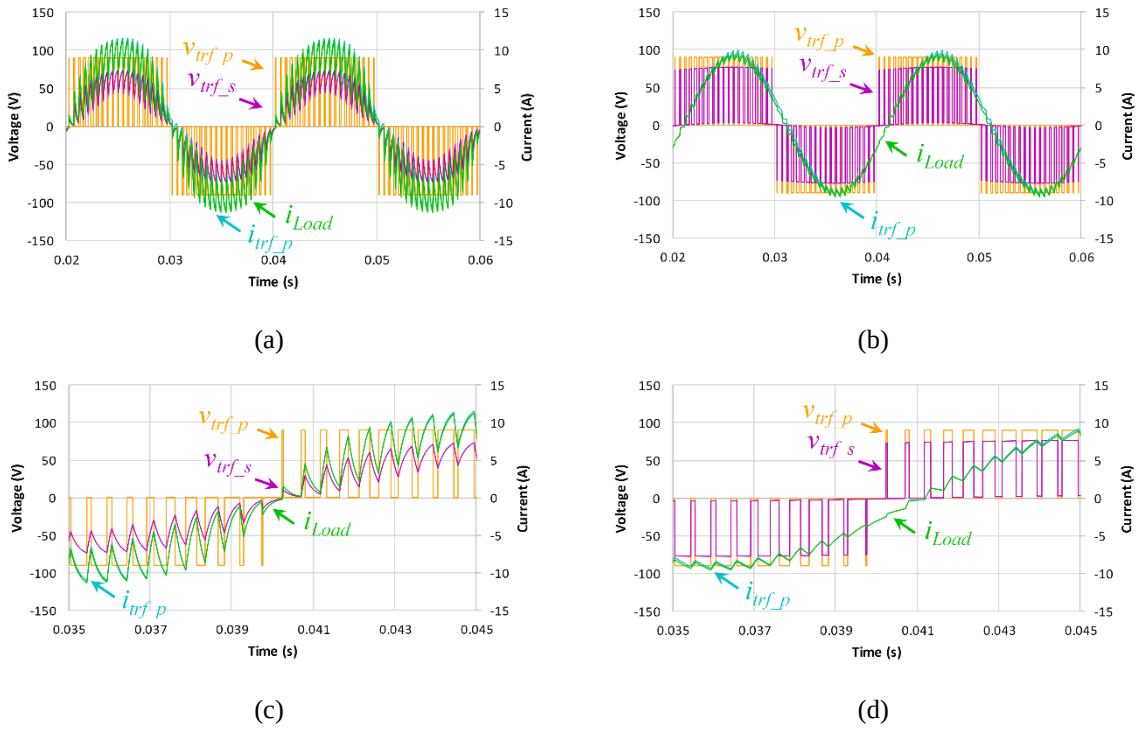

Figure Ap. K.2 – Simulation result of the computational model developed for the ferrite transformer T_{trf_f} considering voltages and currents on the primary and secondary side: (a) without coupling inductor; (b) with coupling inductor; (c) detailed results without coupling inductor; (d) detailed result with coupling inductor.

Based on this analysis, the experimental test was carried out with the remaining transformers, thus adding an inductor at the output, between the transformer and the load. The experimental results are presented in Figure Ap. K.3. Consequently, it is possible to verify that the voltages of both the primary, v_{trf_p}, and the secondary side, v_{traf_s}, present a pulsed waveform. In turn, the waveform of the current in the primary, i_{trf_p}, and in the secondary side, i_{trf_s}, presents a sinusoidal waveform.

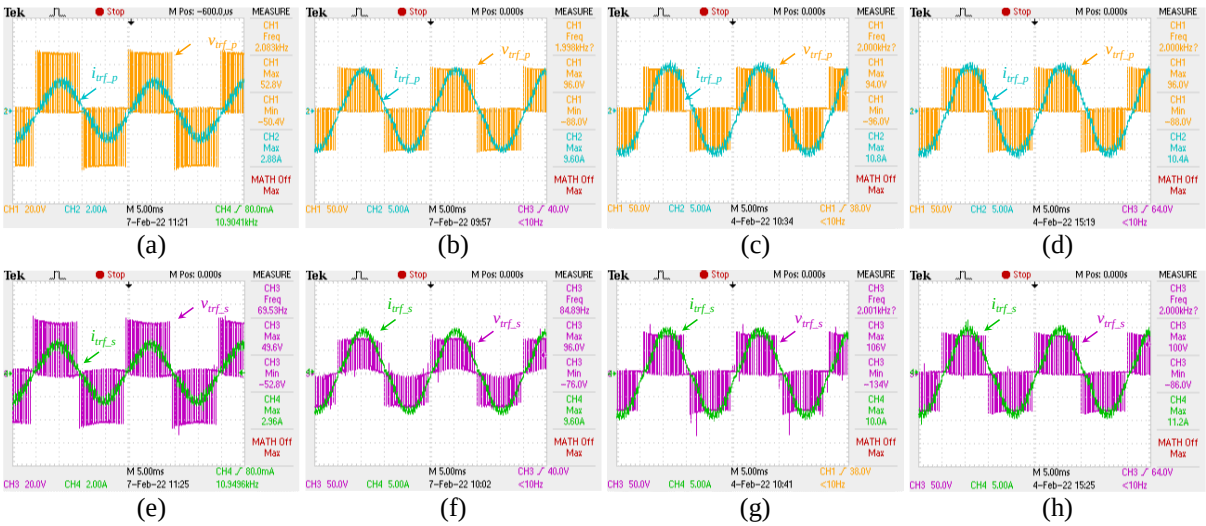

Figure Ap. K.3 – Experimental results of the primary voltage of the transformers (v_{trf_p}) and primary current (i_{trf_p}), with coupling inductor and a resistive load of 6.5 Ω: (a) T_{trf_f}; (b) T_{trf_fp}; (c) T_{trf_a}; (d) T_{trf1}; (e) T_{trf_f}; (f) T_{trf_fp}; (g) T_{trf_a}; (h) T_{trf1}.

Figure Ap. K.4 proves that with the insertion of the inductor, the v_{trf_s} presents a more square waveform, following better the waveform of v_{trf_p}. This effect is more evident in the T_{trf_f} compared to the results presented above in the section on the ferrite transformer analyses.

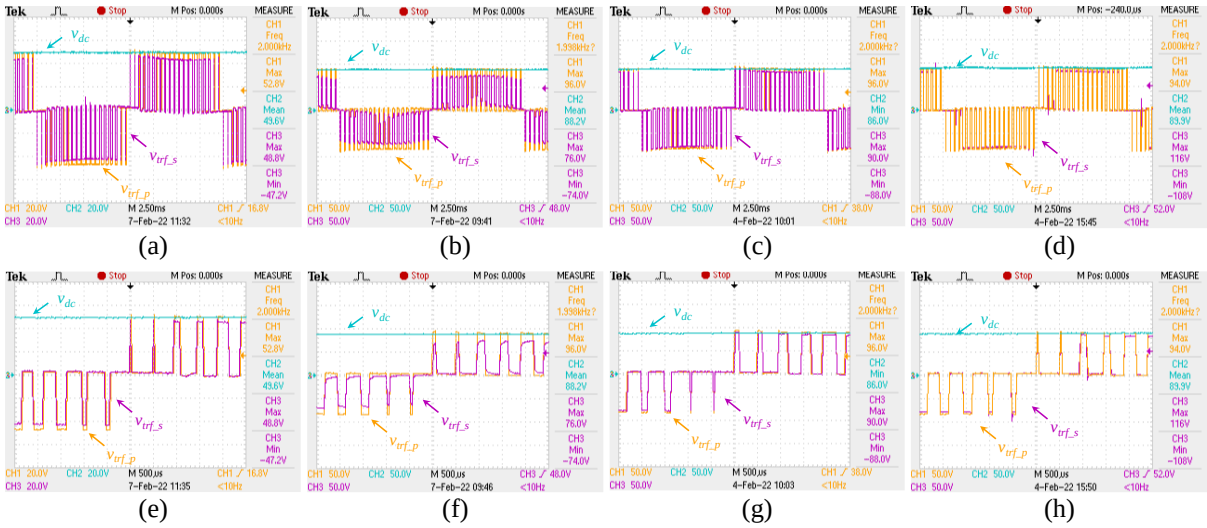

Figure Ap. K.4 – Experimental results of the primary and secondary voltages of the transformers (v_{trf_p} and v_{trf_s}) and the voltage on the dc-link (v_{dc}), with coupling inductor and a resistive load of 6.5 Ω: (a) T_{trf_f}; (b) T_{trf_fp}; (c) T_{trf_a}; (d) T_{trf1}; (e) T_{trf_f}; (f) T_{trf_fp}; (g) T_{trf_a}; (h) T_{trf1}.

Finally, the results obtained from the voltage and current waveforms in the load are presented in Figure Ap. K.5. To mention that the power converter is operating in an open-loop, with modulation of 80%.

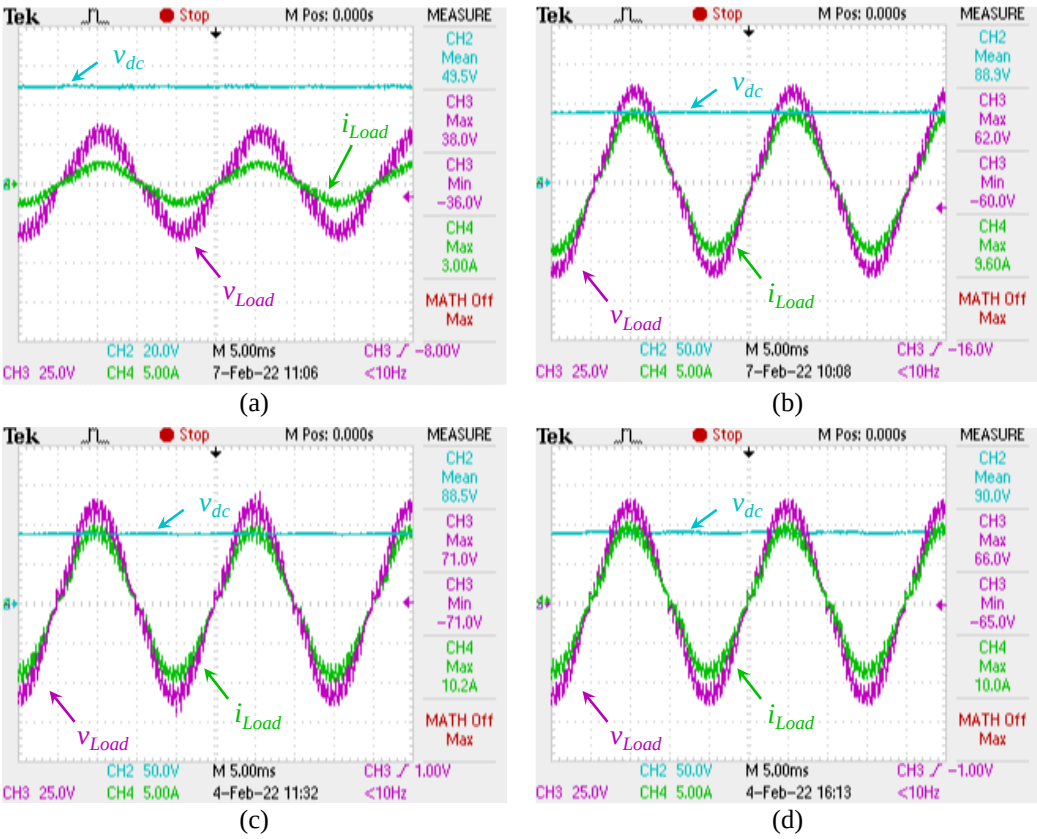

Figure Ap. K.5 – Experimental results of the voltage and current on the load (v_{Load} and i_{Load}) and the voltage on the dc-link (v_{dc}), with coupling inductor and a resistive load of 6.5 Ω: (a) T_{trf_f}; (b) T_{trf_fp}; (c) T_{trf_a}; (d) T_{trf1}.